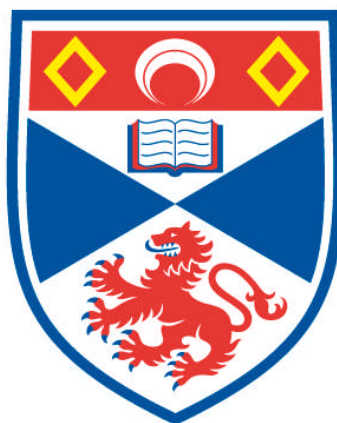


**DEVELOPMENT OF TUBULAR HYBRID DIRECT CARBON  
FUEL CELL AND PYROLYSIS OF BIOMASS FOR  
PRODUCTION OF CARBON FUEL**

**Alfredo Damiano Bonaccorso**

**A Thesis Submitted for the Degree of PhD  
at the  
University of St Andrews**



**2013**

**Full metadata for this item is available in  
Research@StAndrews:FullText  
at:**

**<http://research-repository.st-andrews.ac.uk/>**

**Please use this identifier to cite or link to this item:**

**<http://hdl.handle.net/10023/3597>**

**This item is protected by original copyright**

# **Development of Tubular Hybrid Direct Carbon Fuel Cell and Pyrolysis of Biomass for Production of Carbon Fuel**

A thesis submitted for the title of Ph.D.

by

**Alfredo Damiano Bonaccorso M.Sc.**

University of St Andrews

Supervised by Prof John T.S. Irvine



University  
of  
St Andrews

**Submitted October 2012**

I, Alfredo Damiano Bonaccorso, hereby certify that this thesis, which is approximately 45000 words in length, has been written by me, that it is the record of work carried out by me and that it has not been submitted in any previous application for a higher degree.

I was admitted as a research student in November 2008 and as a candidate for the degree of Doctor of Philosophy in November 2012, the higher study for which this is a record was carried out in the University of St Andrews between 2008 and 2012.

Date ..... Signature of candidate .....

I hereby certify that the candidate has fulfilled the conditions of the Resolution and Regulations appropriate for the degree of Ph.D. in the University of St Andrews and that the candidate is qualified to submit this thesis in application for that degree.

Date ..... Signature of supervisor .....

In submitting this thesis to the University of St Andrews I understand that I am giving permission for it to be made available for use in accordance with the regulations of the University Library for the time being in force, subject to any copyright vested in the work not being affected thereby. I also understand that the title and the abstract will be published, and that a copy of the work may be made and supplied to any bona fide library or research worker, that my thesis will be electronically accessible for personal or research use unless exempt by award of an embargo as requested below, and that the library has the right to migrate my thesis into new electronic forms as required to ensure continued access to the thesis. I have obtained any third-party copyright permissions that may be required in order to allow such access and migration, or have requested the appropriate embargo below.

The following is an agreed request by candidate and supervisor regarding the electronic publication of this thesis:

Access to printed copy and electronic publication of thesis through the University of St Andrews.

Date ..... Signature of candidate.....

Date ..... Signature of supervisor .....

# Acknowledgments

This research is dedicated to my parents and my girlfriend Bianca who supported me every day with their love and patience. I would also like to thank a close friend, Fausto, for his unwavering trust in my abilities. Of course heartfelt thanks also go to all of the people I met in St Andrews who helped my personal and professional growth.

I would also like to extend my gratitude to my supervisor, Professor John TS Irvine, for both giving me the opportunity to work with him and leading my professional development.

Many thanks also go to Mr Robert Marshall for helping me with the pyrolysis process, as well as for the varied and interesting conversations we sustained, both professional and personal.

A warm thank you to all of the JTSI group, especially Enrique, Thui, Harold, Cristian and Cairong, who supported my project and ideas, assisting me in better comprehending scientific problems and ultimately for being good friends.

Thanks also to all the member of staff who helped me with different tests, especially Mrs Sylvia for TGA and surface analysis and Ross for the SEM.

## ABSTRACT

This study involved two avenues of investigation: a new concept of Direct Carbon Fuel Cell (DCFC) and the production of carbon from biomass.

The new concept of DCFC merges a solid oxide electrolyte and a molten carbonate electrolyte called the “hybrid direct carbon fuel cell” using tubular geometry. The tubular cell was chosen for several reasons, such as sealing process, reduction of stress during the sintering process and reduction of the final size of the stack. In addition, it makes the fuelling process easier than in planar geometry.

The previous tests carried out on tubular hybrid direct carbon fuel cell at the University of St Andrews showed promising results. In fact, a power of 85 mW was achieved at 800°C. However this temperature was too high and so the focus of the new project was on decreasing the operating temperature to 650°C, replacing the YSZ electrolyte used in the previous configuration with an electrolyte such as GDC, which showed better performance at low temperature.

YSZ was substituted for GDC in the anodes and cathode in order to prevent an increase in the interface resistance due to the possible reaction between electrolyte and electrodes at the interface.

Anodes with different proportions of NiO and GDC were investigated in order to understand the electrochemical phenomena in the presence of GDC compared to YSZ.

Three different electrical configurations were investigated by AC impedance studies because the electrochemistry of the cell changes as function of the position and the surface of the current collector, which is dipped into the anode chamber. Performance improved when the surface area of the current collector increased, which combined a silver wire with strip of nickel mesh. Two types of seals (552 ceramabond and ToKu adhesive) and the sealing process were also studied in order to prevent leakage, which affects the performance of the entire cell. The leakages were reduced using a composite seal composed of alumina paste and a combination of flexi disks of mica and alumina fibre disk.

In the preliminary test using 70-30% wt NiO GDC and LSM-GDC with composite nickel mesh and silver wire current collector and the composite seal, a promising value of power of 191mW was achieved at 700°C using GDC electrolyte.

The value of power was improved by reducing the thickness of the electrolyte and the cathode manufacture. However, the best performance was achieved when LSM-GDC cathode was replaced with LSCF- GDC. LSCF was chosen for the promising results shown at low temperature, and a power of 240mW was achieved at 650°C when it was used as the cathode in our cell.

The carbon fuel used for these fuels was a medium density fibreboard pyrolysed at 500°C. The choice of this carbon fuel was based on the production and characterization of carbon fuels in this project. The investigations were focused on the production and characterization of carbon fuel from biomass such as MDF

and pellet wood produced by pyrolysis. Secondary products resulting from the pyrolysis process were also investigated in order to use them as alternative fuels. All of the types of carbons produced and 3 commercial carbons were characterized by SEM, XRD, infrared spectroscopy, surface area and elemental analysis, while their electrochemical performances were investigated by hybrid direct carbon fuel cell with planar geometry. The investigations highlight that the structure of the carbon used does not affect the performance of the cell, which is in fact affected by the ability of the carbon to gasify in the presence of carbonate.

# Contents

<b>1. INTRODUCTION .....</b>	<b>1</b>
<b>1.1 ENERGY SOURCES AND GLOBAL CONSUMPTION .....</b>	<b>1</b>
<b>1.2 ECONOMIC SITUATION AND FUEL SOURCES.....</b>	<b>4</b>
<b>1.3 ENVIRONMENTAL AND HEALTH ISSUES.....</b>	<b>8</b>
<b>1.4 RENEWABLE ENERGY AND GLOBAL AND EU POLICY .....</b>	<b>12</b>
<b>1.5 AIMS OF THESIS.....</b>	<b>14</b>
<b>1.6 FUEL CELL TECHNOLOGY.....</b>	<b>15</b>
1.6.1. Background.....	16
1.6.2. Solid oxide fuel cells .....	24
1.6.3. Molten Carbonate Fuel Cell .....	28
1.6.4. Direct Carbon Fuel Cell .....	33
1.6.4.1. History of DCFC.....	36
1.6.4.2. DCFC with molten carbonate electrolyte.....	37
1.6.4.3. Molten Hydroxide Electrolyte .....	39
1.6.4.4. DCFC with solid electrolyte.....	42
1.6.4.5. DCFC combining SOFC and Liquid anode.....	46
<b>1.7. REFERENCES.....</b>	<b>51</b>
<b>2. BACKGROUND .....</b>	<b>56</b>
<b>2.1 ANALYSIS OF HYBRID DIRECT CARBON FUEL CELL.....</b>	<b>56</b>
2.1.1. Principles.....	58
2.1.2. Mechanism of electrochemical oxidation of carbon .....	60
2.2.1. Components and design of HDCFC.....	65
<b>2.3. ELECTROLYTE .....</b>	<b>67</b>
2.3.1. Solid electrolyte .....	67
2.3.2. Secondary electrolyte (carbonate salts).....	70
2.3.3. Composition of Carbonate salts.....	72
2.3.4. Activity of carbonate salts on cell performance.....	73
<b>2.4. CATHODE .....</b>	<b>75</b>
2.4.1. Structure and properties of cathode.....	76
2.4.3. Current collector.....	82
<b>2.5. ANODE .....</b>	<b>83</b>
2.5.1. Properties of anode materials.....	84
2.5.2. Microstructure .....	85
2.5.3. Triple phase boundary and mechanism of reaction .....	86
<b>2.6. CARBON FUEL IN HYBRID DIRECT CARBON FUEL CELL .....</b>	<b>87</b>
2.6.1. Roles of the carbon fuel in HDCFC.....	88
2.6.2. Pyrolysis process .....	91
2.6.3. Biomass.....	92
2.6.4. Bio-carbon .....	95
<b>2.7. REFERENCES.....</b>	<b>97</b>
<b>3.0. EXPERIMENTAL PART .....</b>	<b>100</b>
<b>3.1. PYROLYSIS PLANT DESIGN.....</b>	<b>100</b>
3.1.1. Reactor.....	101
3.1.2. Condenser and blocking solution.....	103
<b>3.2. CELL MANUFACTURING AND ANALYTIC TECHNIQUE. ....</b>	<b>104</b>
3.2.1. Tape casting.....	104

3.2.2.	<i>Principles</i> .....	105
3.2.3.	<i>Slurry components</i> .....	106
3.2.3.1.	<i>Solvent</i> .....	107
3.2.3.2.	<i>Binder and plasticizer</i> .....	108
3.2.3.3.	<i>Surfactant</i> .....	109
<b>3.3.</b>	<b>X-RAY DIFFRACTION ANALYSIS (XRD)</b> .....	<b>109</b>
3.1.1.	<i>Theory of X-ray diffraction</i> .....	109
3.3.2.	<i>Diffraction of X-ray in crystal structure</i> .....	112
3.3.3.	<i>Miller indices</i> .....	115
3.3.4.	<i>X-ray diffraction methods</i> .....	115
<b>3.4.</b>	<b>SCANNING ELECTRON MICROSCOPY (SEM)</b> .....	<b>116</b>
3.4.1.	<i>Principles</i> .....	118
3.4.2.	<i>EDS</i> .....	120
3.4.2.1.	<i>Instruments</i> .....	121
<b>3.5.</b>	<b>THERMO GRAVIMETRIC ANALYSIS (TGA)</b> .....	<b>121</b>
3.5.1.	<i>Principles</i> .....	122
3.5.2.	<i>Instrument</i> .....	123
<b>3.6.</b>	<b>SURFACE AREA ANALYSIS</b> .....	<b>123</b>
3.6.1.	<i>BET theory</i> .....	124
3.6.2.	<i>BET plot</i> .....	125
<b>3.7.</b>	<b>IMPEDANCE SPECTROSCOPY</b> .....	<b>126</b>
3.7.1.	<i>Principles</i> .....	127
3.7.2.	<i>Impedance spectroscopy applied to ceramic electrolyte</i> .....	129
3.7.3.	<i>Two-terminal a.c. impedance experimental set-up</i> .....	131
3.7.3.1.	<i>Electrodes</i> .....	131
3.7.3.2.	<i>Furnace and jig for two-terminal a.c. impedance</i> .....	132
3.7.4.	<i>Fuel cell testing</i> .....	134
3.7.5.	<i>Description of an electrochemical response from the electrical circuit</i> .....	135
<b>3.8.</b>	<b>REFERENCES</b> .....	<b>137</b>
<b>4.0.</b>	<b>CARBON FUEL CHARACTERIZATION</b> .....	<b>137</b>
<b>4.1.</b>	<b>RESULTS AND DISCUSSION</b> .....	<b>137</b>
<b>4.2.</b>	<b>MEDIUM DENSITY FIBREBOARD</b> .....	<b>137</b>
<b>4.3.</b>	<b>PELLET WOOD</b> .....	<b>138</b>
<b>4.4</b>	<b>. THERMOGRAVIMETRIC STUDIES OF BIOMASSES</b> .....	<b>139</b>
4.4.1.	<i>Studies of degradation mechanism of biomass</i> .....	140
4.4.2.	<i>IR investigation of degraded biomass</i> .....	146
<b>4.5.</b>	<b>PYROLYSIS PARAMETERS</b> .....	<b>148</b>
<b>4.6.</b>	<b>PRODUCTION OF SECONDARY PRODUCTS FROM PYROLYSIS</b> .....	<b>149</b>
4.6.1.	<i>Characterization of bio oil</i> .....	150
4.6.2.	<i>Bio-oil characterization</i> .....	152
<b>4.7.</b>	<b>CHARACTERIZATION OF CARBON FUEL</b> .....	<b>158</b>
4.7.1.	<i>Carbon from biomass</i> .....	159
4.7.2.	<i>Activated carbon</i> .....	163
4.7.3.	<i>Aerogel fiberboard carbon</i> .....	167
4.7.4.	<i>Beer carbon</i> .....	170
4.7.5.	<i>Graphite</i> .....	176
4.7.6.	<i>Carbon Black</i> .....	178
4.7.7.	<i>Studies of thermal stability on commercial and non-commercial carbons</i> .....	181
<b>4.8.</b>	<b>ELECTROCHEMICAL REACTIVITY OF SEVERAL CARBON FUELS</b> .....	<b>190</b>
<b>4.9.</b>	<b>SUMMARY</b> .....	<b>194</b>

<b>5.</b>	<b>CHARACTERIZATION OF SOLID OXIDE FUEL CELL COMPONENTS .....</b>	<b>193</b>
<b>5.1.</b>	<b>RESULTS AND DISCUSSIONS .....</b>	<b>193</b>
5.1.1.	<i>Oxygen Ion membranes.....</i>	194
5.1.1.1.	<i>Studies of electrochemical performance of <math>Y_{0.08}Zr_{0.92}O_{1.96}</math> and <math>Ce_{0.9}Gd_{0.1}O_{1.95}</math>.....</i>	197
5.1.1.2.	<i>Reduction studies of <math>Ce_{0.9}Gd_{0.1}O_{1.95}</math> under 5% hydrogen .....</i>	201
5.1.2.	<i>Anode .....</i>	203
5.1.2.1.	<i>Studies of compatibility of different compositions of NiO-GDC .....</i>	203
5.1.2.2.	<i>Studies of electrical performance of anode with different composition .....</i>	206
5.1.3.	<i>Cathode.....</i>	212
5.1.3.1.	<i>Studies of LSM-YSZ and LSM-GDC cathodes.....</i>	212
5.1.3.2.	<i>Studies of LSM-GDC tape and painted LSM-GDC .....</i>	218
5.1.3.3.	<i>Studies of LSM-GDC tape and painted LSCF-GDC.....</i>	221
5.1.3.4.	<i>Comparison of a commercial <math>La_{0.4}Sr_{0.4}MnO_{3-\delta}</math> and <math>La_{0.4}Sr_{0.6}Co_{0.2}Fe_{0.8}O_{3-\delta}</math>.....</i>	223
<b>5.2.</b>	<b>SUMMARY.....</b>	<b>227</b>
<b>5.3.</b>	<b>REFERENCES .....</b>	<b>228</b>
<b>6.</b>	<b>ELECTROCHEMICAL PERFORMANCE OF DIFFERENT CONFIGURATION OF HDCFC .....</b>	<b>230</b>
<b>6.1.</b>	<b>INTRODUCTION .....</b>	<b>230</b>
<b>6.2.</b>	<b>INVESTIGATION OF ELECTRICAL CONFIGURATIONS.....</b>	<b>231</b>
6.2.1.	<i>Cell manufacturing .....</i>	233
6.2.2.	<i>Electrochemical investigation by ac impedance .....</i>	235
6.2.3.	<i>Nickel mesh and NiO stability in carbonate salts .....</i>	239
<b>6.3.</b>	<b>INVESTIGATION OF LEAKAGES BY OPEN CIRCUIT VOLTAGE. ....</b>	<b>243</b>
6.3.1.	<i>Studies of microstructure of sealing materials.....</i>	246
6.3.2.	<i>Effect of composite seals on the OCV voltage.....</i>	249
<b>6.4.</b>	<b>STUDIES OF HYBRID DIRECT CARBON FUEL CELL CONFIGURATIONS .....</b>	<b>252</b>
6.4.1.	<i>Presence of <math>CO_2</math> has a major influence on DCFC behaviour.....</i>	260
6.4.2.	<i>Effect of GDC thickness on the <math>R_s</math> value.....</i>	265
<b>6.5.</b>	<b>EFFECT OF DIFFERENT TYPE AND MANUFACTURE OF CATHODE ON FUEL CELL PERFORMANCE.....</b>	<b>268</b>
6.5.1.	<i>Studies of painted LSM-GDC cathode on HDCFC performance.....</i>	268
6.5.2.	<i>Studies of painted LSCF-GDC cathode on HDCFC performance.....</i>	270
6.5.3.	<i>Effect of LSCF on the operation temperature .....</i>	274
<b>6.6.</b>	<b>SUMMARY.....</b>	<b>276</b>
<b>6.7.</b>	<b>REFERENCES .....</b>	<b>277</b>
<b>7.</b>	<b>CONCLUSIONS.....</b>	<b>277</b>
<b>7.1.</b>	<b>FUTURE WORK.....</b>	<b>282</b>

## Abbreviations and symbols

<b>Tl</b>	<b>Low temperature</b>
<b>Th</b>	<b>High temperature</b>
<b>SOFC</b>	<b>Solid oxide fuel cell</b>
<b>MCFC</b>	<b>Molten carbonate fuel cell</b>
<b>AFC</b>	<b>Alkaline fuel cell</b>
<b>PAFC</b>	<b>Phosphoric acid fuel cell</b>
<b>PEMFC</b>	<b>Polymeric electrolyte membrane fuel cell</b>
<b>DCFC</b>	<b>Direct carbon fuel cell</b>
<b>HDCFC</b>	<b>hybrid direct carbon fuel cell</b>
<b>Q<sub>fc</sub></b>	<b>Heat produced inside the fuel cell</b>
<b>Q<sub>rev,fc</sub></b>	<b>Heat produced inside a reversible fuel cell</b>
<b>μ</b>	<b>Thermodynamic Efficiency</b>
<b>Δ<sub>r</sub>H</b>	<b>Enthalpy of reaction</b>
<b>Δ<sub>r</sub>S</b>	<b>Entropy of reaction</b>
<b>ΔG<sup>0</sup></b>	<b>Free Energy of Gibbs standard</b>
<b>TEC</b>	<b>Thermal Expansion Coefficient</b>
<b>C<sub>rs</sub></b>	<b>Carbon with reactive sites</b>
<b>GDC</b>	<b>Ceria Doped Gadolinia</b>
<b>YSZ</b>	<b>Yittria stabilized zirconia</b>
<b>LSM</b>	<b>Lanthanum Strontium manganese oxide</b>
<b>LSCF</b>	<b>Lanthanum Strontium Cobalt Iron oxide</b>
<b>LPGDC</b>	<b>Layer protection</b>
<b>TPB</b>	<b>Triple Phase Boundary</b>

# 1. Introduction

## 1.1 Energy sources and global consumption

Throughout the 20<sup>th</sup> and 21<sup>st</sup> centuries, significant industrial development has led to the exponential growth of the world population and consequently a demand for large quantities of energy needed to sustain the global community. This high energy demand has been met using energy sources such as coal, oil, natural gases and nuclear and hydro energy; the latter two have been relatively unsuccessful until recent years (Figure. 1.1) [1].

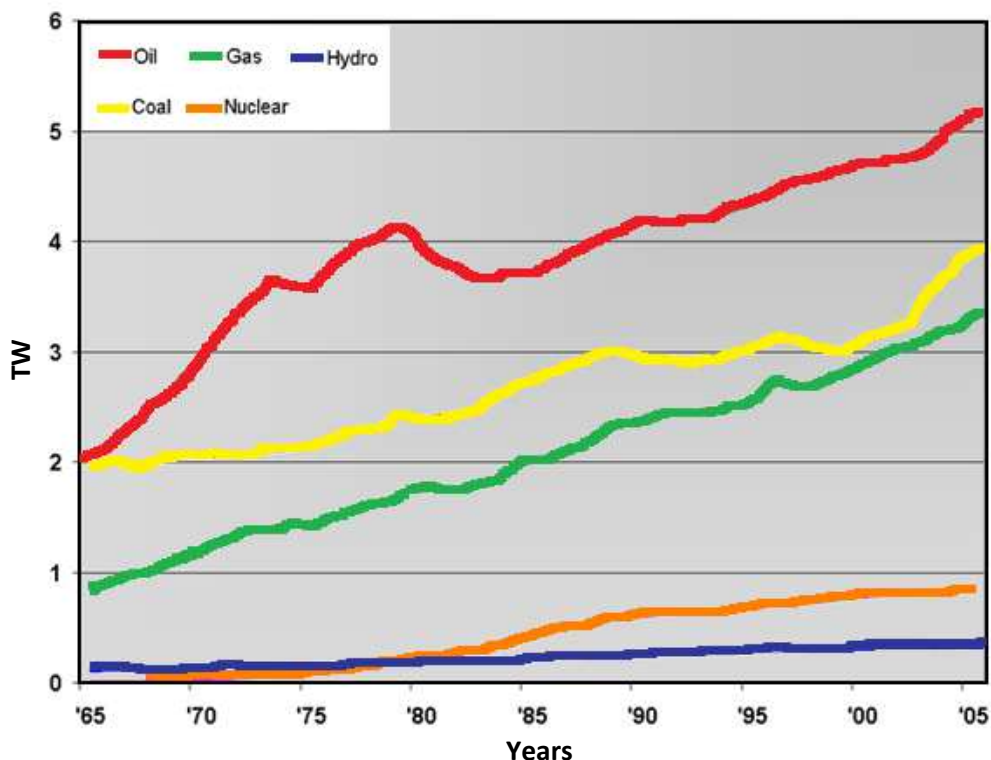


Figure 1.1- Rate of world power usage in Terawatts (TW) of different types of energy sources used from 1965 to 2005 - [1]

Over the last 18 years an important increase in energy supplied and has been observed and it has been quantified by the U.S Energy Information Administration (EIA), as shown in table 1.1:

<b>Years</b>	<b>Energy supplied (TWh)</b>	<b>Power equivalent (TW)</b>
<b>1990</b>	102 569	15 821
<b>2000</b>	117 687	15 395
<b>2005</b>	133 602	18 258
<b>2008</b>	143 851	20 181

---

Table 1.1- Trend of world energy and power supply from 1990-2008. [1]

The increase in energy supplied was recorded at 27% between 1990 and 2008 by analysing the larger amount of energy produced by fossil fuel, the most used source for the production of energy derived from fossil fuels. In fact, in just three years an increase of 33.5% was measured by the U.S Energy Information Administration (EIA), followed by oil and natural gas, as shown in table 1.2:

Energy Source	Energy supplied (TWh)	%
Coal	48 208	33,5
Oil	38 497	26,8
Gas	30 134	20,9
Nuclear	828	5,8
<b>Others</b>	<b>18 733</b>	<b>13,0</b>
<b>Total</b>	<b>143 851</b>	<b>100</b>

Table 1.2- Data of energy power provided by IEA/OECD from 2005 to 2008 related to the type of energy source.

This significant increase in coal consumption is correlated to the industrial development of countries such as China and India over the last 20 years. Thanks to rapid industrial advancement, more than 3 billion people worldwide consume large amounts of energy. Data in the table is confirmed by looking at the energy consumption of major countries in 2008, based on the global energy database by Enerdata[2]. The database shows that energy consumption in the G20 rose by more than 5% in 2009. However, this increase in global energy consumption is actually driven by countries such as China and India with 111% and 42% respectively, meanwhile the total energy consumption is limited by a reduction in energy consumption of 4.5%, 5% and 8.5% for the EU-27 and the USA from 2000 to 2009, ultimately as a result of a reduction in economic activity.[3][4]

Countries	1990	2008	Growth
USA	89,021	87,216	-2 %
EU-27	40,240	40,821	1 %
Middle East	19,422	34,774	79 %
China	8,839	18,608	111 %
Latin America	11,281	14,421	28 %
Africa	7,094	7,792	10 %
India	4,419	6,280	42 %
<b>World</b>	<b>19,422</b>	<b>21,283</b>	<b>1%</b>

Table 1.3- IEA Energy Balances of non-oECD countries 2010 and IEA Energy Balances of oECD countries 2010.

## 1.2. Economic situation and fuel sources.

During the 20<sup>th</sup> century, industrial development, the advent of the automobile and the aeroplane and widespread electricity use increased the demand for fuel. Oil became the dominant fuel because it was cost efficient compared to other energy sources.

Excessive oil consumption over the last century has depleted the world's fuel reserves and as a result its price has increased sharply over the last 20 years. In fact, the price of oil has increased from 5 dollars per barrel in 1920 to 125 dollars in 2010; an increase of more than 1000% in less than a century. Moreover, the most dramatic increase in price was recorded in the last 10 years

as the price per barrel rose from 35 dollars in 2002 to 125 in 2010. Such a drastic increase can be attributed to a number of factors, such as the economic crisis, globalization and the rapid development of previously underdeveloped countries such as China and India. As a direct result of the extreme increase in oil prices, coal has become the principal fuel used to produce electrical energy. The largest amounts of coal are used in countries such as India and China, which are not bound by the Kyoto Protocol, as using coal enables them to be competitive in the global market.

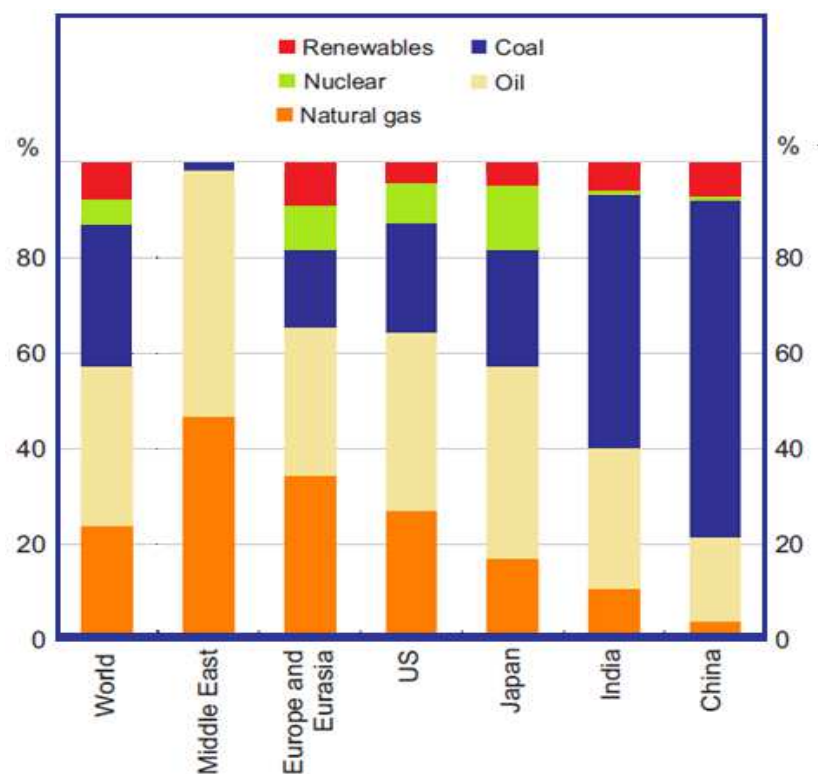


Figure 1.2 - Statistic review of BP2011 – percentages of different types of fuel as function of the geographic area.

Today one of the principal uses of coal is in the production of electrical energy because it is the cheapest fuel available, giving countries a competitive edge in the global market.

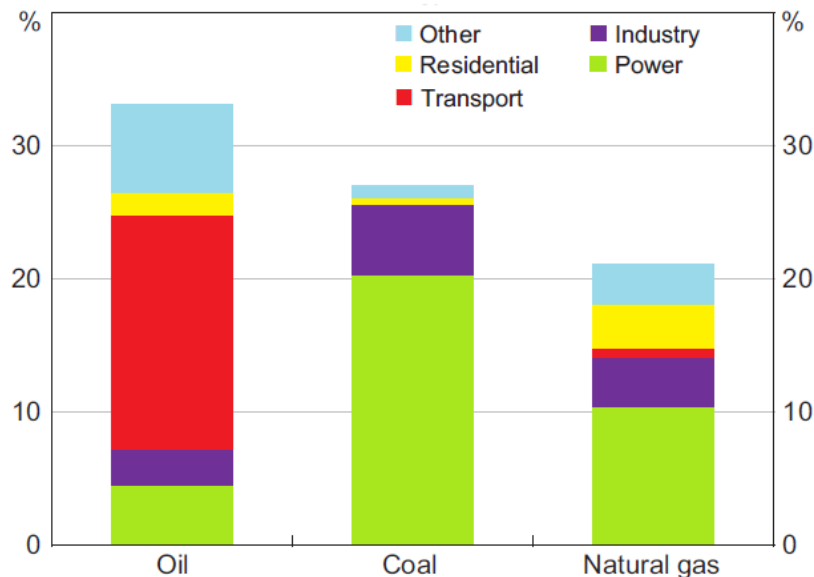


Figure 1.3- International Energy Agency source on the percentage of fossil fuels such as oil, coal and natural gas employed in different logistic sectors [5].

Coal is the most widely used fuel for the production of electricity not only because it is cost efficient but also because it is estimated that remaining coal reserves will last 190 years, compared with oil and natural gases which are estimated at 47 and 61 years respectively.

The price of coal is significantly lower than the price of natural gas and oil, firstly because the total amount of coal is higher than the amount of natural gas and oil. Secondly, price is dependent on demand.

In fact, if we observe the respective prices of coal, oil and natural gas, it is clear that coal is cheaper per unit of mass than other sources (table 1.4).

Fuels	1990	2010
Coal	1.4	3.0
Crude Oil	5.0	20.0
Gas	3.8	14

\*Price are expressed in American dollars and the value of dollars are normalized respect to 1 million of BTU produced

Table 4- Variation in price of different types of fuel between 1990 and 2010.

It is visible from the table that the increase in price is greater than coal and it coincides with the development of underdeveloped countries, as well as with the increase in world population over the last 20 years. However, these increases are also correlated to the depletion of fuel reserves. In fact, reserves of 250, 67 and 83 years were estimated for coal, oil and natural gas respectively in 1990 compared with 118, 46 and 58 years estimated today. Such significant reductions in the amount of remaining fuel are responsible for the sharp increase in fuel prices over the last 20 years. In fact, the price of coal has increased by 400%, oil by 100% and natural gas by 800% and it is likely that this steep upward trend will continue until the reserves have been completely exhausted.

The sharp increase in fuel price and rapid consumption of fuel increase the risk of a global economic collapse and subsequent social unrest.

### **1.3. Environmental and health issues**

The excessive consumption of fuel does not simply affect the global market as detailed previously, but it also has a huge impact on the environment. In fact, the combustion of generic fuel produces and lets a large quantity of poisonous substances into our atmosphere that affect the life of all human beings by contaminating air, water and plants/crops.

The direct combustion of these fuels produces smoke that is composed of two types of phases: one of these is a gaseous phase consisting of CO<sub>2</sub>, NO<sub>x</sub>, SO<sub>x</sub> and dioxin, and the other a solid fraction called 'particulate' that consists of micro particles of carbon. The production of these two phases is the main cause of environmental issues because while on the one hand the gaseous part affects the environment by producing acid rain, air pollution, global warming, hazardous waste, ozone depletion, smog and water pollution, on the other hand the second phase has a negative impact on the environment as it causes a reduction of irradiation on the earth, causing the classic effect of dimming warming. Furthermore, both phases are responsible for serious conditions affecting human health, such as lung cancer and disorders of the respiratory system.

To date, the temperature control instrument able to show fluctuations of the temperature of the land and oceans of the world has recorded an increase in temperature of  $0.74^{\circ}\text{C}$ , whilst a climate model has been hypothesised by the Intergovernmental Panel on Climate Change (IPCC), predicting an increase of  $1.5\text{-}1.9^{\circ}\text{C}$  in the lowest emission scenario to  $3.4\text{ - }6.1^{\circ}\text{C}$  in the highest[10]. Such a drastic increase in temperature can cause a rise in sea level, desertification and the extinction of living species and reduction of the agricultural yield. In order to avoid and combat the previously described phenomena, a significant change in the use of technologies and human lifestyle is necessary.

With regards to reducing of greenhouses gases, a specific protocol was drawn up at Kyoto. The greenhouse effect is the process by which absorption and emission of infrared radiation by gases in the atmosphere warms the planet. Greenhouse gases consist largely of steam, constituting 36%-70%, as well as carbon dioxide ( $\text{CO}_2$ ) at 9%–26%, bio-methane ( $\text{CH}_4$ ) at 4%–9% and ozone ( $\text{O}_3$ ) at 3%–7% percent [11][12][13].

In the last century, the amount of methane and  $\text{CO}_2$  gases has increased by 36% and 148% respectively since 1750, thus registering the highest levels at any given moment over the last 800,000 years. More than 75% of the increase of  $\text{CO}_2$  is dependent upon the combustion of fossil fuels, while the remaining 25% is due to land changes such as deforestation [14].

The percentage of greenhouse gas emissions is distributed in different areas of the world, as shown in figure 1.5:

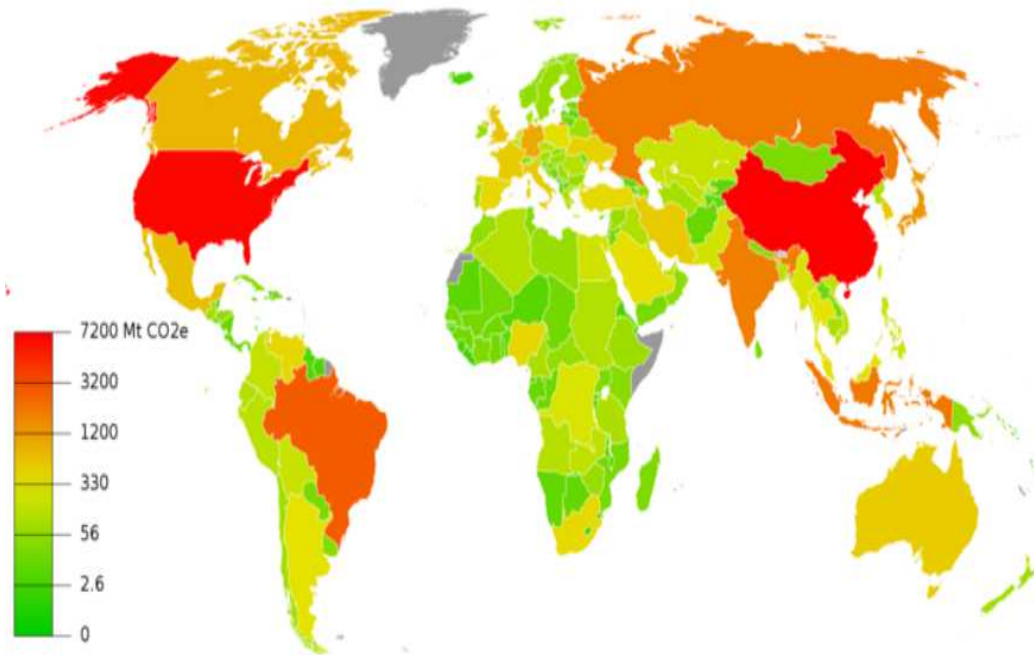


Figure 1.5- Map of the distribution of the total greenhouse gas emissions in 2005, including land-use change. [15][16]

North America and China are the biggest producers of greenhouses gases in the world. The effect of greenhouse gases is not only limited to global warming but is also the cause of acid rain, which affects plants, aquatic animals and infrastructure. In fact, when water comes into contact with gases such as  $\text{CO}_2$ ,  $\text{NO}_x$  and  $\text{SO}_x$ , acidic substances are produced as shown in equations 1.1 and 1.2.





Absorption of this acid into the ground and water changes their pH, affecting forests, freshwater, soil and aquatic life-forms, as well as damaging human health. For example, soil biology and chemistry can be seriously afflicted because the enzymes of soil microbes are sensitive to pH variations and this affects the characteristics of the soils, consequently affecting agriculture and plant growth. However, greenhouse gas emissions are not the sole environmental concern caused by the combustion of fuel, because, as previously explained, the combustion process leads to the production of small particles which cause global dimming. In fact, the particulates produced, which fluctuate in the atmosphere for a long time, affect the amount of direct radiation at the surface of the earth as they reflect sunlight. This reduction of the irradiation on the earth's surface affects the hydrological cycle which is responsible for the evaporation and precipitation of water on the earth's surface.

In addition, the production of particulate in the atmosphere is responsible for respiratory diseases and cancer. In fact, a large number of studies that have been carried out on both humans and animals reveal that subjects exposed to these micro particles were afflicted with asthma, lung cancer, cardiovascular issues and birth defects[17][18].

Furthermore, a large number of deaths have been attributed to this problem. Since 2000, 22,000-52,000 deaths per year in the United States and 200,000 deaths per year in Europe have been linked to the particulate effect [19].

In conclusion, the use of these types of fuel (coal, oil and natural gas), technology that combusts fuel to produce energy and the sharp increase in total global population are responsible for the rapidly worsening state of the environment, economy and human health. Furthermore, the demand for energy is growing so quickly that the fuel reserves are not enough to provide energy for the next few centuries. For all of these reasons, new energy sources must be studied and improved in order to make all countries energetically independent.

Currently, clean sources of energy and technology called ‘renewable energy’ are being used to reduce the effect of pollution. However, they are not yet well-developed enough to totally replace convention fuel, despite the fact that in the last 20 years the use of renewable energy has grown to reach 16% of the total energy supplied to the world, with 10% coming from traditional biomass which is used primarily for heating, 3.4% from hydroelectricity and 2.6% from solar panels and wind turbines [20].

#### **1.4. Renewable energy and Global and EU Policy**

The term “renewable energy” is attributed to sources that can be replenished naturally and thus have an unlimited use such as sunlight, wind, rain, tides and

geothermal heat. Since they are natural elements, they are not involved in combustion and their power can be converted into electrical energy by using specific devices such as wind turbines, thus reducing greenhouse gases and the impact of pollution. In addition, these energy sources are free and readily available which detracts from the consumption of fossil fuel and price fluctuations as a result of the free market.

Country blocks such as North America, the EU and Asia are investing extensively in wind power plants which have an annual growth rate of 30% with a worldwide installed capacity of 198 Giga-watts (GW) and cumulative global photovoltaic (PV) installations supplied an amount of electrical energy over 40 GW[21-22]. Yet these policies are not enough to counterbalance the high demand for energy, or to reduce gas emissions. To this end, new technologies must be improved and other types of renewable energy such as biomass and bio-oil must be used.

Biomass is defined as renewable organic material that comes from plants, forestry, agriculture and urban sources. Biomass can be converted to heat or electricity and even used as transport biofuel.

Biomass can be solid if from plants, wood and straw or gaseous if from organic waste and landfill waste, or indeed liquid if from harvests such as wheat, rapeseed and soy. During combustion the amount of carbon dioxide given off by this renewable energy source is counterbalanced by the amount absorbed when the plant grows. The greatest problem caused by biomass is borne from the

---

cultivation and fuel production processes used. In addition, the technology used to convert this energy source is not yet fully developed, which in turn reduces its efficiency. Despite this, the European commission has opened a National Biomass Action Plan to promote its use. The EU Biomass Action Plan (BAP) of December 2005 identified 32 key activities for boosting the bio-energy market (COM(2005)628final). One of these key actions stated that “the Commission will encourage Member States to establish national biomass action plans (nBAPs)”[21].

The directive on renewable energy set for all Member States will achieve a 20% share of energy from renewable sources by 2020 and a 10% share of renewable energy in the transport sector.

## **1.5 Aims of thesis**

The previous analysis of the various problems caused by the utilization of petrol, coal and natural gases have led us to find a solution and develop a technology that prevents these problems and permits us to use biomass and urban solid waste (wood, medium fiberboard, food residue, feedstock and cuttings), as fuel instead of other kinds of renewable energies previously described.

The advantages of these are easily visible compared to hydrogen energy.

In addition, this fuel has the full support and encouragement of the European Commission, as the biomass action plan is pushing scientists to focus their skills on the production of technology that is able to convert biomass fuel to electrical energy producing no negative impact on the environment. For this reason, research groups at the University of St Andrews decided to pay attention to direct carbon fuel cell technology that is able to use biomass and more specifically to a new concept of direct carbon fuel cell which is a combination of two fuel cell technologies: solid oxide fuel cell and molten carbonate fuel cell.

This project has a dual scope: Firstly, to improve the performance of the cell and secondly to improve the performance of the fuel by studying the structure, chemical composition and parameters of pyrolysis.

The bio-carbon which is used to feed the cell is obtained by pyrolysis of biomass. This process gives the chance to reuse heat produced by the combustion of biomass and in addition it provides bio-oil that can be used as secondary fuel.

## **1.6 Fuel cell technology**

Fuel cells are electrochemical devices that convert the chemical energy in fuels into electric energy directly, promising power generation with high efficiency.

They are essentially continuously operating batteries which produce electrical energy by oxidation of fuel such as methane, hydrogen and carbon usually using air. They are considered secondary energy sources since their principal fuel must be produced by using primary energy sources, such as nuclear, solar or wind energy.

### 1.6.1. Background

The concept of fuel cells has old origins. In fact, the first person to develop the concept was the British chemist R. Grove in 1839. The first cell consisted of two tubes filled with platinum and a solution of nitric acid. By connecting the two wires to a power source, the electrolysis of water produced hydrogen and oxygen gases which were held separate by the tubes. When the power source was not supplied to the cell, it ran inversely, producing electricity. This occurred because the hydrogen and oxygen gases react spontaneously, caused by the exothermic reaction they produce.

The first winning fuel cell was run by Francis Bacon in 1932. This cell used alkaline electrolyte, hydrogen and oxygen as reductant and oxidant respectively, while nickel was used as electrode. In 1959 Bacon and his colleagues built the first fuel cell with a power of 5kW [23]. As a result of this, a large number of scientists started studying and developing new types of fuel cell, especially in the aerospace field where PEMFC and AFC have been used by NASA in their

space craft. Nowadays, fuel devices are used in a wider range of applications than previously described, for example in the automotive sector.

Today, all of these fuel cells follow the same principles used by Grove in his prototype, but the anode, cathode and electrolyte are assembled to form a sandwich, as shown in figure 1.6

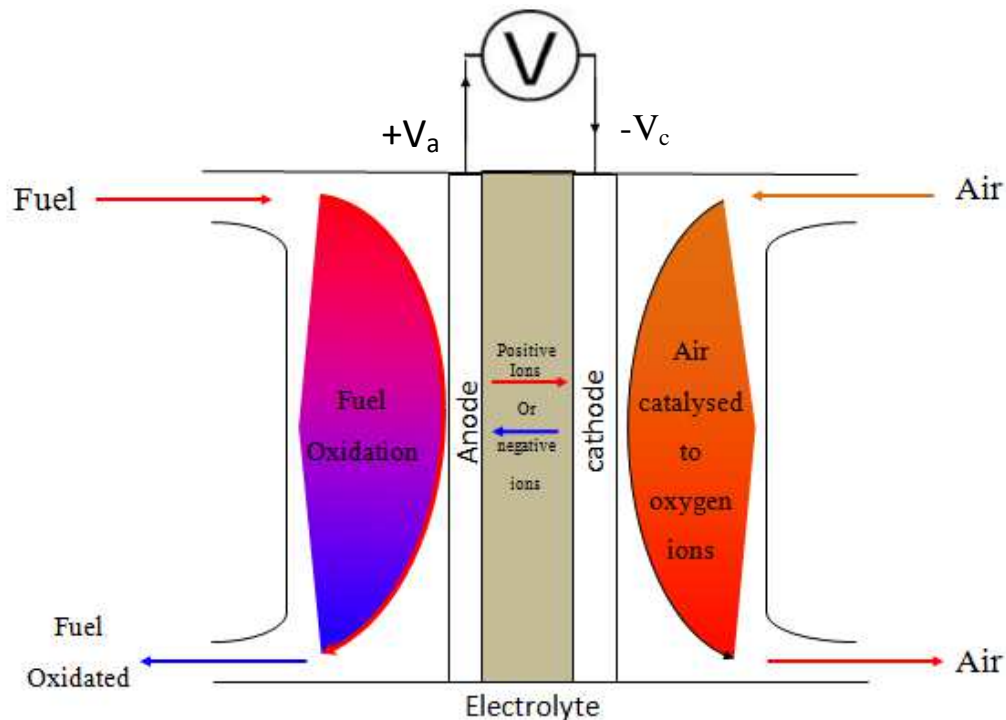


Figure 1.6 – Schematic representation of a fuel cell device.

In this schematic representation, we can observe different components in the fuel cell: anode, cathode and electrolyte. The circuit is closed by connecting anode and cathode with an interconnecting wire which helps electrons to migrate from anode to cathode. In fact, in the anodic chamber the fuel reacts with the ions which come from the electrolyte, reducing the fuel. Of course, the

conversion of the reaction is limited by the polarization degree of both electrodes. During oxidation, the electrons produced pass through electrode wire to be used by the cathode to reduce the secondary fuel feed into the cathode chamber (in general fuel is air and/or carbon dioxide). The ions that pass through the electrolyte depend on the nature of the electrolyte and they determine the type of cell.

The usual geometry of these kinds of device is flat in order to maximise the contact surface and the electrodes are thin and porous so as to minimize the resistance caused by the ion diffusion and increase the surface reactions.

The success of this type of device is due to different advantages that they pose compared to the commercial and mature technology that is used to produce electrical energy. These advantages are as follows:

- Fuel cell technology is not limited by the Carnot efficiency and for this reason the theoretical maximum value of efficiency recorded for this kind of device is higher than for a steam turbine.
- Emissions of a stationary fuel cell plant are 10 times less than those of a normal power generator. In fact, fuel cells which operate using hydrogen produce water and in general the amount of waste produced is small.
- Fuel cells are essentially simple with few or no moving parts.

- The fuel cell power plant produces very little noise compared to conventional steam or gas turbine power plants.
- Fuel cells do not produce large volumes of toxic substances and no ash residual formation is visible during fuelling of the cell.

Despite these advantages, the devices also pose disadvantages:

- Manufacturing problems are still limiting the performance of the cell. In fact, studies on sealing materials, anode degradation and high operating temperature are still being carried out to improve the performance of each component.
- There is no hydrogen infrastructure to supply coast-to-coast delivery of hydrogen fuel, for this reason fuel cells are being developed to provide alternative fuel storage and delivery methods such as DCFCs, MCFCs and PAFCs.
- Fuel cells are extremely expensive to manufacture. In fact, the cost for automotive applications is of \$10 to \$50 per kW for 4000hrs of lifespan while the cost for a stationary plant is \$1000 per kW for 40000hrs of lifespan (or life time) [23][24].

The main benefit of this device is its efficiency.

Fuel cells are more efficient than other devices that convert fuel into electrical energy because other devices are subject to the Carnot cycle.

---

However, before demonstrating this, a thermodynamic approach will be used to describe the benefit of fuel cell.

The fuel cell is a device which converts the free Gibbs energy of the combustion reaction of fuel with an oxidant into electrical energy. This conversion occurs fully in a theoretical and reversible system. The notion of a reversible fuel cell presupposes that the chemical potential produced by the fuel at the anode and cathode should be totally converted into the electrical potential at each gas composition without having any diffusion effect between the gaseous phases. This means that the total chemical energy can be expressed with the following equations:

**Chemical energy of the fuel = heat energy + electrical energy**

The balance between each energy can be represented by the 1<sup>st</sup> thermodynamic law.

$$\Delta H = Q - W \quad \text{Eq. 1.3}$$

Where  $\Delta H$  is the chemical energy which can be considered by the free Gibbs enthalpy of reactions, while  $W$  is the electrical energy that represents the work

done by the electrons crossing from anode to cathode per unit of time and  $Q$  in the heat energy produced during the chemical reaction.

$$W = E \cdot I(\Delta t) \quad \text{Eq. 1.4}$$

Where  $E$  is the electrical potential and  $I(\Delta t)$  is the current produced by the electron flow in a  $(\Delta t)$ .  $I(\Delta t)$  can be written as  $NF$  where  $N$  is the moles of electrons and  $F$  is the Faraday constant. If we consider the cell reversible, the  $Q_{fc}$  (heat produced) is equal to  $Q_{rev,fc}$  for a reversible condition we can say:

$$\Delta H = -nFE \quad \text{Eq. 1.5}$$

In a reversible cell when the work is maximized it is possible to approximate the  $nFE$  to the total energy, so if we write the energy as function of the free Gibbs energy we obtain the following equation:

$$\Delta G = \Delta H - T\Delta S \quad \text{Eq. 1.6}$$

A reversible system can be described by the 1<sup>st</sup> and 2<sup>nd</sup> laws of thermodynamics. If we consider hydrogen and oxygen respectively as fuel and oxidant, the

reaction which takes place produces electrons and  $\Delta G$  can be associated with the chemical energy.

$$\Delta G = \Delta G^0_{\text{products}} - \Delta G^0_{\text{reagent}} \quad \text{Eq. 1.7}$$

But  $\Delta G = -nFE$  so

$$E = - \frac{\Delta G}{nF} \quad \text{Eq. 1.8}$$

Since fuel cells use fuel which reacts and releases energy, the fuel cell efficiency is described as the ratio of the electrical energy produced to the heat that is produced by reaction between the fuel and oxidant (Enthalpy of reaction or  $\Delta H_r$ ).

$$\mu = \frac{W}{Q} = \frac{nFE}{\Delta H} \quad \text{Eq. 1.9}$$

If we calculate the efficiency ( $\mu$ ) for a cell that uses hydrogen as fuel, we can calculate an efficiency of 83%, while for a steam turbine that works at 400°C and condenses steam at 50°C, the efficiency is limited by the Carnot cycle and is calculated by the following equation:

$$\mu = 1 - \frac{T_l}{T_h} \qquad \text{Eq. 1.10}$$

And so an efficiency of 52 % is obtained. The efficiency is function of the temperature; in fact the efficiency increases with the increase in operating temperature. This is not valid for fuel cells because  $\Delta G$  decreases with an increase in temperature and this demonstrates that fuel cells are not limited by the Carnot cycle. This advantage of fuel cells makes them promising energy converter devices. Different types of fuel cells have been developed to satisfy market demand as well as to solve the problem of storage and delivery of hydrogen, which until now has been the main cause of the relatively limited development of this technology throughout the world. Each of these has specific advantages that are related to the type of fuel and electrolyte used and each type of cell is shown in figure 3.

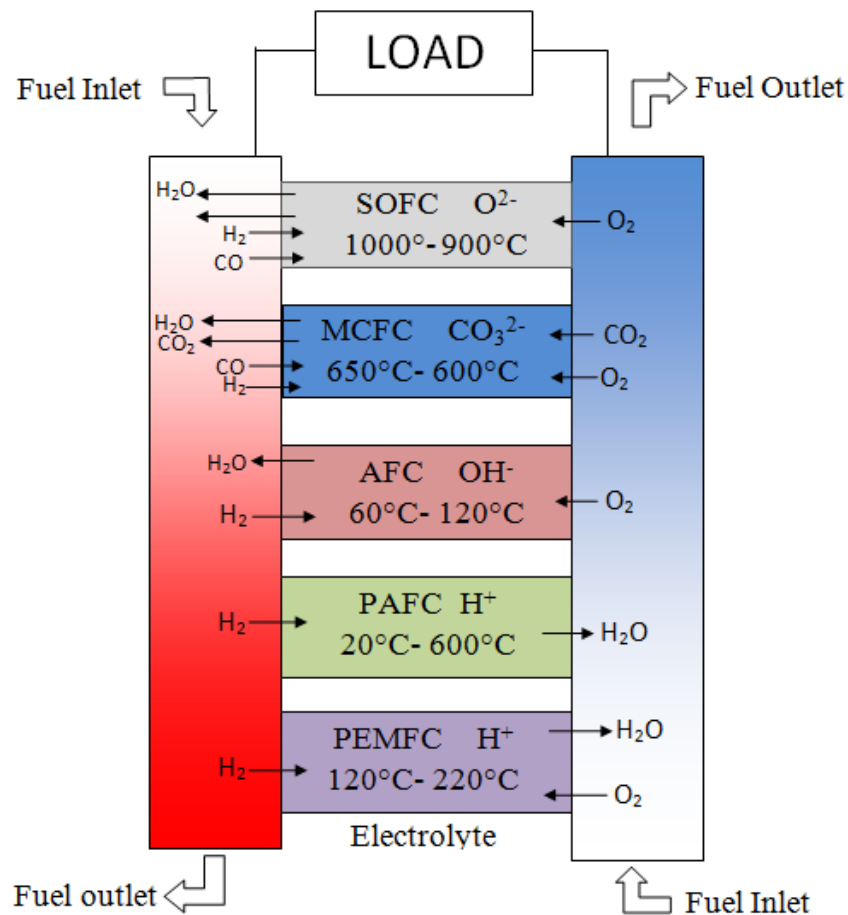


Figure 1.7 - Schematic representation of different types of fuel cells that are characterized by the type of electrolyte used and by the operation temperature [25].

### 1.6.2. Solid oxide fuel cells

The solid oxide fuel cells are characterized by a ceramic electrolyte which consists of zirconia stabilized with Ytria. This ceramic material has a very particular property: it is an insulator at low temperature but a conductor at high temperature. The first person to discover this was Nernst, who used a zirconia filament to produce an incandescent light.

The first use of zirconia as electrolyte dates back to 1930 when Baur and Preis used a crucible of zirconia stabilized with 15% of yttria as an electrolyte, whilst iron was used as anode and magnetite as cathode [26]. They observed that a current was produced when hydrogen or carbon monoxide were used as fuel and oxygen as oxidant, thus they realised that it could be used as a battery. However, many problems delayed the development of this technology, such as manufacturing issues, cathode degradation and high values of ohmic resistance. In the 1950s the first thin disk of stabilized zirconia was built with anode and cathode on its sides. Fuel and oxidant were brought into the anode and cathode respectively using alumina tube as shown in figure 1.9.

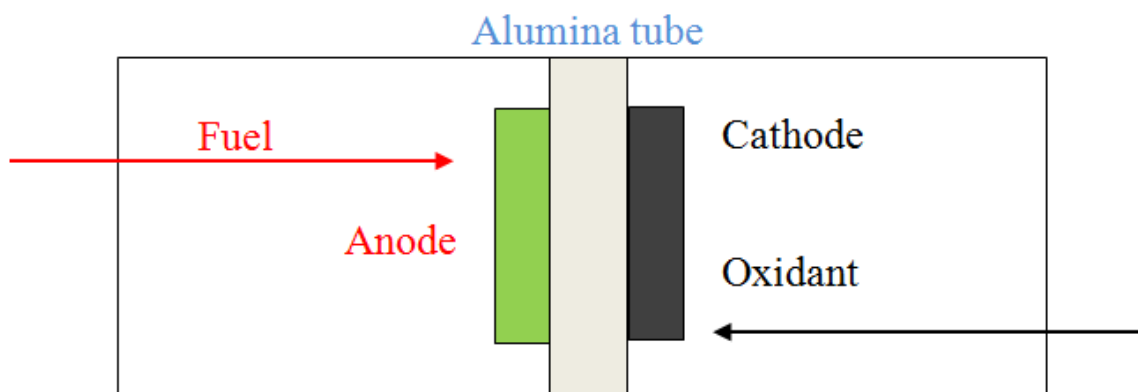


Figure 1.8- Schematic description of a single button cell composed of a solid oxide electrolyte, anode and cathode. An alumina tube was used to separate the fuel from the oxidant gas.

Based on the same principle, a multicell device (stack) was built, separating each cell by using an interconnector that united the cell and divided the gas

channel which supplied fuel at the anode and oxidant at the cathode, as shown in figure 1.10.

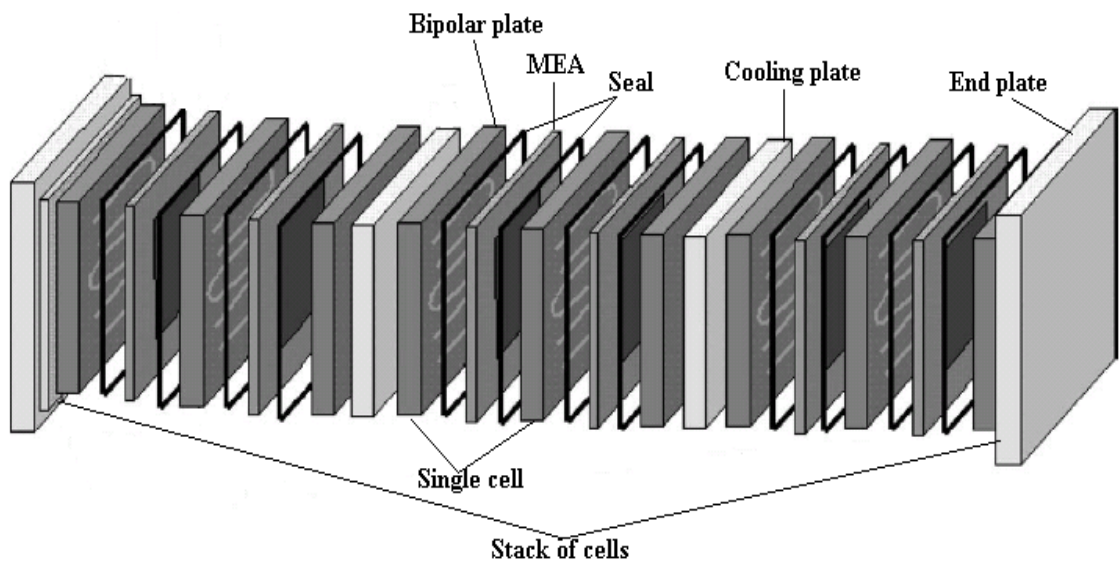


Figure 1.9 - Schematic description of a multi cell stack composed of a bipolar plate and final plate that closes the stack.

Several problems were observed in this cell, which were due to the sealing, different TEC between the anode, electrolyte and cathode that were the cause of cracks, manufacture of electrolyte, percolation between anode and electrolyte and cathode oxidation.

The geometry of the cell was another issue because it affected the contact surface and the electrochemical behaviour, influencing the performance and the output of the current.

Most of these problems have been solved, albeit not entirely. In spite of this, solid oxide fuel cells are well-developed.

At present, four of the most pertinent problems are the utilization, production and storage of the fuel supply for this kind of cell and the operation temperature.

The first problem is due to the storage and delivery of hydrogen, which must be stored under particular conditions. In fact, hydrogen partially reacts with oxygen ions, which results in a significant amount of fuel being obtained in the exhaust gases and affects overall efficiency of the cell. This correlation was studied by Kuang and the study demonstrates how the partial oxidation of the fuel affects the performance of the entire cell, estimating the maximum efficiency at 800°C at around 76%[27].

The second problem for SOFC is connected to the use of hydrocarbon. In fact, in this case, an internal reforming system has to be incorporated into the fuel cell system in order to produce the hydrocarbon.

In addition, the hydrocarbon produced must be purified of poison substances contained in the coal, which reduce the performance of the cell. In addition, using an internal reforming device and the fact that gas needs to be purified increase the cost of manufacture and maintenance of the system. All of these methods are really expensive as a result of the energy lost in keeping hydrogen liquefied, as well as the elevated cost of the storage tank itself.

The second problem is high operation temperature. In fact, this type of fuel cell has to work at high temperature because the performance of ceramic electrolyte decreases as an effect of the direct relation between temperature and the diffusion of oxygen ions.

---

High temperature can affect the resistance of the various seals and it can cause corrosion due to the reaction between oxygen and stainless steel. In addition to the physical chemical problems, the high operation temperature affects the total cost of the fuel cell both in terms of the energy that must be supplied to the device so as to maintain the temperature constant at 900°C and the cost of materials which have to resist the degradation phenomena.

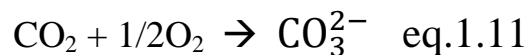
### 1.6.3. Molten Carbonate Fuel Cell

The first scientists able to run a molten carbonate fuel cell for 6 months were G.H.J. Broers and J.A.A. Ketelaar in 1960. After them, other people developed molten carbonate fuel cells improving the performance and reducing manufacture costs.

The efficiency, low manufacture costs and long operation life (40000 hrs) have made this technology a possible candidate for the production of electrical energy. The principles of this technology are similar to the SOFC, but rather than using a ceramic electrolyte as in SOFC, this fuel cell works by using a liquid electrolyte which consists of a mixture of carbonate salts of lithium, potassium and sodium that are contained in a porous ceramic structure.

One of the most important characteristics of molten carbonate fuel cells is that they can work using hydrogen and carbon monoxide.

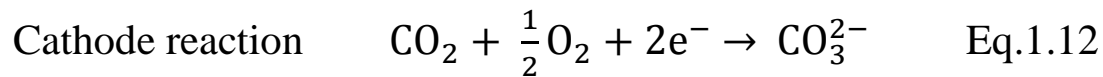
This allows for the use of a large variety of fuels such as natural gases, gaseous fuel derived from biomass or coal, gasoline, diesel and propane that are produced by an internal reforming process in a single step. The selling point of this type of cell is that these cells are able to work at lower temperature than the classic solid oxide fuel cell. This characteristic makes this type of fuel cell low cost and an ultra-clean technology and it has the advantage of the variety of fuels used. For all of these reasons, this technology is enjoying great success in the global market. In fact, today over 50 sub-megawatt units are working worldwide (Asia, Europe, USA). As explained previously, the molten carbonate fuel cell uses an alkaline carbonate mixed at different percentages (62:38 or 60:40 of Li and K carbonates) that provides oxygen ions. The electrochemistry of this device involves the formation of carbonate ions from the reaction between oxygen and carbon dioxide as shown in eq.1.11:



As explained previously, the molten carbonate fuel cell uses an alkaline carbonate mixed to different percentages (62:38 or 60:40 of Li and K carbonates) that provided oxygen ions.

---

The electrochemistry of this type of fuel cell involves the formation of carbonate ions from the reaction between oxygen and carbon dioxide as shown in eq.1.12



The carbonate ions pass through the electrolyte and anode to react with fuel, producing water and CO<sub>2</sub> as shown in figure 1.10.

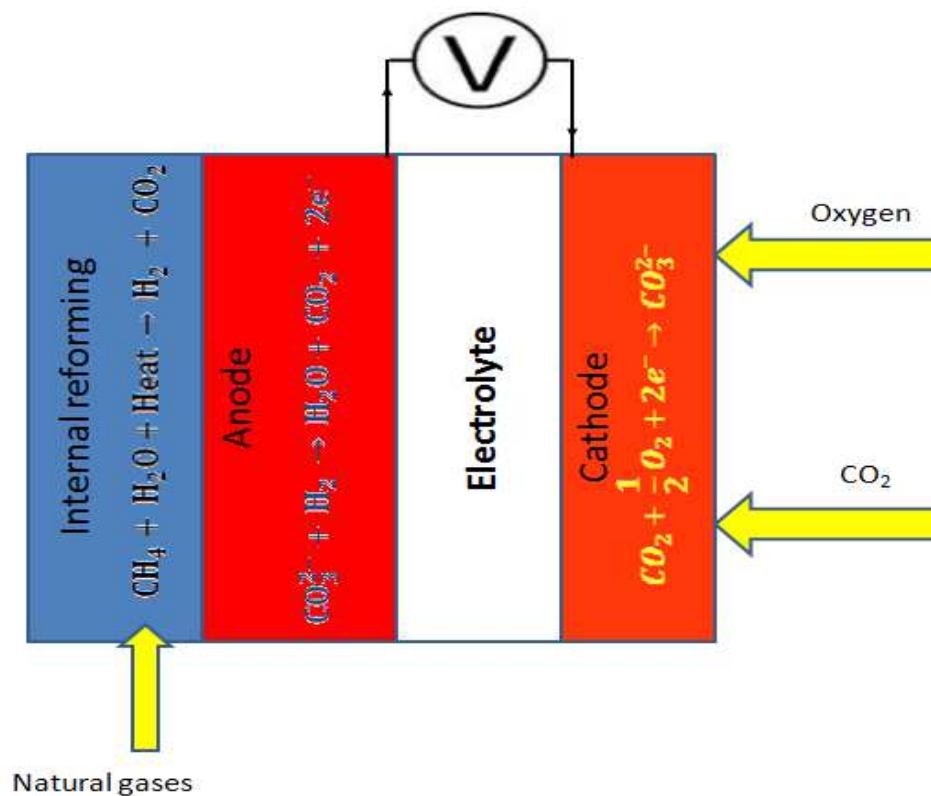


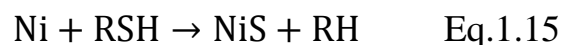
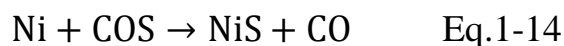
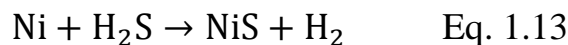
Figure 1.10- Schematic representation of a MCFC with internal reforming system connected directly to the anode.

Cathode reaction	$O_2 + CO_2 + 4e^- \rightarrow 2CO_3^{2-}$ (1)
Reforming reaction	$CH_4 + H_2O + Q \rightarrow H_2 + CO$ (2)
Anode reaction	$H_2 + CO_3^{2-} + H_2O \rightarrow CO_2 + 2H_2O + 2e^-$ (3)
Overall reaction	$2H_2 + O_2 \rightarrow 2H_2O$ (3)

Table 1.4- Mechanism of fuel oxidation in MCFC with internal reforming of natural gases.

The reforming reaction is a highly endothermic reaction and it must be carried out at a range of temperatures between 750°C and 850°C to produce the fuel for the anodic reaction, which is strongly exothermic, and it produces water that is a reactant for the reforming process. This analysis led us to understand that these two processes are complementary.

The greatest problem for this kind of cell is impurities, such as sulphur and halogens that are contained in the fuel before being reformed. They react with the catalyst metals, reducing the catalytic performance of the metal. In particular, sulphur show strong chemisorptions with nickel, as shown in the following mechanism:



Where the NiS is really stable. Different processes of desulfurization were studied to improve the performance of the cell and the reforming process, such as activated carbon bed, zeolite or the hydro-sulfurization process. In addition, new anodes were developed in order to reduce the reactivity of anode with the impurities contained in the fuel while new electrolyte and cathodes were developed in order to improve the performance of the cell. The principle materials used for anodes in molten carbonate devices were alloys of Ni-Al or Ni-Cr because they have a double effect: firstly they are good catalysts for reforming and for activating the reaction in the anode; secondly the alloys guarantee a life time of 18,000 hrs. In addition, it was observed that metals as Cu, Co, Al or Cr improved the dimensional stability of the anode, protecting the anode from cracks[28-30]. NiO material was used as cathode because it has small dissolution in carbonate and it is easily controlled by the electrolyte composition and by the operation pressure and temperature.

Today, other types of materials are used to reduce the dissolution of NiO such as  $\text{LiCoO}_2$  and  $\text{LiFeO}_2$  which do not show dissolution phenomena.

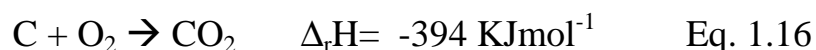
An electrolyte support, as explained previously, is used to separate the anode and cathode. It has to have a porous structure which permits ion conductivity and gas diffusion. In addition, it must immobilize the molten carbonate salts. In general, the electrolyte matrix consists of  $\text{LiAlO}_2$  which has shown promising results to date.

---

The molten carbonate fuel cell has operation limitations. Firstly, they require a recirculation system of CO<sub>2</sub> to prevent the decomposition of carbonate in the electrolyte and a flux of CO<sub>2</sub> has to be purged into the cathode. Secondly, they need a reforming step that converts a primary fuel such as natural gas or coal to a secondary fuel (hydrogen) which must be cleansed of poison substances such as halogens or sulphur, increasing the cost of fuel and maintenance of the device used to clean the primary fuel. Thirdly, the use of molten carbonate at high temperature produces a corrosion effect that reduces the lifetime of materials. For this reason the bipolar plates must be coated with alumina, or borosilicate [31] or Ti/Al/N/O composite material [32], co-deposited chromium and aluminium [33]. Lastly, they use hydrogen as fuel and the conversion of this fuel in the anodic chamber does not fully occur, reducing the performance and the efficiency of the cell.

#### 1.6.4. Direct Carbon Fuel Cell

This device shows a significantly greater efficiency than other fuel cells analysed until now, for two different reasons: Firstly the conversion of fuel in these kinds of device is total, as shown in equation 1.16:



The thermodynamic efficiency  $\mu$  can be calculated by the ratio between free energy of Gibbs  $\Delta G$  and enthalpy of reaction  $\Delta_r H$

$$\mu = \frac{\Delta G}{\Delta_r H} = 1 - T \frac{\Delta_r S}{\Delta_r H} \quad \text{Eq. 1.17}$$

The value of efficiency exceeds 100% because of the positive value  $\Delta_r S=1.6$  KJmol<sup>-1</sup>. As the enthalpy of reaction is larger than the entropy of reaction that depends on the temperature, the variation of the efficiency is negligible.

This value is significantly higher compared to the oxidation of hydrogen and methane and the value of efficiency exceeds 100% because of the positive value  $\Delta_r S=1.6$  KJ mol<sup>-1</sup> as shown in figure 6

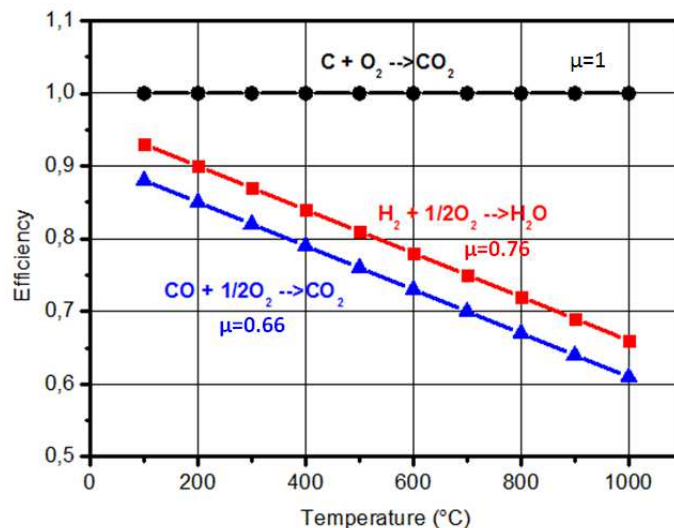


Figure 1.11 - Theoretical thermodynamic efficiency calculated by the ratio between free energy of Gibbs and enthalpy of reaction at a range of temperature between 100°C and 1000°C.

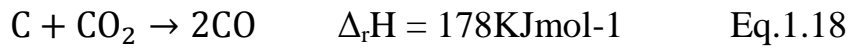
Secondly, the energy density provided by the carbon (20 kWh l<sup>-1</sup>) is ten times higher than for hydrogen (2.4 kWh l<sup>-1</sup>). In addition, the amount of CO<sub>2</sub> produced can be captured more easily than in a traditional thermal power plant. This kind of device can use biomass as carbon and in that case the balance of CO<sub>2</sub> sequestered is negative [34].

The mechanism of oxidation of carbon in the anode chamber is still under investigation. Cooper et al. suggested a mechanism where oxygen ions are desorbed and adsorbed on the carbon surface through a reactive site on the carbon surface (C<sub>rs</sub>) as shown in table 1.5 [35][36].

$C_{rs} + O^{2-} \rightarrow C_{rs}-O^{2-}$	1st oxygen adsorption	(1)
$C_{rs}-O^{2-} \rightarrow C_{rs}O + 2e^{-}$	fast discharge of 2e <sup>-</sup>	(2)
$C_{rs}O + O^{2-} \rightarrow C_{rs}O-O^{2-}$	Slow oxygen adsorption	(3)
$C_{rs}O-O^{2-} \rightarrow CO_{2,ad} + 2e^{-}$	Fast discharge e	(4)
$CO_{2,ad} \rightarrow CO_2$	Desorption	(5)

Table 1.5- Mechanism of carbon oxidation in the DCFC with molten carbonate electrolyte.

These reactions have high activation energy and they require high operation temperatures (500°C-1000°C) and a catalyst to be able to reduce the activation energy. However, the high operation temperature can cause CO<sub>2</sub> to react with carbon (Boudouard reaction)



CO can be oxidized again into CO<sub>2</sub>. This secondary oxidation affects the voltage because the amount of CO<sub>2</sub> is involved in secondary reaction. This reaction is a thermodynamically favoured at temperatures exceeding 750°C, but it can take place at temperatures lower than 750°C if it is catalysed by Ni or Fe metal, because they decrease the activation energy.

#### *1.6.4.1. History of DCFC*

The first concept of direct conversion of carbon to electrical energy in fuel cells was patented by William W. Jacques in 1896[37]. After Jacques, no scientists had been able to replicate his results and for this reason the scientific community lost interest in this type of technology. In 1970, Weaver and his co-worker were able to prove that the oxidation of carbon can open a new, promising window in power generation using carbon [38-40].

In the last 20 years, the development of DCFC has been significant and three different types of DCFC have been developed to date: DCFC with molten carbonate electrolyte, hydroxide DCFC and solid oxide fuel cell.

*1.6.4.2. DCFC with molten carbonate electrolyte*

DCFC with a molten carbonate electrolyte employs a mixture of carbonate of Li and K salt in mole percentage of 32% and 68% respectively and carbon in the anodic chamber. The utilization of carbonate salts in the anodic chamber drastically improves the contact between the solid part of the fuel and the anode layer. Furthermore, the carbonate salts show high ionic conductivity and good conductivity under CO<sub>2</sub> flow.

At present, John Cooper and co-workers are the main investigators of this technique at the Lawrence Livermore National Laboratory (LLNL, USA). Their concept of DCFC is based on an alumina tube whereby the mixture of carbon fuel and carbonate salts is deposited directly inside in contact with the anode that is supported on one side by a porous ceramic separator. On the other side of the porous ceramic, a cathode is in contact with air and CO<sub>2</sub>, where the latter is used to prevent the decomposition of carbonate salts on the other side the anode (see figure 1.11)[40-42]

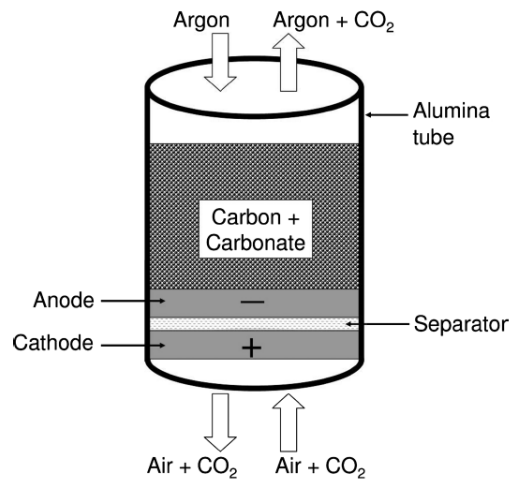


Figure 1.11- Schematic representation of a DCFC with molten carbonate electrolyte investigated by John Cooper at the Lawrence Livermore National Laboratory (LLNL, USA)[40-42].

The operation temperature of this kind of cell is higher than traditional molten carbonate fuel cells (range between 750°C and 850°C) because the carbonate inside the anodic chamber has to be totally molten to allow the diffusion of particles of carbon to the anode and to improve the surface of contact.

The inert separator of porous ceramic is saturated with molten carbonate and allows the carbonate ions to diffuse both into anodic chamber and in the cathode. However, this is a limitation of this type of cell because an internal or external recycle of CO<sub>2</sub> has to be installed in the cell to prevent the decomposition of carbonate.

The carbon dioxide is considered in the reaction both in anode and cathode as shown below:

Cathode reaction	$O_2 + CO_2 + 4e^- \rightarrow 2CO_3^{2-}$	(1)
Anode reaction	$C + 2CO_3^{2-} \rightarrow 3CO_2$	(2)
Overall reaction	$C + O_2 \rightarrow CO_2$	(3)

Table 1.6- Electrochemical reaction involved in the DCFC with solid electrolyte.

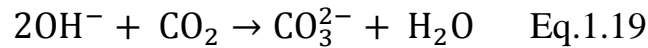
The cathode of this type of fuel cell is based on Li because it is catalytically active. The anode consists of small particle sizes of carbon connected to a layer of nickel metal that is used as current collector[35][36][43-45].

The main issue with this cell is due to the corrosive effect of carbonate in the anodic chamber and the limited choice of materials that can be used to prevent the corrosive effect. Nickel metal is one of the materials which are subject to the corrosive process, as will be explained later.

#### 1.6.4.3. Molten Hydroxide Electrolyte

Molten hydroxide is a variation of molten carbonate DCFC because it uses an alkaline hydroxide instead of using alkaline carbonate salts. In contrast with molten carbonate, the molten hydroxide shows a lower ionic conductivity in the range between 400°C and 750°C but the corrosive process shown with hydroxide salts is reduced and it prevents the Boudouard reaction for the low

operation temperature (400°C). Large electrochemical oxidation activity of carbon is achieved using hydroxide at a given over-potential. [35][46-48]. The reaction that governs the entire process is the following - eq. 1.19:



An insufficient amount of water leads to the consumption of electrolyte by the reaction of OH<sup>-</sup> ions, pushing the reaction to the production of carbonate ions.

The reactions involved in the anode and cathodes are the following:

Cathode reaction	$\text{O}_2 + 2\text{H}_2\text{O} + 4\text{e}^- \rightarrow 4\text{OH}^-$	(1)
Anode reaction	$\text{C} + 4\text{OH}^- \rightarrow \text{CO}_2 + 2\text{H}_2\text{O} + 4\text{e}^-$	(2)
Overall reaction	$\text{C} + \text{O}_2 \rightarrow \text{CO}_2$	(3)

Table 1.7- Electrochemical reactions involved in the DCFC with melted hydroxide electrolyte.

In order to minimize this effect, humidified air flow is purged to the cathode. Excess water in the electrolyte also increases the ionic conductivity of the molten hydroxide because it introduces polar molecules [35][36][49].

The configuration is different from Cooper's configuration. The representative configuration of DCFC with Hydroxide electrolyte is investigated by the Scientific Application & Research Associates (SARA,USA).

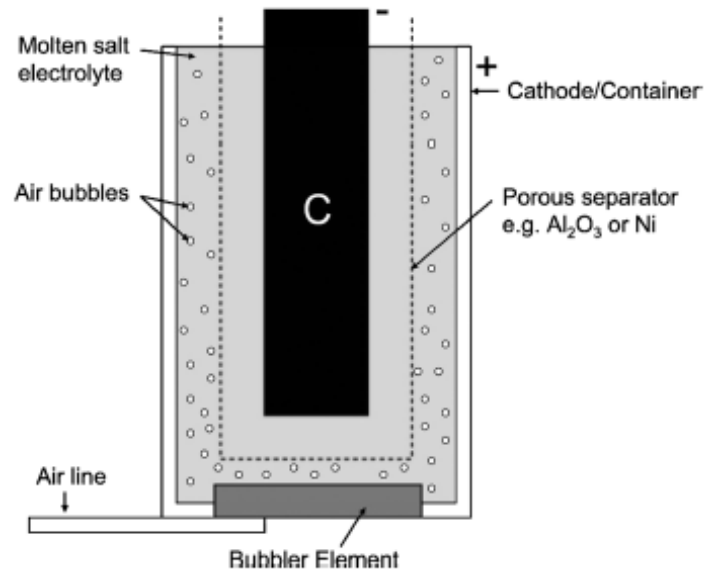


Figure 1.12- Schematic description of a DCFC with alkali hydroxide by the Scientific Application & Research Associates (SARA,USA)[50-53].

The container consists of a Fe-Ti alloy that is used as cathode and current collector. Ti is used to improve the stability of the iron of the container. Iron is used for good catalytic activity. The humidified air is purged into the electrolyte solution and the electrolyte is separated from the cathode by an alloy of Ti doped Ni that is totally impermeable to air bubbles but is able to diffuse hydroxyl and metal ions both in the anode and electrolyte[35][50-51].

#### *1.6.4.4. DCFC with solid electrolyte*

Until now, every configuration shown had problems with corrosion caused by carbonate or hydroxide salts. The utilization of solid oxide as electrolyte minimized this problem because ceramic materials are resistant to different fuels and inorganic salts. For this reason, solid electrolyte is a strong candidate to be used in DCFC.

The only problem is that this type of electrolyte such as YSZ is due to the operation condition. In fact, they have to work over 700°C in order to have acceptable ionic conductivity. This high temperature promotes the Boudouard reactions, losing fuel during operation. Recently, studies on this type of cell are focused to reduce the operation temperature. Up to date, the lower limit for operation temperature is 600°C. In order to reach this type of operation temperature ceramic material such as ceria doped gadolinia (GDC) are used. GDC ceramic electrolyte has good ionic conductivity at temperatures over 600°C[46] and it is not reactive with low cathodes that contains cobalt such as LSC or LSCF [47].

As solid oxide electrolyte provides oxygen ions, the only oxidant agent required at the cathode is either air or oxygen gas, removing all sorts of recycle loops.

The half-cell reactions are provided in table 1.7:

Cathode reaction	$O_2 + 4e^- \rightarrow 2O^{2-}$	(1)
Anode reaction	$C + 2O^{2-} \rightarrow CO_2 + 4e^-$	(2)
Overall reaction	$C + O_2 \rightarrow CO_2$	(3)

Table 1.7- Electrochemical reactions involved in the DCFC with solid electrolyte.

The main problems for this kind of configuration arise from physical contact between anode and fuel because imperfect adhesion between them reduces the surface of contact, affecting the current and power density.

For this reason various designs of DCFC with solid electrolyte have been investigated by different companies and scientists. Several examples of these designs are outlined below. The first design is presented by the Bavarian Centre for Applied Research (ZAE Bayern). They use a ceramic electrolyte of Zirconia stabilised Ytria (YSZ) and two aluminium oxide tubes to separate the anodic chamber from the cathodic chamber. To maintain the physical contact between electrolyte and fuel, a pellet of carbon was placed on top of the cell and constant pressure was applied to it.

The pellet has to have high porosity to allow the gases to pass through without negatively affecting the physical contact.

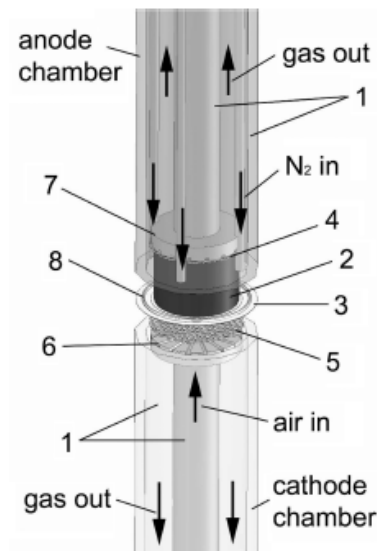


Figure 1.13- DCFC with solid oxide electrolyte developed at the Bavarian Centre for Applied Research (ZAE Bayern).[48]

This cell was investigated using two different carbons: an amorphous material (Vulcan XC 72 high surface area 250 m<sup>2</sup>/gr) and graphitic carbon (GFG 50M surface area 20 m<sup>2</sup>/gr). The carbon with a higher surface area has shown a power density two orders of magnitude higher than graphitic carbon.

This means that the activation energy of carbon fuel with a higher surface area is lower than the activation energy of carbons with lower surface energy.

Another configuration of DCFC consists of a solid ceramic electrolyte combined with a fluidised-bed in the anodic compartment and it was developed at Stanford University, Palo Alto, California.

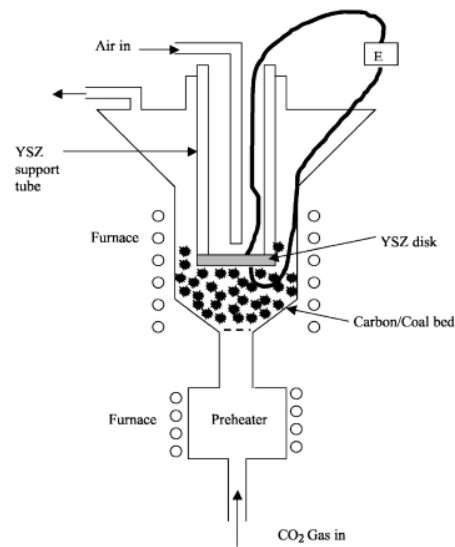


Figure 1.14- Schematic description of a DCFC combining SOFC with fluidised-bed technologies [53-54].

The carbon is loaded into the chamber and a flow of  $\text{CO}_2$  is used to improve the physical contact between the carbon and anode surface. The  $\text{CO}_2$  flow reacts in situ with carbon, producing CO by the Boudouard reaction at high temperature and CO was electro oxidised to  $\text{CO}_2$  again.

Cathode reaction	$\text{O}_2 + 4\text{e}^- \rightarrow 2\text{O}_2^-$	(1)
Anode reaction	$\text{C} + \text{CO}_2 \rightarrow 2\text{CO}$	(2)
	$2\text{CO} + 2\text{O}_2^- \rightarrow 2\text{CO}_2 + 4\text{e}^-$	(3)
Overall reaction	$\text{C} + \text{O}_2 \rightarrow \text{CO}_2$	(4)

Table 1.18- Mechanism of carbon oxidation in the DCFC with solid electrolyte.

This configuration was investigated by Andrews Lee et al. from CEE and the investigations were carried out at 900°C using two different kinds of fuel: carbon obtained by pyrolysis of almond shell and CO pure gas. The power achieved was similar but the value obtained by using CO pure gas was slightly higher than carbon from biomass. The maximum peak of power density was achieved at  $140 \text{ mWcm}^{-2}$  at a cell voltage of 0.5V.[54]

#### 1.6.4.5. *DCFC combining SOFC and Liquid anode*

One of the main problems observed for DCFC combining SOFC was the physical contact of the carbon with the anode. To solve this problem, a different configuration of DCFC combined electrolyte and cathode of a SOFC with a liquid anode.

Two different liquid anodes were investigated: liquid tin-based anode and liquid carbonate salts-based anode. The liquid anode served as an electrochemical mediator, preventing the problems of physical contact between fuel and solid electrolyte.

The first type was investigated by CellTech Power (MA, USA) and consisted of a solid electrolyte with a liquid tin anode (Sn). The Tin (Sn) can be electrochemically oxidised to  $\text{SnO}_2$  by oxygen ions that come from the electrolyte. At this point the  $\text{SnO}_2$  is reduced by the carbon fuel to Sn and Carbon is oxidized to  $\text{CO}_2$ . The mechanisms are showed in the table 7 [55][56]

---

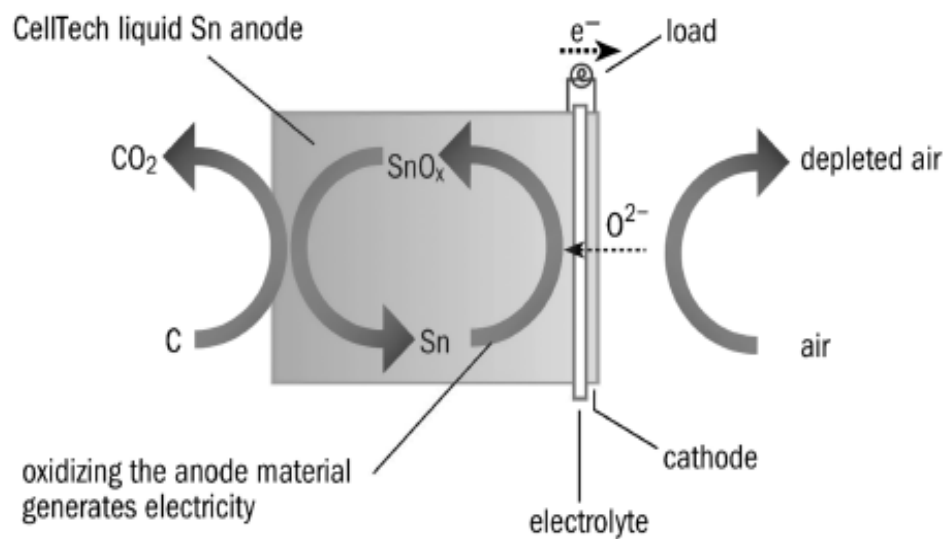


Figure 1.14-Schematic description of DCFC with solid oxide electrolyte and a liquid anode based on the electrochemical oxidation of Sn to SnO<sub>x</sub> [55].

Cathode reaction	$O_2 + 4e^- \rightarrow 2O^{2-}$	(1)
Anode reaction	$C + SnO_2 \rightarrow 2CO_2 + Sn$	(2)
	$2Sn + 2O^{2-} \rightarrow 2 SnO_2 + 4e^-$	(3)
Overall reaction	$C + O_2 \rightarrow CO_2$	(4)

Table 1.9- Mechanism of carbon oxidation in the DCFC with liquid anode and solid electrolyte.

A notable limitation of this technology is the high operation temperature, recorded at 1000°C. Furthermore, a low cell voltage (0.64V) was achieved for this cell with a voltage efficiency of around 82%. The advantage of this type of

liquid anode is its high tolerance to the impurities contained in the carbonaceous fuel derived from biomass, coal and gasoline.

On the other hand, in the second type a liquid carbonate salts-based anode was used. In fact, a mixture of carbonate salts contained ions K, Li and or Na were mixed with carbon particles. Different geometries of these types of cells were investigated at the University of St Andrews (UK) and at the Stanford Research Institute (SRI International) in Menlo Park (CA, USA)

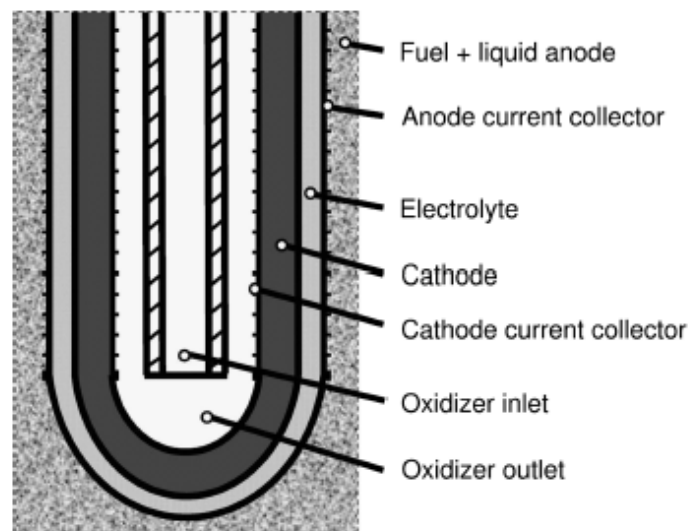


Figure 1.15- Set-up at SRI International (tubular design): SOFC cell with a liquid carbonate-based anode.

The schematic representations of possible mechanisms of the reactions that take place in the liquid anode are shown below:

Cathode reaction	$O_2 + 4e^- \rightarrow 2O^{2-}$	(1)
Anode reaction	$2O^{2-} + CO_2 \rightarrow 2CO_3^{2-}$	(2)
	$C + 2CO_3^{2-} \rightarrow 3CO_2 + 4e^-$	(3)
Overall reaction	$C + O_2 \rightarrow CO_2$	(4)

Table 1.9- Electrochemical reaction involved in the DCFC with liquid anode and solid electrolyte.

In the anode side, the reaction takes place in two different steps: firstly at the interface solid electrolyte/liquid anode where carbonate ions are formed by the reaction between  $CO_2$  and oxygen ions and the second step in which carbon fuel is converted to carbonate ions to produce  $CO_2$  and electrons.

In fact, the carbonate salts serve as an electrochemical mediator to the reaction between oxygen ions and carbon fuel. Furthermore, the cathode is separated from the carbonate salts, avoiding contact between the carbonate salts and cathode and possible corrosion phenomena of the cathode.

In the cathode side, air is purged on the cathode without  $CO_2$  because unlike Cooper's configuration, these types of configurations need no  $CO_2$  recirculation system [56][57].

The maximum peak of power density of  $300 \text{ mWcm}^{-2}$  at  $0.5\text{V}$  was recorded for this configuration at  $700^\circ\text{C}$  while an output of  $170 \text{ mWcm}^{-2}$  has been reached at  $0.84\text{V}$  (voltage efficiency of 82%). [58]

The different configurations previously discussed have shown that DCFC are favourable due to their versatility and the fact that various carbon fuels can be used. In fact, a variety of very copious low cost carbonaceous fuels including coal, coke, tar, biomass and organic waste can be used directly without internal or external reforming, as used in molten carbonate fuel cell.

In addition, the direct electrochemical oxidation of carbon to electrical energy, which overcomes the emission problem of combustion gases and the limitations displayed by the classic thermal cycle, makes this technology and carbon fuel an exciting opportunity for scientists and for the development of clean technology.

The different configurations have demonstrated advantages and disadvantages; most related to the high operation temperature and physical contact between solid fuel and solid electrolyte.

These disadvantages spur scientists to develop new solutions that allow for improvements in performance. In the next chapter we will analyse a new concept of DCFC with a solid ceramic electrolyte and a secondary electrolyte, composed of a mixture of carbonate salt and carbon fuel.

The configuration investigated at the University of St Andrews is similar to the SRI configuration because it uses a carbonate in the anode chamber [59][60].

---

However, it provides conceptual differences and differences in terms of electrochemistry, which will be described in the following chapter, explaining and comparing the advantages and disadvantages.

## 1.7. References

- [1] Energy - Consumption "Consumption by fuel, 1965–2008" (XLS). Statistical Review of World Energy 2009, BP. July 31, 2006. Retrieved 2009-10-24.
  - [2] World energy use in 2010: over 5% growth, Enerdata Publication
  - [3] State of the World 2009, Worldwatch Institute, 2009
  - Energy in Sweden 2010, Facts and figures Table 55 Regional energy use, 1990 and 2008
  - [4] IEA Key energy statistics 2010 Population page 48 forward
  - [5] <http://www.rba.gov.au/publications/bulletin/2011/sep/pdf/bu-0911-3.pdf>
  - [6] Irena Twardowska and Sebastian Stefaniak-Polish Academy of Sciences, Institute of Environmental Engineering, 34, M. Skłodowska-Curie St., 41-819 Zabrze, Poland
  - [7] Treatment of Uncertainty], in IPCC AR4 SYR (2007)
  - [8] Section 2.4: Attribution of climate change, in IPCC AR4 SYR (2007)
  - [9] America's Climate Choices: Panel on Advancing the Science of Climate Change; National Research Council (2010). Advancing the Science of Climate Change Washington, D.C.: The National Academies Press. ISBN 0309145880.
  - [10] Solomon, S.; Qin, D.; Manning, M.; Chen, Z.; Marquis, M.; Averyt, K.B.; Tignor, M.; and Miller, H.L.. ed. Climate Change 2007: The Physical Science Basis. Contribution of Working Group I to the Fourth Assessment Report of the Intergovernmental Panel on Climate Change. Cambridge University Press. ISBN 978-0-521-88009-1 (pb: 978-0-521-70596-7).
  - [11] Kiehl, J.T.; Trenberth, K.E. (1997). "Earth's Annual Global Mean Energy Budget" (PDF). Bulletin of the American Meteorological Society 78 (2): 197–208.
  - [12] Schmidt, Gavin (6 Apr 2005). "Water vapour: feedback or forcing?". RealClimate. Retrieved 21 April 2009.
  - [13] Russell, Randy (May 16, 2007). "The Greenhouse Effect & Greenhouse Gases". University Corporation for Atmospheric Research Windows to the Universe. Retrieved Dec 27, 2009.
  - [14] Houghton, J.T.; Ding, Y.; Griggs, D.J.; Noguer, M.; van der Linden, P.J.; Dai, X.; Maskell, K.; and Johnson, C.A.. ed. Climate Change 2001: The Scientific Basis. Contribution of Working Group I to the Third Assessment
-

Report of the Intergovernmental Panel on Climate Change. Cambridge University Press. ISBN 0-521-80767-0

[15] Bruce, J.P.; Lee, H.; and Haites, E.F.. ed. Climate Change 1995: Economic and Social Dimensions of Climate Change. Contribution of Working Group III to the Second Assessment Report of the Intergovernmental Panel on Climate Change. Cambridge

[16] Liverman, D.M. (2008). "Conventions of climate change: constructions of danger and the dispossession of the atmosphere" (PDF). *Journal of Historical Geography* 35 (2): 279–296. doi:10.1016/j.jhg.2008.08.008. Retrieved 2011-05-10

[17] C. Arden Pope IIIa\* & Douglas W. Dockeryb - *Journal of the Air & Waste Management Association* –Vol. 56, 6, 2006, 709-742;

Public health importance of triggers of myocardial infarction: comparative risk assessment *Lancet* 2011; 377: 732 - 740 Date published: Feb. 25, 2011

[18]M.Hills Freda Alexander- *Statistical Methods Used in Assessing the Risk of Disease Near a Source of Possible Environmental Pollution: A Review* -*J.R. stat. Soc. A*- 152 , (1989), part 3, pag353.

Michael Hills and Freda Alexander

[19]REN21 (2011). "Renewables 2011: Global Status Report". p. 17.

[20]Lars Kroldrup. Gains in Global Wind Capacity Reported Green Inc., February 15, 2010.

[21] James Russell. Record Growth in Photovoltaic Capacity and Momentum Builds for Concentrating Solar Power Vital Signs, June 3, 2010.

[20][http://ec.europa.eu/energy/renewables/bioenergy/national\\_biomass\\_action\\_plans\\_en.htm](http://ec.europa.eu/energy/renewables/bioenergy/national_biomass_action_plans_en.htm)

[22] Kuang Ken, Áron Varga- *Fuel Cell Electronics Packaging* -Chapter 2 pag.5

[23] A.B. Lovins and B.D. Williams, "A strategy for the Hydrogen Transition", Rocky Mountain Institute, 1999

[24][www.nfcrc.uci.edu/journal/article/fcarticleE.htm](http://www.nfcrc.uci.edu/journal/article/fcarticleE.htm), National Fuel Cell Research Center at the University of California

[25] *Recent Trends in Fuel Cell Science and Technology*-R.K.Shah- Edited by S. Basu

[26]E. Baur and H. Preis, *Z Elektrochem.*, 43,(1937),727

[27]Huayang Zhu, Robert J.Kee *Journal of Power Sources*161, 2, (2006), Pages 957-964

[28] Hossein Ghezal-Ayagh, Mohammad Farooque and Hansraj C. Maru- *Recent trend of in fuel cell science and technology* (2003)

[29] Lee CG, Ahn KS, Lim HC, Oh JM. *J Power Sources* 2004;125:166–71.

[30] Tagawa T, Yanase A, Goto S, Yamaguchi M, Kondo M. *J Power Sources* 2004;126:1–7.

[31]Pascual MJ, Valle FG, Duran A, Berjoan R. *J Am Chem Soc* 2003;83(11):1918–26.

- [32] Kim HC, Alford TL. Fuel cell having  $TiAl_xNyO_z$  deposited as a protective layer on metallic surface. PCT Int. Appl., WO2004038842, 2004.
- [33] Park HH, Lee MH, Yoon JS, Bae IS, Kim BI. Corrosion resistance of austenitic stainless steel separator plate for molten carbonate fuel cell. *Metals Mater Int* 2003;9(3): 311–7.
- [34] D. Rastler, Technical report 1013362, EPRI, 2006.
- [35] K. J. Vetter, *Electrochemical Kinetics: Theoretical and Experimental Aspects* Academic Press, New York ~1967!
- [36]. N. J. Cherepy, R. Krueger, K. J. Fiet, A. F. Jankowski and J. F. Cooper, *J. Electrochem. Soc.*, 2005, 152(1), A80.
- [37] W.W. Jacques, US Patent No. 555,511 (1896).
- [38] R.D. Weaver, S.C. Leach, A.E. Bayce, L. Nanis, *Direct Electrochemical Generation of Electricity from Coal*, SRI, Menlo Park, CA, USA (Report SAN-0115/105-1, available from National Technical Information Service, NTIS), 1979.
- [39] R.D. Weaver, S.C. Leach, L. Nanis- *Proc. 16th Intersoc. En. Conv. Eng. Conf.*, ASME, NY, USA (1981), p. 717
- [40] R.D. Weaver, L. Tietz, D. Cubicciotti, *Direct use of Coal in a Fuel Cell: Feasibility Investigation*, Report for USA EPA, Office of R&D, EPA-650/2-75-040, 1975.
- [41] B. Heydorn and S. Crouch-Baker, *Fuel Cell Rev.*, 2006, 2(6), 15.
- [42]. J. F. Cooper, US patent 2006/0057443 A1, 2006.
- [43]. D. Cao, Y. Sun and G. Wang, *J. Power Sources*, 2007, 167(2), 250.
- [44] W. H. A. Peelen, K. Hemmes and J. H. W. de Wit, *High Temp. Mater. Processes*, 1998, 2(4), 471
- [45] J. F. Cooper, URCL-TR-210346, LLNL, 2005
- [46] J. F. Cooper, Presented in *Direct Carbon Fuel Cell Workshop*, NETL, Pittsburg, PA, USA, 30th July, 2003
- [47] J. F. Cooper, R. Krueger and N. Cherepy, US patent 2002/0106549 A1, 2002.
- [48] S. Nurnberger, a R. Buřar, a P. Desclaux, a B. Franke, a M. Rzepka\* a and U. Stimmingab: *Energy Environ. Sci.*, 2010, 3, 150–153
- [49] J. F. Cooper, Presented in *International Conference on Fuel Cell Science, Engineering and Technology*, Rochester, NY, USA, June 14–16, 2004
- [50] P. V. Pesavento, US patent 2001/6200697 B1, 2001.
- [51] S. Zecevic, E. M. Patton and P. Parhami, US patent 2005/0282063 A1, 2005.
- [52] S. Zecevic, E. M. Patton, P. Parhami, Presented in *Direct Carbon Fuel Cell Workshop*, NETL, Pittsburg, PA, USA, 30th July, 2003
- [52] S. Zecevic, E. M. Patton and P. Parhami, *Carbon*, 2004, 42(10), 1983
- [53] A C. Rady, S. Giddey, S. P. S. Badwal, Bradley P. Ladewig, Sankar Bhattacharya –*Energy Fuels* - 2012, 26, 1471–1488

- [54] Andrew C. Lee, Siwen Lib, Reginald E. Mitchell and Turgut M. Gürb - Electrochem. Solid-State Lett. 11, (2008), 2, B20-B23
- [55] Thomas Tao, Linda Bateman, Jeff Bentley and Michael Slaney ECS Trans. 2007 volume 5, issue 1, 463-472
- [56] W. McPhee and T. Tao, Presented in Fuel Cell Seminar & Exposition, Phoenix, AZ, USA, October 28-30, 2008.
- [57] T. Tao, Presented in Fuel Cell Seminar, Direct Carbon Fuel Cell Workshop, Palm Springs, CA, USA, 14th November, 2005.
- [58] D. Rastler, Technical report 1016170, EPRI, 2008
- [59] K. Pointon, B. Lakeman, J. Irvine, J. Bradley and S. Jain, J. Power Sources, 2006, 162(2), 750.
- [60] S. L. Jain, Y. Nabaie, B. J. Lakeman, K. D. Pointon and J. T. S. Irvine, Solid State Ionics, 2008, 179, 141

## 2. Background

In the following chapter, each component of the hybrid direct carbon fuel cell and its physical chemistry properties will be outlined so as to best understand the results presented in later chapters.

In the hybrid direct carbon fuel cell, as in any fuel cell device, each component has specific physical chemistry properties (e.g. its chemical structure, composition and catalytic activity) which play an important role in the evolution of the electrochemical phenomena and as a result on the final performance of the cell. By changing these properties, the electrochemical phenomena can be altered in order to improve the performance of the cell. In addition, the electrochemical phenomena are affected by the manufacture and geometry of each component. For this reason it is important to outline the unique characteristics of each component and to understand how they can modify the final performance of the cell.

### 2.1 Analysis of Hybrid Direct Carbon Fuel Cell

The hybrid direct carbon fuel cell has been developed at the University of St Andrews (UK) as a hybrid variant of DCFC, merging a DCFC with solid oxide electrolyte and a DCFC with carbonate electrolyte[59][60]. It aims to solve most

---

of the problems associated with DCFC, such as the physical contact between the solid electrolyte and carbon fuel.

In the configuration of HDCFC, a solid ceramic material is used as the electrolyte interspaced between the anode and cathode layers and a mixture of carbonate salts is mixed with the carbon fuel which is in direct contact with the anode, as demonstrated in figure 2.1:

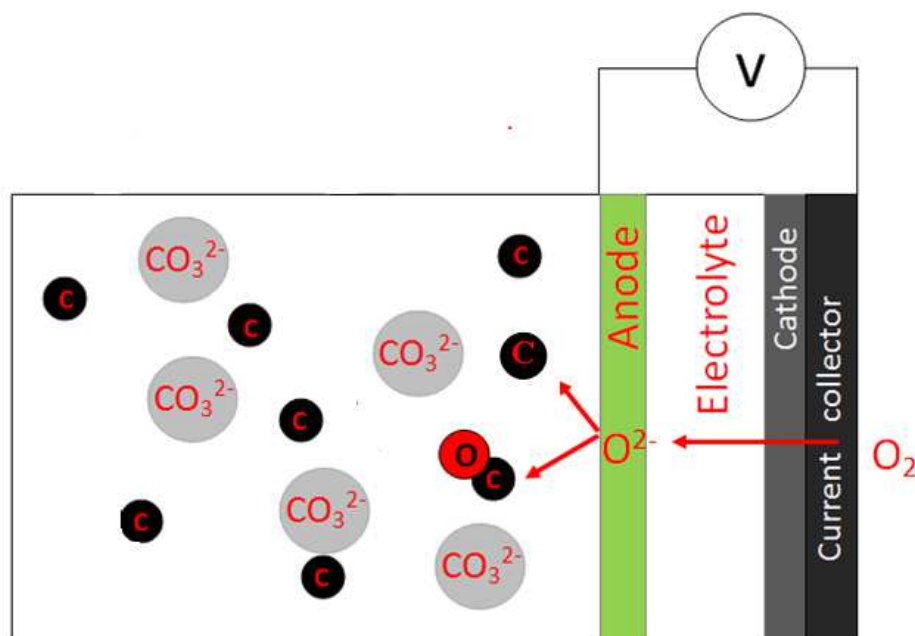


Figure 2.1- Schematic representation of a hybrid direct carbon fuel cell.

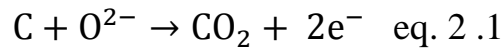
This configuration can work with virtually any type of carbonaceous fuel, such as coal, biomass and pyrolysis of solid urban waste, making this cell highly versatile.

### 2.1.1. Principles

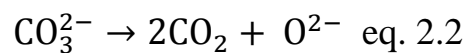
As explained previously, the hybrid direct carbon fuel cell is a merger of the solid oxide fuel cell and molten carbonate fuel cell and, as in any DCFC, it utilizes the electrochemical oxidation of carbon to produce electrical energy. However, the carbon oxidation mechanism is affected by the simultaneous presence of two different electrolytes: a ceramic electrolyte that conducts oxygen ions and a liquid electrolyte on the anode side that works as a mediator.

The simultaneous presence of a double electrolyte modifies the oxidation mechanism of carbon. In fact, these fuel cells were merged in order to eliminate the limitations noticed in other configurations, as explained in the previous chapter. One such limitation was caused by the interaction between the solid fuel and the solid electrolyte. The introduction of a liquid electrolyte in the anode region has produced two effects: Firstly, it has extended the anode electrolyte region, increasing the surface area for anode reactions and secondly it has facilitated removal of the solid problem that was present in most DCFCs. In addition, the decision to use carbonate salts in the anode side removed the need for a CO<sub>2</sub> recycle system as in Cooper's configuration, hence reducing manufacture costs [41][59].

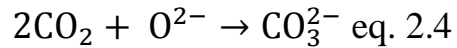
In the HDCFC, oxygen is reduced to oxygen ions at the surface of the cathode and then the oxygen ions pass through the solid oxide electrolyte to reach the anode. At the anode, carbon fuel is oxidised to CO<sub>2</sub> following eq. 2.1:



The anode side is composed of a mixture of carbon and carbonate and the molten carbonate produces a double effect: Firstly, it improves the transport mass and the interaction of carbon fuel inside the anode chamber. Secondly, the carbonate inside the anode chamber works as a mediator because during decomposition at high temperature it provides oxygen ions that oxidise carbon to CO<sub>2</sub> as described in eq. 2.2 and 2.3:



On the other hand, the oxygen produced by the ceramic membrane reacts with CO<sub>2</sub> gas inside the anodic chamber to recondition the carbonate ions.

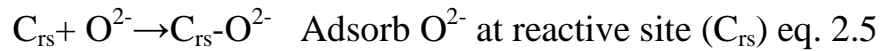


The regeneration of carbonate ions is useful for keeping the entire system neutral.

### 2.1.2. Mechanism of electrochemical oxidation of carbon

In the previous paragraph, a generic and schematic explanation of total carbon oxidation to  $\text{CO}_2$  was provided. However, the carbon oxidation mechanism is not fully understood because many factors can influence it, subsequently favouring one mechanism over another.

A variety of possible mechanisms have been hypothesised by different scientists as function of the different configurations and designs of the anodic chamber in which the carbon was oxidised. For example, John Cooper hypothesised a mechanism in which the phenomena of adsorption and desorption are involved, as well as discharge between the surface of the anode, which is catalytically activated by Ni metal, and the reactive site located on the surface of carbon. The bond between the metal and oxygen (Me-O) is very strong. However, carbon has a stronger reactive site ( $\text{C}_{\text{rs}}$ ) than the Me-O. This difference in bond energy favours the adsorption of oxygen ions on the exposed carbon surface[59].



Where  $C_{rs}$  is the reactive site of carbon

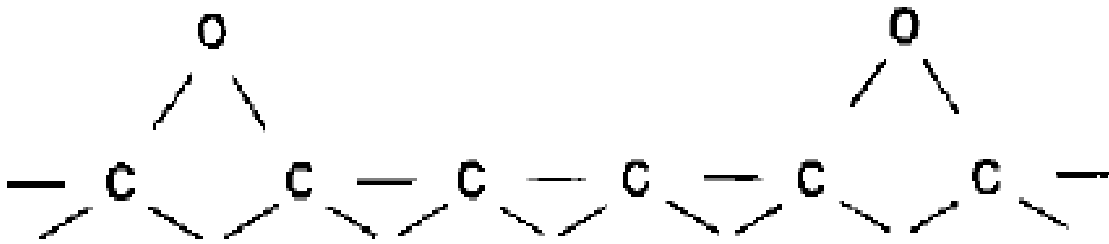
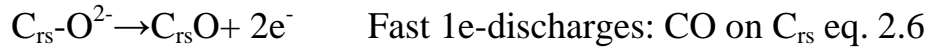
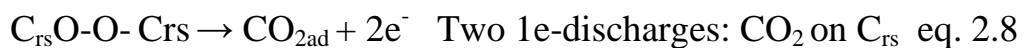
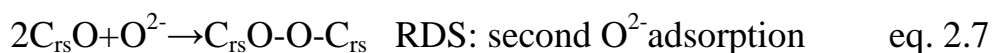


Figure 2.2 - Schematic description of bridge formation between reactive-site C atoms on the exposed carbon surface.[59]

These two semi reactions are characterised by a high kinetic velocity that makes this reaction faster than the desorption reaction, as shown in eq. 2.7:



The bridge between carbon and oxygen is highly unstable and for this reason  $CO_2$  is released.

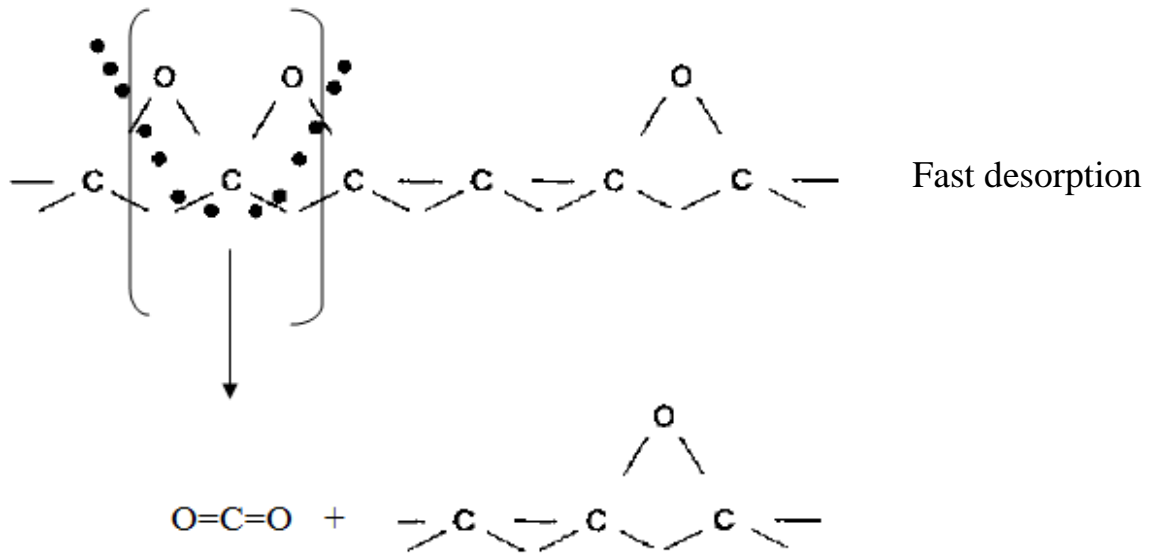


Figure 2.3- Schematic description of adsorption mechanism of oxygen ions and desorption of  $\text{CO}_2$  between reactive-site C atoms on the exposed carbon surface [41][59].



In the DCFC with solid electrolyte, the mechanism of oxidation of carbon in the anodic chamber is different from that presented by Cooper because the carbon fuel is not mixed with the carbonate salts matrix; rather it is in direct contact with the anode and electrolyte.

A mechanism for this type of cell was proposed by Prof. Turgut M. Gür and al. who proposed a “shuttle” mechanism in which carbon is oxidised to CO<sub>2</sub> through an intermediate step of oxidation (CO formation was conceived)[63].

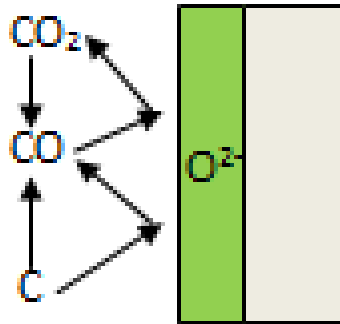


Figure 2.4- Schematic description of a coordinate reaction mechanism (“Shuttle” mechanism) in which the solid carbon fuel and oxygen ions react at the anode surface.

In this mechanism, CO is produced by an intermediate step where C reacts with oxygen ions by the ‘Boudouard reaction’:



The mechanism proposed occurs on the anode surface and in the TPB [60][61].

In the HDCFC, the mechanism is considered to be midway between the Cooper and Gür mechanisms because the cell is a combination of DCFC with molten carbonate and DCFC with solid oxide electrolyte.

In fact, considering the entire anodic chamber of HDCFC including the anode surface, the following mechanism can be observed:

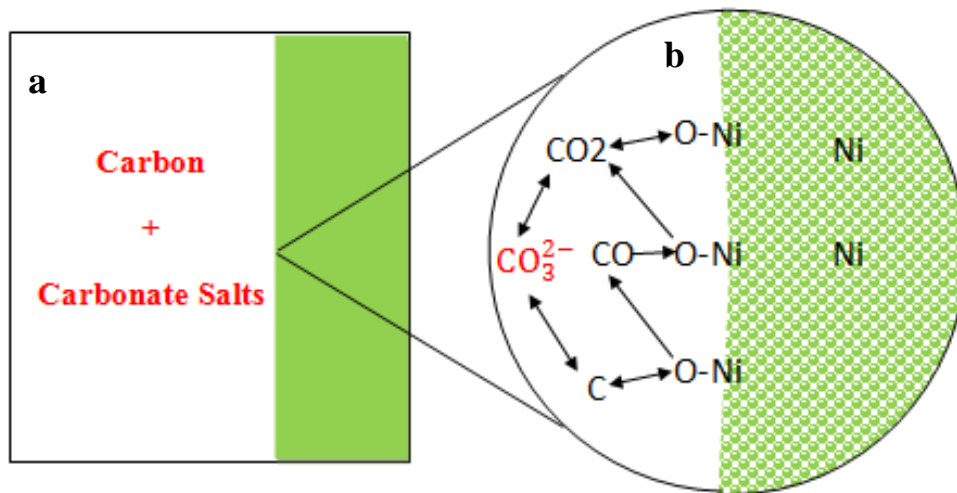
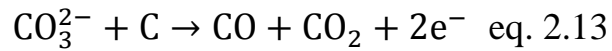
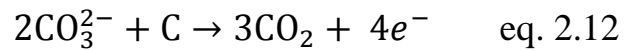


Figure 2.5 - Hybrid direct carbon fuel cell a) schematic description of anodic chamber with carbon fuel mixed with carbonate salts b) zoom of surface mechanism of reaction on the NiO-GDC porous anode during the electrochemical oxidation of carbon in the presence of carbonate salts.

At the interface between anode and electrolyte, Ni is oxidised to NiO by the oxygen ions that come from the solid oxide electrolyte. On the other hand, NiO is reduced to Ni by carbon at the anode surface and carbon is oxidised both partially to carbon monoxide and totally to carbon dioxide.

The presence of carbonate in the anodic chamber favours the electrochemical oxidation of carbon, following eq. 2.12 and 2.13:



### 2.2.1. *Components and design of HDCFC*

Fuel cell performance depends both on the design and the physical and chemical composition of each component of the cell.

Designing a fuel cell involves an accurate study of intrinsic characteristics and the limitations of each component when used under operating conditions. As a result, components are chosen in accordance with the type of fuel used, tolerances between materials, the catalytic activity both of the anode and cathode, the resistance of sealing materials to the chemical agent and mechanical stress. However, there are several parameters to consider when designing a cell which are not directly related to the component material, such as flow rate and pressure of the gases, operating temperature, and poison of the anode by substances such as sulphur, the type of electrolyte and the geometry of the cell. All of the aforementioned factors play an important role in the performance of the fuel cell because these both directly and indirectly drive the electrochemical phenomena and consequently the cell performance.

---

Hence an accurate study was carried out on each of these factors in order to obtain the optimal performance.

According to the factors mentioned above, the researchers at the University of St Andrews designed a DCFC cell using a solid oxide electrolyte supported cell with tubular geometry in order to reduce sintering stress, which is the cause of cracks.

The electrolyte supported cell was also chosen in order to prevent short circuit phenomena which are common for anode supported cells because the electrolyte is not very thick and so it is not able to separate the anode from the cathode particularly well.

In the hybrid direct carbon fuel cell, the anode is extended using a mixture of carbonate salt and carbon in a molar ratio of 80/20 in which the carbonate salts function as mediator at high temperature because carbon oxidation takes place in every part of the anode chamber. In fact, in the classic design of the direct carbon fuel cell, the electrochemical oxidation of carbon occurs exclusively at the anode surface, as previously illustrated.

Over the next few paragraphs a detailed description of the components will be provided.

### 2.3. Electrolyte

As presented previously, the hybrid direct carbon fuel cell consists of two electrolytes: the first is a solid ceramic electrolyte, while the other is a secondary electrolyte consisting of a mixture of carbonate salts. It is considered a secondary electrolyte because it does not affect the OCV of the cell but indirectly it acts to improve the oxidation of carbon in the anodic chamber, as shown in eq. 2.13.

#### 2.3.1. *Solid electrolyte*

The solid electrolyte used in the hybrid direct carbon fuel cell consisted of a ceramic material that is stable at high temperatures (over 1000°C). It is a ceramic membrane that has high ionic conductivity at high temperature. In general, these ceramic membranes are not conductive at room temperature but they begin to be conductive after 500°C. Conductivity changes as function of the microstructure of the membrane and in accordance with the dopants used.

Most solid oxide fuel cells utilise Ytria stabilized Zirconia which has a fluorite structure with high ion mobility at high temperatures, due to the addition of Ytria oxide, which is able to increase the oxygen vacancies on the structure of Zirconia because  $Y^{3+}$  takes over  $Zr^{4+}$  in the structure, providing sufficient ion mobility at high temperature. Furthermore, YSZ is also able to physically separate the anode chamber from the cathode chamber, preventing a direct and highly exothermic reaction between air and gaseous fuel.

---

The mechanism involved in a ceramic membrane that diffuses oxygen ions is driven by high temperature conditions and the amount of dopants substances added to the microstructure of the ceramic materials. In the case of Yttria, bi and trivalent dopants create oxygen vacancies in the structure, keeping the charge neutral. This defect is represented by the Kröger-Vink notation[64][65]:



At high temperature, the oxygen is reduced to oxygen ions on the cathode side that must be able to conduct both ions and electrons. The oxygen ions produced on the cathode side interact with the electrolyte surface, producing a diffusion of oxygen through the vacancies that are caused by the difference in valences between Y and Zr. The diffusion of oxygen ions runs from the cathode side to the anode side in which they react with the fuel to produce electrons that are conducted on the cathode site to reduce the oxygen on the cathode surface. This movement of ions in the electrolyte creates a difference in potential between anode and cathode in the semi-cell. The diffusion of oxygen ions in the electrolyte determines the efficiency of the cell because the faster the diffusion of oxygen from the cathode side to the anode side, the better the performance achieved by the cell.

---

However, the diffusion of oxygen ions is limited by the concentration of the dopants and the thickness of the electrolyte layer. In fact, Ikeda and Sakurai have demonstrated that amounts of Ytria higher than 8% reduce the ionic conductivity of YSZ [66]. This effect was clarified by other researchers through the distribution of vacancies on the YSZ lattice. In fact, Li, Hafskjold and others hypothesised that the vacancies were bound to Y and with high amounts of Y they were trapped. On the other hand, authors such as Steele and Fender, Veal et al. and Catlow et al. hypothesised that vacancies were preferentially connected to Zr by different diffusion mechanisms and that the excess amount of dopants reduces oxygen ion conductivity[66-72].

The diffusion is also limited by the thickness of the electrolyte and is governed by Fick law.

$$J = D \frac{\delta \varphi}{\delta x} \quad \text{eq. 2.15}$$

Where J is the concentration of oxygen ions as function of time

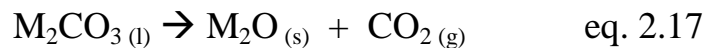
$$\frac{\delta \varphi}{\delta t} = D \frac{\delta^2 \varphi}{\delta x^2} \quad \text{eq. 2.16}$$

and D is the diffusion constant that gives information on the velocity of the flow.

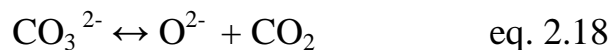
### 2.3.2. Secondary electrolyte (carbonate salts)

The hybrid direct carbon fuel cell is characterized by an extension of the anode produced by filling the anode chamber with a mixture of carbonate salts at different molar ratios and carbon fuel. The mixture of carbonate salts has a double effect:

The first effect is related to the mediator activity. The composition of the carbonate salts and the percentage of each component are very important for the performance of the cell because the acidity and the mobility of metal ions affect the stability and electrochemical behaviour of the cell. In fact, if we consider the decomposition of the carbonate salts, the formation of oxacidic species such as CO<sub>2</sub> that are highly reactive can be observed. These species are characterized by the following equation:



Where l,s and g are the liquid, solid and gaseous phases respectively while M is a generic metal. This equilibrium is shown in eq. 2.18:



The equilibrium is thermodynamically governed by equilibrium constant:

---

$$K = \frac{a(M_2O)P(CO_2)}{a(M_2CO_3^{2-})} \quad \text{eq. 2-19}$$

Where  $a(M_2O)$  is the activity of the oxide and  $a(M_2CO_3)$  is the carbonate salt melt while  $P(CO_2)$  is the partial pressure of the gas. The  $O^{2-}$  is an acid species (oxoacid) and the acidity of the salt melt can be regulated by the partial pressure of carbon dioxide or the concentration of oxacid species, while the value of activity is one. In this case, the activity coefficient for carbonate of Li and K cannot be considered one because they do not form an ideal mixture and the equilibrium constant is also dependent upon the activity of the single salts and the percentage of both salts in the mixture. A theoretical calculation of equilibrium constant at  $700^\circ\text{C}$  for a system of Li and K carbonate salt was tabled and the value of  $\log K$  was 4,92[73][74]. This means that the equilibrium is shifted to the formation of oxoacid species that are highly reactive and they react with the carbon contained in the mixture.



CO is a soluble gas in molten carbonate and it is transported to the anode where it reacts with oxygen ions that come from the electrolyte.

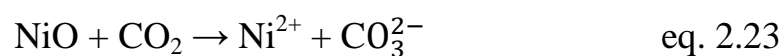
The second effect is connected to the improvement of the transport mass and the improvement of physical contact between the anode and fuel that are the main issues in the direct carbon fuel cell. In fact, the carbonate salts are liquid at high temperature and they are characterised by the chaotic flux and high pressure caused by the high temperature, increasing the mobility of the fuel in the anodic chamber.

### 2.3.3. *Composition of Carbonate salts*

In the hybrid direct carbon fuel cell, the carbonate salt mixture is in direct contact with the ceramic anode that consists of a ceramic part (YSZ or GDC) and a metal oxide such as NiO, which is in equilibrium with Ni metal during cell operation.

A major problem observed regarding NiO is that while it is in contact with carbonate salts it is partially soluble and it tends to diffuse from the anode to the carbonate solution causing a nickel decrease in the anode structure.

This effect can reduce the conductive activity of the anode and also reduce the performance of the cell. The phenomenon of nickel dissolution becomes worse at high CO<sub>2</sub> partial pressures:



According to recent studies, there is evidence of a lower dissolution of NiO in carbonate salts if the acidity of the salts is low. The acidity scale of the common alkali metal carbonates is (basic)  $\text{Li}_2\text{CO}_3 > \text{Na}_2\text{CO}_3 > \text{K}_2\text{CO}_3$  (acidic). The two different eutectic mixtures 62%  $\text{Li}_2\text{CO}_3 + 38\% \text{K}_2\text{CO}_3$  and 52%  $\text{Li}_2\text{CO}_3 + 48\% \text{Na}_2\text{CO}_3$  were tested and they showed the lowest dissolution [75].

In our studies, a eutectic mixture of 62%  $\text{Li}_2\text{CO}_3 + 38\% \text{K}_2\text{CO}_3$  was chosen to reduce the dissolution of NiO in the carbonate mixture.

#### 2.3.4. *Activity of carbonate salts on cell performance*

Although carbonate salts have a positive effect on the performance of the hybrid direct carbon fuel cell, they can also negatively affect the performance of the cell by reducing the lifetime of constituent components of the cell such as the electrode and current collectors, due to the highly corrosive nature of the carbonate at high temperatures. Furthermore, the mixture of carbonate salts also affects cell performance by increasing the ohmic and polarization resistance when present in large amounts. This phenomenon was studied by Dr Cairong Jiang at the University of St Andrews.

The electrochemical oxidation of carbon in both the presence and absence of carbonate were investigated by impedance spectroscopy.

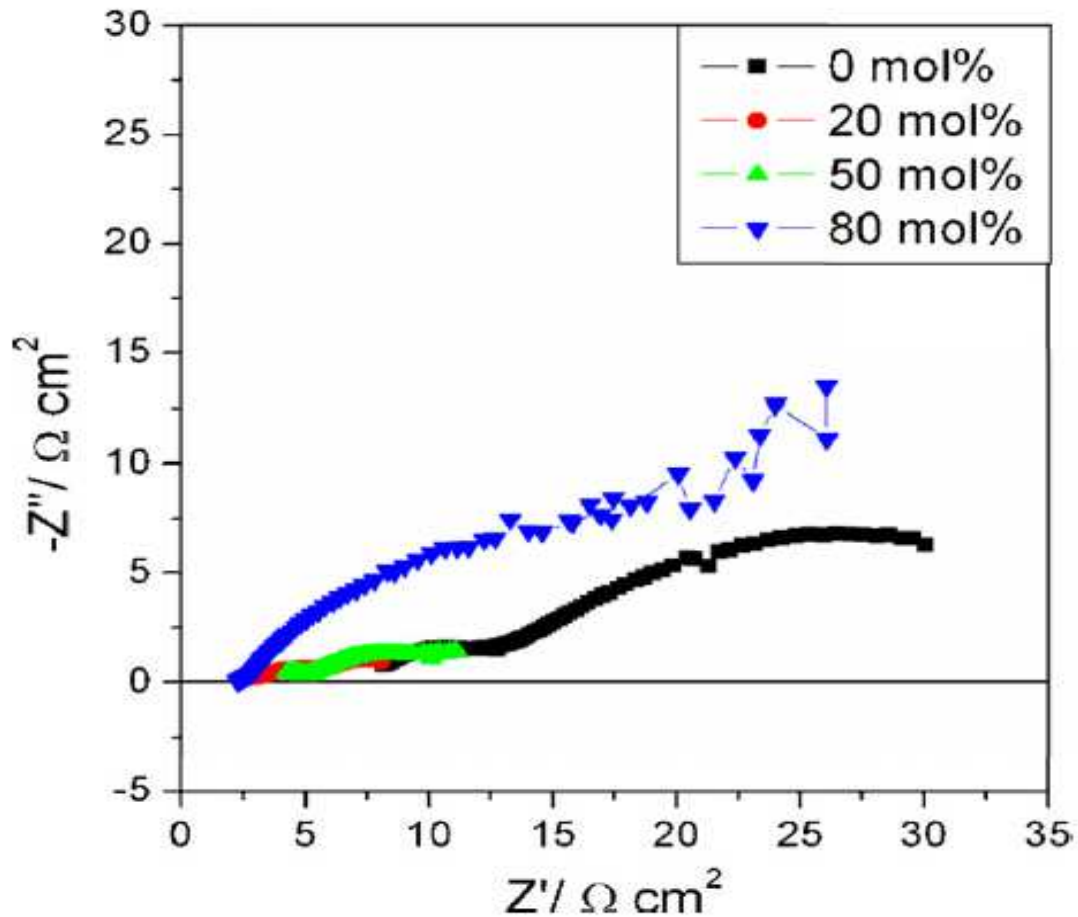


Figure 2.6 - Effect of the carbonate content in mol% on the HDCFC polarization resistance at 750 °C [76].

At a carbon ratio of 100%, a high value for polarization resistance was observed due to the solid/solid contact between the carbon fuel and electrolyte. However, the polarization resistance and the ohmic resistance decreased drastically at a carbon/carbonate ratio of 80/20% respectively. This decrease is due to the conductive nature of the carbonate salts and the enhanced contact between fuel and solid electrolyte. No further improvement was observed by adding 50% of carbonate. The total resistance increased drastically again at a value of carbonate

of 100%. In this case, the ohmic resistance was better than the ohmic resistance shown with 100% of carbon due to the conductive nature of the carbonate.

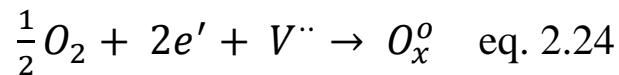
## **2.4. Cathode**

The cathode is one of main components in the fuel cell device. It works to electrochemically reduce oxygen to oxygen ions on its surface, which in turn react with the fuel at the anode surface by passing through the electrolyte. Its properties and characteristics affect the kinetic of the entire reaction. As a result, each cathode must have a particular structure in accordance with the needs of fuel cell in which it is used. For example, a solid oxide fuel cell, that is to say the fuel cell closest to industrialisation, requires a cathode able to catalyse the reduction reaction of molecular oxygen to oxygen ions. These oxygen ions are diffused through a ceramic membrane, transporting the oxygen ions produced at the cathode surface to the anode. On the other hand, the molten carbonate fuel cell requires a cathode that is able to catalyse the reaction between  $\text{CO}_2$  and oxygen to produce carbonate ions that must be diffused through the carbonate electrolyte to the anode in order to then react with the fuel.

In the hybrid direct carbon fuel cell, the activity of the cathode is the same as that of a solid oxide fuel cell because it is directly connected to the solid ceramic electrolyte and consequently it is separated from the carbonate electrolyte.

### 2.4.1. Structure and properties of cathode

Most of cathode materials used in the past for SOFC were electronically conductive and able to reduce the oxygen at the surface, producing oxygen ions as a result of an electrochemical reaction. The overall reaction is written in Kröger-Vink notation as follows:



Platinum was one of the first cathodes employed in solid oxide fuel cells at low temperature [77-79].

However, it was not able to offer enough high performance because of the over-potential produced at the cathode during the operation condition [80-81]. After platinum, a perovskite structure was used for the cathode because it has high electronic conductivity and minimal activity in terms of ion conductivity.

The perovskite structure employed in SOFC is a Lanthanum Strontium Manganese Oxide. Mixed oxides have the general formula  $ABO_3$  and the ability to change and/or substitute cation composition at sites A and B. In Lanthanum Strontium Manganese oxide structure, La and Sr are located in A-site while Mn is located in B-site as shown in the figure 2.7:

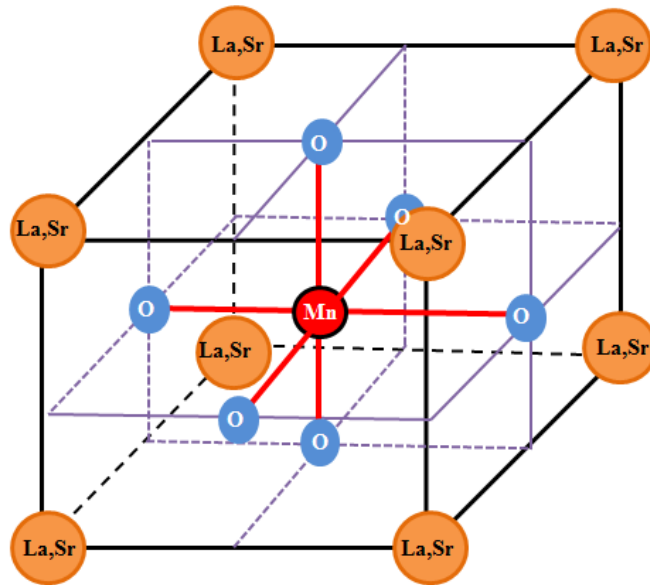


Figure 2.7 - Perovskite structure of  $\text{LaSrMnO}_{3.8}$  in which site A is occupied by the La and Sr while site B is occupied by the Mn.

There are different theories about the catalytic activity of oxygen reduction of LSM but all of these theories converge with regards to the oxygen vacancies that are formed at high temperature on the surface of the material. In fact, Hee Y. Lee and co-workers hypothesised that at high temperature the oxygen vacancies were produced along the triple phase boundary, diffusing them in the entire surface of LSM [82].

The catalytic activities are enhanced when LSM is polarized because it increases the concentration of oxygen vacancies on the surface. However, the efficiency of LSM and in particular Pt is limited by their high electronic conductivity and poor ionic conductivity, which in turn limit the reaction solely on the interface between electrolyte/electrode.

### 2.4.2. Triple phase boundary (TPB)

As previously stated, Lanthanum Strontium Manganese Oxide (LSM) and Pt are electron conducting materials and poor ionic conducting materials and this limits the electrochemical reaction in the triple phase boundary. The triple phase boundary zone is a physical point in which the oxidant or fuel, electrolyte and cathode/anode meet. It is the only point at which the reduction of oxygen to oxygen ions takes place in the cathode. In an active catalyst material such as Pt which is a total electrons conductor or LSM mixed conductor material, the only surface of contact where the electrochemical reduction can take place is at the interface between the catalyst and the electrolyte (YSZ) as shown in the figure 2.8

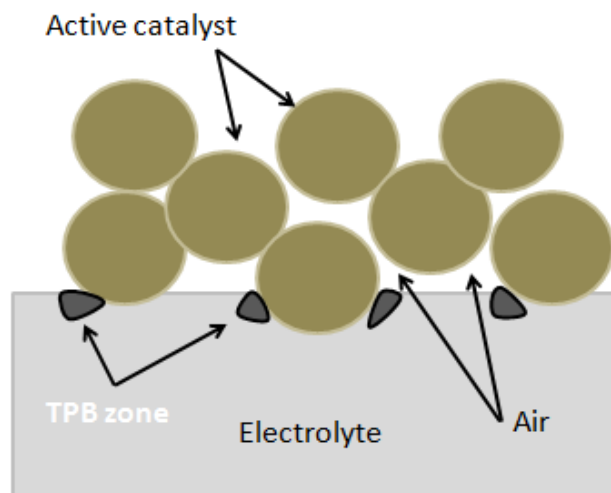


Figure 2.8 - Schematic representation of the triple phase boundary zone between an active catalyst material, electrolyte and gaseous phase.

In order to improve the contact between LSM, electrolyte and air, it is necessary to extend the triple phase boundary, increasing the ion conductivity of the cathode

---

material. In fact, a good cathode needs to be both an ionic conductor and an electron conductor.

The need to extend the triple phase boundary led scientists in two different directions: In the first case, scientists replaced LSM with a single phase mixed conductor such as  $\text{La}_{1-x}\text{Sr}_x\text{Co}_{1-y}\text{Fe}_y\text{O}_{3-\delta}$  (LSCF). In the second case, LSM active catalyst was mixed with ionically conductive materials such as YSZ or GDC in a porous microstructure, thus increasing the surface of contact as shown in figure 2.9:

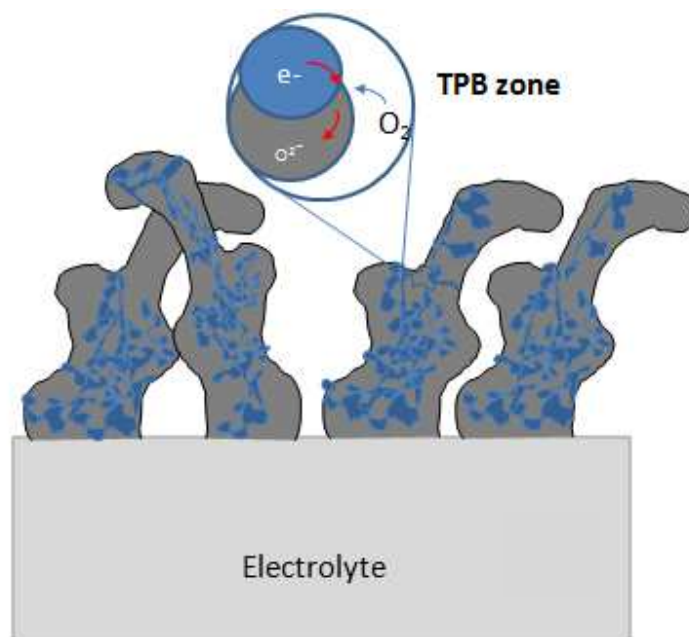


Figure 2.9 - Schematic representation of a triple phase boundary in a system with an active catalyst mixed with ionically conductive materials.

As illustrated in the figure above, after mixing LSM with YSZ, the triple phase boundary increases because the contact surface between air, catalyst and

---

electrolyte is larger and is stretched to the entire thickness of the cathode. This effect can be explained graphically by drawing the cathode side of a solid oxide fuel cell and the flow of electrons and oxygen through to the cathode.

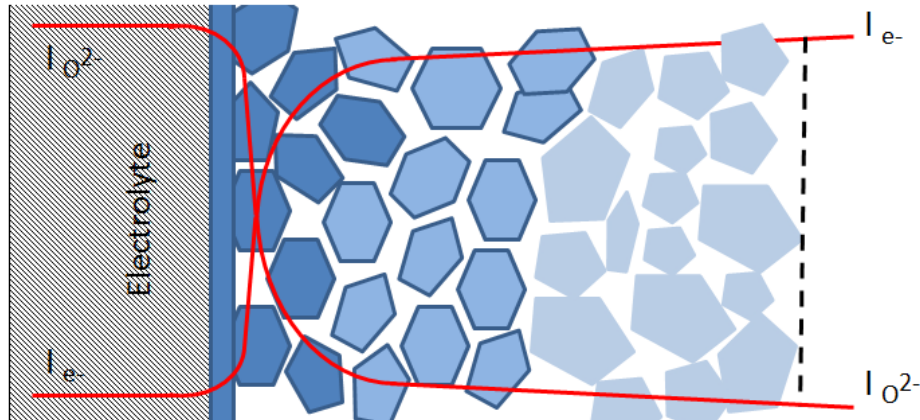


Figure 2.10 - Schematic representation of the impedance response of a mixed contacting electrode. The variation of the electron current and ion current as function of the cathode length. The ion current is inversely proportional to the electron current because electrons are involved in the reduction of oxygen in the initial part of the cathode and the concentration of oxygen ions increases close to the electrolyte cathode interface.

Mizusaki et al. estimated that the TPB length of LSM is proportional to the reaction rate for unit of area [82-86]. In addition, H. Fukunaga et al. demonstrated that adding YSZ to LSM increases the length of the triple phase boundary, reducing the over potential of the cathode[87].

This analysis shows that the mixture between an electron conductor and an ion conductor improves the performance of the cathode, compared to a system with only an electron conductor. The mechanisms of electrochemical oxidation are not

so simple because the reaction can take place in two phases, as shown in the figure 2.11:

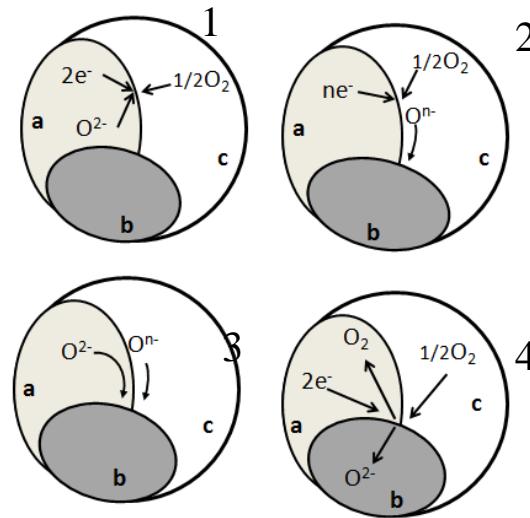


Figure2.11 - Possible mechanisms on the three phases:  
a) perovskite b) electrolyte c) air

Mechanisms:

- (1) Incorporation of oxygen into the bulk of the electronic phase.
- (2) Adsorption and/or partial reduction of oxygen on the surface of the electronic phase.
- (3) Bulk or surface transport of  $O^{2-}$  or  $O^{n-}$ , respectively, to the a/b interface; Electrochemical charge transfer of  $O^{2-}$  or combinations of  $O^{n-}$  and  $e^-$ , a/b interface;
- (4) Rates of one or more of these mechanisms wherein the electrolyte itself is active for generation and transport of electro-active oxygen species.

These possible mechanisms of electrochemical reduction of oxygen affect the cathode activity according to a variety of parameters, such as bulk transport path,

chemical capacitance, co-limit kinetic and the sensitivity of interface resistance to various factors.

Taking into consideration the previous cases where a pure electron conductor (Pt) or a mixed ionic conductor material were used (LSM-YSZ), we can observe that in the first case the reaction is limited only on interface electrode/ electrolyte and so it is limited only on the material surface. On the other hand, the oxygen reduction occurs on the surface of the material but oxygen ions are transported through the bulk of the material to the electrode/electrolyte interface. In last case, the oxygen diffusion is not limited and this drives the process by improving the performance of the cell and reducing the activation energy of the reduction reaction. However, if oxygen diffusion is strongly involved in the bulk, this can create secondary reactions between the oxidant and reducing substance which affects the performance of the cell because an increase in the capacitance is easily observable, causing an interruption of current. Thus, the capacitance is a good indicator of the interface and/or bulk degree of the materials involved.

#### 2.4.3. Current collector

In the previous paragraph, a description of the mechanism of oxygen reduction was presented and two different cathodes were used. The performance of a mixed ion-conducting cathode was considered to be better than that of an electron-conducting material because a greater active surface was observed.

However, during the sintering process the number of active sites is reduced and the interaction between electrode/electrolyte interfaces reduces the electron-conductivity of the electrodes. For this reason, the electrode is usually covered by a well-conducting current collector and electrodes sintered in-situ demonstrate good performance in different studies, even if the durability of the current collectors was limited as function of the operating temperature [83][84-85].

M. J. Jørgensen et al. demonstrated in their studies carried out on the LSM current collector, that performance is a function of the sintering temperature of the current collector. In fact, at a sintering temperature of 1150°C with two layers of current collectors, better polarization resistance results were achieved, despite the density sintering degree being low. This phenomenon can be explained by the increased TPB presented by a less sintered layer compared with a more sintered layer[89].

## **2.5. Anode**

In electrochemistry, the anode is the part of the cell in which oxidation reactions between the oxidant and the fuel take place and the electrons produced flow out towards the external part of the circuit, through to the electrically conductive interconnector.

An operative anode must possess the following characteristics:

- ✓ Good catalytic activity able to oxidise the fuel.

- ✓ High electrochemical, dimensional and morphological stability. In addition, it must be inert to possible poisonous substances like sulphur.
- ✓ Highly electron-conductive materials at high operation temperature.

It must be porous in order to guarantee the correct transport mass of fuel to improve the oxidation phenomenon.

In order to satisfy these criteria, the anode must be composed of a metallic part as well as a ceramic part that stabilises the structure of the anode and extends the triple phase boundary.

### 2.5.1. Properties of anode materials

One of the commercial anodes used in solid oxide fuel cells is a mixed metal ceramic anode that consists of Ni and YSZ. The main companies that use this type of anode are Ceramic Fuel Cells Limited and Electric Power Development Co. [92][93]. Ni is used because it is resistant to high temperatures and reduction environment. In addition, it is compatible with most of the SOFC components. However, nickel metal has some disadvantages, such as its expansion under oxidant atmosphere and the fact that it is limited to work under natural gas because Ni tends to form carbon at the surface of the anode, blocking the catalytic site and reducing the performance of the cell. Ni metal is a good electron conductor but it has poor dimensional stability and in order to improve this, a ceramic material is added to it. Furthermore, the addition of a ceramic material

---

stabilises the TEC of pure Ni in order to make it compatible with YSZ electrolyte. The portions of YSZ play an important role in the formation of a conductive path to diffuse oxygen ions.

In the hybrid direct carbon fuel cell, the anode used is NiO-YSZ or NiO-GDC because the reduction of nickel oxide to Ni occurs in situ by using carbon fuel. This increases the volume of the pores because the volume of NiO is greater than Ni metal. This in turn improves the transport mass of the gases and liquid phases in the pores.

### 2.5.2. Microstructure

The microstructure of the anode is very important for the performance of the cell and its performance depends on the fabrication method. The Ni-YSZ cement and air should form a percolating network and this is very important for electron conductivity and oxygen ion conductivity, as well as gas fuel. In fact, the percolating network is the representation of the length of the TPB that is directly proportional to the performance of the cell, as explained previously. In the state of the art, Ni-YSZ thickness is around 100  $\mu\text{m}$  and the percentage of Ni in the cement must be higher than 30% in order to guarantee a certain minimum electron conductivity, while the degree of porosity must be around 30-50% in order to provide adequate gas diffusion into the entire anode structure [84-97]

YSZ has to be able to stabilise the structure and balance the shrink effect between Ni and electrolyte. This is achieved by mixing different YSZ powders with different sized particles. The morphology of Ni-YSZ cement must be modified when this anode is used for the hybrid direct carbon fuel cell because the mechanism of reaction on the anode surface involves both the solid fuel and gaseous fuel. In fact, the amount of nickel is increased to a minimum range between 45%-65% for two reasons: Firstly, this amount of nickel improves the electron conductivity of the anode and secondly, nickel metal plays an important role in the catalytic activity of the carbon. Furthermore, the volume of pores must be higher because a small pore volume for capillarity effect could be filled with the molten carbonate, reducing the catalytic activity.

### 2.5.3. Triple phase boundary and mechanism of reaction

Thus far the characteristics of the anode have been outlined but no mechanism of reaction between anode and fuel had been illustrated. In cases where the anode is used in solid oxide fuel cells, the type of fuel used is gaseous and the reaction mechanism occurs on the triple phase boundary as well as occurring at the cathode. In both cases the microstructure was organised so as to increase the contact surface of the triple phase boundary.

In the hybrid direct carbon fuel cell, the situation in the anode chamber is more complex than in the anode chamber of solid oxide fuel cells because in the

---

former, more than 3 phases are involved and in addition a solid fuel is used. Furthermore, the anode is extended in the HDFC by the presence of molten carbonate salts where electrochemical reactions take place between carbonate ions and carbon fuel, producing electrons and gases that react again in the anode cement (Ni-YSZ), together with carbon, as shown in eq. 2.10, 2.11, 2.12 and 2.13.

This description of the anode and the possible mechanism of reaction in the anodic chamber demonstrate that, as in the hybrid direct carbon fuel cell, the anode mechanism cannot be limited only to the triple phase boundary; we need to consider the total reaction that takes place in the anodic chamber. These complex mechanisms were investigated by impedance spectroscopy analysis in order to understand the electrochemical behaviour of the whole anodic cell and to determine whether the strongest contribution is due to the reaction that occurs in the mixture of carbonate/carbon or the reaction that occurs on the surface of the anode.

## **2.6. Carbon fuel in hybrid direct carbon fuel cell**

One of the important points of hybrid direct carbon fuel cells is the use of carbon fuel instead of hydrogen fuel because it presents more advantages than hydrogen:

- Higher energy density than hydrogen (20 kWh/l for carbon, 2.4kWh/l for hydrogen)

- Higher electrochemical oxidation of carbon compared to the oxidation of hydrogen:



- More readily-available than hydrogen. Despite the fact that hydrogen is readily available in nature, it needs to be produced by water or by hydrocarbure cracking.
- Easier to store than hydrogen because it does not require special storage facilities and it is easier to transport than hydrogen and other organic fuels.

In addition, carbon oxidation produces pure  $\text{CO}_2$  gases that can be captured and stored for other uses (CCS), whereby the gas is pumped underground, for example into depleted oil tanks. Alternatively it can be adsorbed in solvent or functional solids, or can be used as an activator gas in the preparation of active carbons.

#### 2.6.1. Roles of the carbon fuel in HDCFC

The most important characteristic of hybrid direct carbon fuel cells is the use of carbon as fuel. This type of fuel cell can use different types of carbons as fuel, such as coal, bio-char, carbon and black graphite and for this reason they are more versatile than other types of cells. However, the electrochemical

---

performance of HDCFCs depends on the properties of the carbon fuel, such as particle size, purity, surface area and lattice disorder, and in particular the latter two properties, as demonstrated by Cherepy and Jain[36][59].

Impurities as well as surface area and lattice affect the performance of the cell and a pure carbon fuel is obtained through pyrolysis, cracking of hydrocarbon or directly from coal mines. The last two methods of carbon production are not “green” processes because they produce large amounts of toxic substances which affect the environment in general, the geologic substrate and human health. Moreover, the production of carbon from the cracking process of hydrocarbon is limited by the amount of hydrocarbon in the world and its manufacture process is not green. Today, the pyrolysis of biomass is considered the optimum method for obtaining carbon for several reasons: Firstly, it is a clean method because sub-products like bio oil and bio gas can be used in the fuel cell and are not released into the atmosphere, as shown in the diagram (2.12):

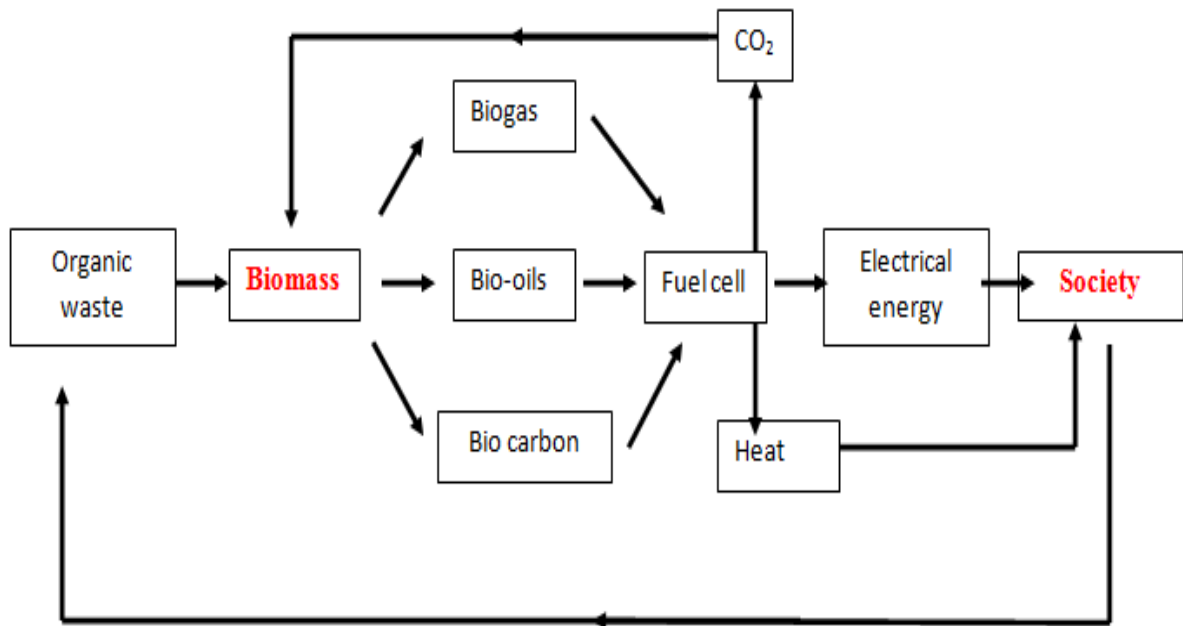


Figure 2.12- Diagram of the utilization of the cycle of biomass from pyrolysis to the production of electrical energy and heat for the entire community.

Secondly, using biomass which comes from renewable and non-renewable stocks (e.g. wood, paper, straw, nutshells and humid solid waste), facilitates sustainable energy production.

Thirdly, the pyrolysis process for the production of carbon can use solid organic waste (e.g. plastic, tyres) instead of biomass, but in this case there are often more impurities and an additional purification step could be required.

In our case, the pyrolysis process focused on the pyrolysis of biomass because it is the best method for obtaining a pure carbon which is easier to characterise (both using electrochemical and physical methods) than the carbon obtained from the pyrolysis of plastic material.

### 2.6.2. Pyrolysis process

Pyrolysis is a special case of thermolysis and it is most commonly used for organic materials in the absence of oxygen. It occurs only at high temperatures (e.g. above 300°C for wood; it varies for other materials) because it is an endothermic process. In general, the pyrolysis of organic substances produces three different phases: The solid phase consisting of carbon, the gaseous phase that consists of incondensable gases and a third phase consisting of condensable gases. The condensable gases composed of high weight molecular substances, produce liquid after being condensed.

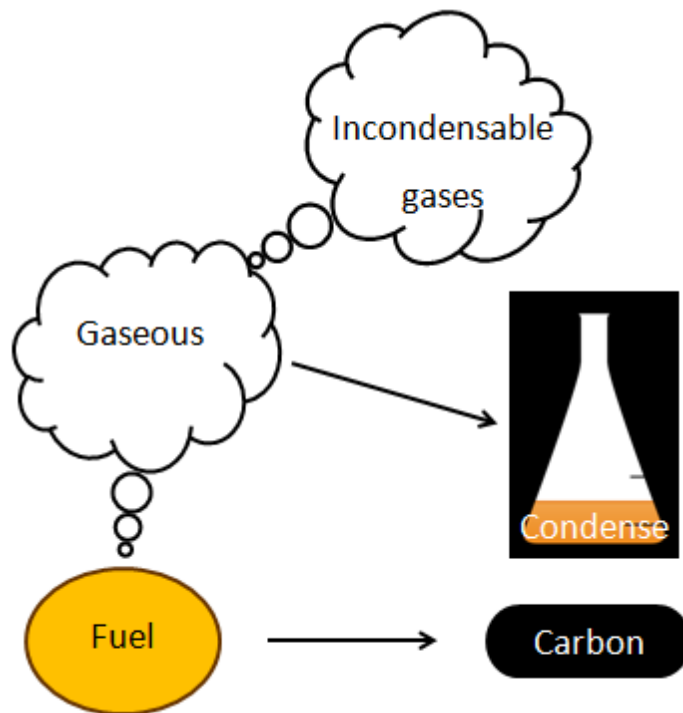


Figure 2.13- Schematic description of the different phases that are formed during the pyrolysis process. Fuel is the organic substance.

Extreme pyrolysis, which leaves only carbon as residue, is called carbonization and is also related to the chemical process of charring.

In the past this process was used heavily in industrial chemistry in the production of active carbon and it has recently been employed in the production of bio-oil or syngas and bio-char from biomass.

The composition of the three phases changes in relation to the pyrolysis temperature, type of pyrolysis process (i.e. fast pyrolysis, flash pyrolysis) and type of reactor (fluid bed, stationary etc.).

Several types of organic matter can be used as feedstock for pyrolysis. For example, suitable plant material such as green waste, sawdust, waste wood and woody weeds can be used, as well as agricultural sources like nut shells, straw, cotton trash, rice hulls and switch grass. In addition, animal waste such as poultry litter and dairy manure can be pyrolysed.

In recent years, the pyrolysis process has been applied to plastic materials such as tyre, but this pyrolysis is more complex and compared to using biomass, a larger amount of toxic products from combustion are yielded and subsequently released into the environment.

### 2.6.3. Biomass

Biomass is a carbon-based substance composed of a mixture of organic molecules containing hydrogen, as well as atoms of oxygen, often nitrogen and also small

---

quantities of other atoms, including alkali, alkaline earth and heavy metals. In general, biomass consists of cellulose and lignin compounds and their respective percentages can change as function of the type of biomass in question. The percentage of lignin and cellulose contained in the biomass are very important because they affect the quality of carbon produced. In fact, the residual carbon mass of the biomass after the pyrolysis process is dependent on the percentage of lignin as well as pyrolysis temperature.

Cellulose is an organic compound with the formula  $(C_6H_{10}O_5)_n$ ; a polysaccharide consisting of a linear chain of several hundred to over ten thousand  $\beta(1\rightarrow4)$  linked D-glucose units, as shown below:

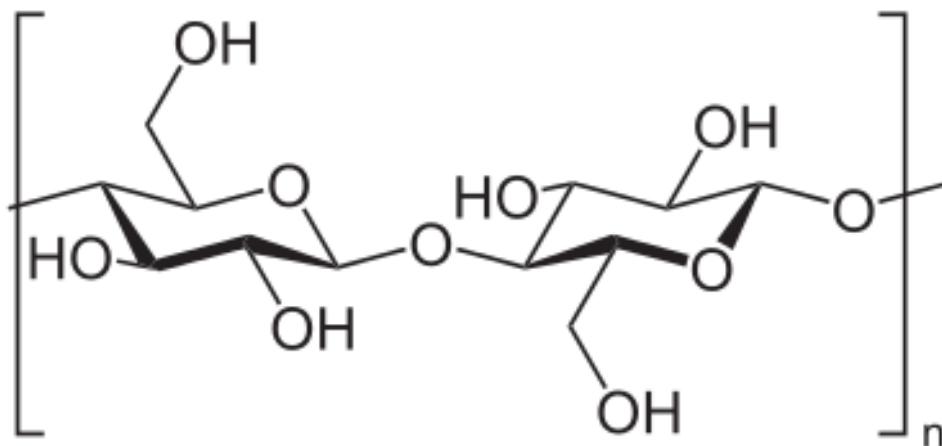


Figure 2.14- Monomeric unit of  $\alpha$  cellulose presents in the biomass.

On the other hand, lignin is an organic substance that consists of cell, fibres and vessel and it is impossible to precisely define its structure because it changes as function of the type of plant. However, it is possible to provide a common

---

definition of lignin that is represented by a dendritic structure phenyl propene, as shown in figure 2.15:

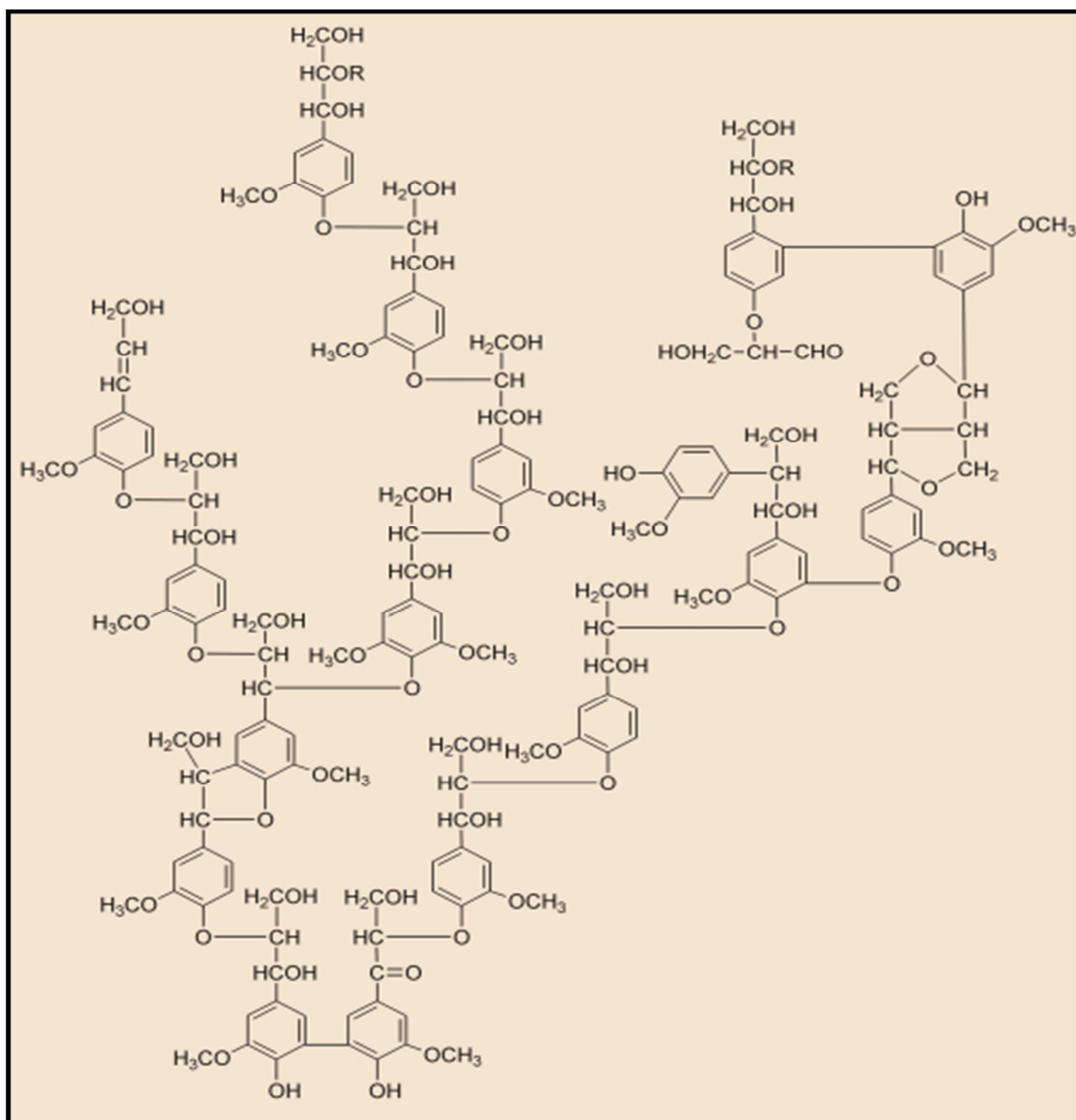


Figure 2.15- Structure of lignin as the main component of biomass.

The different structures of lignin and cellulose allow us to understand why a high percentage of cellulose reduces both the residual mass the overall performance of carbon products.

Biomass contains a large amount of mineral salts that come from the soil and these can affect the performance of the cell because this material can reduce the acidity or the conductivity of the carbonate salts in the anode chamber. In general, biomass has a higher lignin than cellulose content.

#### 2.6.4. Bio-carbon

The residual solid part generated by the pyrolysis process is generic carbon or bio-carbon when it is used as biomass. Bio-carbon is an amorphous type of carbon that is rich in mineral salt compounds and its carbon structure is less complex than lignin. Its complexity is function of the operation temperature of the pyrolysis reactor. In fact, the degradation phenomena are more visible at high temperature than at low temperature because the large amount of energy generated favours the breaking of the functional group as well as a rearrangement of the structure, which favours the formation of small molecules or giant agglomeration. At low temperatures the energy provided is not enough to favour this arrangement.

A generic structure of bio-carbon can be hypothesized as shown in figure 1.5

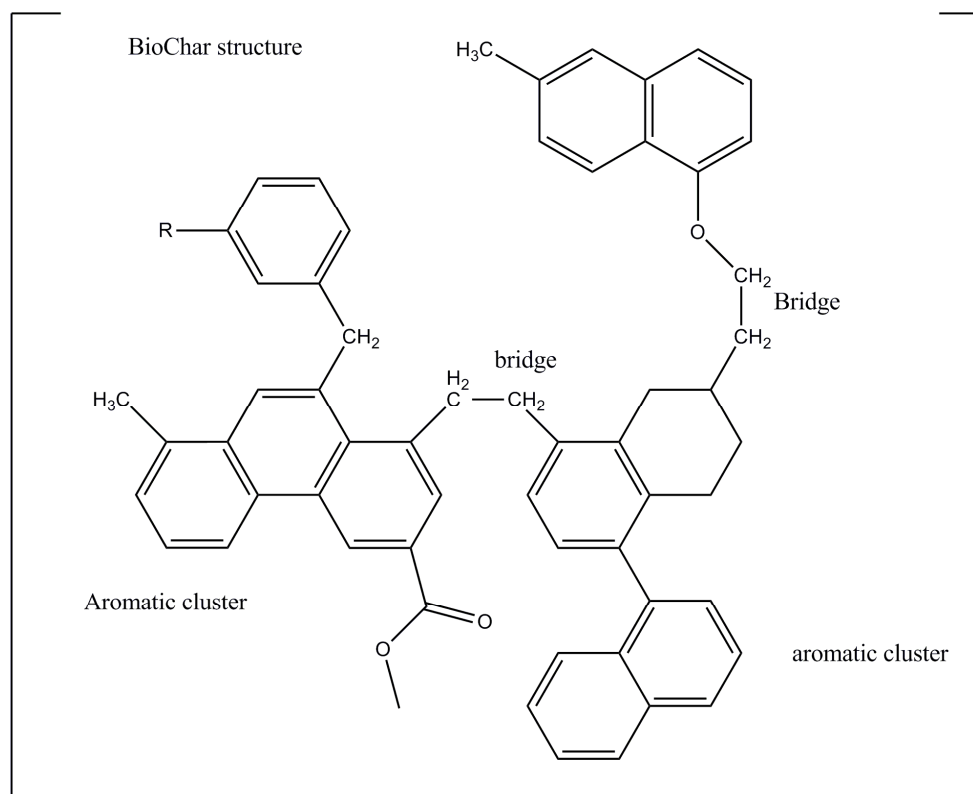


Figure 2.16- Structure of bio-char originated by pyrolysis of biomass at 500°C [97][98].

The carbon structure of a generic biomass pyrolysed at temperatures ranging between 450-550°C is composed of aromatic and aliphatic clusters, most of which originate from the rearrangement of the carbon structure, that are linked by  $CH_2$ ,  $CH_2-CH_2$  and  $CH_2-CH_2-O$ - bridges.

The number of clusters and bridges are function of temperature but can also be affected by the flow rate and ramp rate values. The presence of a high number of clusters and bridges in the structure of bio-carbon is connected to the amorphous structure[99].

This type of carbon can be particularly reactive due to partial degradation. This characteristic could improve the performance of completely pyrolysed carbon because the oxidation of carbon is difficult and this requires high activation energy.

For reasons previously outlined, bio-carbon is a good candidate for the fuel used in a direct carbon fuel cell.

## 2.7. References

- [61] A.S. Lipilin, I.I. Balachov, L.H. Dubois, A. Sanjurjo, M.C. McKubre, S.Crouch-Baker, M.D. Hornbostel, F.L. Tanzella, US Patent. Number:20060019132 (2006)
- [62] J. Robert Selman -Direct Carbon Fuel Cell Workshop -July 30, 2003
- [63] Brentan Alexander, Reginald E. Mitchell, and Turgut M. Gür. *J. Electrochem. Soc.* (in press)
- [64] B. R. Alexander, R. E. Mitchell, T. M. Gür, *ECS Trans.* (in press)
- [65] J.H. Park and R.N. Blumenthal, *J. Electrochem. Soc.* 136,2867 (1989).
- [66] T. Takahashi. *Physics of Electrolytes*, ed. J. Hladik. Academic Press, 989 (1972)
- [67] S. Ikeda, O. Sakurai, K. Uematsu, N. Mizutani, M. Kato, *J. Mater. Sci.* 20 (1985) 4593
- [68] X. Li, B. Hafskjold, *J. Phys. Condens. Matter* 7 (1995) 1255.
- [69] D. Steele, B.E.F. Fender, *J. Phys. C; Solid State Phys.* 7 2 3 (1974) 1.
- [70] B.W. Veal, A.G. Mckale, A.P. Paulikas, S.J. Rothman, L.J. Nowicki, *Physica B* 150 (1988) 234.
- [71] C.R.A. Catlow, A.V. Chadwick, G.N. Greaves, L.M. Moroney, *J. Am. Ceram. Soc.* 69 (1986) 272.
- [72] C.R.A. Catlow, A.V. Chadwick, A.N. Cormack, G.N. M. Leslie, L.M. Moroney, *Mat. Res. Soc. Symp.Proc.* 60 (1986) 173.
- [72] Lux H., *Z. Electrochem.* 45 (1939) 303.
- [74] M. Cassir', C. Belhomme - *Plasmas & ions* (I 999) 1, 3-15
- [75] J. Larminie, A. Dicks - *Fuel Cell Systems Explained*-Wiley and Sons (2000)
- [76] C. Jiang, J.T.S. Irvine - *Journal of Power Sources* 196 (2011) 7318 – 7322
- [77] H. Huang, M. Nakamura, P.C. Su, R. Fasching, Y. Saito, F.B. Prinz, *J. Electrochem.Soc.* 154 (2007) B20–B24.

- [78] K. Kerman, B.K. Lai, S. Ramanathan, J. Power Sources 196 (2011) 2608–2614.
- [79] Y. Yan et al. - Journal of Power Sources 206 (2012) 84– 90 85
- [80] J. Mizusaki, K. Amano, S. Yamauchi, K. Fueki - Solid State Ionics 22 (1987) 323–330.
- [81] N.L. Robertson, J.N. Michaels, J. Electrochem. Soc. 137 (1990) 129–135
- [82] Hee Y. Lee, Woo S. Cho, and Seung M.oh, H.-D., J. Electrochem. Soc., 142, 2659(1995).
- [83] J. Mizusaki, The Chemical Society of Japan 9 (1988) 1623.
- [84] J. Mizusaki, Denki Kagaku 58 (1990) 520.
- [85] J. Mizusaki, H. Tagawa, K. Tsuneyoshi and A. Sawata, J. Electrochem. Soc. 138 (1991) 1867
- [86] H. Fukunaga et al. I Solid State Ionics 86-88 (1996) I I79- 1185
- [87] M. Juhi, S. Primdahl, C. Manon, M. Mogensen, J. Power Sources 61 (1996) 173.
- [88] H. Fukunaga, M. Ihara, K. Sakaki, K. Yamada, Solid State Ionics, 86–88 (1996) 1179–1185
- [89] M.J. Jørgensen, P. Holtappels, C.C. Appel, Solid State Ionics 70/71 (1994) 59.
- [90] E.P. Murray, T. Tsai, S.A. Barnett, Solid State Ionics 110 (1998) 235.
- [91] M. J. Jørgensen et al. / Solid State Ionics 139 (2001) 1 –11
- [92] R. Bolden, K. Föger, T. Pham, Proc. of the 6th Intern. Symp. on Solid Oxide Fuel Cells (SOFC-VI), Honolulu, Hawaii, USA, Eds.: S.C. Singhal, M. Dokiya, The Electrochemical Society, Inc., Pennington, NJ, USA (1999) 80.
- [93] H. Mori, H. Omura, N. Hisatome, K. Ikeda, K. Tomidal, Proc. of the 6th Intern. Symp. on Solid Oxide Fuel Cells (SOFC-VI), Honolulu, Hawaii, USA, Eds.: S.C. Singhal, M. Dokiya, The Electrochemical Society, Inc., Pennington, NJ, USA (1999) 52.
- [94] S. Primdahl, M. Mogensen, J. Electrochem. Soc. 146 (1999) 2827.
- [95] M. Brown, S. Primdahl, M. Mogensen, J. Electrochem. Soc. 147 (2000) 475
- [96] J. Divisek, R. Wilkenhöfner, Y. Volfkovich, J. Appl. Electrochem. 29 (1999) 153.
- [97] N. Nakagawa, K. Nakajima, M. Sato, K. Kato, J. Electrochem. Soc. 146 (1999) 1290.
- [98] Orendt, A. M.; Solum, M. S.; Sethi, N. K.; Pugmire, R. J.; Grant, D. M. Advances in Coal Spectroscopy; Meuzelaar, H. L. C., Ed.; Plenum Press: New York, 1992; p 250
- [99] Solum, M. S.; Pugmire, R. J.; Grant, D. M. Energy Fuels 1989,3,187

### **3.0. Experimental part**

#### **3.1. Pyrolysis plant design**

The pyrolysis process was detailed in chapter 2 and as previously explained, it is used to produce carbon under an inert atmosphere such as nitrogen or argon, which must not contain any oxygen molecules. During the pyrolysis process, three different components are collected and a pilot plant was designed and built so as to capture the different fractions.

The plant consists of three different components: pyrolysis reactor, condenser and solution trap. The pyrolysis reactor is the heart of the plant in which the biomass is pyrolysed in an inert atmosphere. The condenser and solution trap are the secondary parts of the plant in which the heavy fraction and light fraction of volatile gases are condensed and trapped respectively. Uncondensed gases such as hydrogen, methane, carbon monoxide and carbon dioxide are detected and can be captured using a multilayer of active carbon filter or used as fuel to feed the pyrolysis furnace.

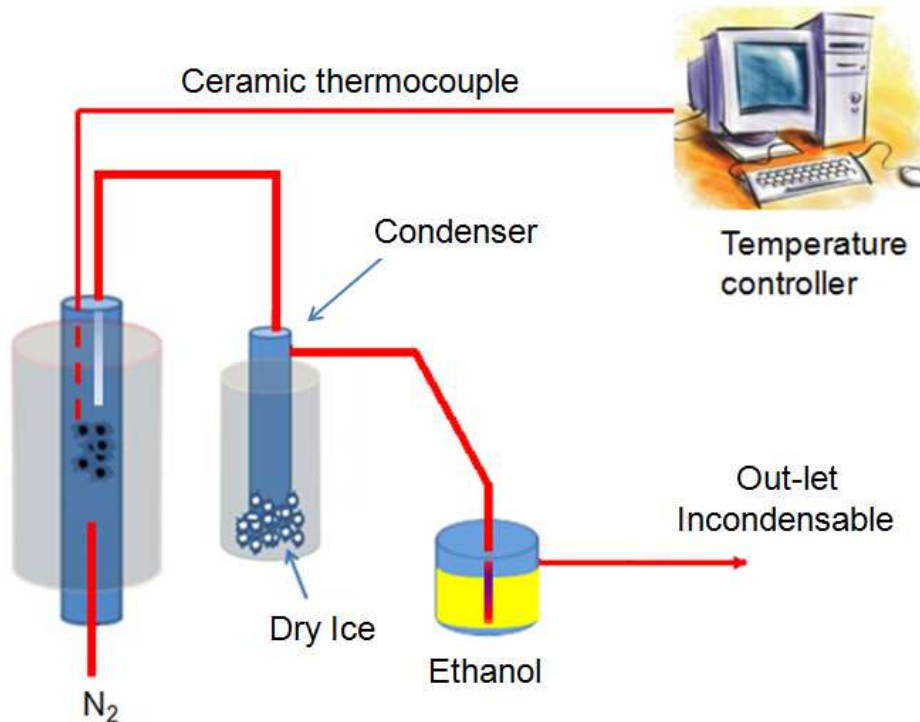


Figure 3.1- Schematic design of pyrolysis plant developed at the University of St Andrews for the pyrolysis of bio-mass. This plant is suitable both for traditional pyrolysis and for fast pyrolysis.

### 3.1.1. Reactor

The reactor consists of a stainless-steel chamber that is protected from any possible reaction with carbon or gases by using a quartz tube that separates the carbon by way of a metallic mantel. In fact, carbon reacts with stainless steel at high temperature and it can be responsible for weakening the structure of the reactor.

The reactor is shown in figures 3.2 and 3.3



Figure 3.2- Picture of the pyrolysis reactor and relative inlet and outlet tubes to keep the atmosphere inert and collect gas.

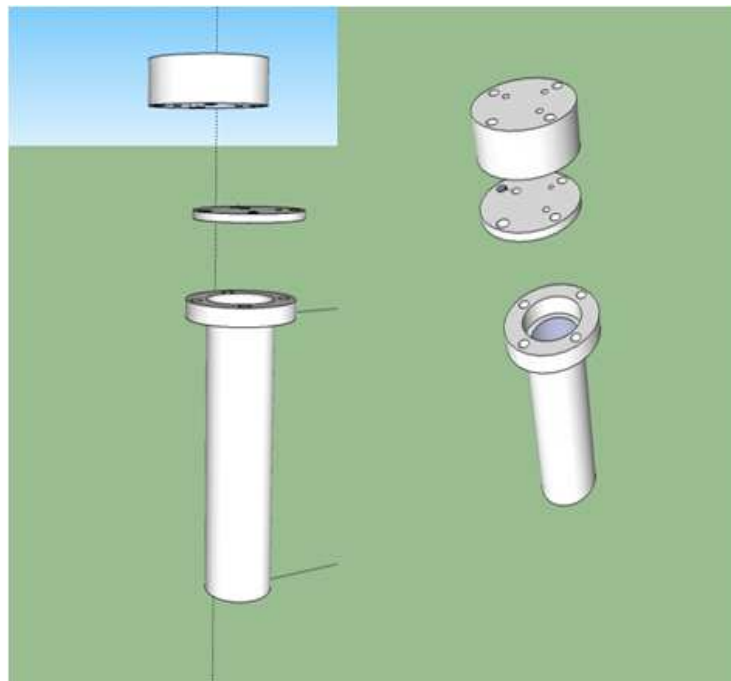


Figure 3.3– 3D figure of pyrolysis chamber (designed using Google sketch up)

Internally, there is a disc of glass ceramic material (maccor) that has low thermal conductivity and exhibits good thermal shock resistance and mechanical toughness compared to conventional glass with similar thermal and mechanical properties [100]. It is used as a separator between the top part of the reactor and the internal quartz of tube so as to prevent gas leaks. This type of material was chosen because it can be used in air atmosphere up to 1000°C or in a vacuum system, in which case the temperature cannot exceed 600°C. Furthermore, it has a negligible corrosion effect under acid or basic conditions.

### 3.1.2. Condenser and blocking solution

A condenser is a unit that can condense vapours into liquid, taking advantage of the temperature difference between the reactor (600°C) and the condenser chamber, which is held at lower temperature than the reactor. The specific temperature difference is chosen in relation to the type of gases being condensed. In a classic pyrolysis plant, the condenser uses cold water to condense the gases. However, in the plant used at the University of St Andrews, the condenser was refrigerated using dry ice (-78°C) to ensure that the entire fraction of volatile substances was condensed.

In order to prevent condensation in the tube connecting the reactor and the condenser, the tube was warmed up using warm nitrogen gases coming from the

---

reactor. Heat dispersion from the tube was prevented by covering the whole tube length with an insulator material.

The light fraction contained in the carrier gases was trapped in ethanol solution. Ethanol solution was chosen because it shows greater affinity with light fraction than with THF, acetone, a 30-70% mixture in volume of water and acetone and water after carrying out different tests.

### **3.2. Cell manufacturing and analytic technique.**

Having analysed each component, a brief description of cell manufacture and analytic techniques used to investigate the performance of the cell will be illustrated in the next paragraphs.

#### 3.2.1. Tape casting

Tape casting is also known as “doctor blading” and “knife coating” and is an important ceramic forming technique used in the production of thin and flexible tape. It was developed more than 50 years ago for the production of ceramic capacitors with improved dielectric properties and smaller footprints, as required by the emerging microelectronics industry [101-104].

Today, this process is widely used in many industries such as plastic, paper and paint manufacture due to its high versatility, relative simplicity and low realization cost compared with other methods such as dry pressing, slip casting

---

or injection moulding. It allows the formation of thin tape with large area and high reproducibility under scale-up conditions. The thin ceramic sheets are essentially two dimensional structures.

### 3.2.2. Principles.

The liquid mixture for the tape casting process is a slurry made from a suspension of ceramic, metal or polymer particles in an organic solvent or water, mixed together with plasticizers and/or binders that are able to increase the elasticity and the dimensional stability of the tape after casting. The actual tape is formed when the slip is cast onto a flat surface by doctor blade to a non-adhesive carrier plastic film.

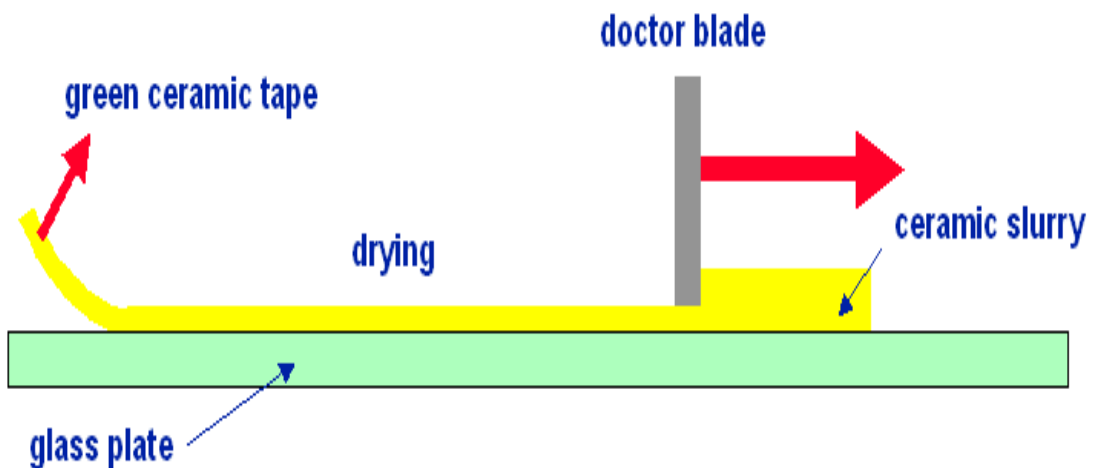


Figure 3.4- Schematic representation of a tape casting machine with a single doctor blade barrier.

After the slip has been cast, the wet tape must be dried to prevent any solvent being trapped in the film and passing to the next steps to be formed.

The slurry must constantly be kept under the same temperature conditions because throughout the casting process the viscosity of the slurry can affect the casting and the homogeneity of the film. The doctor blade gap between the blade and the carrier defines the wet thickness of the tape being cast.

### 3.2.3. Slurry components

The slurry formulation for tape casting process is a complex mixture of different components and each has a particular function within the mixture.

Generally the slurry for tape casting is composed of a ceramic, metallic or mixed powder, solvent plasticizer, binder and surfactants. The duty of this material is to facilitate the fabrication of the shape and the green density of the tape.

The powder is the most important part of the formulation because it characterises the performance of the final product after firing. For this reason, it is very important to characterise the physical chemistry properties (i.e. particle size and distribution and surface area) of the powder before mixing. In fact, using a ceramic powder with smaller particles favours the intrinsic sintering quality more than large particles[100][101].

In fact, the particle size distribution is responsible for the bulk density of the tape as fine particles are more difficult to pack due to the higher surface energy that is the driving force in sintering a dense final product.

Another important parameter to consider in a powder is surface area. It is a value that gives an indication of the ability of the powder to adsorb organic additives such as binder, plasticizer, surfactants and solvent. The last components mentioned are additives that complete the formulation and they provide the powder with characteristics that it does not already possess. As a result, it is better to analyse each component separately rather than together.

#### *3.2.3.1. Solvent*

Tape casting is a “fluid forming process” and it must be able to distribute each component homogeneously in the slip. The major part of solvent used for tape casting is non-aqueous but it can be also aqueous. This type of solvent has large diffusion for low toxicity. In the first case, the solvent is known as “solvent-based casting” and in the second case it is called “water-based casting”.

The selection of possible solvents used for tape casting is vast and the choice depends on the type of binder, plasticizer and dispersant used. Usually a single solvent is used to prepare a slurry formulation, however a mixture of solvents is sometimes used because this helps to dissolve the other components more easily than using just a single solvent. In addition, using more solvent helps to control

---

physical parameters such as drying speed, rheological control, cost and safety. For this reason, the majority of solvents used are binary or quaternary mixtures.

### 3.2.3.2. *Binder and plasticizer*

Binders are polymeric materials of different natures that have the task of holding the system together. In fact, they supply the network in which ceramic particles are entrapped.

Binders have a strong effect on the properties of green tape, especially flexibility, printability, smoothness, and durability.

In order to improve the performance of the binder, a plasticizer is added to the slurry. It makes the tape more bendable and reduces the number cracks in the structure of the tape during the process of forming and assembly of the different layers.

The plasticizer is used in particular when the tape must be formed following a specific shape, e.g. tubular, or to favour the lamination process between additional layers [100][103].

### 3.2.3.3. *Surfactant*

Surfactant agents are particular substances that are able to affect dispersion, wetting, high density, porosity, deflocculating, slip stability, green strength and any other property that affects the casting process.

They are substances which are able to energetically modify the particle surface, changing the characteristics of ceramic materials; for example by increasing or decreasing the surface energy or surface chemistry. These substances are able to make particles do what they are usually unable to [100].

## **3.3. X-ray Diffraction analysis (XRD)**

X-ray scattering techniques are a family of non-destructive analytical techniques which reveal information about the crystal structure, chemical composition and physical properties of materials and thin films. These techniques are based on observing the scattered intensity of an X-ray beam hitting a sample, as a function of incident and scattered angle, polarization and wavelength or energy.

### 3.1.1. Theory of X-ray diffraction

X-ray diffraction techniques are based on the elastic scattering of electromagnetic X-rays with a wavelength around  $1\text{\AA}$  ( $10^{-10}$  m). X-rays are produced by the rapid deceleration of a charged particle of sufficient kinetic energy, such as an electron.

---

X-rays derived from the collision of electrons against their target are composed of different wavelengths. The intensity of these wavelengths depends on the voltage applied when at the time of the x-ray. X-rays are used in most diffraction experiments, using monochromatic x-rays which are produced by striking a beam of electrons (accelerated at range from 20-30kV by the high voltage maintained across the two electrodes contained in the x-ray tube) against a metal target, often composed of Cu.

The electrons inside the tube produce continuous radiation caused by their deceleration along the length of the tube. This white radiation is called Bremsstrahlung. There are noticeable, characteristic peaks in the continuous spectrum when the electrons have enough energy.

The electrons that strike the metal target possess enough energy to ionize the metal, thus removing an electron from its first level. This effect causes a rearrangement of the electrons in the orbital of the metal. In the case of Cu, an electron in an outer orbit (2p or 3p) drops down to occupy the vacancy and the energy released in the transition manifests itself as radiation, as shown in figure 3.5:

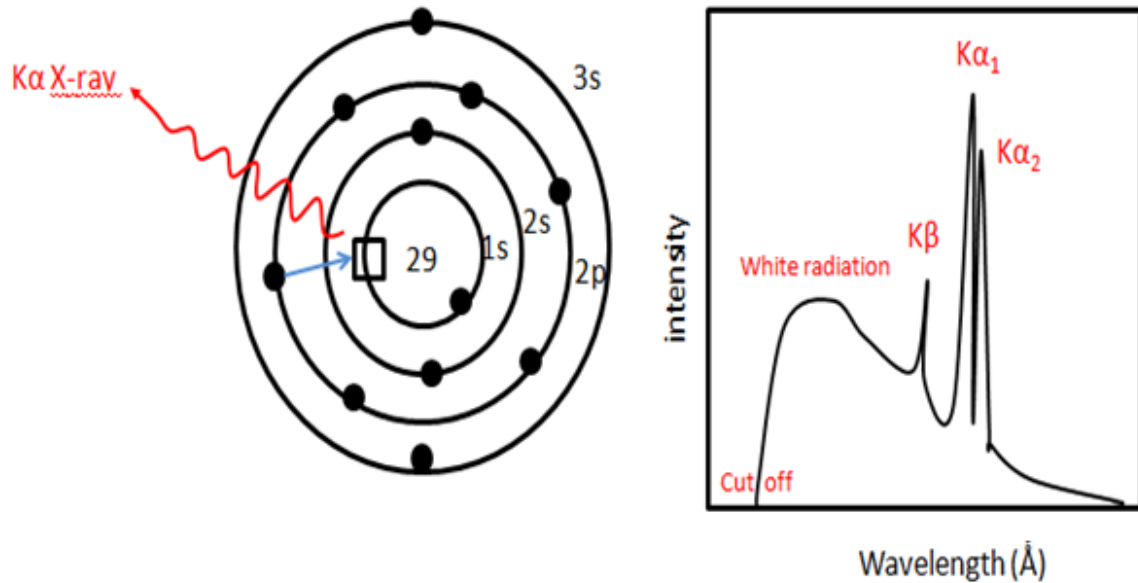


Figure 3.5 - Schematic representation of the Cu  $K\alpha$  X-ray generation.

Each transition is characterised by a fixed value of energy: for example the transition  $2p \rightarrow 1s$  is called  $K\alpha_1$  and it has a wavelength of  $1.541\text{Å}$ . It is the transition with maximum intensity.

The beam of electrons required to produce the X-ray radiation is produced by a tungsten filament and the electrons are accelerated to the anode by a difference of potential of around 30 kV. The electrons strike the Cu which is fixed to the anode and thus X-rays are produced. The tube which the beam passes through is held under a vacuum to prevent oxidation phenomena of the filament. The radiation leaves the chamber in which it is produced by passing through a Be window.

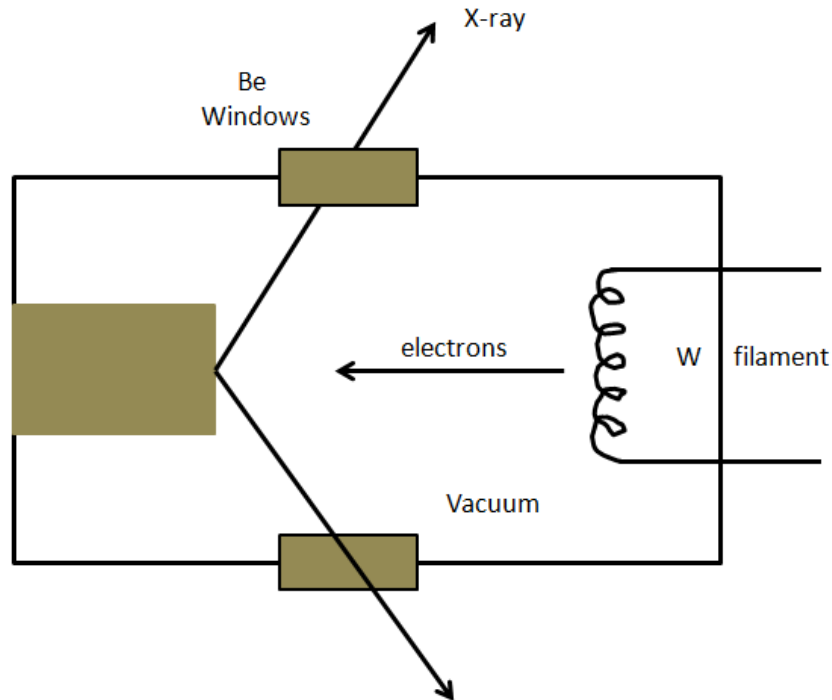


Figure 3.6 - Schematic design of the X-ray tube with a tungsten filament.

### 3.3.2. Diffraction of X-ray in crystal structure

X-ray diffraction is a technique used to investigate the crystal structure. In fact, x-ray radiation, which passes through a material of regular structure that consists of points located at the same distance from each other, is subject to diffraction phenomena in all directions when the incident radiation collides against a regular structure in which the particle size is of similar scale to the incident radiation. A constructive interference will be visible if the diffracted beam is in phase with all other beams diffracted, as shown in figure 3.7.

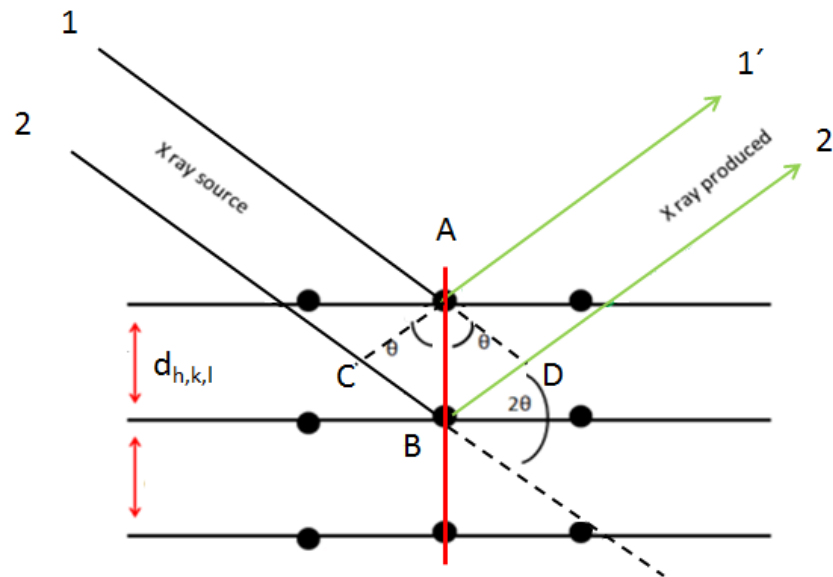


Figure 3.7- Schematic description of the diffraction of a wave that produced constructive interference in directions 1 and 2.

If we consider the diffracted beams 1 and 2 that scatter by atom A and B and the path difference for the rays 1A1' and 2B2' is shown in eq. 3.1:

$$CB + BD = d \sin \theta + d \sin \theta \quad \text{eq. 3.1}$$

Where the  $\theta$  is the diffraction angle formed by the incident ray after diffraction. Scattered rays will be in phase if the condition in which the path difference is equal to a whole number  $n$  of wavelength is satisfied, eq.3.2:

$$CB + BD = n\lambda \quad \text{eq. 3.2}$$

The  $n$  number represents the order of diffraction.

Thus combining eq3.1 and 3.2:

$$n\lambda = 2 d_{hkl} \sin \theta \quad \text{eq.3.3}$$

The diffraction is satisfied when the two rays follow Bragg's law.

Diffraction takes place when the wavelength of the wave motion is the same order of magnitude. This means that the value of  $\sin\theta$  cannot exceed unity:

$$\frac{n\lambda}{2d} = \sin \theta < 1 \quad \text{eq.3.4}$$

Therefore  $n\lambda$  must be less than  $2d$  and the smallest value of  $n$  must be 1 in order to have diffraction.

The most comprehensive description of scattering from crystals is given by the dynamical theory of diffraction, which considers the wave field in the periodic potential of the crystal and takes into account all multiple scattering effects. In fact, the crystal potential by itself leads to refraction and specular reflection of the waves at the interface with the crystal and delivers the refractive index of the Bragg reflection [107].

### 3.3.3. Miller indices

The miller index notation,  $hkl$ , defines a set of parallel crystallographic planes that traverse the  $a$ ,  $b$ ,  $c$ , axes at  $a/h$ ,  $k/b$ ,  $l/c$  [108]

### 3.3.4. X-ray diffraction methods

Bragg's law can be experimentally applied to an x-ray source of known wavelength, measuring the  $\theta$ . In fact, it is possible to determine the spacing  $d$  of various planes in a crystal structure if  $\lambda$  and  $\theta$  are known. The x-ray measurements are fulfilled by using an x-ray spectrometer. The instrument works by using a monochromatic x-ray radiation incident on the crystal that can be oriented to any angle. The x-ray beam diffracted on the solid produced a beam of refraction rays that were measured by a detector, as shown in figure 3.8:

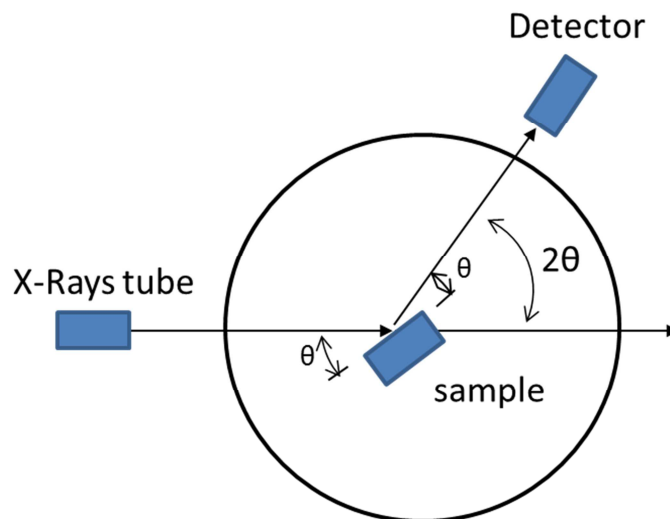


Figure 3.8 - Schematic representation of XRD experiment.

The characteristic detectors used are a Geiger counter or a scintillation counter which scan a range of  $2\theta$  ( $10 < \theta < 80$ ) at a constant angular velocity.

The different diffractions of the x-rays beams give a spectrum XRD pattern that is formed by peaks of  $2\theta$ . Knowing the wavelength of x-rays and the  $2\theta$  angle, it is possible to determine the spacing  $d$  of various planes in a crystal structure.

A Philips powder X- ray diffractometer was used to investigate the possible formation of an extra phase in the fuel cell components after sintering. In addition, it can be used to investigate possible degradation phenomena of the anode, cathode and electrolyte after being tested in extreme conditions. In fact, degradation phenomena produce a new phases that are correlated with the formation of extra peaks in the diffractogram.

### **3.4. Scanning Electron Microscopy (SEM)**

Another method for the investigation of the structure or microstructure of a solid object is microscopy. There are different microscopies such as optical, polarizing and electron microscopies. SEM is extremely versatile for providing structural information over a large range of magnitude. In addition, it complements optical microscopy for the investigation of texture and surface features of powder and pieces of solid materials. The depth of focus of this microscopy provides a high definition pseudo 3D picture of the structure.

Its resolution can reach a few nm and it can operate at magnifications that are easily adjusted from about 10x-300,000x. The SEM produces not only topographical information, but it also provides information concerning the composition near surface regions of the material. SEM microscopy is composed of several parts, as shown in figure 3.9:

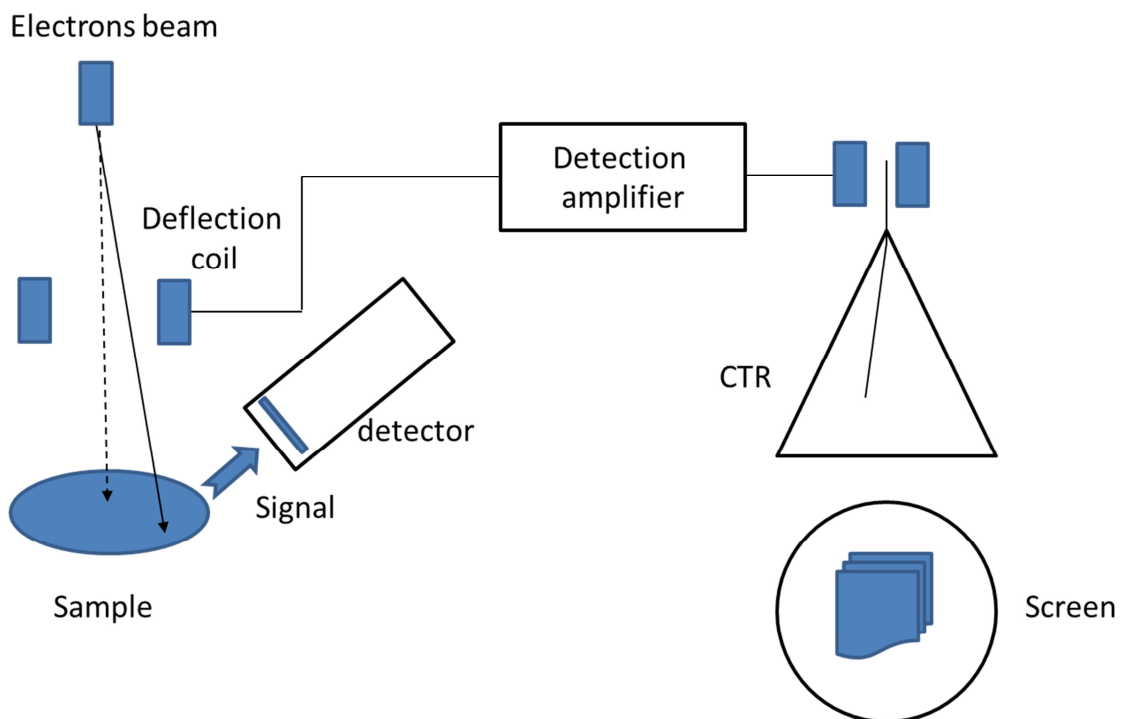


Figure 3.9- Schematic description of the operation and components of scanning electron microscopy[109].

The figure above shows the main components of the SEM instrument. It is composed of an electron column containing the electron source, the magnetic

focusing lenses, the sample vacuum chamber and the stage region, and the electronics console that contains the scanning control.

The scope of the electron gun is to produce a source of electrons emanating from a point as small as a spot. The principle electron sources are thermionic tungsten, LaB<sub>6</sub> and hot and cold field emission.

Lenses or condenser lenses are used to focus the electron beams on the sample. By applying a different intensity of current to these lenses, it is possible to get a variation of the focal length and the divergence. A change in focal length is directly proportional to the intensity of current applied, while the divergence is inversely proportional.

#### 3.4.1. Principles

Scanning electron microscopy is a type of electron microscopy that can capture images of samples by scanning with electron beams in a raster scan pattern. The electron beams interact with the atoms producing the emission of electrons and photons from the surface, as explained by figure 3.10:

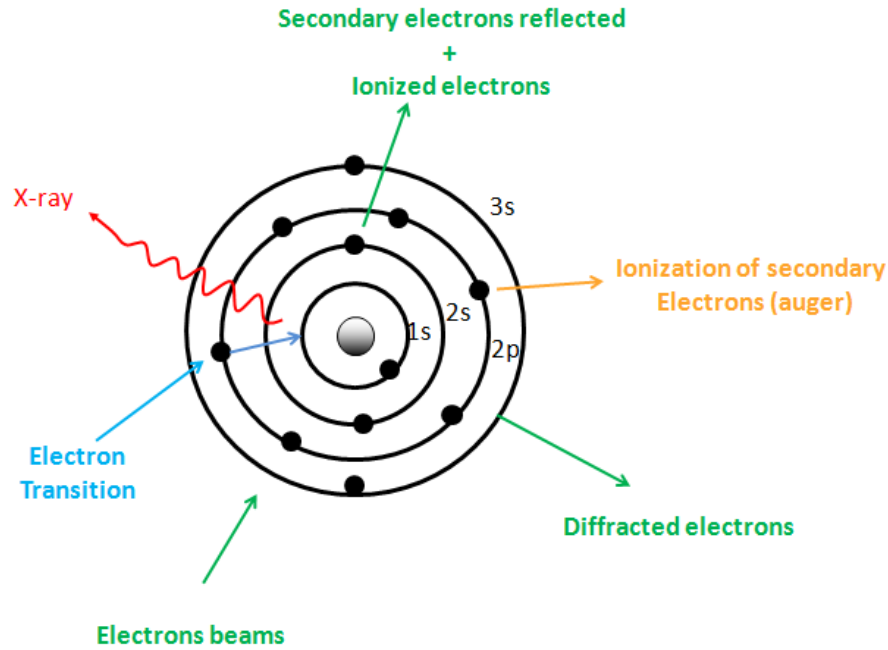


Figure 3.10- Schematic description of the different phenomena that occur when the sample is struck by an electron beam in the SEM chamber held under vacuum to minimize the interaction.

The SEM images are produced by the different sources of charged particle that originate from the collision of the electron beams on the surface sample and these can be classified in three different ways: secondary electron images, back scattering electrons images and elemental x-ray map.

The secondary electrons can be further divided into three groups: SEI, SEII and SEIII; SEI is the result of the incident beam with sample at the point of entry; SEII is produced by the back scattering electrons on the sample exit and SEIII is also produced by the back scattering electrons, but only from electrons which have exited the surface of the sample and as the interactions are caused by SEM components, they are not related to the sample [109].

All of these produce an electrical signal which can be utilised to modulate the brightness of the cathode ray tube (CRT) in which the x-y input are driven simultaneously to the x-y of the voltage, rastering the electron beams. Every point of the sample that is struck by the beams is mapped onto a correspondent point on the screen. The depth of focus of this microscopy provides a pseudo 3D picture of the structure with high definition.

### 3.4.2. EDS

Energy dispersive x-ray spectroscopy (EDS) is used to detect x-rays from all the elements in the periodic table that have a Z value above 4 if the minimum detection limit is 0.02wt%. It follows that the minimum detection limit (MDL) increases to 0.1wt% if the value of Z is 11[110].

Most of the applications of EDS are in the electron column of instruments such as SEM or TEM. It is a technique used for qualitative and quantitative analysis of elements contained in a sample. Since it used for x-ray radiation caused by the collision of the electrons beams on the sample, they must have enough energy in order to produce x-rays radiation. Hence, ESD analysis uses a higher accelerating voltage than the accelerating voltage normally used.

In fact, EDS uses the same principle as XRD technique to produce x-rays radiation, as shown in figure 3.10, and as broadly explain in paragraph 3.1.1.

#### 3.4.2.1. Instruments

The most important component of the EDS instrument is the presence of diode formed by a silicon crystal in which lithium atoms are dispersed.

The presence of lithium atoms in the silicon matrix compensates for the low concentration of grown-in impurity atoms by neutralizing them. In fact, during the diffusion process, silicon is the fundamental component while lithium remains p-type at one end and n-type at the other.

When the x-ray enters the fundamental region of the detector, the n-type ionizes a silicon atom by photoelectric effect, resulting in an x-ray or an Auger electron, which produces a number of electron-hole pairs in the silicon. The charges produced move freely under the action of an applied bias field through the silicon matrix to the detector contacts. The out-put signal is amplified in order to be processed by the analog-to-digital converter[110].

### **3.5. Thermo gravimetric analysis (TGA)**

Thermo-gravimetric analysis or TGA is a type of testing that is performed on samples to determine changes in weight in relation to change in temperature. Such analysis relies on a high degree of precision in three measurements: weight, temperature, and temperature change. As many weight loss curves look similar, the weight loss curve may require transformation before results can be

---

interpreted. A derivative weight loss curve can be used to determine the point at which weight loss is most apparent. Again, interpretation is limited without further modifications and de-convolution of the overlapping peaks may be required. TGA is commonly employed in research and testing to determine the characteristics of materials such as polymers, to determine degradation temperatures, the absorbed moisture content of materials, the level of inorganic and organic components in materials, the decomposition points of explosives and solvent residues. It is also often used to estimate the corrosion kinetics in high temperature oxidation.

### 3.5.1. Principles

The principles upon which this instrument is based are simple. It measures the amount and rate of change in the mass of a sample as function of temperature in a controlled atmosphere. This technique can analyse materials that show either mass loss or gain due to decomposition, oxidation or loss of volatiles (such as moisture). It is especially useful for the study of polymeric materials, including thermoplastics, thermosets, elastomers, composites, films, fibres, coatings and paints.

### 3.5.2. Instrument

The analyser usually consists of a high-precision balance with a pan (generally platinum) loaded with the sample. The pan is placed in a small electrically heated oven with a thermocouple to accurately measure the temperature. The atmosphere may be purged with an inert gas to prevent oxidation or other undesired reactions. A computer is used to control the temperature.

Analysis is carried out by raising the temperature gradually and plotting weight against temperature. The temperature in many testing methods routinely reaches 1000°C or more, but the oven is so well insulated that an operator would not be aware of any change in temperature even if standing directly in front of the device. After the data is obtained, curve smoothing and other operations may be necessary to find the exact points of inflection.

### 3.6. Surface area analysis

The surface area is the measurement that permits quantification of the surface area of a solid object that is exposed and it is expressed in meters squared.

In the case of a powder, the surface area is the measure of its size, shape and irregularity and a technique commonly used to measure it is the BET method, which correlates the ability of a solid to adsorb a gas such as nitrogen on the surface of the solid under particular conditions [111].

The common unit of surface area measurement is  $\text{m}^2/\text{g}$ . This type of measurement provides important information on the solid state field about the capacity of a solid to adsorb a liquid or gas on its surface.

### 3.6.1. BET theory

BET theory, developed by Brunauer, Emmett and Teller, is based on the physical adsorption of gas molecules on a solid surface [111].

The concept of the theory is an extension of the Langmuir theory, which is a theory for monolayer molecular adsorption to multilayer adsorption with the following hypotheses: (a) gas molecules physically adsorb on a solid in infinite layers; (b) there is no interaction between each adsorption layer; and (c) Langmuir theory can be applied to each layer. The resulting BET equation is expressed as follows:

$$\frac{1}{v \left[ \left( \frac{P_0}{P} \right) - 1 \right]} = \frac{c}{v_m c} \left( \frac{P_0}{P} \right) + \frac{1}{v_m c} \quad \text{eq. 3.4}$$

$P$  and  $P_0$  are the equilibrium and the saturation pressure of adsorbents at the temperature of adsorption,  $v$  is the adsorbed gas quantity (for example, in volume units), and  $v_m$  is the monolayer adsorbed gas quantity.  $c$  is the BET constant, which is expressed by (2):

$$c = \exp\left(\frac{E_1 - E_L}{RT}\right) \quad \text{eq. 3.5}$$

$E_1$  is the heat of adsorption for the first layer, and  $E_L$  is that for the second and higher layers and is equal to the heat of liquefaction.

$$\frac{1}{\theta} \left( \frac{\varphi}{1-\varphi} \right) \quad \text{eq. 3.6}$$

### 3.6.2. BET plot

Equation (1-2.12.1.) is an adsorption isotherm and can be plotted as a straight line with  $1 / v[(P_0 / P) - 1]$  on the y-axis and  $\varphi = P / P_0$  on the x-axis according to experimental results. This plot is called a BET plot. The linear relationship of this equation is maintained only in the range of  $0.05 < P / P_0 < 0.35$ . The value of the slope  $A$  and the y-intercept  $I$  of the line are used to calculate the monolayer adsorbed gas quantity  $v_m$  and the BET constant  $c$ . The following equations can be used:

$$v_m = \frac{1}{A+1} \quad \text{eq. 3.7}$$

$$c = 1 + \frac{A}{I} \quad \text{eq. 3.8}$$

The BET method is widely used in surface science for the calculation of surface areas of solids by physical adsorption of gas molecules. A total surface area  $S$  total and a specific surface area  $S$  are evaluated by the following equations:

$$S_{\text{BET, total}} = \frac{(v_m N_s)}{V} \quad \text{eq. 3.9}$$

$$S_{\text{BET}} = \frac{S_{\text{total}}}{a} \quad \text{eq.3.10}$$

The theory previously illustrated is applied to any instrument that is able to determine the surface area of a solid material.

### 3.7. Impedance spectroscopy

The development of batteries and energy storage devices pushed the development of techniques for investigating and characterising systems with a solid-solid or solid-liquid interface. In the interface of any device, the physical properties, electrical charge and composition affect the electrical conductivity of the system because polarization phenomena occur in the interface when it is subjected to the

---

difference of potential. The intensity of polarization depends on the type of interface.

This leads to the development of impedance spectroscopy, a powerful new method capable of characterizing many properties of materials and their interface with electrodes.

### 3.7.1. Principles

In several voltammetric techniques (e.g. polarography, potential step methods and square wave voltammetrics) a perturbation is applied to the electrochemical system which moves from its equilibrium state. Electrochemical Impedance Spectroscopy (EIS) applies A.C. signals of selected frequencies and small amplitude (5-10 mV). By varying the frequency of the signal, a selective perturbation of different physic-chemical phenomena can be performed, thus allowing the identification of their separate contributions. The response is usually interpreted in terms of equivalent circuits, i.e. the electrical circuit (a combination of components connected in series / parallel) which gives the same response as the investigated real system and each response is dependent on the temperature, oxygen partial pressure and current/voltage. Each component represents a particular phenomenon (Faradic resistance, double layer capacitance etc.). The response of an electrochemical cell when it is subjected to an external voltage perturbation in the form:

.....

$$V(t) = V_{\max} \sin(\omega t) \quad \text{eq. 3.11.}$$

This cannot be described by a simple resistance, since the existence of reactive components causes a phase displacement,  $\varphi$ , of the current which flows through the circuit:

$$I(t) = I_{\max} \sin(\omega t + \varphi) \quad \text{eq. 3.12.}$$

Using the complex notation and the Euler's formulae:

$$V(t) = V_{\max} (\cos(\omega t) + i \sin(\omega t)) = V_{\max} e^{-i\omega t} \quad \text{eq.3.13.}$$

$$I(t) = I_{\max} (\cos(\omega t + \varphi) + i \sin(\omega t + \varphi)) = I_{\max} e^{i(\omega t + \varphi)} \quad \text{eq. 3.14}$$

The impedance  $Z$  is given by:

$$Z = \frac{V(t)}{I(t)} = \frac{V_{\max} e^{i\omega t}}{I_{\max} e^{i(\omega t + \varphi)}} = Z_{\max} e^{-i\varphi} = Z_{\max} (\cos \varphi + i \sin \varphi) \quad \text{eq.3.15}$$

Thus, it is convenient to use the complex plane:

$$Z_{\max} = Z_{\text{real}} + iZ_{\text{im}} \quad \text{eq. 3.16}$$

The scalar  $Z$  in the impedance modulus given by:

$$Z_{\max} = \sqrt{(Z_{\text{real}})^2 + (Z_{\text{im}})^2} \quad \text{eq. 3.17}$$

and is proportional to the ratio between the voltage modulus and the current modulus. This representation is useful for evaluating the relationship between the oscillating current and the potential.

These relationships may depend on frequency. Impedance data is usually represented in the Nyquist plot (imaginary part of  $Z$ ;  $Z''$  vs. its real part  $Z'$  vs.  $\omega$ ).

### 3.7.2. Impedance spectroscopy applied to ceramic electrolyte

Electrical homogeneities in ceramic electrolyte, electrode/electrolyte interface, surface layer on glass and ferro-electricity can all be probed by successfully using the impedance spectroscopy technique. In impedance spectroscopy, the impedance of the sample is measured over a wide range of frequencies, typically 0.1 to  $10^6$  Hz. Some samples of electrolyte are measured in a wider range of frequencies, such as between 0.1 and  $10^{13}$  Hz. The ceramic materials have different regions which are characterized by a resistance and a capacitance, usually placed in parallel in this way:

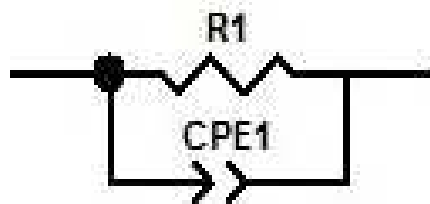


Figure 3.9- Schematic representation of a resistance and capacitance placed in parallel.

The characteristic relaxation time or time constant,  $\tau$ , of each “parallel RC element” is given by the product of R and C in the following equation:

$$\tau = RC \quad \text{eq. 3.18}$$

$$\omega_{\max} RC = 1 \quad \text{eq. 3.19}$$

In the frequency domain, RC elements are separable due to relations shown in equation 3.19 which holds at the frequency of maximum loss,  $\omega_{\max}$ , in the impedance spectroscopy.

In the impedance spectrum, it is usually possible to identify different RC elements and assign them to appropriate regions of the sample and it is possible to quantify the value of each individual component. A common type of impedance spectrum for electroceramic data is presented in the form of imaginary  $Z''$  against real  $Z'$  and we can distinguish attributable features: intra grain or bulk and intergrain, or grain boundary regions. Each parallel RC element gives rise to a semicircle from which the component R and C can be extracted. In fact, the R values from the intercept on the  $Z'$  axis and C can be obtained from equation 3.19 at the frequency of each semicircle. It is possible to attribute an electrochemical phenomenon to the values obtained, as shown in the table [112].

CAPACITANCE	PHENOMENON RESPONSE
$10^{-12}$	Bulk
$10^{-11}$	Minor second phase
$10^{-11} - 10^{-8}$	Grain boundary
$10^{-10} - 10^{-9}$	Bulk ferro-electric
$10^{-9} - 10^{-7}$	Surface layer
$10^{-7} - 10^{-5}$	Sample –electrodes interface
$10^{-4}$	Electrochemical reaction

Table 3.1- Electrochemical phenomena correlated to the capacitance value calculated by impedance spectroscopy [112].

### 3.7.3. Two-terminal a.c. impedance experimental set-up

In this project, a Solatron 1260 and a Solatron 1280 digital were used to apply a.c. current at fixed potential (50mV) to a ceramic disc or to a tubular cell, using a two-terminal technique. The samples were analysed in a large range of frequencies depending on the type of instrument used: Solatron 1260, from 0.01 Hz to 1MHz or Solatron 1280 from 0.01Hz to 20kHz.

The instrument was interfaced to a PC which was used to set up instrument parameters using specific software: Z-plot and Z-View.

#### 3.7.3.1. Electrodes

For electrolyte investigation and semi-cells, the electrodes applied to the sample were Pt paste or silver paste, which were painted on each side of the electrolyte.

The electrodes were sintered at 500°C and 900°C for silver and platinum respectively and they were held for one hour at target temperature in order to prevent “blistering” or low adhesion after cooling the sample.

### 3.7.3.2. Furnace and jig for two-terminal a.c. impedance

The impedance jig consists of two alumina tubes whereby the sample pellet is held by the compressive forces of the two tubes. The silver wire is passed through the thin fore in the tube and the terminal part of the silver wire is in direct contact with the electrode sample. A thermocouple is posited close to the sample in order to ensure that the temperature is accurate.

The set-up is shown in figure 3.10:

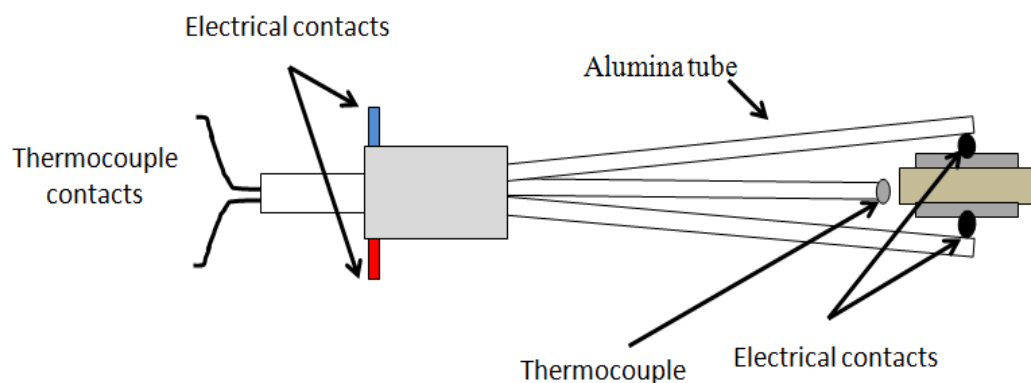


Figure 3.10- Schematic illustration of an ac impedance jig with two terminals in silver wires and thermocouples next to the sample to monitor temperature variation.

The same set-up was used to investigate the performance of the anode and the cathode electrodes. In fact, a thin disk of electrolyte material (200 $\mu\text{m}$ ) was laminated both with a cathode thin layer (60  $\mu\text{m}$ ) and anodes on both sides of the electrolyte to investigate the electrode performance.

The atmosphere was set-up as function of the electrode characterised. In fact, air was used for the cathode and 5% hydrogen was used for the anode at a range of temperatures between 550°C and 900°C, recording data both from the heating ramp and the cooling ramp. The electrical contacts were formed using silver paste as current collector.

The response of electrodes was visible at low frequency:  $R_1$  is the polarization resistance of both electrodes and the single value of resistance is half of the entire value of  $R_1$ .

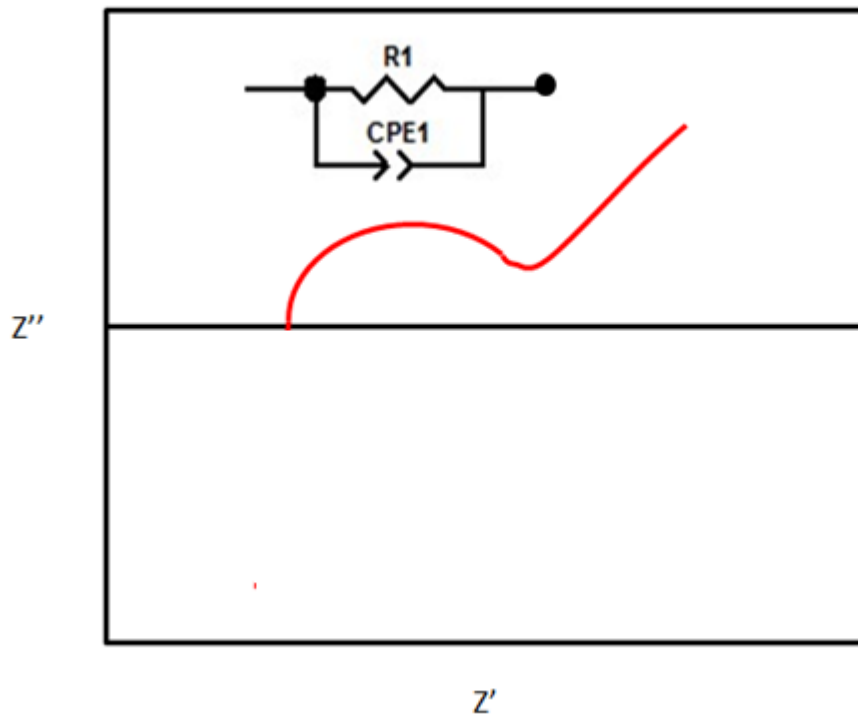


Figure 3.11- Generic impedance spectra of a symmetric cell without grain boundary effect. The semi-arc reported represents the value of polarization produced by interface between electrode and electrolyte and the value is characterised by a capacitance value of  $10^{-7}$  -  $10^{-5}$  F.

#### 3.7.4. Fuel cell testing

The set-up of the cell consisted of the anode, electrolyte and cathode. On the anode side the current collections were a combination of silver paste and silver wire, whilst a ceramic pure electron-conductive material combined with a silver paste and silver wire was used to form the electrical contact in the cell.

The measurements carried out in this type of cell were chosen to investigate the power and current produced as well as the electrochemical behaviour of the

.....

whole cell, which was studied by a.c. impedance spectroscopy at a range of frequencies between 0.1Hz to 20kHz.

Tests were carried out using a Solatron 1280 applying a voltage amplitude of 10 mV to reduce the perturbation of electrochemical phenomena.

### 3.7.5. Description of an electrochemical response from the electrical circuit

The electrochemical response provided by an impedance spectroscopy test can be correlated to electrical components such as resistance, capacitor and inductor, constructing a fit for an “equivalent circuit”.

However, these fits are only approximate models because they provide a description of a linear system, even though it is in fact not a linear system.

In order to optimise these fits, small amplitude signals are used so as to be able to consider a.c. currents linear. In addition, the construction of equivalent circuits related to the electrochemical behaviour is limited by the effect of geometry on current distribution and the dependence of conductivity and interface capacitance on frequency. A representative equivalent circuit is shown below:

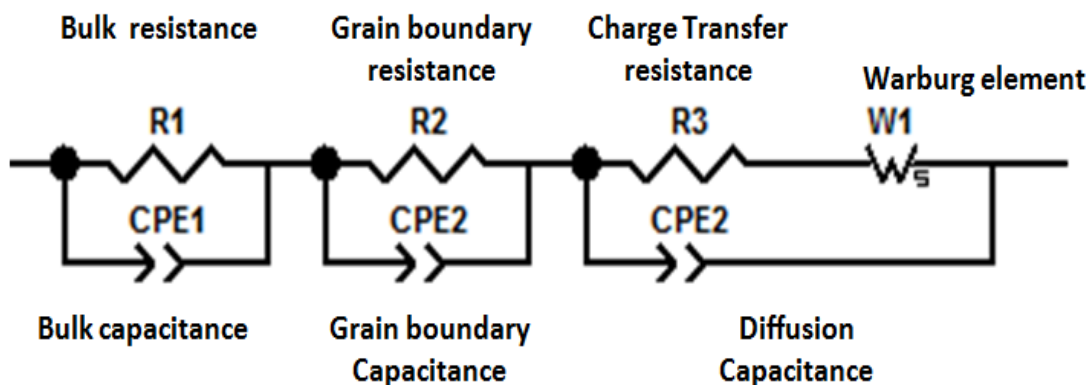


Figure 3.12- Modelling of an equivalent circuit for a typical solid crystalline electrolyte.

In this equivalent circuit the resistances are the conductive paths and they can represent the bulk conductivity or they can account for the chemical steps that occur on the electrode[113]. Meanwhile the capacitor and inductance are associated with phenomena such as polarization region and specific adsorption at the electrodes and they are the components which do not avoid the distinction between ideal and real resistor. However, these phenomena can be minimized by working at a wide range of frequencies which are able to model a real resistor as ideal resistor.

In the equivalent circuit, “distributed elements” are used to improve the fit of the depressed arc. In fact, the capacitive components have some intrinsic resistance characteristics. The distribution is connected to the diffusion of phenomena and the microscopic characteristic of the materials. This phenomenon is exemplified by Constant Phase Element (CPE).

This is characterised by the inhomogeneity both of composition and the surface of the interface between electrolyte and electrode.

Another type of distribution element is represented by “Warburg Impedance”.

This element is often used to model semi-infinite linear diffusion that is caused by large planar electrodes. This element is independent of the frequency and its phase angle is constant at  $45^\circ$ .

### 3.8. References

- [100] <http://www.corning.com/docs/specialtymaterials/pisheets/Macor.pdf>
- [101] Twiname, Eric R. and Mistler, Richard E., "Tape Casting," Ceramic Innovations in the 20th Century, Edited by John Wachtman Jr., The American Ceramic Society, 1999, p. 54.
- [102] C. Williams, Doctor-blade process, in F.F.Y. Wang (ed.), Treatise on Materials Science and Technology, Vol. 9, Ceramic Fabrication Processes, Academic Press, New York, 1976, pp.173-198.
- [103] R.E. Mistler, D.J. Shanefield and R.B. Runk, Tape casting of ceramics, in G. Onoda Jr and L.L. Hench (eds.), Ceramic Processing Before Firing, Wiley, New York, 1978, pp. 411-448.
- [104] E.P. Hyatt, Making thin, flat ceramics: a review, Am. Ceram.Soc. Bull., 65 (4) (1986) 637-638.
- [105] R. Moreno, The role of slip additives in tape casting technology: Part I-- Solvents and dispersants, Am. Ceram. Soc. Bull., 71 (10) (1992) 1521-1531;
- [106] R. Moreno, The role of slip additives in tape casting technology: Part II-- Binders and plasticizers, Am. Ceram. Soc. Bull., 71 (11), (1992) 1647-1657;
- [107] Cowley, J. M. (John Maxwell), 1923- Diffraction physics /by John M. Cowley. Amsterdam :North-Holland Pub. Co. ;New York :American Elsevier, 1975- ISBN 0-444-10791-6
- [108] Neil W. Ashcroft and N. David Mermin, Solid State Physics (Harcourt: New York, 1976)
-

- [108] Elements of X-rays Diffraction - D.B:Cullity, S.R.Stock- Prenticelle hall-2001
- [109] Encyclopedia of materials characterization - C. Richard Brundle, Charles A. Evans, Jr., Sham Wilson-1992- Manning Publications Co
- [110] S.Brunauer, P.H.Emmett and E.Teller- Adsorption of gases in multi-molecular layer"- Am.Ceram.Soc.Bull.- 60,(1938),309;
- [111] Fundament of Impedance. Spectroscopy- second edition-. J. Ross Macdonald William B. Johnson –2005 – ISBN 0-471-64749-7
- [112] John T.S. Irvine, Derek Sinclair and Antony R. West –Adv. Mater. 2 (1990) 132;
- [113] R.A. Armstrong, M.F. Bell and A.A. Metclafe – Electrochemistry report 6 (1978) 98-127;

## **4.0. Carbon fuel characterization**

### **4.1. Results and discussion**

As previously outlined, biomass is largely carbon-based, although it generally has a high oxygen content, leaving an estimated carbon content of around 70-80%. The remaining 10% is composed of oxygen and 10% hydrogen, nitrogen and sulphur.

Depending on the type of the biomass, its lignin and cellulose content varies. The lignin and cellulose content is extremely important because it determines the calorific value of the carbon produced. For this reason, two different types of biomass were chosen as the starting material to be pyrolysed: medium density fibreboard, which is available as solid waste, and pellet wood which is already used as fuel for the burners.

### **4.2. Medium density fibreboard**

MDF is a wood product formed by breaking down softwood into wood fibres, often in a defibrator, combining it with wax and a resin binder and forming panels by applying high temperature and pressure. It is made up of separated fibres (not wood veneers) but can be used as a building material similar in application to plywood. It is much denser than normal particle board and its name is derived

from the distinction in densities of fibreboard. Large-scale production of MDF began in the 1980s.



Figure 4.1- Medium density fibreboard – composite material consisting of lignin fibres impregnated with formaldehyde resin with a density of 400-600 Kg/m<sup>3</sup>.

### **4.3. Pellet wood**

Wood pellets are a type of wood fuel generally made from compacted sawdust. The pellets are extremely dense and can be produced with a low humidity content (below 10%) that allows them to be burned with very high combustion efficiency. Emissions such as NO<sub>x</sub>, SO<sub>x</sub> and volatile organic compounds from pellet burning equipment, are, in general, minimal in comparison to other forms of combustion heating, making this one of the less-polluting heating options available.

The energy content of wood pellets is approximately 4.7-4.9 MWh/tonne. Pellet combustion releases carbon dioxide, but the use of pellet fuels arguably has a low net lifecycle impact because the carbon dioxide released is ultimately consumed in the growth of the trees or biomass products used to produce the pellets; this

process takes approximately 15 years for trees and as little as one season for crop-based biomass to sequester the carbon released by their combustion.



Figure 4.2- commercial pellet wood formed by sawdust and ground wood chips with density 180 – 500 kg/m<sup>3</sup>

#### **4.4. Thermogravimetric studies of biomasses**

As mentioned in the previous paragraph, biomass is a wood material composed of cellulose and lignin, which are complex organic substances. These substances are unstable at high temperature and related to the operation conditions, these substances can be oxidised under air or they can be decomposed under an inert environment such as nitrogen or Argon. The decomposition process is a complex mechanism in which defragmentation and rearrangements take place at high temperature. This is the principle on which is based the pyrolysis process. Studies of pyrolysis process were carried out on both materials, in order to comprehend the defragmentation and rearrangement mechanisms through the analysis of all products obtained by pyrolysis and optimize the pyrolysis process.

The studies of oxidation and decomposition mechanisms were investigated by thermo-gravimetric analysis (TGA). In fact, the variation in weight recorded at different temperature and time provides us information on the type of process that is taking place at that temperature. In addition, this information was used to optimize the process parameters of the pyrolysis pilot plants.

### 4.4.1. Studies of degradation mechanism of biomass

A thermo-gravimetric instrument (NETZSCH STA 499T) was loaded with an amount of biomass between 8mg to 10mg in an alumina crucible and put in the TG chamber. The oxidation studies were carried out purging air into the TG chamber with a flow rate of 25ml/min whereas the decomposition studies were carried out purging nitrogen with a flow rate of 25ml/min. Both tests were carried out by increasing the temperature from room temperature to 900°C using a ramp rate of 20°C/min and the sample was held at 900°C for 5h in order to ensure complete decomposition and degradation.

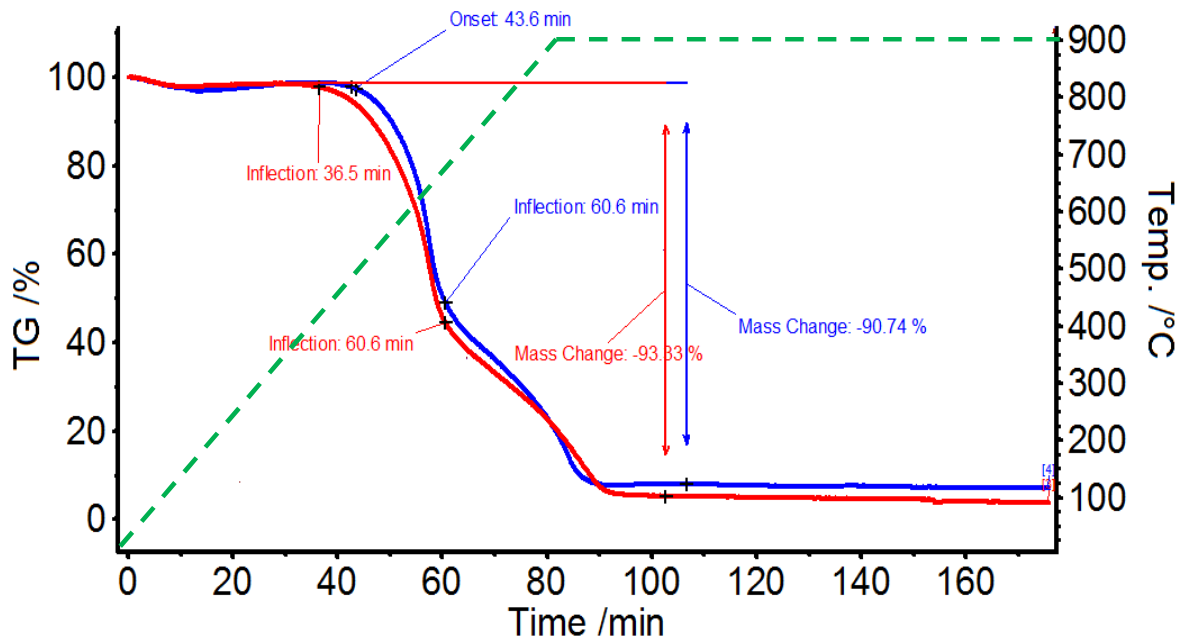


Figure 4.3- Thermogram of biomass under oxidising atmosphere (air). Flow rate of air is 25ml/min and the ramp rate is 10°C/min. The final temperature was 900 °C and it was held for 5hrs. — Residual mass of mdf 6.67%. — Residual mass 9.26% for pellet wood.

Thermogram above shows the typical oxidation behaviour of biomass under air.

Thermogram shows two different inflection curves that represent two different steps of oxidation:

- Oxidation of cellulose (range 230°C -300°C)
- Oxidation of lignin (range 300°C - 500°C)

In the case of mdf, the degradation phenomenon occurs earlier than in pellet wood and this is due to the presence of formaldehyde resin that has a degradation temperature of around 200°C. This is clearly observed by the different inflection

points marked on the thermogram. The residual mass is 9.26% for pellet wood and 6.67% for mdf. The residual mass consists of an agglomeration of carbon (aromatic cluster) highly stable at high temperatures both under oxidant and inert environments. In fact, the weight of the residual mass was stable at 900°C for 5 hrs. Small amounts of mineral salts absorbed (around 100ppm) by the plant were observed, analysing mdf and pellet wood using the Agilent 7500 series ICP-MS spectrometer .

The same types of biomass were also investigated under inert atmosphere to study the best parameters for pyrolysis.

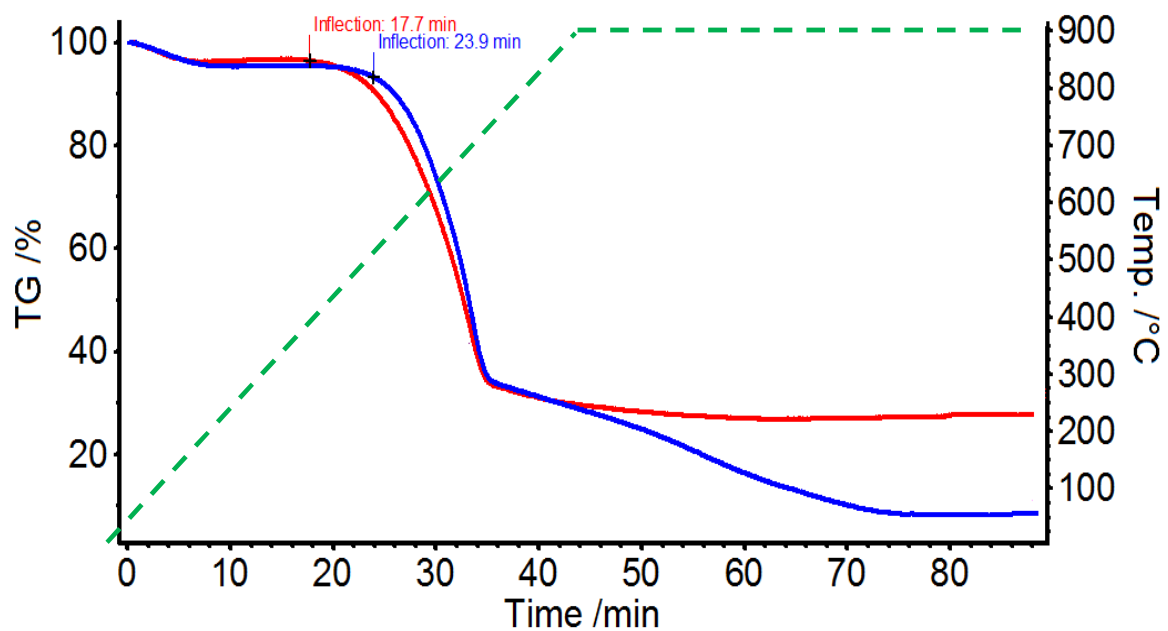


Figure 4.4- Zoom of thermogram of decomposition of biomass under inert atmosphere ( $N_2$ ) in a range between 0 min-80min. Flow rate of  $N_2$  was 25ml/min and the ramp rate is 20°C/min. The TGA analysis was carried out between 25 °C and 900°C and the temperature was held constant for 5hrs at 900°C. Residual mass of — mdf 30% — 9.67% pellet wood.

When pyrolysis was carried out under nitrogen atmosphere, the degradation started at a lower temperature than when using air. This phenomenon may be due to the difference between oxidation mechanism and the decomposition mechanism. In the first case, the oxygen in air reacts with the biomass, producing small molecules such as carbon dioxide, carbon monoxide, hydrogen, water, C<sub>2</sub> and C<sub>3</sub> substances. Instead, nitrogen is an inert gas and it does not react with biomass during the process of pyrolysis. In this case, the weight loss is caused by the breaking up of chemical bonds through the increase of temperature and their rearrangements in more stable chemical compound at that temperature. The decomposition produces two different products: volatile products composed of a heavy fraction such as phenol, nitro-derivatives, ketones, carbohydrate and a light fraction composed of methane, carbon dioxide, carbon monoxide and hydrogen. The second product group is composed of condensed carbon structures such as naphthalene that are stable at temperatures up to 1000°C. These mechanisms can be evaluated analysing the first derivative of the weight loss as function of the time curve ( $dx/dt$ ), shown in figure 4.5:

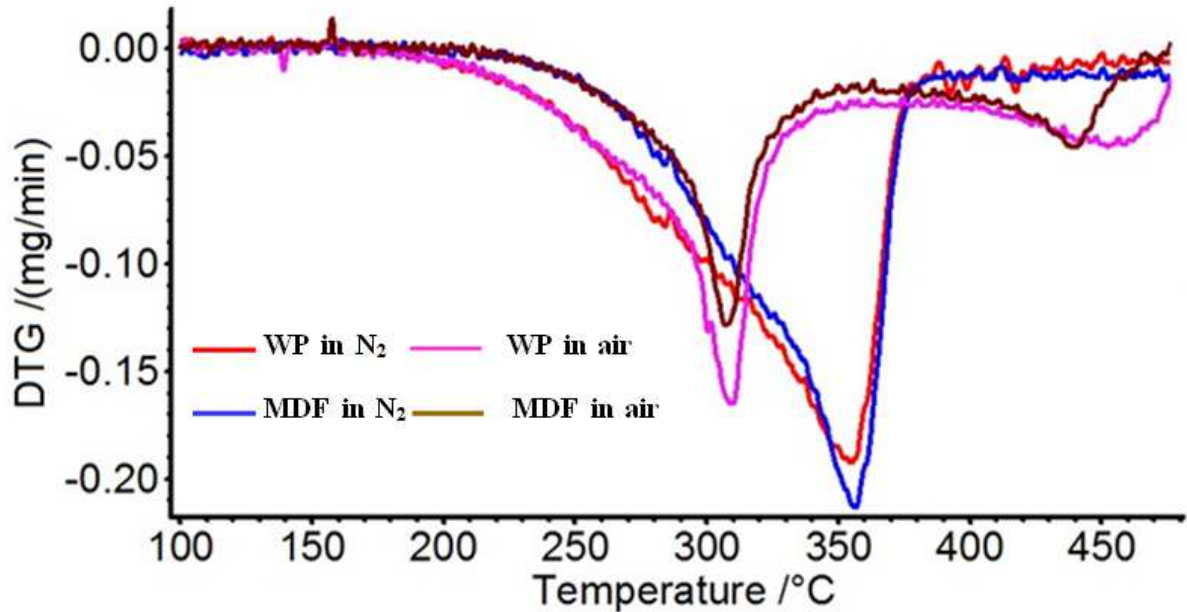


Figure 4.5- Derivative of the TGA curve as function of the time for mdf and wood pellet burnt both in air and nitrogen, using a flow rate of 25ml/min and ramp rate 20°C/min. Tests were carried out at 900°C.

By analysing the graph, it is visible that onset of decomposition is faster than for the oxidation process and it occurs because oxygen is more reactive than nitrogen. Peaks shown in the figure above represent the maximum velocity of degradation of biomass which provides information on the velocity of decomposition and oxidation of each woody material.

By analysing graph 4.5, it is clear that both the decomposition and the oxidation of pellet wood start at a lower temperature than with mdf. This highlights the reactivity of wood pellet. In addition, the oxidation curves are narrower than the decomposition curves and this is due to simple processes that take place during oxidation. Contrarily, the decomposition curve is wider and asymmetrical. The asymmetrical shape is the result of the slow rearrangement of the carbon

structure. In fact, the rearrangement is a slow process in which the carbon skeleton of a molecule is rearranged to give a stable structure at a given temperature and it requires more energy than required during oxidation.

Unlike the oxidation mechanism, this process takes places in multi steps. In both cases, pellet wood is more reactive than mdf. This difference could be caused by the different bulk density of pellet wood and mdf ( $60\text{kg/m}^3$  and  $100\text{kg/m}^3$  respectively) but also by the larger amount of semi and hemicelluloses contained in wood pellet than in mdf.

The differences in reactivity can be also seen in the thermogram shown in figure 4.6.

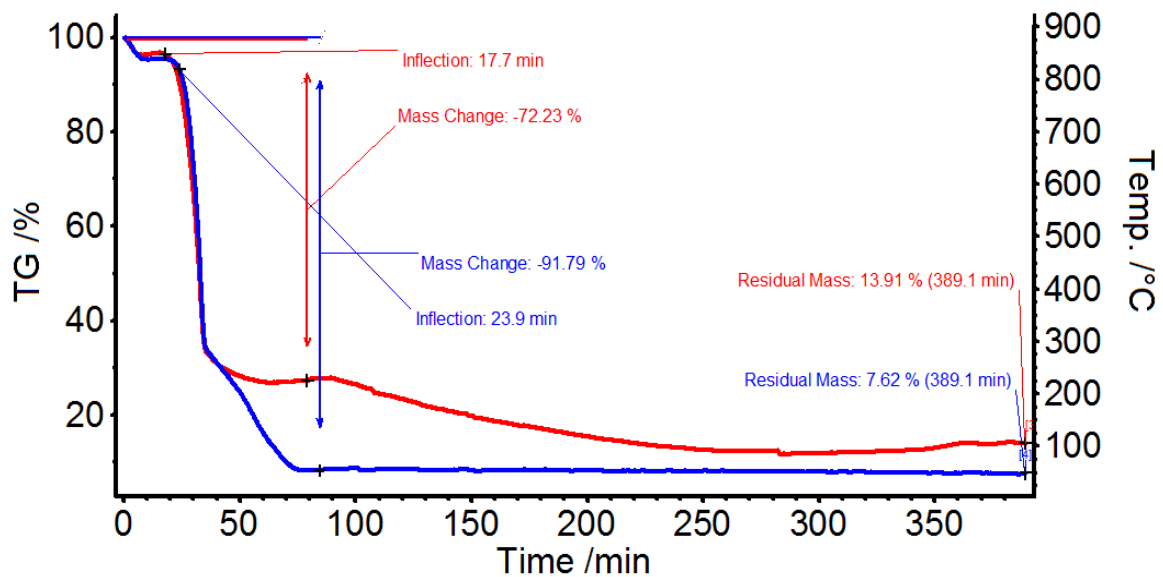


Figure 4.6- Thermogram of decomposition of biomass under inert atmosphere ( $\text{N}_2$ ). Flow rate of  $\text{N}_2$  was  $25\text{ml/min}$  and the ramp rate was  $20^\circ\text{C/min}$ . The TGA analysis was carried out between  $25^\circ\text{C}$  and  $900^\circ\text{C}$  and the temperature was held constant for 5hrs at  $900^\circ\text{C}$ . — Residual mass of mdf 13.91% — 7.67% pellet wood.

In fact, a lower residual mass was observed for wood pellet than mdf. The high reactivity of the pellet wood produced a lower residual mass (9.67%) compared to mdf (28.77 %).

In general, the residual mass of carbon pyrolysed at 450°C should be around 33%. In this case, the residual mass weight achieved for mdf pyrolysed under nitrogen was 28.77 % and this is justified by the high ramp rate used during the test. However, the high ramp rate does not justify the so high weight loss for the wood pellet in which the weight loss is much higher than the expected value.

### 4.4.2. IR investigation of degraded biomass

In order to understand the degradation action, a Perkin Elmer Spectrum GX IR spectrometer was used to investigate the functional groups bonded to the carbon structure obtained after pyrolysis. In fact the degree of degradation is correlated to the number of functional groups that are present in a structure. The IR spectra of degraded biomass (mdf and wood pellet) are shown in figure 4.7 and they are interpreted using IRPA 2.0 software.

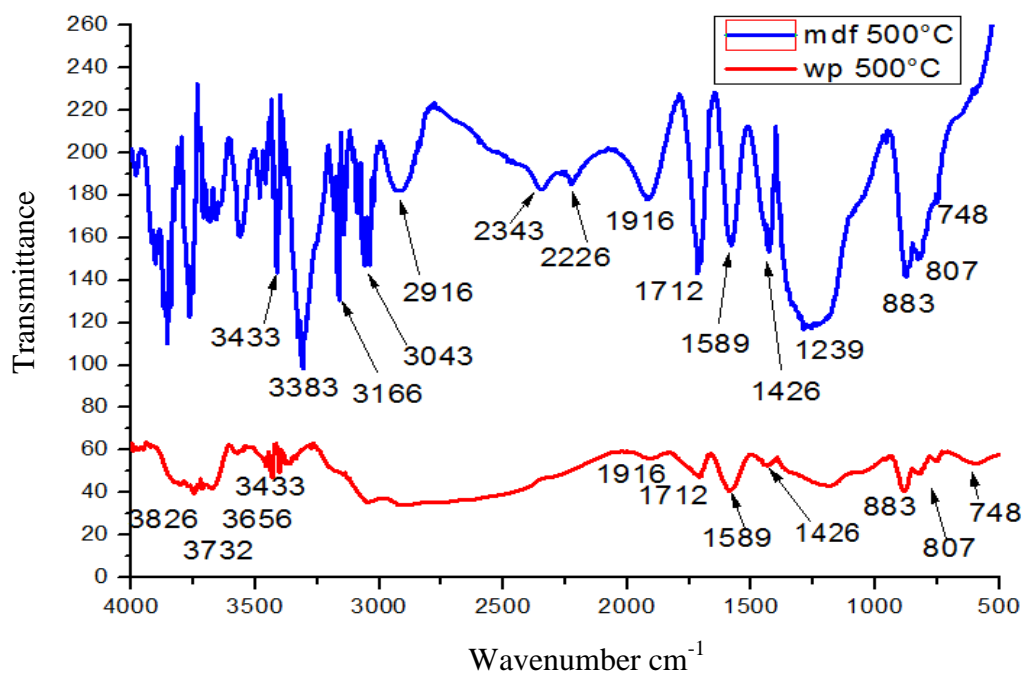


Figure 4.7- FTIR spectra of mdf and wood pellet pyrolysed at 500°C carried out with a Perkin Elmer Spectrum GX in a range between 500cm<sup>-1</sup> to 4000cm<sup>-1</sup>

The first difference in the infrared spectrum is due to the intensity and number of peaks observed in it. The difference in intensity provides information on the degradation degree of each material.

This confirms the total degradation of wood pellet, justifying the residual mass value.

Several peaks can be observed between 3800 and 3200 cm<sup>-1</sup> in the MDF sample and they represent the amino group N-H stretch and -OH group from carboxylic acids. The amino groups in the mdf originate from the presence of urea-formaldehyde resins used to assemble the woody fibres. Instead, a large peak can be seen in the wood pellet sample in the same range. The broad peak is typical of the simultaneous presence of NH and OH group from alcohol and phenol. The

rest of the spectra confirm the groups hypothesised. In fact, peaks correlated to the carboxylic acid are visible at  $1690\text{ cm}^{-1}$  and  $1500\text{ cm}^{-1}$  while the double bond  $\text{C}=\text{C}$  of alkenes are observable at  $2950\text{ cm}^{-1}$  and  $2850\text{ cm}^{-1}$ .

The triple bonds  $\text{C}\equiv\text{C}$  can be seen at,  $2260\text{--}2100\text{ cm}^{-1}$  The aromatic rings are confirmed by the presence of double bonds  $\text{C}=\text{C}$ , single peak at  $3400$  and  $3200\text{ cm}^{-1}$  while the stretching of aromatic  $\text{C-H}$  is represented by peaks between  $880\text{--}800\text{ cm}^{-1}$ .

#### **4.5. Pyrolysis parameters**

Biomass was pyrolysed at  $500^\circ\text{C}$  so as to partially decompose the structure of the lignin meanwhile totally decomposing the structure of the cellulose, because it is highly unstable at high temperatures. The biomasses were held for 30 min at  $500^\circ\text{C}$  to complete the partial oxidation of the structure.

A partially reduced bio-carbon was chosen as fuel because it can complete pyrolysis inside the anode chamber, producing secondary products that improve the total performance of the cell. In fact, an additional amount of fuel is provided by the internal pyrolysis of the bio-mass in the anode chamber.

The partial oxidation of lignin causes the rearrangement of more stable structures such as aromatic and aliphatic clusters which can be decomposed slowly by the oxygen ions coming from the ceramic membrane.

Each carbon produced was characterised by BET, TGA, IFTR, XRD and SEM analysis in order to investigate the chemical and physical properties and microstructure of each carbon fuel that can affect the performance of the cell, as investigated by Cooper and co-workers [45]. However, an analysis of the secondary products obtained during the pyrolysis process is necessary to understand the type of substances produced by the decomposition of pellet wood and mdf.

#### **4.6. Production of secondary products from pyrolysis**

As explained in the previous chapter, the pyrolysis process provides different products, such as oil and non-condensable gas, and their percentage is related to the operation temperature and inevitably also to the particular pyrolysis process employed.

In this case, the pyrolysis process, as described in the previous paragraph, was a conventional pyrolysis process carried out at 500 °C under nitrogen atmosphere using a ramp rate of 10°C/min both on mdf and wood pellet.

10gr of biomass were loaded into the reactor, which was closed hermetically and nitrogen gas was purged at 20ml/min for 5 min into the reactor in order to remove all traces of oxygen inside the reactor.

The formation of gases that contain both bio-oils and incondensable gas in was observed at the range of temperatures between 300°C to 450°C and the fume was

---

condensed using a condenser held at  $-69^{\circ}\text{C}$  in order to be sure to condense all of the oil contained in the pyrolysis fume. Then, these oils were collected and analysed by both GC mass and IR spectroscopy. Fast pyrolysis was also investigated to compare the formation of oil production as function of the ramp rate of the process. In fact, the principles of fast pyrolysis are based on the decomposition of biomass, increasing the temperature using a high ramp rate. Fast pyrolysis uses also a higher operation temperature than conventional pyrolysis. This high ramp rate favours the decomposition of the biomass and consequently this helps bio-oil formation.

The bio-oil produced was analysed by GC-mass and infrared spectroscopy in order to provide a qualitative analysis of the oil content while micro GC was used to investigate the percentage of incondensable gas produced by pyrolysis.

### 4.6.1. Characterization of bio oil

The decomposition products are transported by the carrier gas ( $\text{N}_2$ ) from the reactor chamber ( $300^{\circ}\text{C}$  to  $450^{\circ}\text{C}$ ) and they are condensed at  $-68^{\circ}\text{C}$ . The two oils were obtained by pyrolysing the mdf using two different pyrolysis processes. The first was a conventional pyrolysis process carried out at  $500^{\circ}\text{C}$  increasing the temperature with a ramp rate of  $10^{\circ}\text{C}/\text{min}$  and holding the sample for 30 min at  $500^{\circ}\text{C}$ . The second process used was fast pyrolysis carried out at  $600^{\circ}\text{C}$  increasing the temperature with a ramp rate of  $25^{\circ}\text{C}/\text{min}$  and the sample was held

---

at 600°C for 10 min. In both pyrolysis processes, a flow rate of 40ml/min was maintained. The appearance of the oils is shown in figure 4.8:



Figure 4.8- Bio-oil produced by either mdf or wood pellet a) conventional pyrolysis carried out under nitrogen flow purged into the chamber at 40ml/min at 500 °C using a ramp rate of 10°C /min and holding the sample at 450°C for 30min. b) fast pyrolysis carried out under nitrogen using a flow rate of 40ml/min, at 600°C using a ramp rate of 25°C /min and holding the sample at 600°C for 10 min.

The two oils shown in the figure above are different colours: the first sample is light brown and it is produced by pellet wood while the oil produced by mdf is dark brown. The colour of the oil depends on the type and amount of organic substances contained in the biomass.

The amount of oil produced from mdf by conventional pyrolysis and fast pyrolysis was 38%vol and 65%vol respectively. However, the amount of oil produced by pyrolysing wood pellet was 36% and 60%. Clearly these results are

affected by different factors such as the type of biomass, gas flow rate and residence time.

#### 4.6.2. Bio-oil characterization

The bio-oils obtained were analysed by GC-MS in order to distinguish the different fractions and identify the individual substances contained within the mixture. On the other hand, the infrared spectroscopy (FTIR) and elemental analysis were carried out on the oils produced as complementary analysis to the GC-MASS spectrometer in order to quantify the percentage of organic components such as C, H, N, S and O, as well as to comprehend how these elements were bound together. All of these techniques are helpful for constructing the type of molecules contained in the mixture.

The elementary analysis carried out on oils obtained by conventional and fast pyrolysis of mdf and wood pellet is shown in the tables 4.1 and 4.2:

<b>Elements</b>	<b>Mdf</b>	<b>Pellet wood</b>
<b>Carbon</b>	56.23%	58.28%
<b>Hydrogen</b>	7.01%	6.86%
<b>Nitrogen</b>	3.52%	1.45%
<b>Sulphur</b>	0.01%	0.03%
<b>Oxygen</b>	33.23%	33.39%

Table 4.1- Elemental analysis of bio-oils obtained by conventional pyrolysis of mdf and wood pellet carried out at 450°C using a residence time of 30min.

<b>Elements</b>	<b>Mdf</b>	<b>Pellet wood</b>
<b>Carbon</b>	60.13%	61.19%
<b>Hydrogen</b>	6.48%	6.92%
<b>Nitrogen</b>	2.42%	0.09%
<b>Sulphur</b>	0.01%	0.03%
<b>Oxygen</b>	30.96%	31.60%

Table 4.2- Elemental analysis of bio-oils obtained by conventional pyrolysis of mdf and wood pellet carried out 600°C using a residence time of 10 min.

These samples were then tested by gas chromatography spectrometry in order to separate the single molecules contained in the mixture.

Samples for the GC-mass spectrometry were prepared taking a millilitre of oil and diluting it with 2ml of acetone in order to reduce the intensity of the peaks. The sampling of bio oils analysed was done following the same procedure for all samples in order to observe the variation of the intensity of each peak as function of the pyrolysis process.

The chromatogram of the bio oil produced by conventional pyrolysis is shown below:

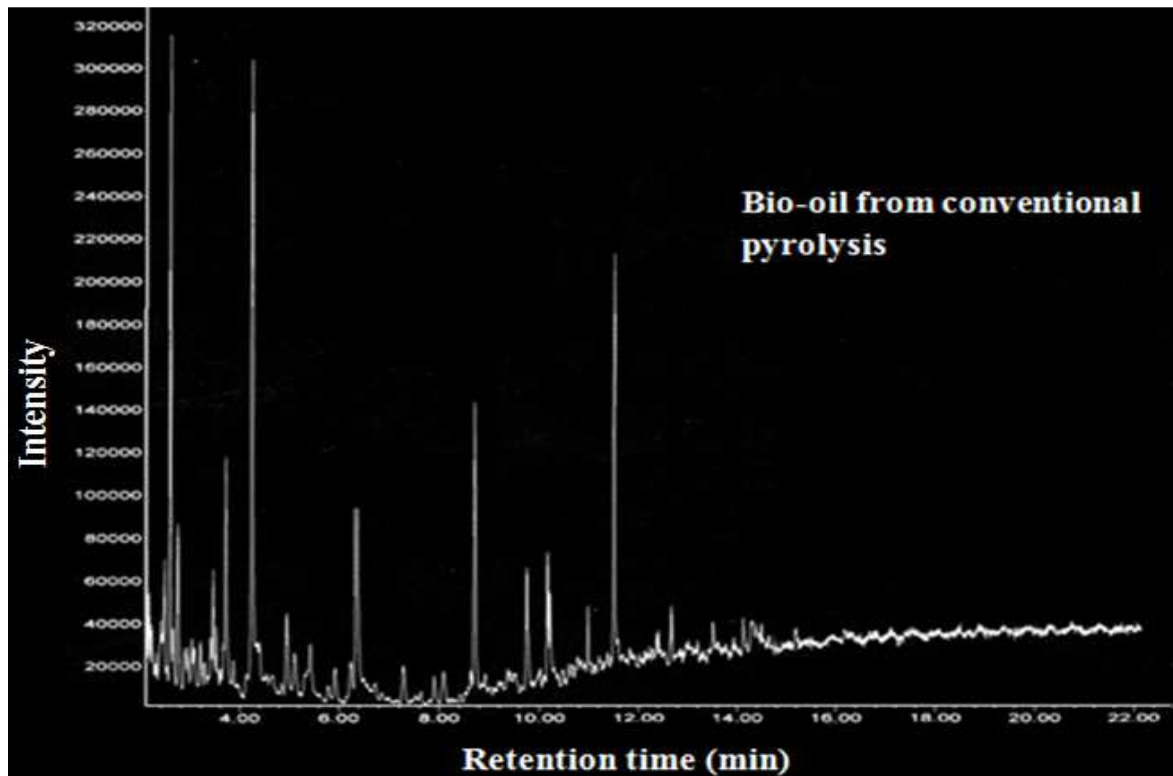


Figure 4.9- Chromatogram of bio-oil obtained by conventional pyrolysis of mdf carried out at 500°C under nitrogen with a flow rate of 40ml/min.

The bio-oil obtained by conventional pyrolysis shows several peaks of different chemical substances that, given the low retention time, seem to be small molecules with lower affinity with the column. Each of the peaks related to a

single chemical substance and the peaks were analysed using an internal mass spectrometer contained inside the GC. The mass spectra obtained experimentally were compared with other spectra contained in an internal database in order to determine the possible substance detected. The identification of each substance occurs by comparing the fragmentation path of each molecule. In fact, the fragmentation path is specific for each molecule.

The same analysis was carried out on the bio-oil obtained by fast pyrolysis. The spectrum is very similar to the spectrum shown in figure 4.9, but extra peaks can be seen in it at high retention time, as shown in figure 4.10:

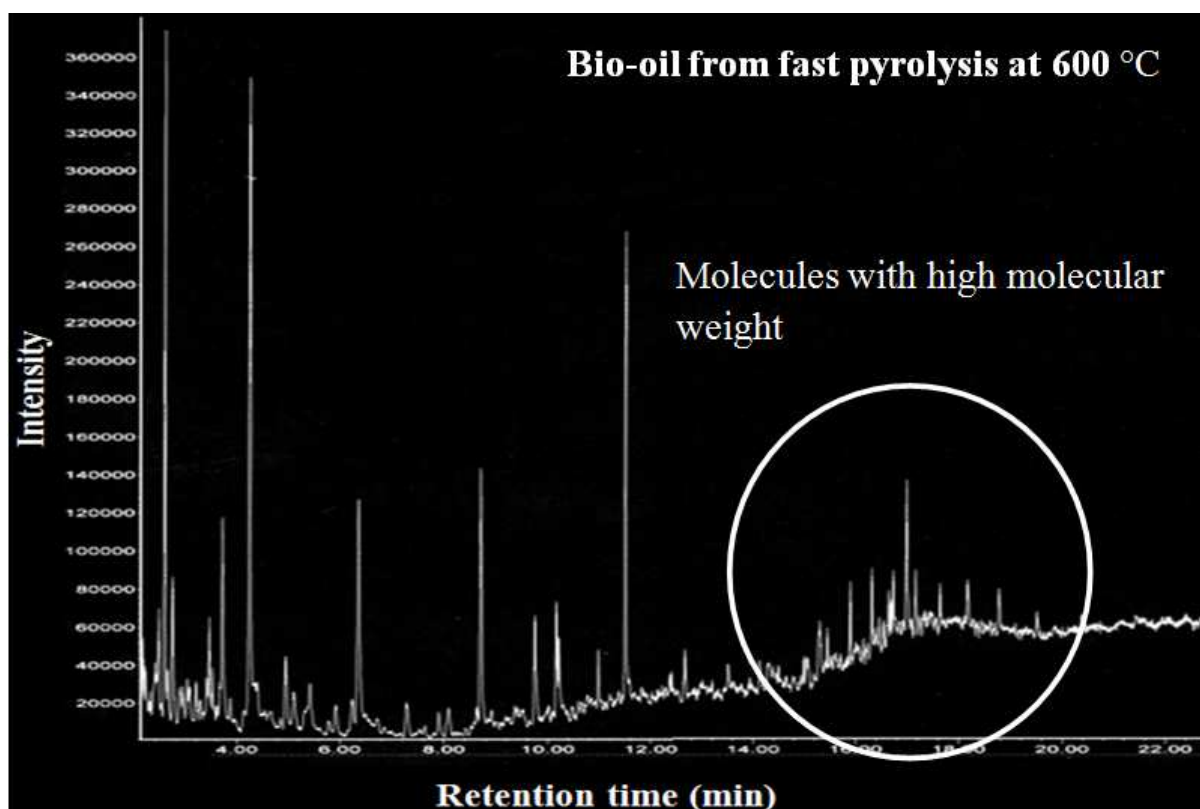


Figure 4.10- Chromatogram of bio-oil obtained by fast pyrolysis of MDF carried out at 450°C under nitrogen with a flow rate of 20ml/min.

These extra peaks are caused by the formation of molecules with high molecular weight and high polarity, such as complex sugar, that are formed as a consequence of the fast ramp rate and the high energy supplied to the biomass in a few seconds. The samples are also investigated by infrared spectroscopy in order to confirm data obtained by gas chromatography-spectrometry analysis. Two different infrared spectra are shown in figures 4.11 and 4.12:

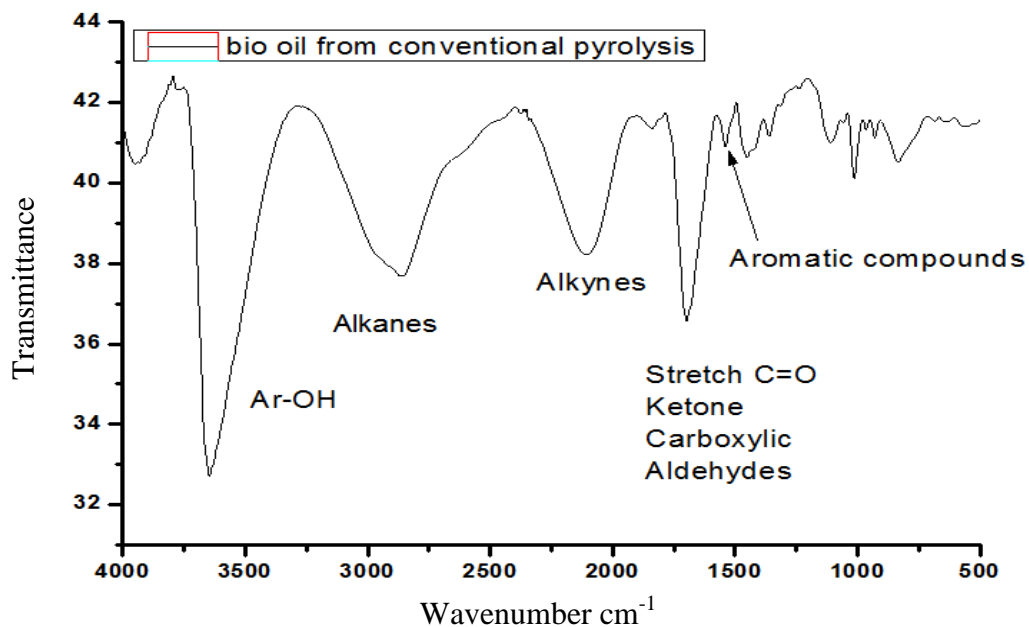


Figure 4.11- Infrared spectrum of bio-oil produced by conventional pyrolysis carried out at 450°C under inert atmosphere of nitrogen. Oils were condensed at -68°C. Analysis was carried out with FTIR, following a multi-scanning program (10 scans per sample).

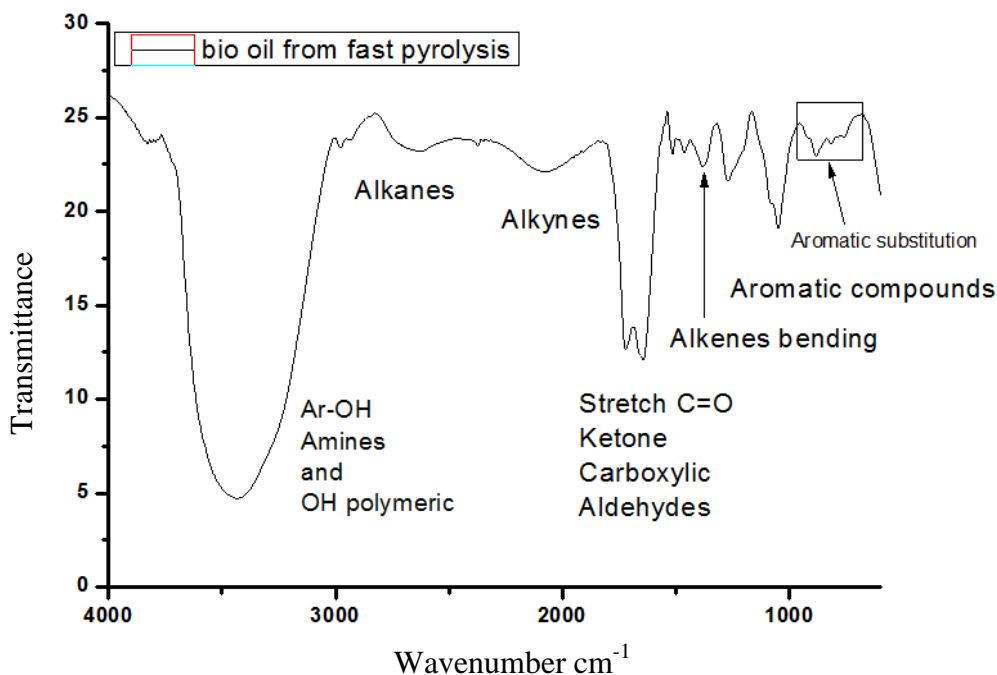


Figure 4.12- Infrared spectrum of bio-oil produced by fast pyrolysis carried out at 600°C under inert atmosphere of nitrogen. Oils were condensed at -68°C. Analysis was carried out with FTIR, following a multi-scanning program (10 scans per sample).

The IR spectra show definite functional groups and in particular aromatic groups, ketone, carboxylic groups, alkenes and alkynes are evident. In the spectrum obtained from oils produced by fast pyrolysis, a large peak is shown between 3600  $\text{cm}^{-1}$  and 3200  $\text{cm}^{-1}$ . This peak is characterized by the presence of polymeric OH and this peak is different for the bio-oil produced by conventional pyrolysis. The polymeric OH confirms the presence of a carbohydrate chain that was detected using the GC-MASS at high retention time values. From the analysis investigations carried out on the bio-oil samples, it was possible to catalogue the different organic substances contained in the bio-oils. In table 4.2, all of the chemical substances contained in both samples are reported:

Nitrogen	Acid	Sugar *
2,2,6,6-tetramethylpiperidone	acetic acid	2,3-anhydro-D-mannosan
benzyl nitrile	propionic acid	1,4:3,6-dianhydro-R
pyridinol		-D- glucopyranose
Indole		levoglucosan
Methylindole		
<b>*only observable in the oils produced by fast-pyrolysis</b>		
Phenol	Aromatic	Ketone
2-methoxy-4-methylphenol	benzene	4-methyl-3-penten-2-one
2-methoxy-4-vinylphenol	toluene	2-cyclopenten-1-one k
o-cresol phenol	styrene	2,3-dimethyl-2cyclopenten-1-
m-cresol	indene	one
2,4-dimethylphenol	methylindene	3-methyl-2-cyclopenten-1-one
3-ethylphenol	naphthalene	3,4-dimethyl-2cyclopenten-1-
4-(1-methylethyl)phenol	methylnaphthalene	one

Table 4.3- Catalogue of the molecules detected in the bio-oils obtained by pyrolysis.

The substances that showed higher intensity were: acetic acid, pyridinol, phenol, o-meta cresol, 4-methyl-3-peten-2-one and cyclopenten-1-one.

#### 4.7. Characterization of carbon fuel

The solid carbonaceous fraction produced by the pyrolysis process was composed of condensed carbon structure contained in functional groups.

Most of the carbons used as fuels can be differentiated from each other by their physical chemical properties, as mentioned previously. Consequently, at the University of St Andrews different types of carbon fuels were produced from biomasses such as mdf and pellet wood. These carbon fuels were also modified in order to change their physical chemical properties. Commercial carbon fuels such

as graphite, and carbon black were also investigated so as to understand their performance as possible fuels.

#### 4.7.1. Carbon from biomass

Carbons obtained by pyrolysis of biomasses such as mdf and pellet wood were pyrolysed at 500°C purging with nitrogen using a flow rate of 40ml/min. The temperature was increased using a ramp rate of 10°Cmin<sup>-1</sup> and holding the sample at 500°C for 30min. These carbons are characterised by their low surface area, 10 g/m<sup>2</sup>, and an amorphous structure which John Cooper's investigations show to have better performance as fuel [36].

Biomass has a crystalline structure arising from the crystalline structure of cellulose it contains. The crystalline structure of cellulose can be observed by XRD investigation of mdf and pellet wood before being pyrolysed.

The spectra carried out on non- pyrolysed mdf and pellet wood show the typical peaks at  $2\theta = 16.25^\circ$ ,  $22.5^\circ$  and  $34^\circ$  of the crystalline cellulose as shown in figure 4.13[96].

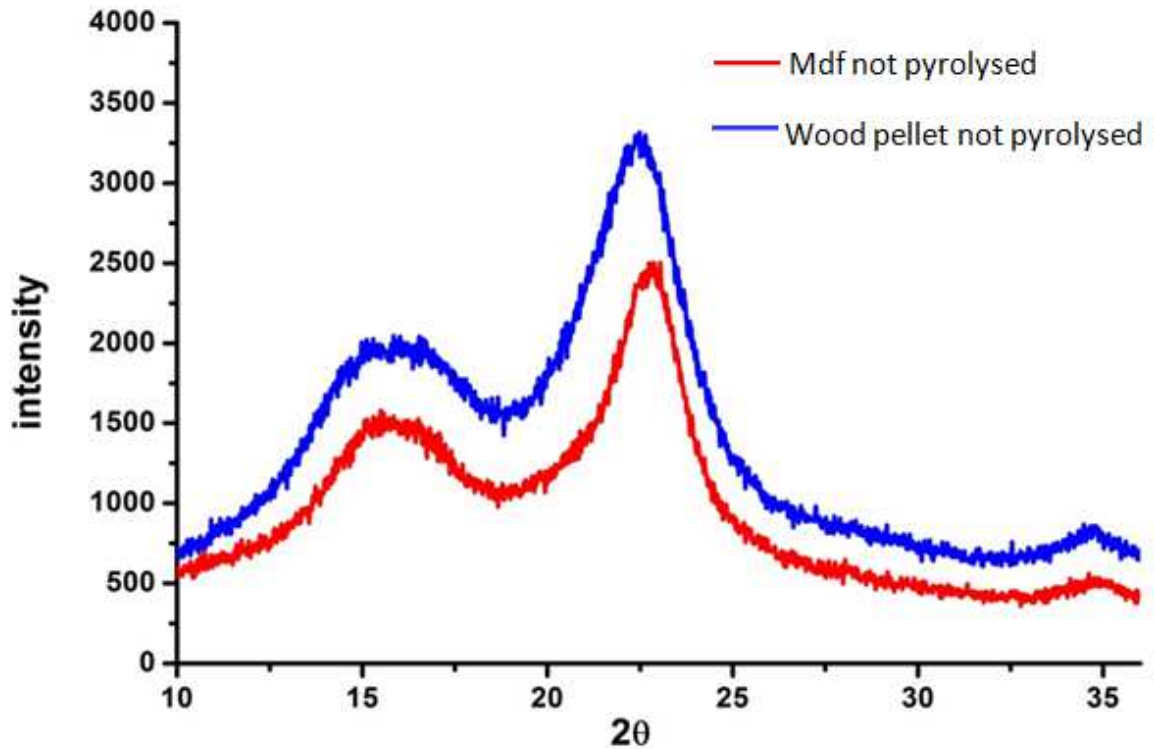


Figure 4.13- X-ray diffraction spectrum of mdf and pellet wood previously milled. The X-ray was carried out on non- pyrolysed powder of mdf and wood pellet.

The peaks are attributed to the cellulose because the lignin structure is totally amorphous and the mineral salt content is too small to be able to detect its crystalline structure.

The crystalline structure of biomass is lost during the pyrolysis of mdf or wood pellet at temperatures higher than 300°C. The loss of crystalline structure was observed when analysing the x-ray the spectra of mdf and wood pellet pyrolysed by conventional pyrolysis. The typical peaks at  $2\theta$  of 16.25°, 22.5° and 34°, which were observed in figure 4.13, disappear completely, as shown in the diffractogram in figure 4.14:

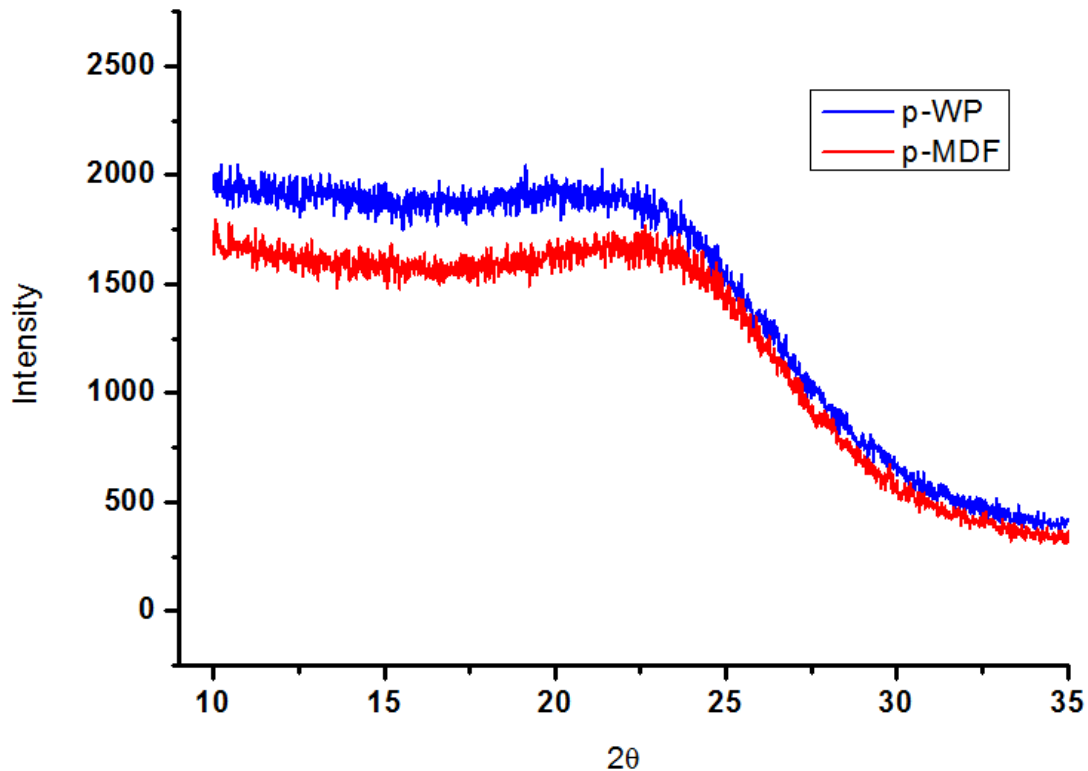


Figure 4.14- X-ray diffraction spectrum of mdf and pellet wood pyrolysed at 500°C under nitrogen atmosphere with a flow rate of 40ml/hr. The temperature was increased using a ramp rate of 10°C min.

In both samples, the carbon obtained from pyrolysis shows an amorphous structure as demonstrated by the X-ray analysis.

The microstructure was also observed by SEM for both samples because the shape of the carbon can affect its electro-oxidation. By analysing the pyrolysed carbons, two different microstructures were observed:

The mdf showed a fibrous structure with an average diameter around 15µm, while the wood pellet showed an irregular structure, as shown in figure 4.15:

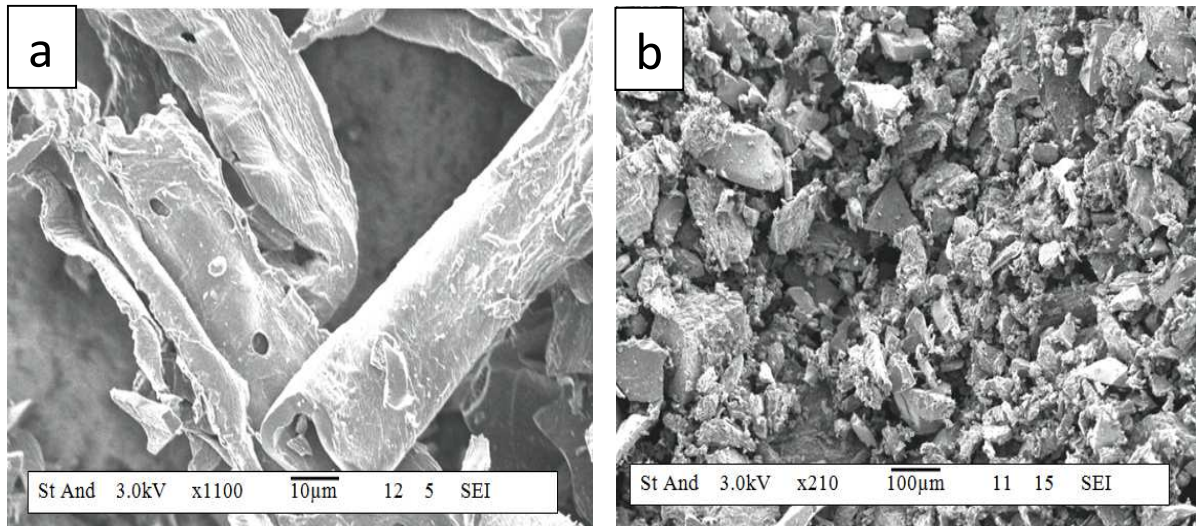


Figure 4.15- SEM picture of carbon produced from pyrolysis of biomass carried out at 500°C under nitrogen with a ramp rate of 8°C min a) mdf b) wood pellet.

The particle size distribution of 100 µm measured by PSD Malven instrument.

Another important parameter that affects the performance of the carbon fuel is the hydrogen content and oxygen bound to the carbon. In fact, the presence of these elements determines the performance of the fuel because they are the first components that react with the oxygen ions provided by the ceramic membrane.

The elementary analyses carried out on wood pellet and mdf are shown in table 4.4:

<b>Elements</b>	<b>Mdf</b>	<b>Pellet wood</b>
<b>Carbon</b>	70.41	67.92
<b>Hydrogen</b>	3.53	3.97
<b>Nitrogen</b>	4.63	2.36
<b>Sulphur</b>	0.00	0.03
<b>Oxygen</b>	21.43	23.18

Table 4.4- Percentage of organic elements in the carbon fuel produced after pyrolysis of biomass at 500 °C under nitrogen with a ramp rate of 8°C min<sup>-1</sup>.

The different elements are organized in different structures and functional groups that are analysed by infrared spectroscopy, as shown in the figure above.

#### 4.7.2. Activated carbon

The activated carbon is a carbon that has been processed using reactive steam at high temperature ( $T > 800^{\circ}\text{C}$ ), increasing both the porosity of the carbon and its surface area. The large surface area modifies the ability of the carbon to adsorb gases. This is a desirable physical chemistry property for a carbon which is used as fuel because during combustion in the anodic chamber secondary gases are produced and their adsorption inside the porous membrane could improve the performance of the fuel.

Usually, a good commercial activated carbon has an area between  $500\text{m}^2/\text{g}$  and  $1000\text{m}^2/\text{g}$  and this value depends on the uses of the carbon. Activated carbons were produced from pellet wood at the University of St Andrews using steam. After pyrolysis of pellet wood, the carbon produced was put into a quartz reactor and the atmosphere of the reactor chamber was cleaned with nitrogen. Wood pellets were activated by using humidified nitrogen with a water content equal to 3% but the maximum surface area measured was  $323.14\text{m}^2/\text{g}$  after 5h at  $800^\circ\text{C}$ . The amount of carbon used for activation was reduced by 50% compared with the original amount used because at that temperature, carbon reacts with water producing CO and  $\text{H}_2$ . The contents of the carbon measured by elementary analysis are 88.03%, which is 20.03% higher than the contents of the carbon which is pyrolysed at  $500^\circ\text{C}$  (70% of carbon). On the other hand, the activation reduced the oxygen content to 10% and this is caused by the reaction between the gas used for the activation gas and the oxygen on carbon surface producing an active site on the surface of the carbon. The hydrogen and nitrogen content decreased to 2.34% and 1.02% respectively. The SEM picture shows the microstructure and the porosity of the carbon:

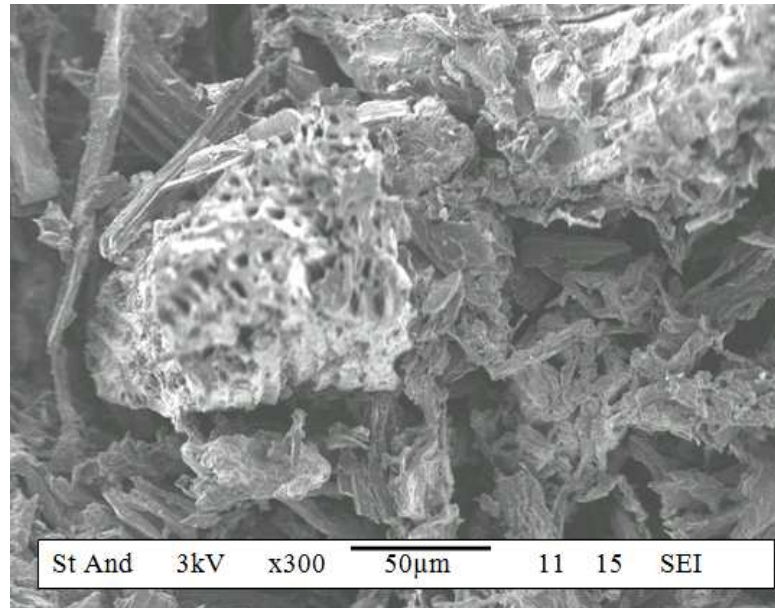


Figure 4.16- SEM picture of wood pellet impregnated with water and pyrolysed at 500°C under nitrogen with a ramp rate of 8°C/min. Carbon was activated using a flow of nitrogen humidified at 6% with a flow rate of 40ml/min at 800°C for 5hrs.

The SEM picture shows the formation of pores on the carbon surface that were produced by the reaction between water and carbon. The high porosity on the carbon surface is related to the high surface area of the carbon. This hypothesis is confirmed by the value obtained by BET analysis that measured a surface area value of 434m<sup>2</sup>/g. In addition, the BET provided information about the pore distribution, confirming the presence of macro pores (30%), micropores and mesopores (70%). The micropores were formed by humidified nitrogen as explained by Molina Sabio and Co-workers[113]. Both are responsible for the high surface area. Water activated carbon was analysed by IR analysis to determine the functional groups on its surface.

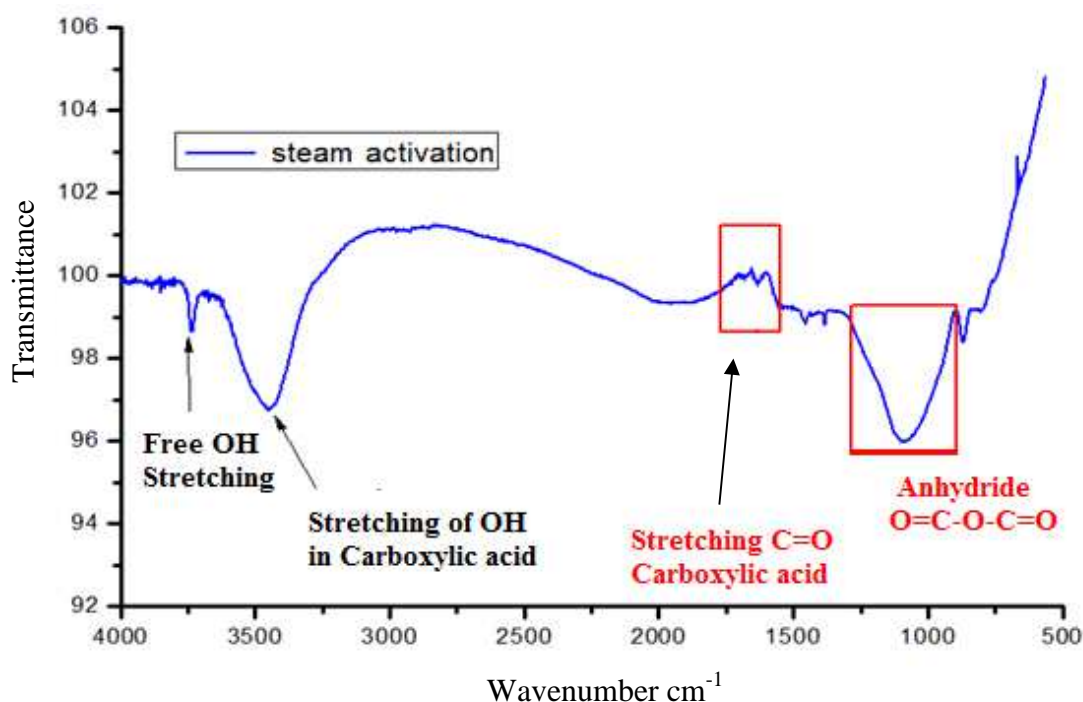


Figure 4.17- Infrared spectrum of activated carbon from pellet wood pyrolysed at 500°C and activated using steam at 850°C.

The IR spectra show some characteristic peaks of OH derived from the reaction of water with carbon 3600-3400  $\text{cm}^{-1}$ . The peak at 3670  $\text{cm}^{-1}$  is due to the free stretching of OH that is not bound by H---H bonds. The stretch of C-O both from carboxylic acid and anhydride are observed at 1690 and 1650  $\text{cm}^{-1}$ . The formation of different CO groups could be caused by the presence of water in the carrier gas. In fact, water reacts with the carbon, producing C=O groups on the surface of the carbon. This could be confirmed by the two broad peaks at 3500 to 3200  $\text{cm}^{-1}$  and at 1260 to 900  $\text{cm}^{-1}$ . The C=C stretch peaks are completely absent because they reacted with water forming OH groups or C=O, depending on the arrangement of the structure.

The water activated carbon was analysed by X-ray diffractometer and its structure was amorphous, as was the other sample pyrolysed.

#### 4.7.3. Aerogel fiberboard carbon

Mdf is a composite material which contains a large amount of urea-formaldehyde resin (40%) used to stick the lignin fibres together. The urea-formaldehyde resin in the mdf was made to react with resorcinol so as to activate the surface of the mdf. The reaction was catalysed by potassium hydroxide in ratio of 0.1:12 for formaldehyde and 0.1: 6 for resorcinol [114-116].

A gram of mdf contains 40% urea-formaldehyde resin, which is composed of 0.2% of free formaldehyde that is able to react with the resorcinol. The resorcinol was made to react with the free formaldehyde adsorbed in the lignin fibres in order to improve the chemical surface of the lignin.

This reaction was carried out in a flask with three necks at 90°C for 5 days. A thermometer, a condenser and a mechanical stirrer were inserted into the three necks. After the reaction, the product was dried overnight in an oven at 80°C, as shown in figure 4.15:

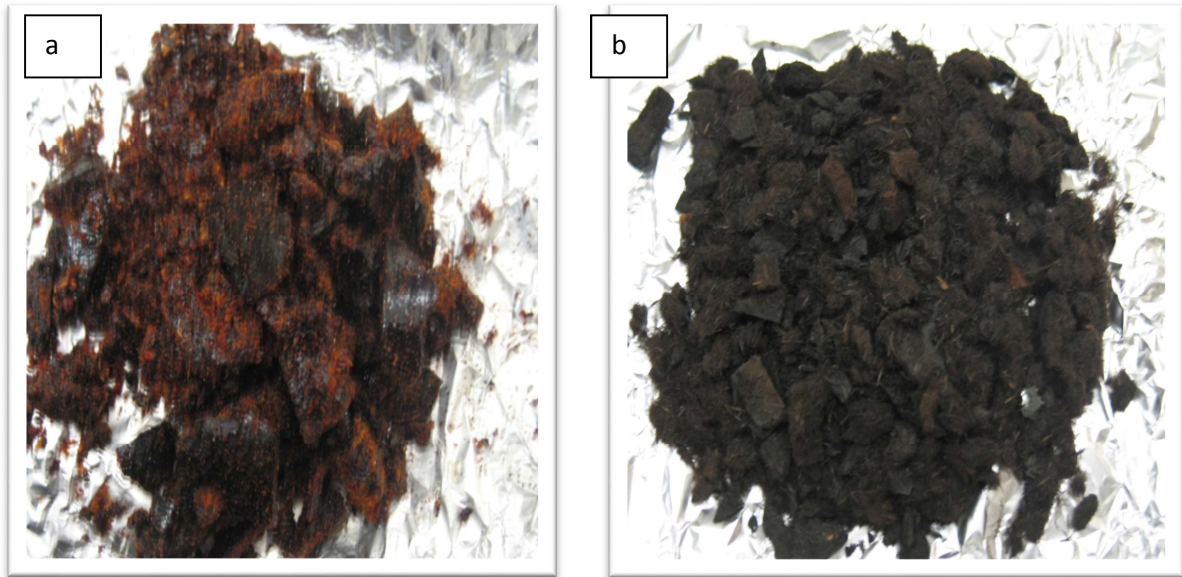


Figure 4.18- Representation of the typical colour of an aero-gel after being dried.

a) aero-gel produced from the reaction between formaldehyde and resorcinol

b) reaction between the free formaldehyde in the mdf and resorcinol.

The sample was pyrolysed at 900°C with a ramp rate of 5°C/min under a nitrogen flow of 40 ml/min. The result was a very light sample in which the lignin fibres were stabilized by the polymerization between the free formaldehyde and the resorcinol. In addition, the surface of the carbon fibre had been activated by the combustion of the polymer which grew on the surface of the fibres. This is clearly visible from the surface area measured by BET instrument, achieving a value of 234.57m<sup>2</sup>/g.

The SEM pictures of the non-pyrolysed aero-gel and pyrolysed aero-gel show that the fibres are stabilised compared to the pyrolysed fibres of the classic mdf, as shown in figures 4.19 and 4.20:

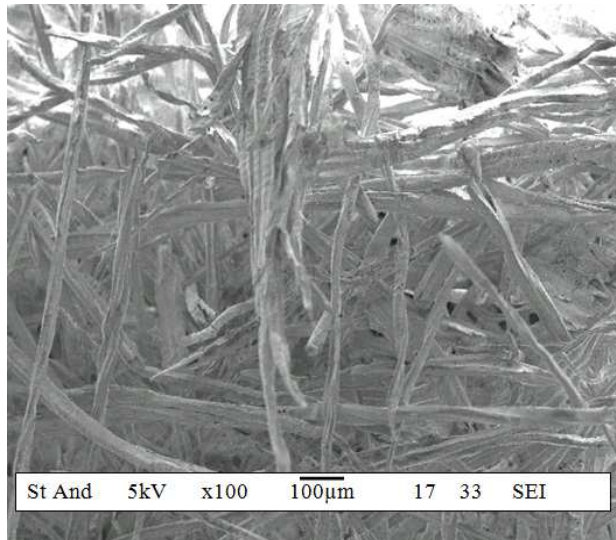


Figure 4.19- SEM picture of mdf fibers after reaction with resorcinol using a catalyst.

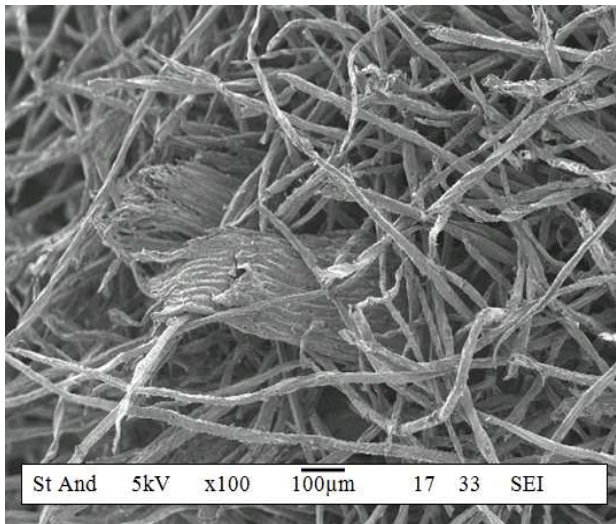


Figure 4.20- SEM picture of mdf fibers after reaction with resorcinol using a catalyst pyrolysed at 800°C for 2hrs under nitrogen with a flow rate of 40ml/min for the production of aerogel carbon.

The surface area measured by a surface analysis instrument was 234.57m<sup>2</sup>/gr and this partial activation was produced from the polymer formed on the surface of the fibres. The infrared spectrum produced from the analysis of aerogel carbon is shown below and it provides information about the possible functional groups.

---

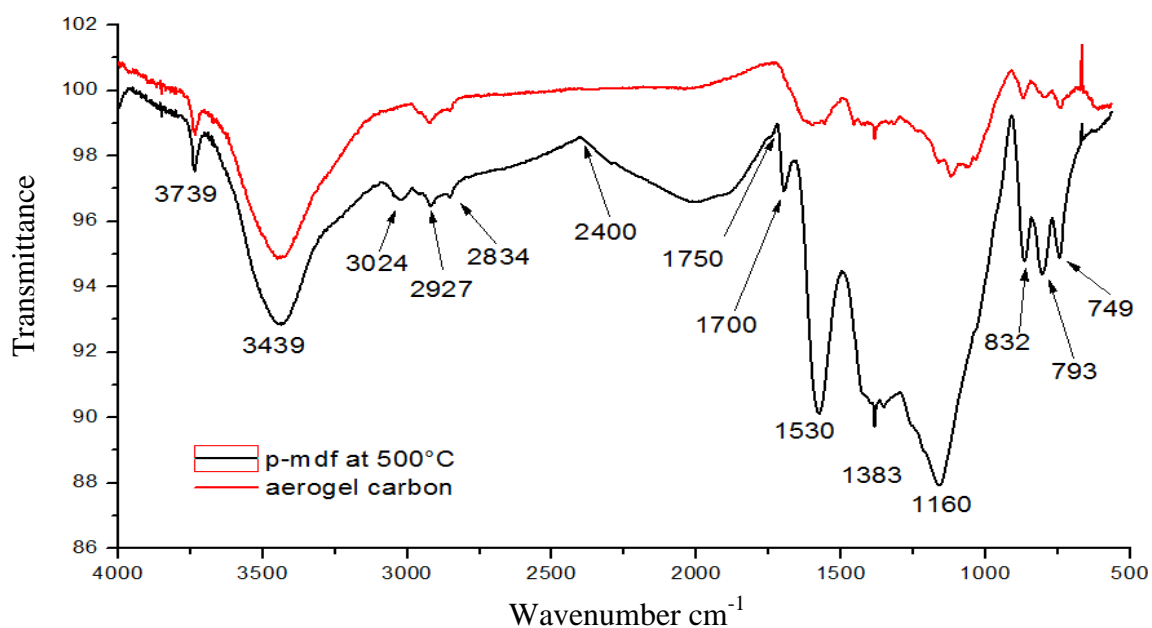


Figure 4.21- Infrared spectra carried out on mdf pyrolysed at 500°C (p-mdf) and aerogel pyrolysed at 800°C.

The broad peak at 3439 $\text{cm}^{-1}$  represents a -NH group derived from the pyrolysed urea-formaldehyde resin. Its intensity decreased as a result of the pyrolysis parameters and consequently the oxidation degree.

Oxidation involves the double bonds (conjugate and isolated) and the C=O group present in the urea-formaldehyde group.

#### 4.7.4. Beer carbon

Beer carbon is a commercial carbon produced from the partial pyrolysis of the residual part obtained from the manufacturing process of beer. The solid waste is obtained during the malting of the barley, in which the barley and other cereals are crushed and mixed with water using a copper or stainless steel vessel. The temperature of mash (cereals plus water) is increased to 78°C in order to activate

the enzyme that converts the starch to sugar and later the sugar to alcohol. After fermentation, the solid part is filtered and pyrolysed at low temperature (200°C). The residual mass contained alcoholic substances, which is clearly visible from the infrared spectrum shown in figure 4.22:

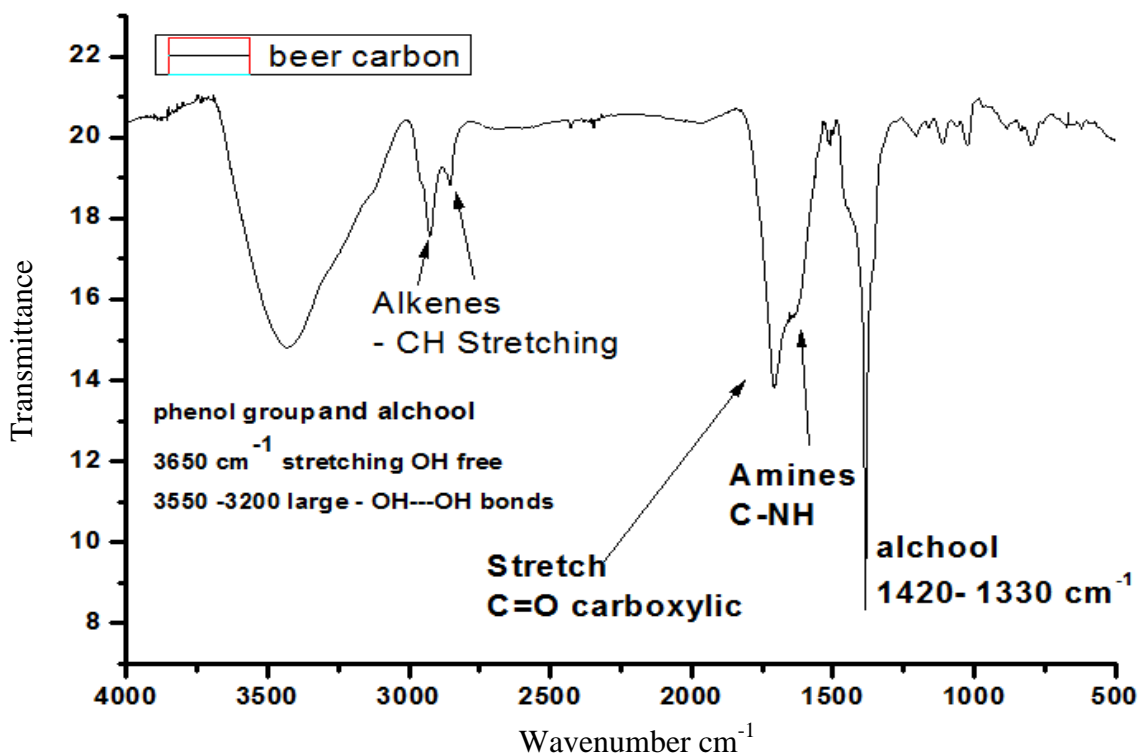


Figure 4.22- Infrared spectra of beer carbon obtained by low temperature pyrolysis of solid waste obtained by the manufacture of the beer.

The spectrum is characterised by different peaks. The main peak is situated in the range between 3650 and 3000  $\text{cm}^{-1}$ . This peak is large because it represents different functional groups containing OH, such as phenol or primary alcohol and carboxylic acid. The extension of the peak over to 3500  $\text{cm}^{-1}$  can indicate the presence of stretching of free OH instead of being bound with hydrogen bonds.

The dimension of the peak is typical of phenol group and alcohol group. However, the presence of carboxylic acid is not excluded as a possible substance that can be detected at ( $3500\text{cm}^{-1}$  and  $3200\text{cm}^{-1}$ ). In the case of OH groups, the peak is extended to  $3700\text{cm}^{-1}$ , meaning that there is an overlapping of the stretching of -NH amines group. The OH from alcohol are bound to alkenes structure that are represented by the two peaks at  $2985$  and  $2885\text{cm}^{-1}$ . At those peaks, the stretching of double bonds C=C could be related to aromatic bond. The carboxylic -OH stretch is confirmed by the peak at  $1714\text{cm}^{-1}$ , which is typical for the C=O group of carboxylic acid and the peak at  $1420\text{cm}^{-1}$ - $1330\text{cm}^{-1}$ . On the other hand, the peak at  $1645\text{cm}^{-1}$ - $1630\text{cm}^{-1}$  represents the amines group. The aromatic structures are confirmed by a set of peaks between  $1207\text{cm}^{-1}$  and  $1011\text{cm}^{-1}$ . Aromatic groups are proved by the presence of three peaks between  $1000\text{cm}^{-1}$  and  $700\text{cm}^{-1}$  that represent the poly-substitution in -ortho, meta and para. The intense peak at  $1383\text{cm}^{-1}$  is the bend of ester sulphate S=O and -CH<sub>3</sub> stretching.

Elementary analysis measures in quantitative way, the percentage of each element in the beer carbon.

---

<b>Elements</b>	<b>Beer carbon</b>
<b>Carbon</b>	52.41
<b>Hydrogen</b>	7.49
<b>Nitrogen</b>	5.81
<b>Sulphur</b>	0.1
<b>Oxygen</b>	33.79

Table 4.5- Elementary analysis of commercial beer carbon produced from the residual solid obtained after the fermentation process of the barley.

The high oxygen content binds to carbon, forming alcohol and carboxylic groups, in which hydrogen is also present. Nitrogen content is in the form of amines.

The solid residue from the manufacture of beer consists predominantly of cellulose and volatile components and for this reason it is unstable at high temperature. In addition, it has a low bulk density. The thermal behaviour is shown in the thermogram figure 4.24:

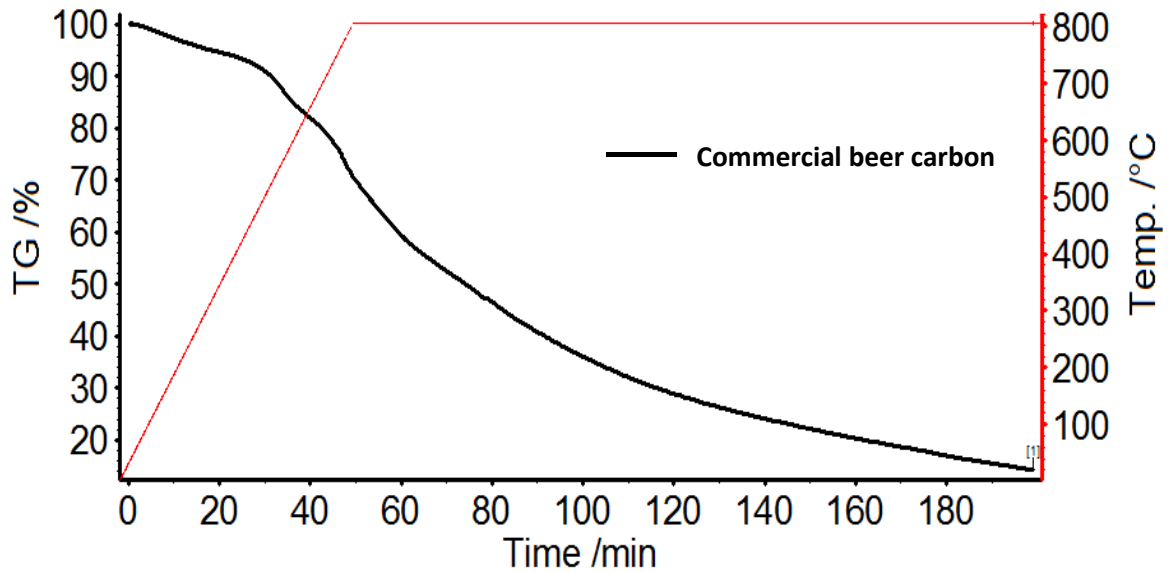


Figure 4.23- Thermogram of carbon beer carried out under nitrogen flow 25ml/min and a ramp rate of 20°C/min holding the sample at 800°C, achieving a residual mass of 14.25%.

In the thermogram, three different weight losses are evident. The first curve is produced by the evaporation of residual alcohol or carbonic anhydrite formed by the fermentation step. The second weight loss is caused by cellulose decomposition. The third weight loss is caused by the rearrangement of the carbon structure that produces small molecules such as carbon monoxide, carbon dioxide and hydrogen.

The high oxygen content could partially oxidise the beer carbon even if the carbon is in an inert environment. This phenomenon could be added to the decomposition caused by the pyrolysis, explaining the sharp weight loss observed during the thermo-gravimetric investigation.

In this case, beer carbon shows an amorphous structure, as shown in figure 4.25:

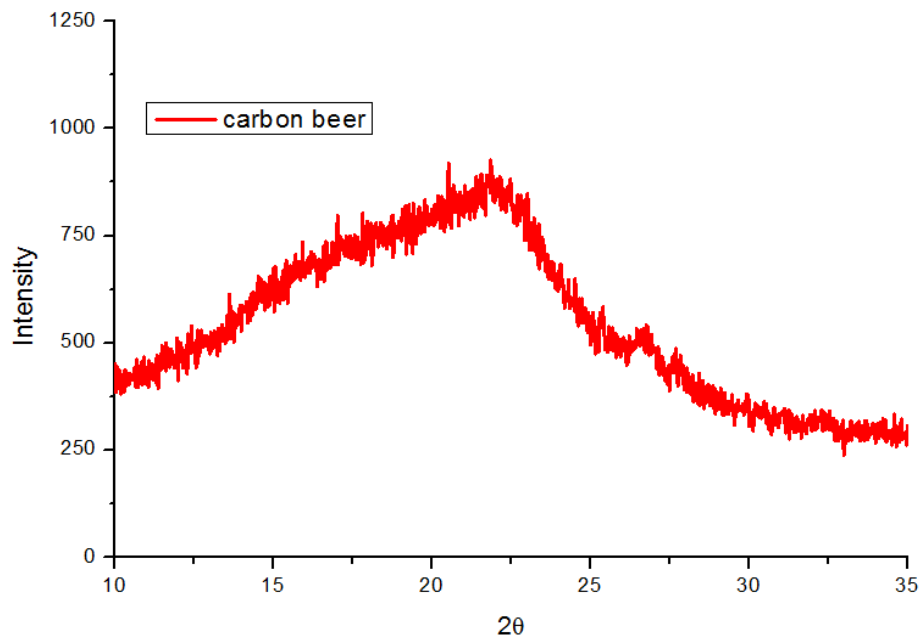


Figure 4.24 - XRD spectra of commercial beer carbon analysed overnight.

The material is pyrolysed because it lost the crystallinity provided by the cellulose structure. The XRD spectra show a poorly defined peak at  $23^\circ$  that is typical for amorphous carbon.

The SEM analyses were carried out to investigate the micro structure and the size of the particles.

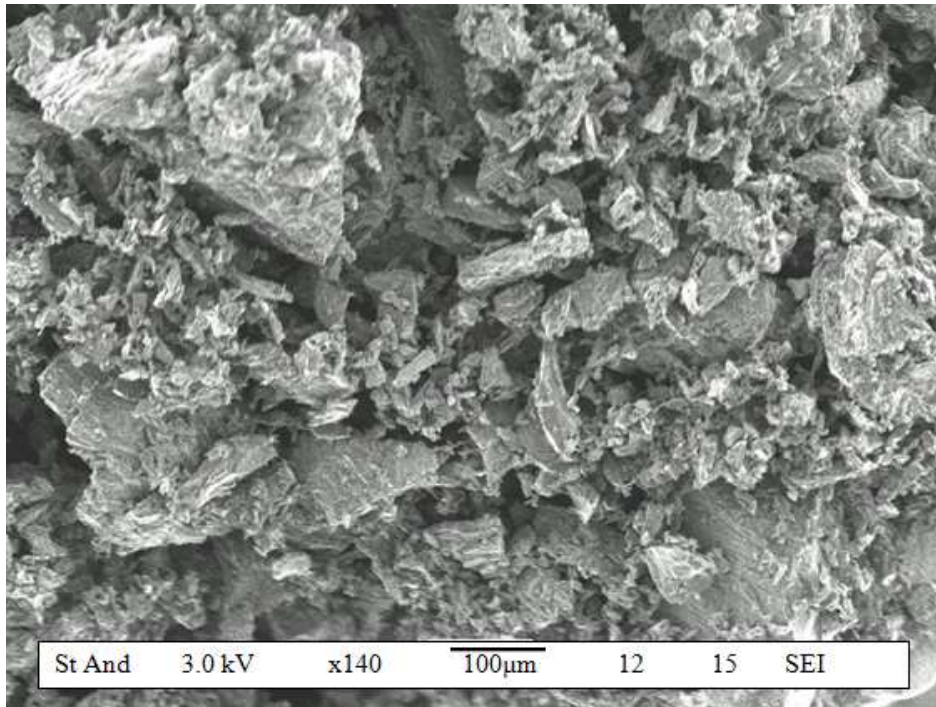


Figure 4.25- SEM picture of carbon beer.

The SEM picture of beer carbon shows large and small particles in a range between 10  $\mu\text{m}$  to 100  $\mu\text{m}$  that are produced by the pyrolysis of the barley. The small particles are obtained from the light part of the barley such as the shell, while the large part is obtained from the grain. Hence, the particle size is not homogeneous.

#### 4.7.5. Graphite

Commercial graphite was used as carbon fuel in order to study the effect of crystallinity of carbon fuel on the fuel cell performance. It is an allotropic form of carbon and it has a layered, multi hexagonal planar structure. This particular

structure provides a typical XRD spectrum that has a peak at  $26^\circ$  due to the graphitic interlayer as shown in figure 4.27:

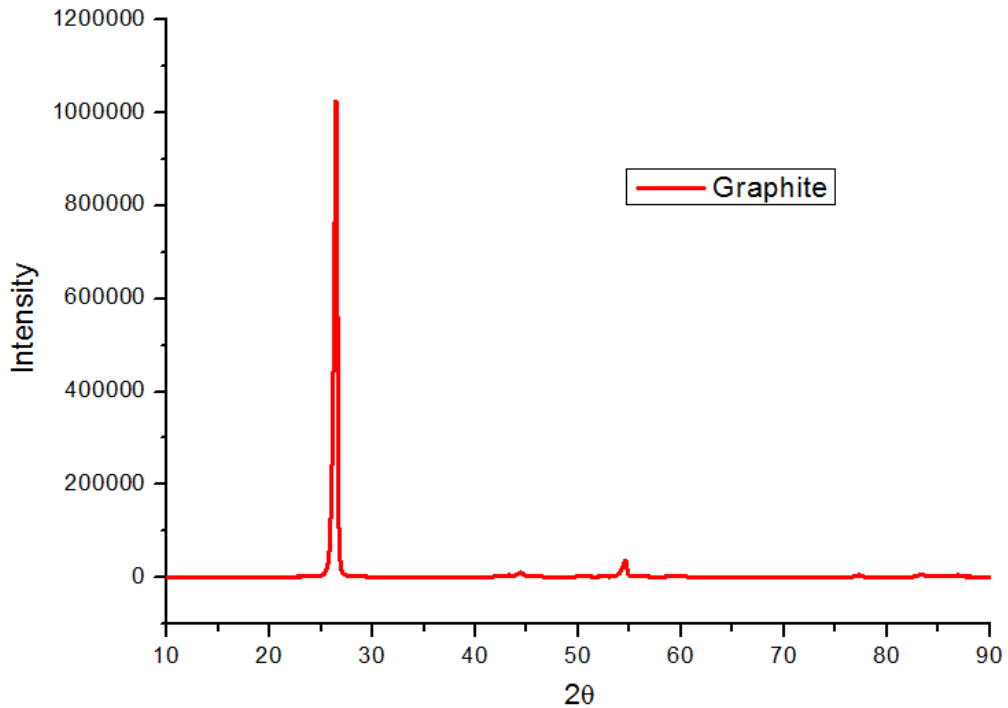


Figure 4.26- X ray spectra of commercial graphite.

The microstructure was investigated by SEM analysis as shown below:

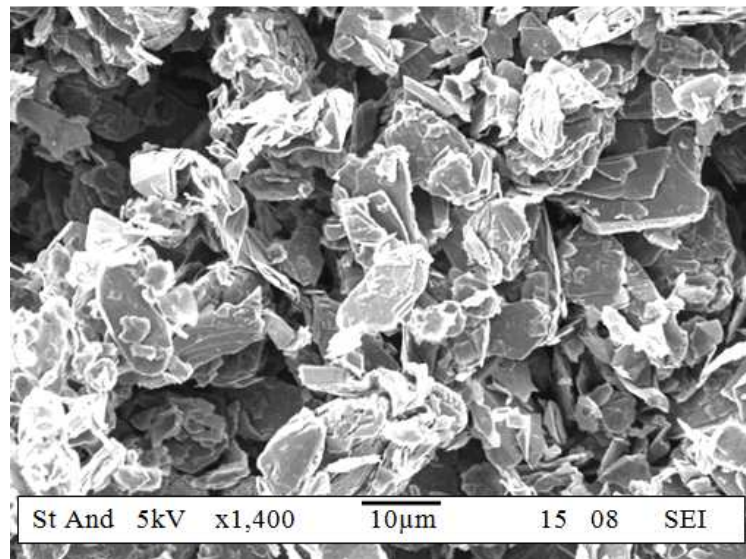


Figure 4.27- SEM picture of commercial graphite.

Graphite shows a flake structure and the dimension of the particle is estimated at around 50  $\mu\text{m}$ .

Elements	Graphite
Carbon	99.9
Hydrogen	0.00
Nitrogen	0.01
Sulphur	0.00
Oxygen	0.00

Table 4.6- elementary analysis of graphite.

Elementary analysis confirms the purity degree provided by the sigma Aldrich.

#### 4.7.6. Carbon Black

Commercial carbon black was used as fuel for the hybrid direct carbon fuel cell.

Carbon black is a secondary product of the incomplete combustion of heavy petrol during fluid catalyst cracking. Carbon black is an amorphous carbon and this is visible from the XRD spectra shown below:

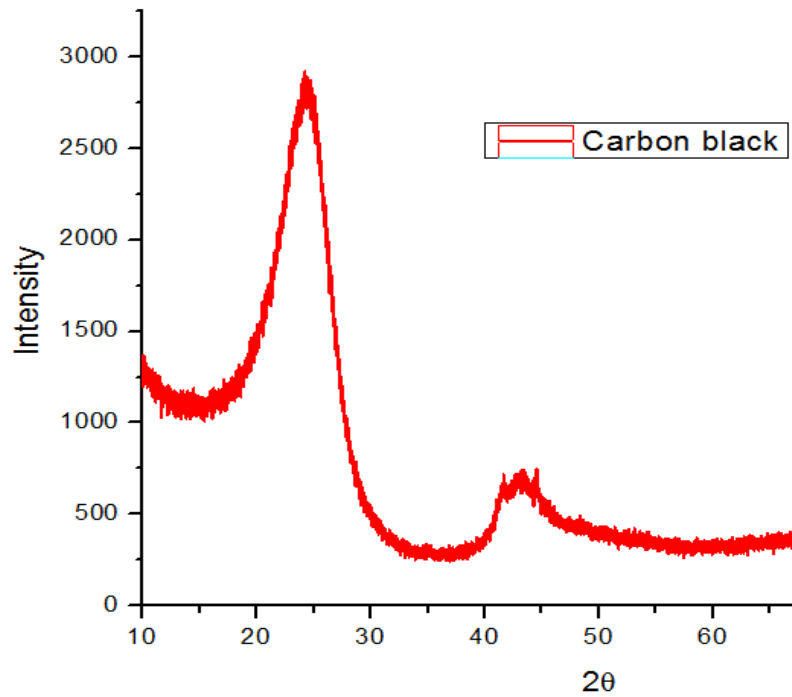


Figure 4.28- XRD spectra of carbon black. Experiment carried out overnight with a Philips instrument.

The microstructure of carbon black was investigated using a scanning electron microscope as shown in figure 4.29:

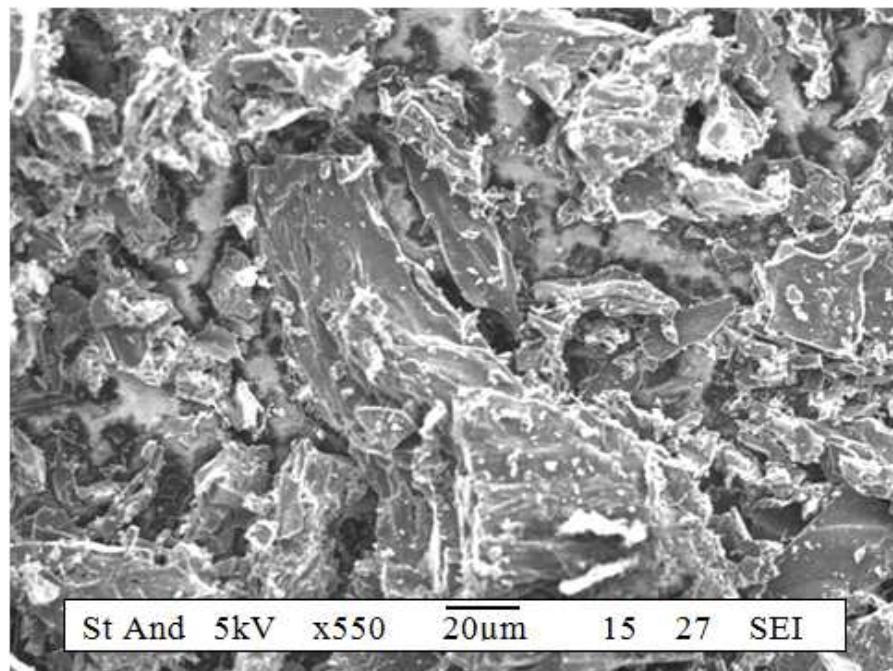


Figure 4.29- SEM picture of commercial carbon black.

The carbon black is shown to have a heavy and dense structure. This type of structure is derived from the type of raw material used. In fact, carbon blacks are a sub product of industrial manufacture of heavy petroleum, ethylene cracking.

The main characteristic of all carbon black is the chemisorbed activity of complex groups containing oxygen (i.e. quinone, phenol and carboxylic group). The degree of chemisorbed products is dependent on the manufacturing process. The infrared spectra indicated the presence of these functional groups, as shown in figure 4.30:

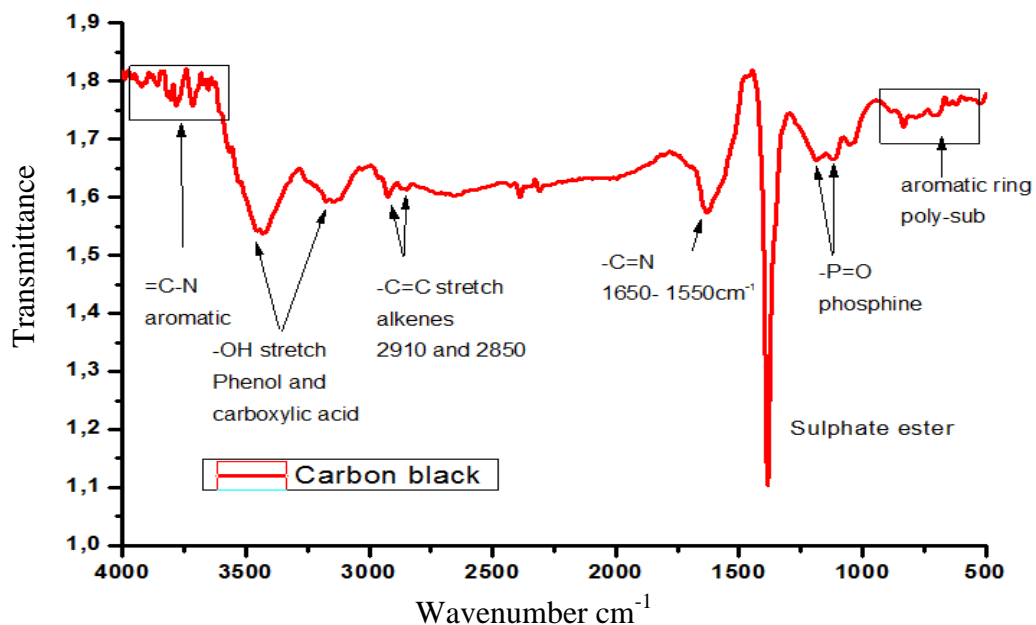


Figure 4.30- Infrared spectra of commercial carbon black.

The spectrum of carbon black is not significantly different from the spectra shown previously because it is characterised by a set of small peaks between 3700 to 3900 $\text{cm}^{-1}$  that can be considered to be the stretching of =C-N typical of

quinine or nitrogen surrounded by aromatic carbons. These groups can be confirmed by the peak at  $1710\text{cm}^{-1}$   $-\text{C}=\text{N}$ .

The number of functional groups in the carbon black is low and depends on the content of carbon in the total structure. Elemental analysis shows low hydrogen and nitrogen content. This suggests that the structure is composed of aromatic clusters such as naphthalene, which does not have a large number of functional groups.

Elements	Carbon black
Carbon	97.02
Hydrogen	---
Nitrogen	0.09
Sulphur	---
Oxygen	2.98

Table 4.7- elementary analysis of carbon black.

#### 4.7.7. Studies of thermal stability on commercial and non-commercial carbons

The thermal stability of commercial carbons (graphite and carbon black) and non-commercial carbons (p-mdf, p-wp, aerogel carbon and activated carbon) were investigated by thermogravimetric analysis in order to quantify the amount of carbon lost when the cell is heated to  $700^{\circ}\text{C}$ .

These tests were carried out under nitrogen in order to prevent possible reactions with other species. The temperature was increased to 800°C, applying a ramp rate of 5°C/min. Samples were held at 800°C for 30 min.

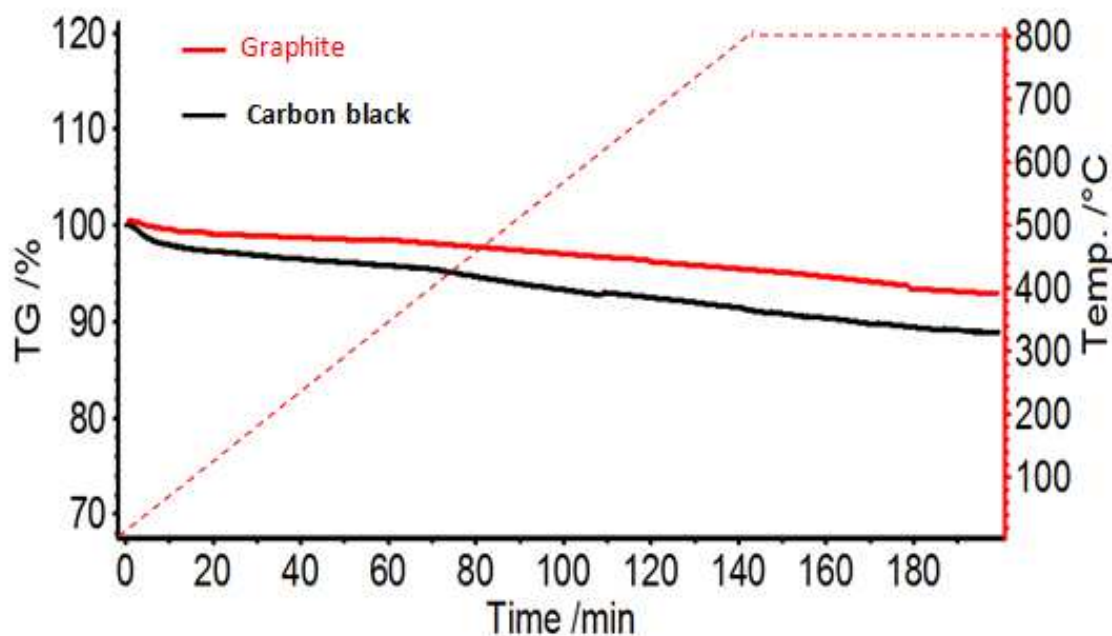


Figure 4.31- Studies of thermal stability of commercial carbons using thermal gravimetric analysis (TGA). The test was carried out increasing the temperature from 25°C to 800°C with a ramp of 5°C/min under inert atmosphere. The weight loss was achieved after keeping the three samples at 800°C for 30 min.

From the thermogram it is evident that graphite is more stable than carbon black.

In fact, a weight loss of 4% was achieved for graphite compared with 10% for carbon black. This is dependent on the high carbon content of graphite (99% C) and the type of carbon structure that is highly resistance to the oxidation. This was dependent on the oxygen content of carbon black reported on the table 4.7. In fact, oxygen is bound to the carbon and carbon monoxide is lost.

The non-commercial carbons such as aerogel, mdf, wood pellet and activated carbon were also investigated by TG analysis, following the same procedure previously described.

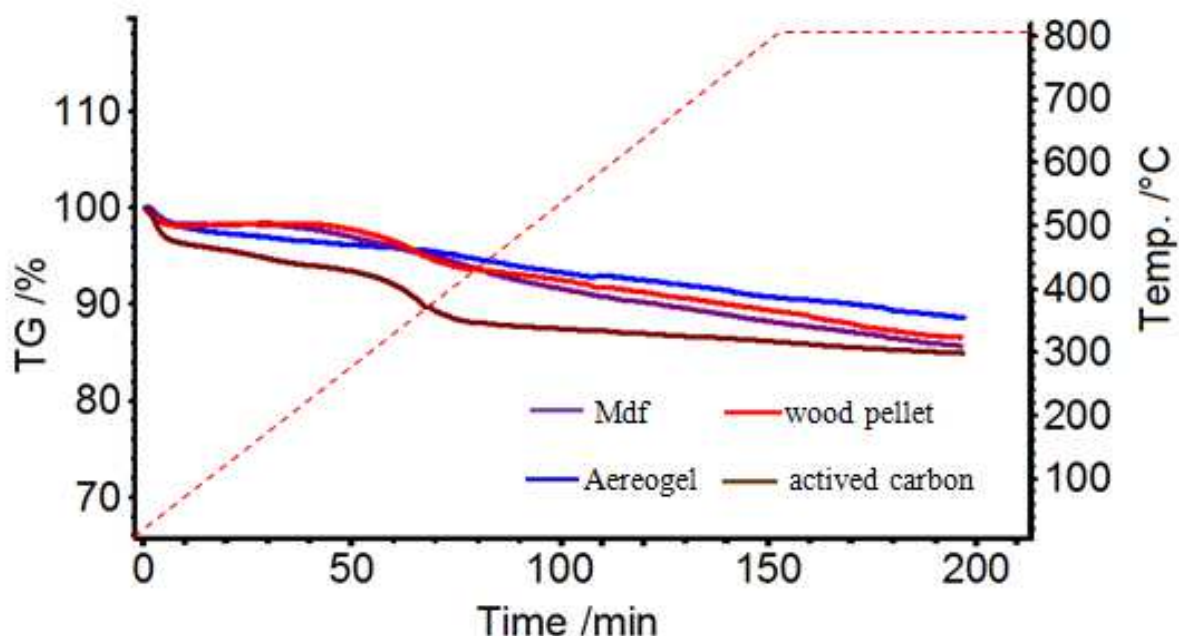


Figure 4.32- Studies of thermal stability of aerogel carbon, mdf and wood pellet pyrolysed by using thermal gravimetric analysis (TGA). The test was carried out increasing the temperature from 25°C to 800°C with a ramp of 5°C/min under inert atmosphere. Each sample was held at 800°C for 30 min.

The aerogel achieved a weight loss of 11.5% and it is more stable than the other samples. Its high stability is due to the polymerized fibres produced during the reaction between formaldehyde and resorcinol. The lowest stability performance was achieved by the activated carbon (-14.5%), which was more reactive because of its high surface area. In fact, the high surface area is proportional to the functional active site such as C=O groups. At high temperature, the C=O are

unstable and this causes weight loss. This could explain the sharp drop observable at 400°C.

The stability of mdf and wood pellet was midway between aerogel and the activated carbon and activated carbon. Their weight loss was caused by completion of pyrolysis that stopped at 450°C.

#### 4.7.8. Effect of carbonate on carbon gasification

Carbon is used as fuel in the HDCFC and this is mixed with carbonate salts ( $\text{Li}_2\text{CO}_3$  and  $\text{K}_2\text{CO}_3$ ). The carbonate salts are highly reactive with carbon at high temperature, producing carbon monoxide and carbon dioxide. In the hybrid direct carbon fuel cell, carbon can react on the surface of the anode but it can also react with the carbonate, producing CO and  $\text{CO}_2$ . This reaction is an important parameter needed to estimate the loss of carbon during the reaction between carbon and carbonate. Both a theoretical and an experimental approach were chosen to comprehend the direction of the reaction between carbon and carbonate. The theoretical approach was investigated by FACTSAGE software. The reacting components ( $\text{C}+\text{CO}_2$ ) were inserted into the system, with an operation temperature of 850°C, one atmosphere and one mole for each component. The calculation was simulated at the equilibrium. The results

obtained by the simulation highlight a high formation of CO as expected in both systems, and a small formation of CO<sub>2</sub> as shown in the table:

Samples	Initial mole	Final mole CO	Final mole CO <sub>2</sub>	C residue
$C + CO_2 \rightarrow 2CO$	1.1E-3	1.08E-3	7.97E-6	7.97E-6
$C + CO_2 + M_2CO_3 \rightarrow 2CO + CO_2$	1.21 E-3	1.08E-3	1.6E-4	0

Table 4.8- Theoretical calculation of carbon graphite oxidation. A- Simulation of carbon graphite oxidation behaviour at 850°C and 1 atm. B- simulation of carbon oxidation behaviour in the presence of carbonate mixture in molar ratio 80:20%.

This small amount of CO<sub>2</sub> in both systems originated from the amount of CO<sub>2</sub> that is unable to react with the stable structure of carbon at 850°C. The simulation was also carried out on carbon mixed with carbonate in molar ratio 80:20. The amount of carbon is completely oxidised in the presence of carbonate. In addition, the amount of carbonate balances the formation amount between CO and CO<sub>2</sub> compared to the system without carbonate. This means that the carbonate favours the gasification process, as shown in table 4.8.

An experimental investigation was carried out by thermogravimetric analysis on p-mdf pure and p-mdf mixed with carbonate under 5% CO<sub>2</sub> and 95% Ar. The temperature for both tests was increased from room temperature to 850°C at 20°C/min. Each sample was held at 850°C for 540 min.

The thermogram shows two different curves:

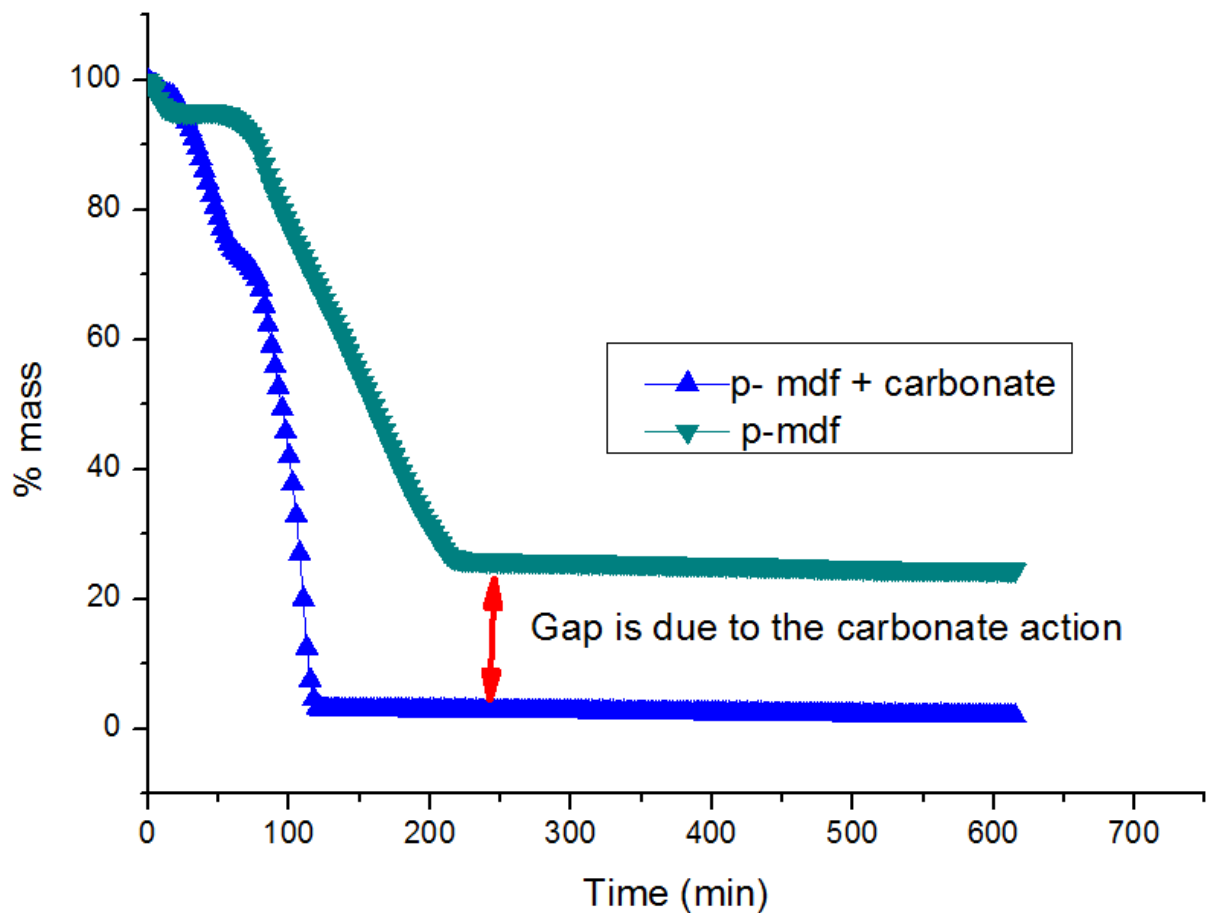
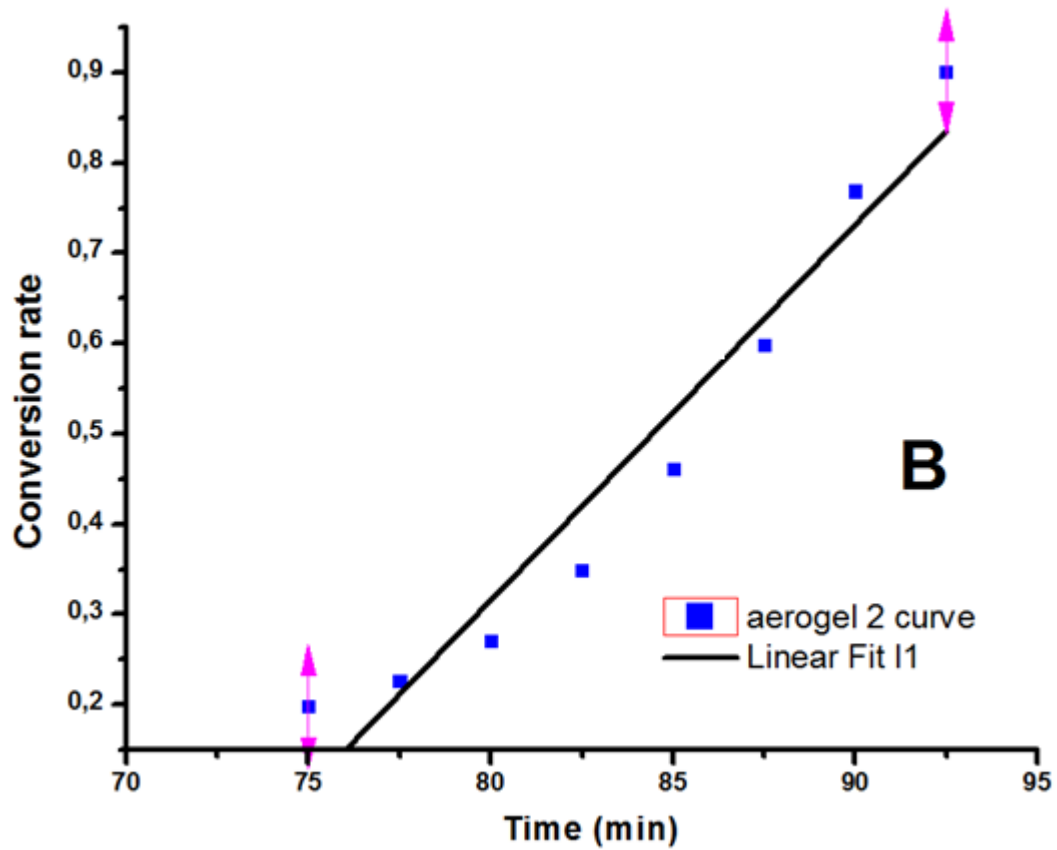
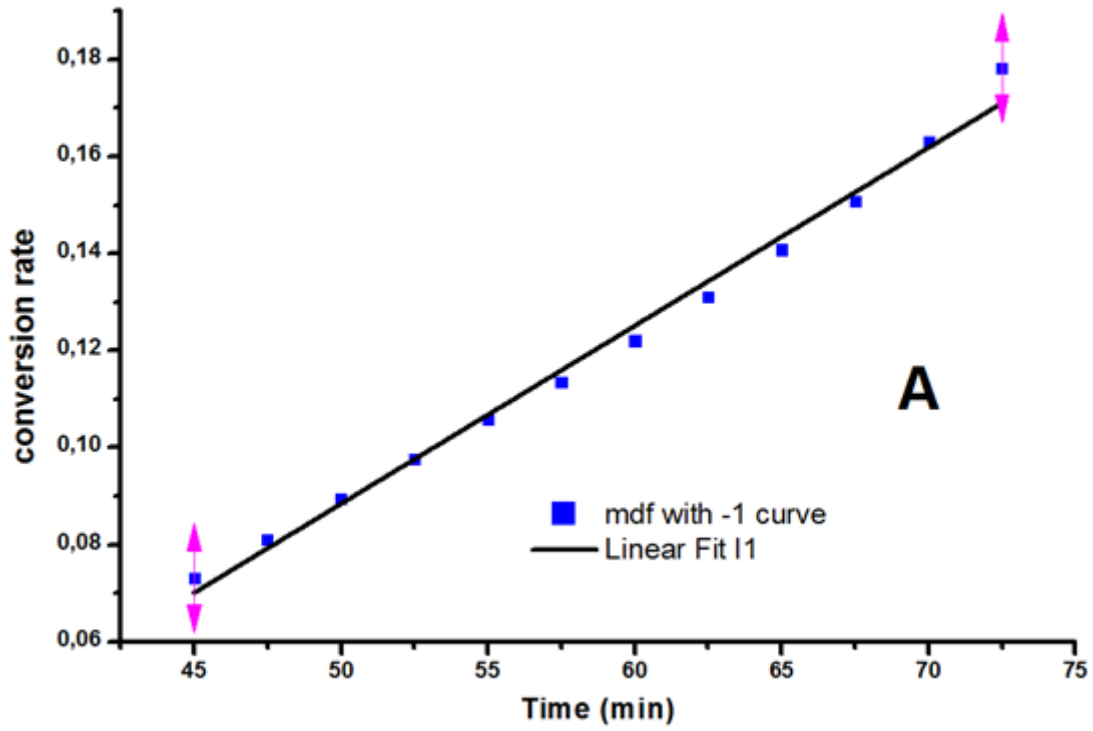


Figure 4.33- Thermogram of mdf carbon fuel carried out under CO<sub>2</sub> environment (25ml/min) using a heating ramp rate of 20°C/min to 850°C.

The p-mdf curve for the system p-mdf without carbonate shows two diverse weight losses: the first drop takes place between room temperature and 850°C but it is very small and it might be caused by oxidation of functional groups and CO<sub>2</sub>. In between the two drops no weight loss is visible. This means that no oxidation reaction takes place. Instead, the second drop is clearly caused by the reaction of carbon with oxygen and hydrogen bound to the carbon. A high residual mass was achieved for the pure p-mdf. This residual mass might be the result of the formation of pure carbon structure which is stable at high temperature and stable under oxidant environment and is much higher than that simulated by the software.

The behaviour was totally different when the p-mdf was mixed with carbonate salts. In fact, three different curves are shown in the curve with p-mdf mixed with carbonate. The first drop is faster than that showed by the curve with p-mdf. In fact, the molten carbonate starts oxidizing the carbon much earlier than the CO<sub>2</sub> gas. The first oxidation involves functional groups bound to the carbon structure. Instead, the second drop is due to the oxidation of carbon structure and decomposition of loss of carbonate.

The differences between both processes were studied, calculating the degradation rate of each curve, as shown in figure 4.34:



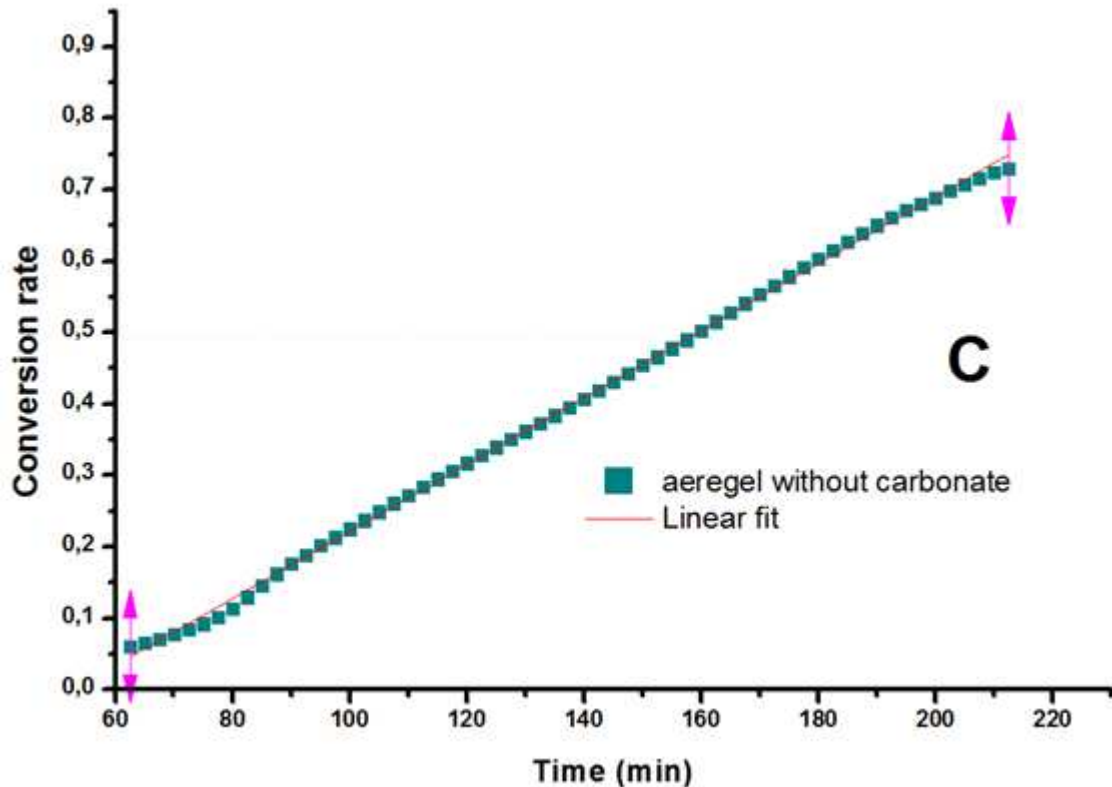


Figure 4.34- Analysis of dropping curve for p-mdf carbon oxidation under  $\text{CO}_2$  carrier gas with and without carbonate A) Initial drop for system with carbonate/p-md B) second drop for the system with carbonate/p-md C) single drop for system without carbonate.

The two graphs shown in figure 4.34 represent the first and the second drop for the curve with p-mdf with carbonate. The first degradation rate is very similar to the degradation rate of p-mdf pure. This means that the process involved in the first part of the oxidation is not affected by the carbonate salts.

The degradation rate for the system with carbonate is one order of magnitude higher than the system without carbonate. This shows that the oxidation of carbon is favoured in presence of carbonate. Liquid carbonate is more reactive than  $\text{CO}_2$  because carbonate ions provide oxygen ions during decomposition that

are more reactive than oxygen bound to CO<sub>2</sub>. In addition, the contact area between the liquid carbonate/solid carbon system is greater than the solid carbon/CO<sub>2</sub> gas system because carbon is dipped into the carbonate salts. In conclusion, the carbonate affects the gasification of carbon producing CO gases.

#### **4.8. Electrochemical reactivity of several carbon fuels.**

The carbon fuel performance of commercial and non-commercial carbons, which were characterised previously, was investigated using a hybrid direct carbon fuel cell with planar geometry. Planar geometry was chosen both for its advanced development and because it provides an easy way to study electrochemical phenomena. In addition, this type of configuration permits the addition of a large amount of carbon-carbonate mixture, which in turn prevents large variation in performance as function of time. The fuel cell tests were carried out using a button cell with YSZ electrolyte and NiO-YSZ anode and LSM-YSZ cathode, which were screen printed respectively on both sides. The configuration of the planar set up is shown below:

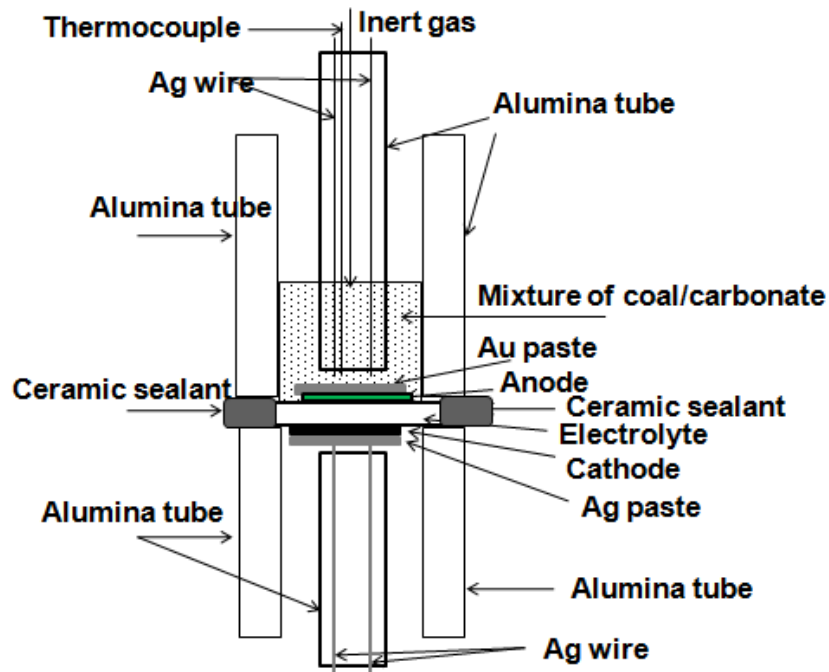


Figure 4.35- Schematic description of the planar cell.

Carbon fuel was tested in a planar cell because its geometry is better for the study of the electrochemical behaviour provided by carbon fuel in the cell. In addition, the amount of carbon and carbonate which can be used in the anodic chamber of a planar cell is higher than in a tubular cell and this makes it possible to have enough carbon fuel to test the carbon for long periods. The carbon fuels previously characterised were mixed with carbonate mixture in ratio 80:20 % wt and then tests were carried out at 750°C under Ar flow and CO<sub>2</sub> atmosphere to prevent the decomposition of the carbonate. I-V plot were used to understand the performance of each sample, as shown in figure 4.36:

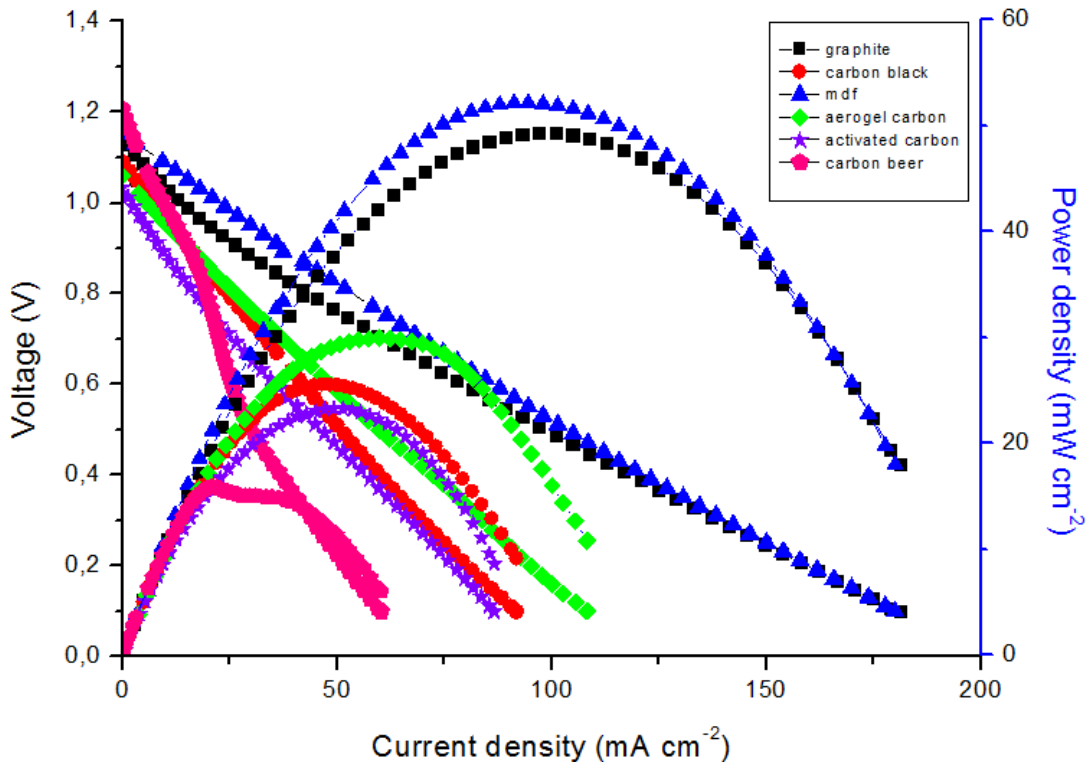


Figure 4.36- I-V curve of different carbon fuels tested using HDCFC in planar configuration. Tests were carried out at 750°C using a Solatron 1280 B.

The I-V curve shows different values of OCV related to the carbon fuels used. This could be caused by the use of argon gas purged into the anode chamber increasing the OCV because it suppresses the CO<sub>2</sub> concentration at the carbon surface. The highest OCV voltage is achieved by the beer carbon. The beer carbon, as presented previously, is highly reactive, causing high carbon consumption and consequently an increase in the carbonate percentage. This suppresses the concentration of CO<sub>2</sub> more than the other less reactive samples than carbon beer because a large amount of the carbon is consumed during the start-up and stand-by conditions of cell. The consumption of carbon is observable from the power achieved during the test. The power achieved was the lowest of

all. Instead, an OCV voltage close to the theoretical OCV was observable for the other carbons. The highest discharge rate,  $100\text{mA}/\text{cm}^2$  at  $0.75\text{V}$ , was achieved both for pyrolysed MDF and graphite. They have different structures: mdf is amorphous while graphite is crystalline, as shown in the XRD pattern. This highlights how the performance of our device is independent of the structure of the carbon fuel. Performances achieved from different carbon fuels demonstrated good performance for p-mdf and graphite carbon fuel, while the worse performance was achieved from carbon beer.

The two activated carbons showed two different behaviours: The carbon aerogel has a discharge rate of  $65\text{ mA}/\text{cm}^2$  which is higher than water activated carbon ( $40\text{ mA}/\text{cm}^2$ ) even if carbon aerogel has a lower surface area ( $236,15\text{ m}^2/\text{gr}$ ) than water activated carbon ( $323.14\text{ m}^2/\text{gr}$ ). This demonstrates that the carbons with small surface area perform better than carbons with large surface area. This phenomenon could be explained by the minimal ability of low surface area carbons to react with carbonate, losing part of the fuel by the gasification process instead of being oxidised electrochemically. This reduces the electrochemical reactivity of the carbon fuel.

#### 4.9. Summary

Several types of carbons with differences in structure, surface area, particle size and percentage of oxygen, hydrogen and carbon, were produced and tested. The electrochemical performance observed from the I-V curve showed that the structure of the carbon fuel is not totally dependent on the structure of the carbon, but it also depends on the reactivity of the carbon. In fact, the highest discharge rate, 100mA/cm<sup>2</sup> at 0.75V, was achieved both for pyrolysed MDF and graphite.

This explains why the carbons with higher surface area achieved a lower discharge rate than carbons with low surface area. In fact, since the active carbons are more reactive, they react easily with carbonate, favouring gasification instead of participating in the electrochemical reaction on the anode surface.

These results are highlighted from the gasification rate calculated for the carbons with both high and low surface areas.

#### 4.10. References

- [113] M. Molina-Sabio, M.T. Gonzalez, F. Rodriguez-Reinoso , A. Sepúlveda-Escribano Carbon Vol. 34, No. 4, pp. 505-509,1996
- [114] Wencui Li, G. Reichenauer, J. Fricke - Carbon 40 (2002) 2955–2959
- [115]Saliger R, Bock V, Petricevic R et al.- J Non-Cryst Solids application - 1997; 221 :144 –50.
- [116] Bock V, Emmerling A, Saliger R, Fricke J. J Porous Mater- 1997;4:287–94.

## **5. Characterization of Solid oxide fuel cell components**

This chapter is focused on the study and characterization of each component of the solid oxide cell. In the first part, the studies focus on the oxygen ion membranes, which work primarily to transport oxygen ions from the cathode to the anode, where the oxidation of fuel takes place. However, the oxygen ion membrane also acts to block the electronic conduction path, favouring the ionic conduction path. In the second part, the study shifts to the electrodes that are responsible for the electro-catalysis of fuel and oxidant in the anode and cathode respectively.

The electro-catalysis in the anode in particular has to be very efficient because it determines the overall efficiency of the cell.

### **5.1. Results and discussions**

In this section, AC impedance data of symmetrical cells are shown and discussed. Each component and symmetrical cell is also investigated by electron microscopy, which is used to observe the microstructure of anode, cathode and electrolyte.

### 5.1.1. Oxygen Ion membranes

As already explained, electrolyte materials are one of the most important parts of the fuel cell because they limit the diffusion of the oxygen ions (oxidant) produced at the surface of the cathode to the anode where the oxidant reacts with the oxidant. The velocity of ion diffusion inside the electrolyte from the cathode to the anode affects the performance of the fuel cell device. The commercial solid oxide fuel cell used as electrolyte is a fluorite structure of yttria stabilised zirconia  $Y_{0.08} Zr_{0.92} O_{1.96}$  that consists of a cubic oxygen lattice with alternate body centres occupied by eight coordinated cations, while the anions occupy the tetrahedral sites. The  $Zr^{4+}$  is too small to maintain the fluorite structure at low temperature. For this reason, the  $Zr^{4+}$  has to be replaced with a large cation in order to stabilise the fluorite structure. Yttria oxide is the cation used to stabilise the zirconia structure. In addition, the introduction of a cation with a lower valence than Zirconia provokes the formation of oxygen vacancies in order to balance out the total charge, which is negative after introduction of  $Y^{3+}$ .



The standard amount used to stabilize the cubic phase of zirconia structure is 8-13%, as shown in figure 5.1:

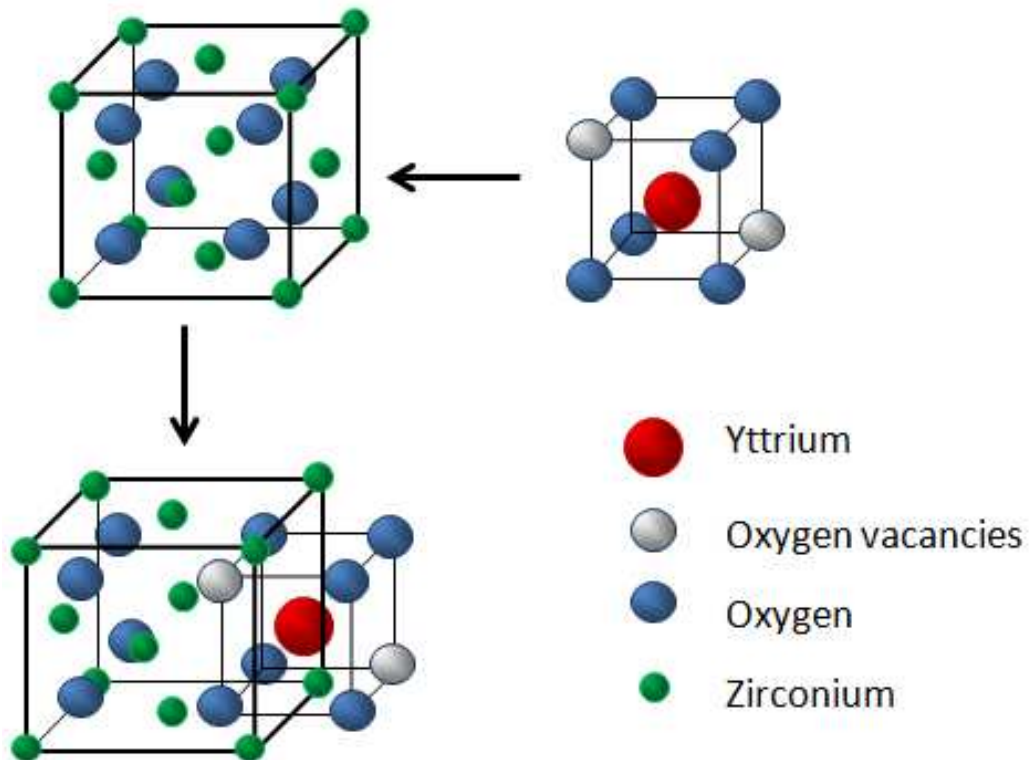


Figure 5.1- Schematic description of stabilization of zirconia oxide after doping of yttria oxide and production of oxygen vacancies produced by introduction of an atom with lower valance of Zr.

This electrolyte has demonstrated high performance at high temperatures ( $0.1\text{Scm}^{-1}$  at  $900^\circ\text{C}$ ) [90]. This type of electrolyte has some limitations. In fact, it is highly conductive at high temperature and as a result, materials capable of resisting high temperatures are required, which increases manufacture costs.

In addition, it requires high temperature which limits the applicability and use of this material in HDCFC because at  $800^\circ\text{C}$  the carbonate salts are highly reactive and unstable because they tend to decompose.

Furthermore, the YSZ electrolyte is unstable in the presence of lithium carbonate because it reacts, producing a stable product like lithium zirconate [117-120].

Over the last years, different types of electrolyte materials were investigated and one of the most promising electrolytes was ceria oxide doped gadolinia, which has been demonstrated to be two or three orders of magnitude more conductive than YSZ at low temperature. This material was investigated for the first time by Steel and co-workers carrying out important studies on the electrical conductivity of GDC materials[121][122]. Ceria doped gadolinia has the same fluorite structure as yttria stabilised zirconia, in which  $Gd^{3+}$  and  $Ce^{4+}$  occupy the same alternate central body. As the zirconia is stabilised, the oxygen vacancies are caused by the introduction of a trivalent cation in the ceria position, which maintains the neutrality of the charge, as shown in eq. 5.2:

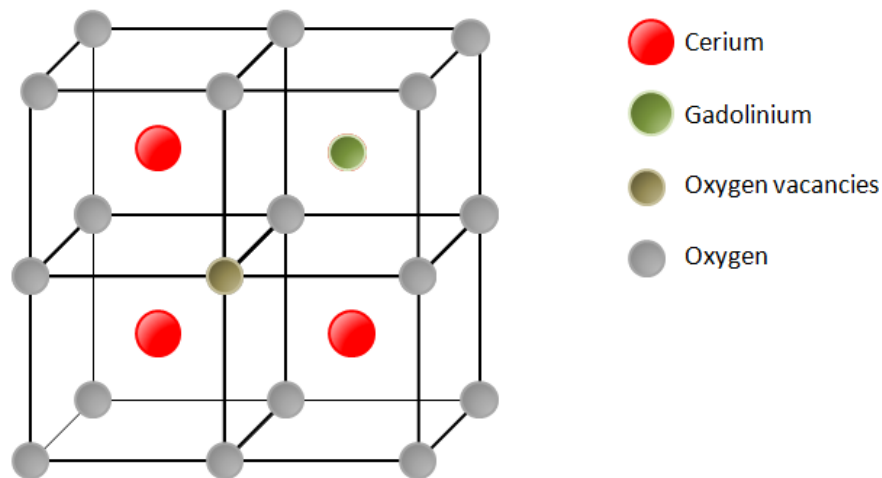
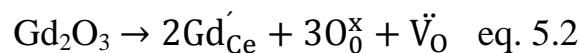


Figure 5.2- Fluorite structure of ceria doped gadolinia with oxygen vacancies.

In literature, interesting results were achieved using this material as electrolyte at low temperature. Results obtained were promising because the material achieved a conductivity of  $0.0095 \text{ Scm}^{-1}$  at  $500^\circ\text{C}$  compared to  $0.0045 \text{ Scm}^{-1}$  for YSZ [123]. At the University of St Andrews, both ceria doped gadolinia oxide ( $\text{Ce}_{0.9}\text{Gd}_{0.1}\text{O}_{1.95}$ ) and yttria stabilised zirconia ( $\text{Y}_{0.08}\text{Zr}_{0.92}\text{O}_{1.96}$ ) were investigated to compare the performance of each material when used as electrolyte for HDCFC.

*5.1.1.1. Studies of electrochemical performance of  $\text{Y}_{0.08}\text{Zr}_{0.92}\text{O}_{1.96}$  and  $\text{Ce}_{0.9}\text{Gd}_{0.1}\text{O}_{1.95}$ .*

Yttria stabilized zirconia ( $\text{Y}_{0.08}\text{Zr}_{0.92}\text{O}_{1.96}$ ) and ceria doped gadolinia ( $\text{Ce}_{0.9}\text{Gd}_{0.1}\text{O}_{1.95}$ ), commercial powders provided by Pi-Kem and Praxair, were tested to investigate their electrochemical performance.

Impedance spectroscopy technique was used to investigate the performance of two commercial powders of electrolyte materials both under air atmosphere and reducing atmosphere (5% hydrogen). A pellet with a diameter of 1.3mm and thickness of 2.0mm was manufactured using a uniaxial static press, after which pellets were sintered at  $1400^\circ\text{C}$  for 5 hrs. The sintering parameters were studied by dilatometry Netzsch DIL 402 C, while the bulk density of 96% was measured by the Archimedes method. The two platinum electrodes were painted, dried at

room temperature for 1hr and sintered at 900°C for 2hrs. The density of the pellet was investigated by SEM analysis as shown in the figure below:

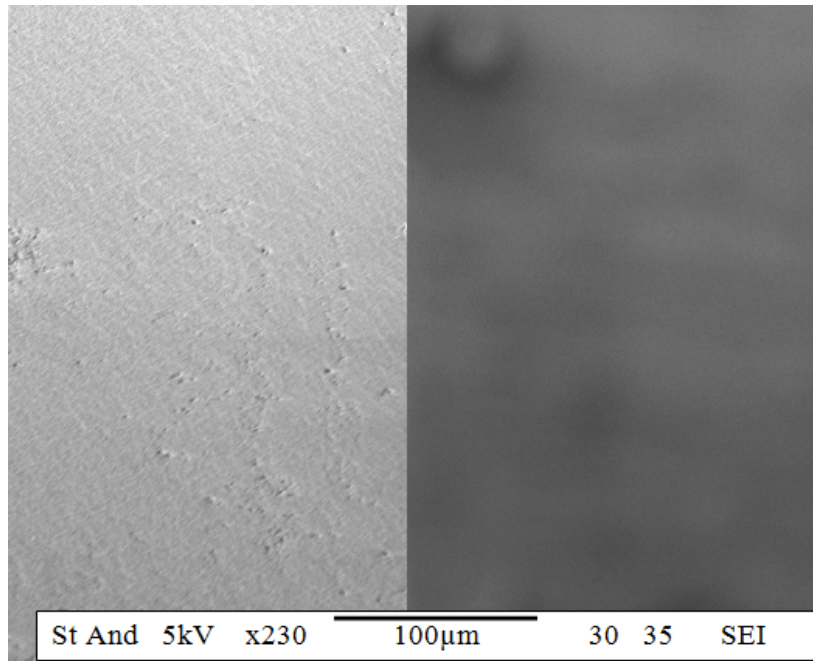


Figure 5.3- SEM picture of cross-section of GDC electrolyte pellet sintered at 1400°C.

The impedance spectroscopy tests were carried out using a Solatron 1260 in a range of frequencies between 0.1Hz and  $10^6$  Hz.

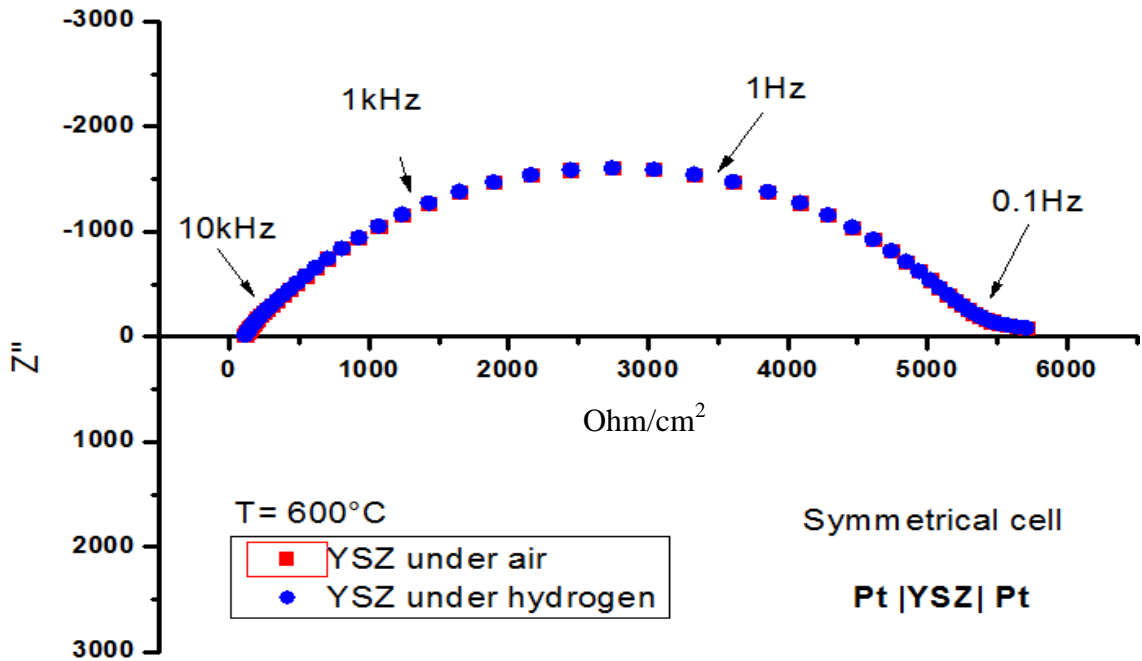


Figure 5.4- Impedance spectra of a symmetrical cell composed of YSZ pellet sintered at 1400°C for 5hrs and two platinum electrodes which were sintered at 900°C for 2hrs. The impedance tests were carried out both under air and 5% hydrogen.

The same tests were carried out for the commercial powder of GDC electrolyte.

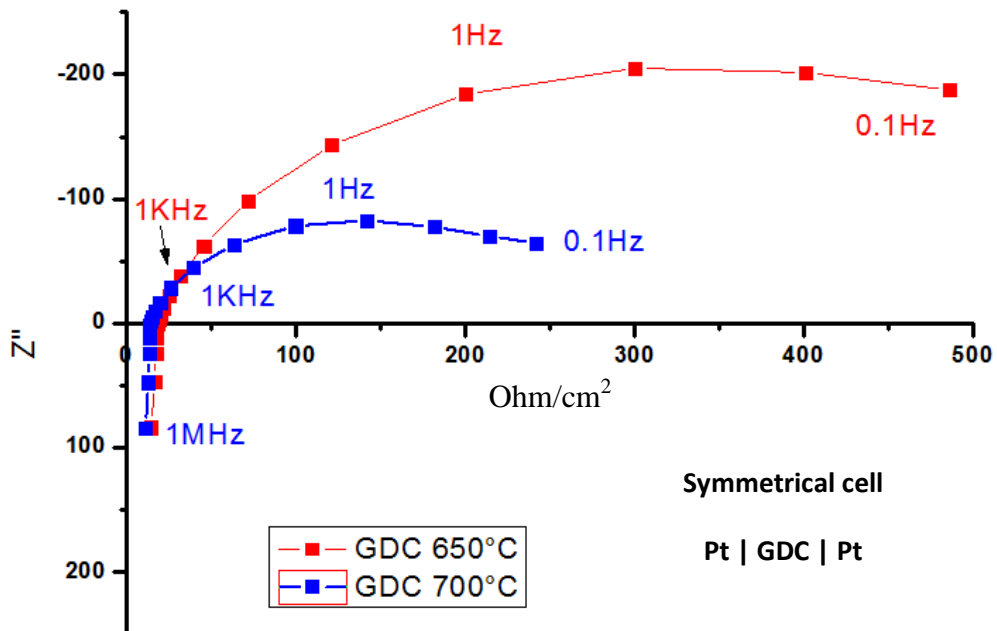


Figure 5.5- Impedance spectra of symmetrical cell composed of a GDC pellet sintered at 1400°C for 5hrs and two platinum electrodes which were sintered at

900°C for 2hrs. The impedance tests were carried out under air at 650°C and 700°C.

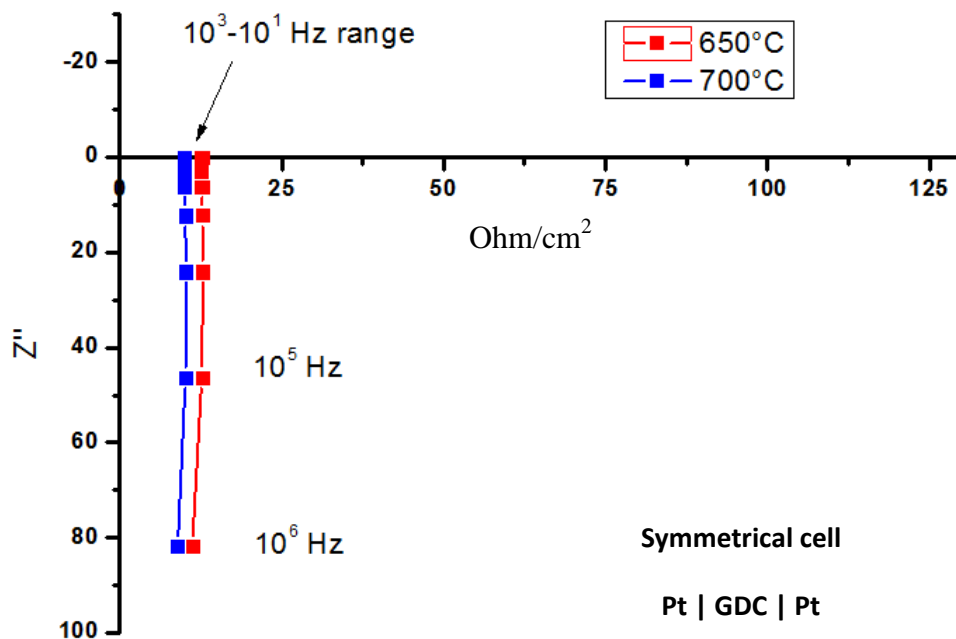


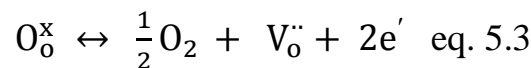
Figure 5.6- Impedance spectra of symmetrical cell composed of a GDC pellet sintered at 1400° for 5hrs and two platinum electrodes which were sintered at 900°C for 2hrs. The impedance tests were carried out under 5% hydrogen at 650°C and 700°C.

The behaviour of GDC electrolyte under hydrogen is visibly different from YSZ electrolyte. In fact, the impedance spectrum of GDC achieved under hydrogen shows a complete absence of the polarization arcs produced by two platinum electrodes. This behaviour can be attributed to the reduction of  $\text{Ce}^{4+}$  to  $\text{Ce}^{3+}$  that increases the GDC capacity for electron conductivity at high temperatures. This phenomenon was expected because it has been observed by many scientists [124-127].

5.1.1.2. *Reduction studies of Ce<sub>0.9</sub>Gd<sub>0.1</sub>O<sub>1.95</sub> under 5% hydrogen*

YSZ and GDC materials are both membranes with high ionic conductivity caused by the oxygen vacancies in their structure, as explained previously. YSZ material is completely stable under a hydrogen atmosphere and so it is the standard membrane used in the solid oxide fuel cell.

Instead, GDC electrolyte is unstable in a hydrogen atmosphere because cerium (IV) is easily reduced to cerium (III) under a reducing environment in accordance with reaction 5.3:



The reduction of ceria was studied in the TGA under hydrogen in order to measure the degree of reduction of ceria (IV) that is directly proportional to the oxygen vacancies produced under reducing atmosphere as shown in the equation eq. 5.4:



Where  $\delta$  is the variation of oxygen in the ceria doped gadolinia structure.

$\delta$  is easily calculable from the percentage weight loss achieved by TGA at 800°C under 5% of hydrogen. In fact, the variation in weight is related to the formation of oxygen vacancies that are in stoichiometric ratio 1:2 with ceria, in accordance

with equation 5.3. The weight loss achieved after testing GDC at 800°C under 5% hydrogen was equal to 0.77% (initial mass 17.815 mg – residual mass 17.678mg).

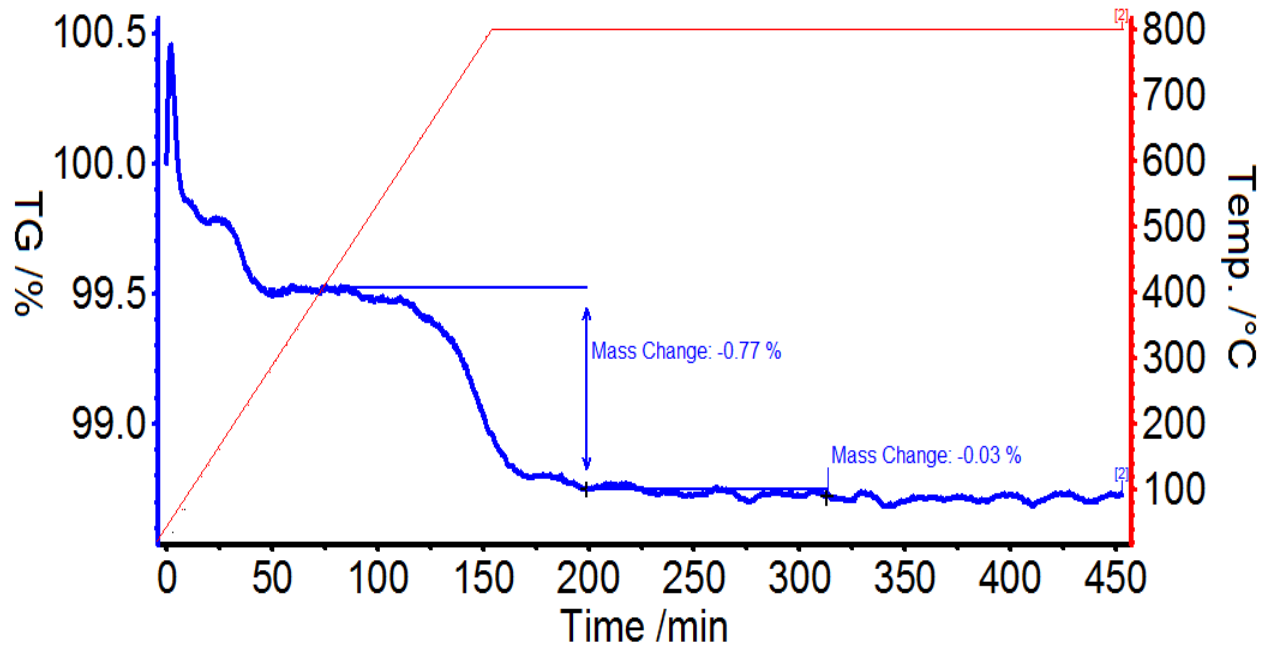


Figure 5.7- Studies of reduction ceria materials under 5 % hydrogen. Temperature was increased using a ramp rate of 5°C/min under a flow of hydrogen of 25ml/min.

The number of moles of oxygen calculated from the weight loss shown in the thermogram is equivalent to 0,083 mole of oxygen. This means that the reduction of  $\text{Ce}^{4+}$  to  $\text{Ce}^{3+}$  under reduction environment is very marked. This result confirms the partial electron conductivity provided by GDC under reducing atmosphere. Moreover, it also explains the absence of arcs in the impedance spectrum of GDC under reducing condition.

### 5.1.2. Anode

In the commercial solid oxide fuel cell, the anode used is a composite material consisting of two phases: a ceramic and a metallic phase. The widespread use of this composite anode as the commercial anode for SOFC is due to different factors: Firstly, YSZ impedes the grain growth of nickel. Secondly, YSZ reduces the TEC value of pure nickel, which is too high to be used in direct contact with the electrolyte. In fact, this mismatch creates high stress on the electrolyte causing cracks on the electrolyte (YSZ:  $11 \times 10^{-6} \text{ K}^{-1}$ ) and (Ni:  $17 \times 10^{-6} \text{ K}^{-1}$ ). In general, the metallic oxide used is nickel oxide, while the ceramic part is yttria stabilised zirconia (yttria 13%). In addition, it is a low cost material with high catalytic performance when hydrocarbons are used. Given the good compatibility between YSZ and Nickel, as well as the low cost of the anode, it has been used as principle anode for commercial fuel cells [128-131].

At the University of St Andrews, a new composition of anode has been studied. In fact, the ceramic phase composed of YSZ was replaced with GDC for two reasons: Firstly, to prevent an increase of interface resistance due to a possible reaction between YSZ contained in the anode and GDC electrolyte and secondly because GDC is a better hydrocarbon catalyst than YSZ [97][98][132-134].

#### 5.1.2.1. Studies of compatibility of different compositions of NiO-GDC

A standard commercial anode for application in SOFC is generally composed of 40% volume of ceramic phase such as YSZ or GDC and 60% of a metal oxide

---

such as NiO, which is reduced to nickel metal in situ. At the University of St Andrews, three different compositions of NiO–GDC (60/40, 70/30 and 80/20) were also investigated (see in A1 preparation slurry for tapes).

Anodes with different formulations were prepared by conventional tape casting process, casting a tape 120  $\mu\text{m}$  thick. Tapes were dried and used to prepare the tape for shrinkage tests. Tests were carried out on square tapes 2.5cm for 2.5 cm that had been previously cut and assembled.

The shrinkage of each tape was observed, measuring the variation in length as well as the significant reduction of the area of a square tape, that were caused by thermal treatment of 5 layers laminated together. Samples were measured both in the first thermal treatment and in the second treatment, as shown in figure 5.8:

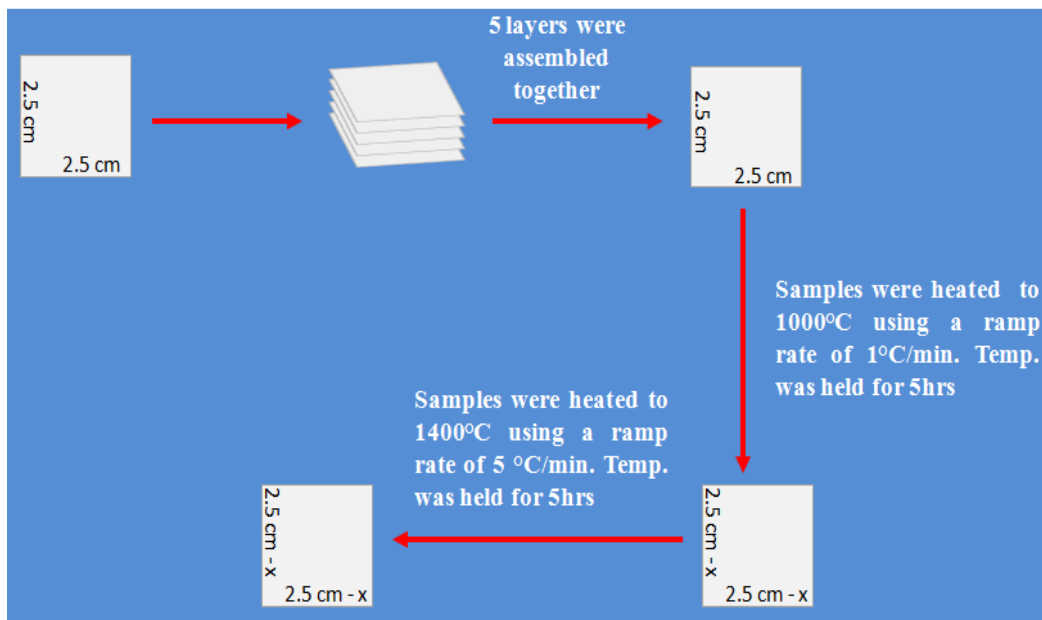


Figure 5.8- Schematic description of procedure methods used to determine the percentage of shrink for the square tape of anode at different compositions.

Sample	Area	A step	% Astep1	A step2	A%step2
A 8020	6.25	5.90	5.6	5.11	<b>18.24</b>
A 7030	6.25	5.96	4.6	5.27	<b>15.68</b>
A 6040	6.25	6.01	3.8	5,35	<b>14.40</b>

Table 5.1- Shrinkage of the three different anodes, measured after the final thermal treatment carried out at 1400°C holding the final temperature for 5h.

The same tests were carried out on the electrolyte tape, measuring a value of 15% at 1400°C and this result confirms that GDC ( $TEC=12.0 \times 10^{-6} K^{-1}$ ) reduces the TEC value of NiO ( $TEC= 15 \times 10^{-6} K^{-1}$ ).

The different tapes were analysed using X-ray diffraction after sintering in order to verify the absence of reaction between NiO and GDC.

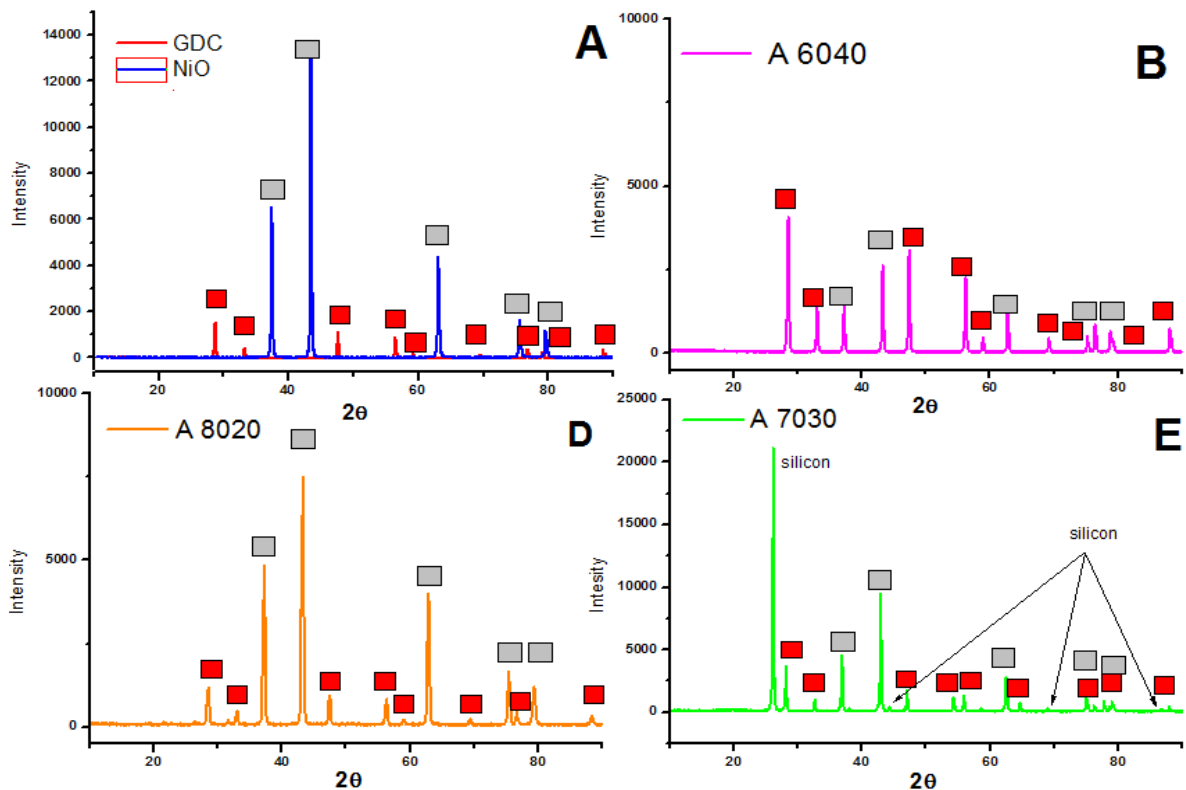


Figure 5.9- X-ray spectra of NiO-GDC anode at different compositions a) single component pure phase b) 60-40 in volume ratio c) 70-30volume d) 80-20 volume.

The x-ray spectra do not show any extra peaks due to the possible reaction between NiO–GDC. However, four extra peaks are observable in the composition 70-30 at 26, 44, 69 and 86. The extra peaks come from the silicon used to mount the tape. These peaks were investigated by PDF database and they match those peaks.

#### 5.1.2.2. *Studies of electrical performance of anode with different composition*

After conducting structural analysis of each anode with different configurations, impedance spectroscopy tests were carried out on symmetrical cells under hydrogen atmosphere (5% hydrogen humidified).

Symmetrical cells were prepared, laminating four circular layers of previously assembled GDC electrolyte (diameter 1.8 cm thickness of 120 $\mu$ m single layer) and a single anode NiO-GDC (diameter 1.2cm-tickness 60  $\mu$ m) layer either side of the electrolyte, as shown in the figure:

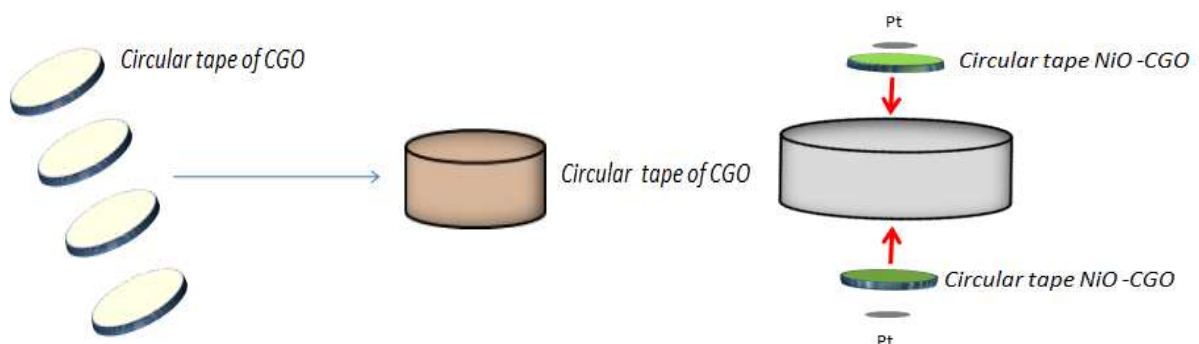


Figure 5.10- Schematic description of assembly of a symmetrical cell composed of GDC electrolyte and anode co-sintered at 1400°C on both sides.

---

The symmetrical cells were then sintered at 1400°C for 5 h and the platinum current collectors were painted and sintered at 900°C for 2h.

The performance of the cell was tested at 550°C, 600°C and 650°C respectively both for the anode with 60-40 and 80-20. Under the reduction atmosphere, the nickel oxide is reduced to nickel metal, which makes the electrons conductive. However, nickel is not the only part which is reduced. In fact, ceria (IV) is also reduced to Ce (III) and it gives an electron contribution, so the equivalent circuit that is able to simulate the AC impedance arc is represented by the figure 5.11 below:

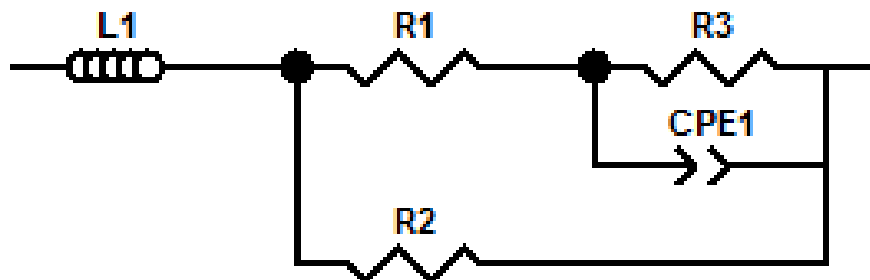


Figure 5.11- Equivalent circuit of hypothesised for a symmetrical cell consists of a GDC electrolyte and two NiO-GDC electrodes.

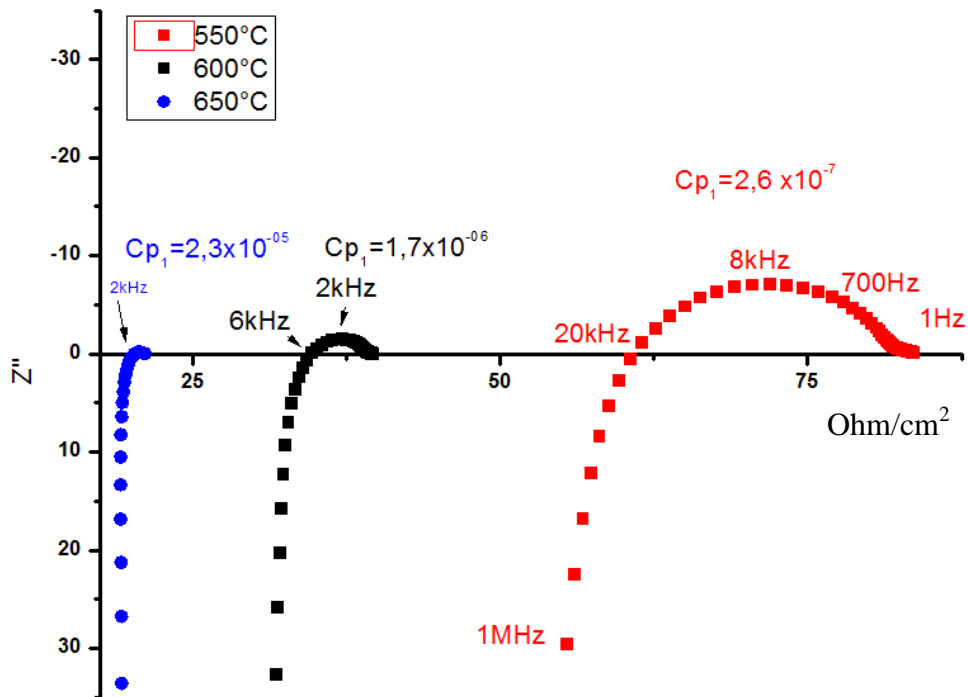


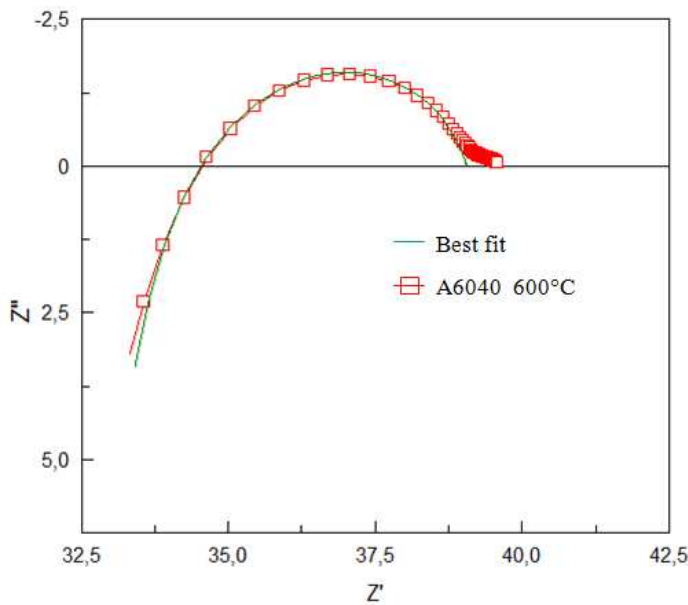
Figure 5.12- Impedance spectrum of symmetrical cell consists of a GDC electrolyte tape 480 $\mu$ m thick and two NiO-GDC anodes with composition 6040 co-sintered at 1400 $^{\circ}$ C for 5h. Two platinum current collectors were painted and sintered at 900 $^{\circ}$  C for 2h. Tests were carried out at 550 $^{\circ}$ C, 600 $^{\circ}$ C and 650 $^{\circ}$ C respectively during the heating ramp applying a voltage of 50mV amplitude.

In the schematic circuit three different resistances can be observed. R1 and R3 are the resistance provided by the ion conductivity, while R2 represents the resistance provided by the electrons formed during reduction. The R2 value decreases, increasing the reduction effect and temperature. An example of simulation was made using Zview software for the arc at 550 $^{\circ}$ C and 600 $^{\circ}$ C of the symmetrical cell with anode composition 60/40.

Temp	L1	R1(Ohm)	R3(Ohm)	R2(Ohm)	CPE(F)
600°C	1E-6	33.9	7.3	750	0.84
550°C	9.7E-5	59	28.8	1300	0.69

Table 5.2- Simulation of an equivalent electrical circuit carried out on the impedance spectra at 500°C and 600°C.

The same simulation was done for the AC impedance at 550 and 650°C. The most significant result was the decrease of R2 from 1300 Ω to 750 Ω.



Fit data obtained by Zview

Component	Resistance value (Ohm)
L1	1 E-6
R1	33.9
R2	750
CPE1	0.84
R3	7.3

Figure 5.13- Impedance spectrum symmetrical cell with anode composition NiO-GDC 60/40 at 600°C fitted using Zview software hypothesising the equivalent circuit shown in figure 5.11.

This effect is strongly marked when the amount of NiO in the anode composition is 80%. In fact, the arc is totally reduced at 550°C, as shown in figure 5.14:

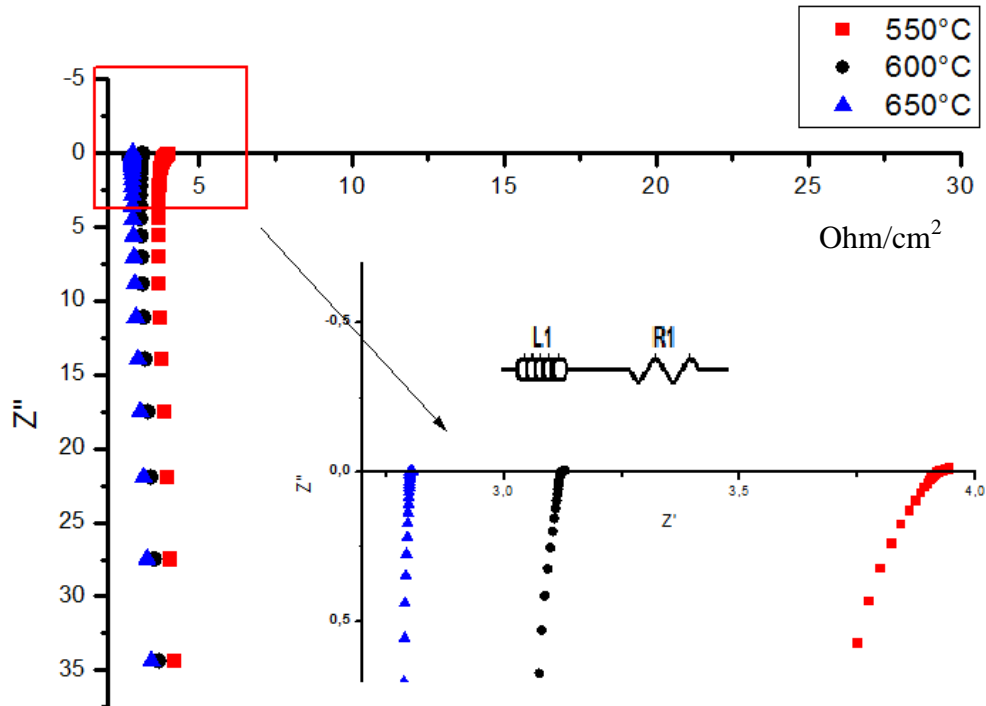


Figure 5.14- Impedance spectrum of symmetrical cell consists of a GDC electrolyte tape 480 $\mu\text{m}$  thick and two NiO-GDC anodes with composition 80/20 co-sintered at 1400 $^{\circ}\text{C}$  for 5h. Two platinum current collectors were painted and sintered at 900 $^{\circ}\text{C}$  for 2h. Tests were carried out at 650 $^{\circ}\text{C}$ , 600 $^{\circ}\text{C}$  and 550 $^{\circ}\text{C}$  respectively during cooling ramp, applying a voltage of 50mV amplitude under hydrogen.

By analysing the AC impedance at 550 $^{\circ}\text{C}$ , it is clear that the polarization arc was cancelled by the high electronic conductivity provided by the nickel metal and the reduction of ceria electrolyte and ceria in the anode. High electron conductivity caused a short circuit phenomenon, in turn decreasing the ohmic resistance. Furthermore, the amount of GDC in the anode is not enough to provide good percolation between the anode and electrolyte. In fact, there were a large number of cracks at the end of test due to bad percolation between anode and electrolyte. This could be another factor which affected the performance of the anode.

The symmetrical cell with anode 70/30 showed intermediate behaviour between the anode with composition 60/40 to 80/20. The arc is maintained because GDC material is enough to guarantee percolation between the anode and the electrolyte interface. The AC spectrum is shown in figure 5.15:

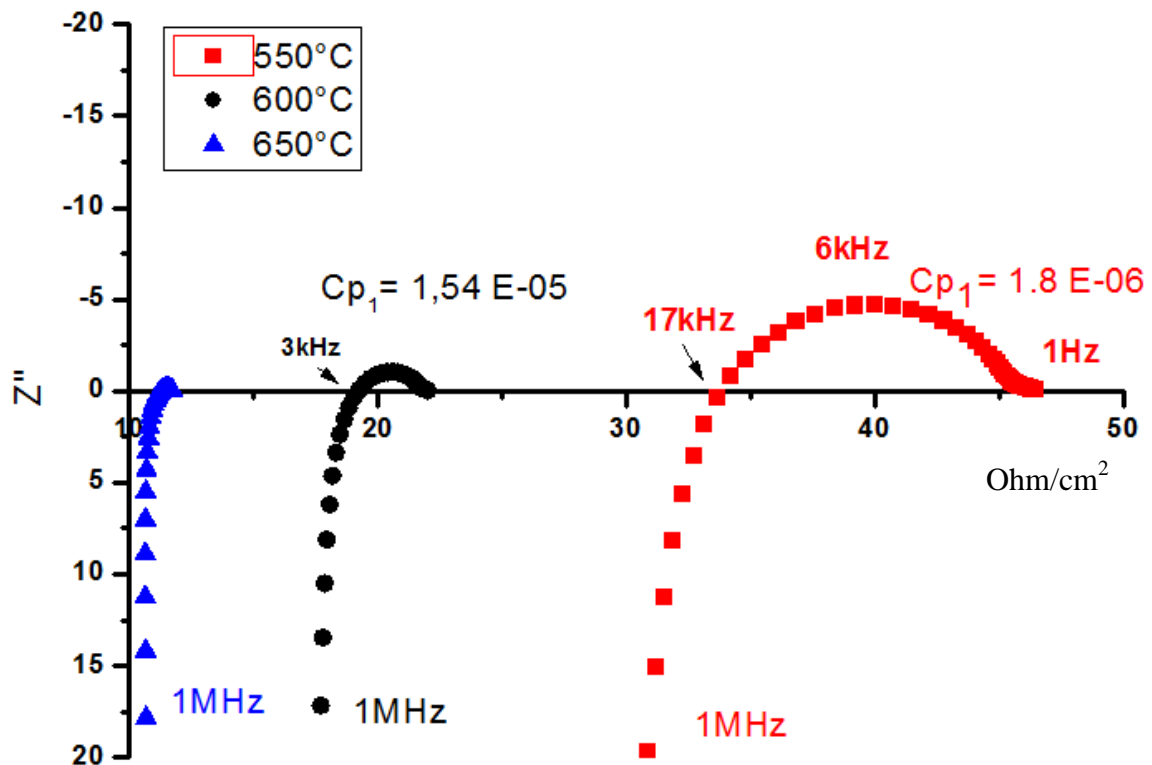


Figure 5.15- Impedance spectrum of symmetrical cell consists of a GDC electrolyte tape 480 $\mu$ m thick and two NiO-GDC anodes with composition 70/30 co-sintered at 1400°C for 5h. Two platinum current collectors were painted and sintered at 900° C for 2 hrs. Tests were carried out at 550°C, 600°C and 650°C respectively applying a voltage of 50mV amplitude.

The best compromise seemed to be the anode of 70/30 composition because it produced high porosity during the reduction of nickel, increasing the TPB and consequently the performance of the anode.

The data were confirmed by measuring the density of the two different anodes after reduction using the Archimedes method. The density is inversely proportional to the porosity. The values obtained from the anode were 43% and 51% porosity respectively for the anodes with 60/40 and 70/30 composition.

### 5.1.3. Cathode

The cathode used in commercial solid oxide fuel cells is Lanthanum Strontium Manganese Oxide ( $\text{La}_{0.8}\text{Sr}_{0.2}\text{MnO}_3$ ), a perovskite typically used in combination with YSZ to improve both the physical contact between cathode and electrolyte and the TPB area [135-142]. This cathode is used particularly in solid oxide fuel cells because of its high compatibility with YSZ electrolyte when it is sintered at a temperature of 1200°C, because Gorte and co-workers demonstrated that at over 1300°C, a solid state reaction takes place, reducing the performance of the cathode[113].

In the next paragraph, studies of LSM-YSZ and LSM-GDC cathodes, different methodologies of cathode preparation and a new cathode will be illustrated and compared.

#### 5.1.3.1. Studies of LSM-YSZ and LSM-GDC cathodes

Two different formulations for the tape casting process were prepared mixing commercial Lanthanum Strontium Manganese Oxide ( $\text{La}_{0.8}\text{Sr}_{0.2}\text{MnO}_3$ ) with YSZ

---

or GDC material. Two tape formulations consisting of LSM-GDC and LSM-YSZ were cast using a tape casting machine.

The symmetrical cell with two different cathodes was prepared following the procedure previously illustrated for anodes in figure 5.10.

The symmetrical cells were tested in oxygen and at a range of temperatures between 550°C and 650°C, collecting the ac data during both the heating ramp and cooling ramp.

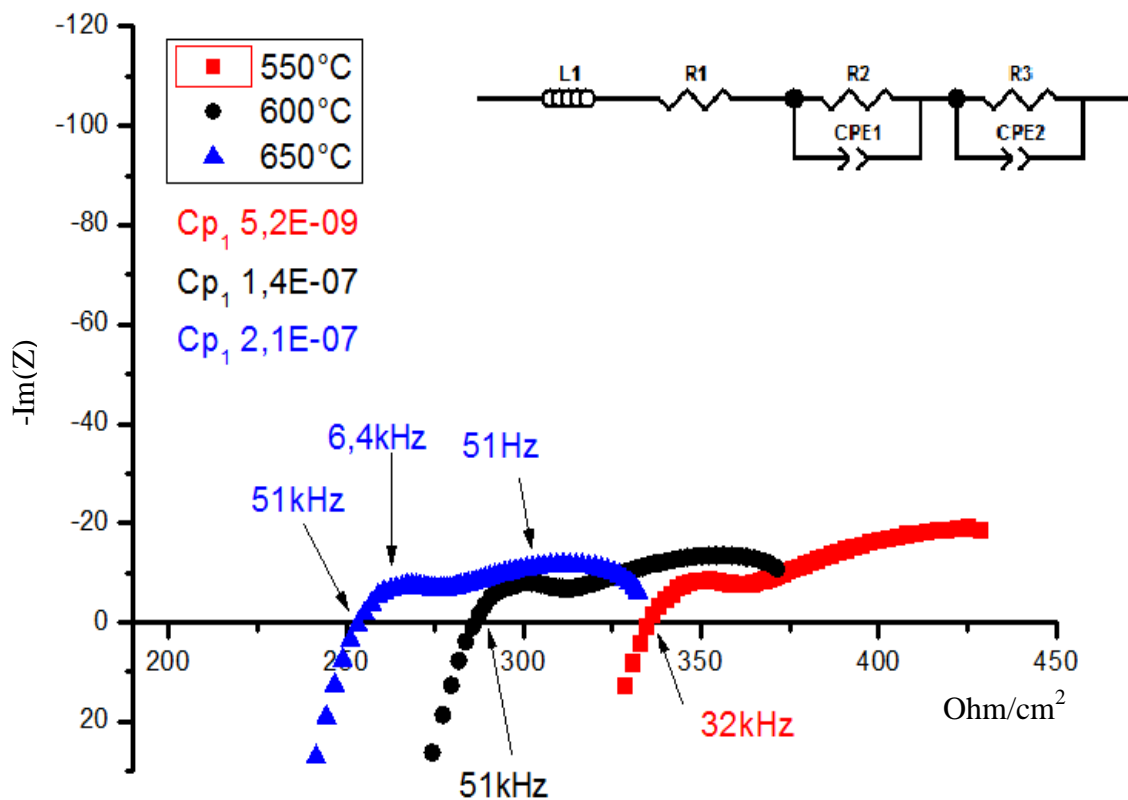


Figure 5.16- AC impedance spectrum of symmetrical cell consists of a GDC electrolyte and two electrodes with composition of 50/50 LSM-YSZ. The symmetrical cells were co-sintered at 1400°C for 5h and AC impedance tests were carried out at a range of temperatures between 550°C and 650°C during heating ramp, applying a voltage of 50mV amplitude under air.

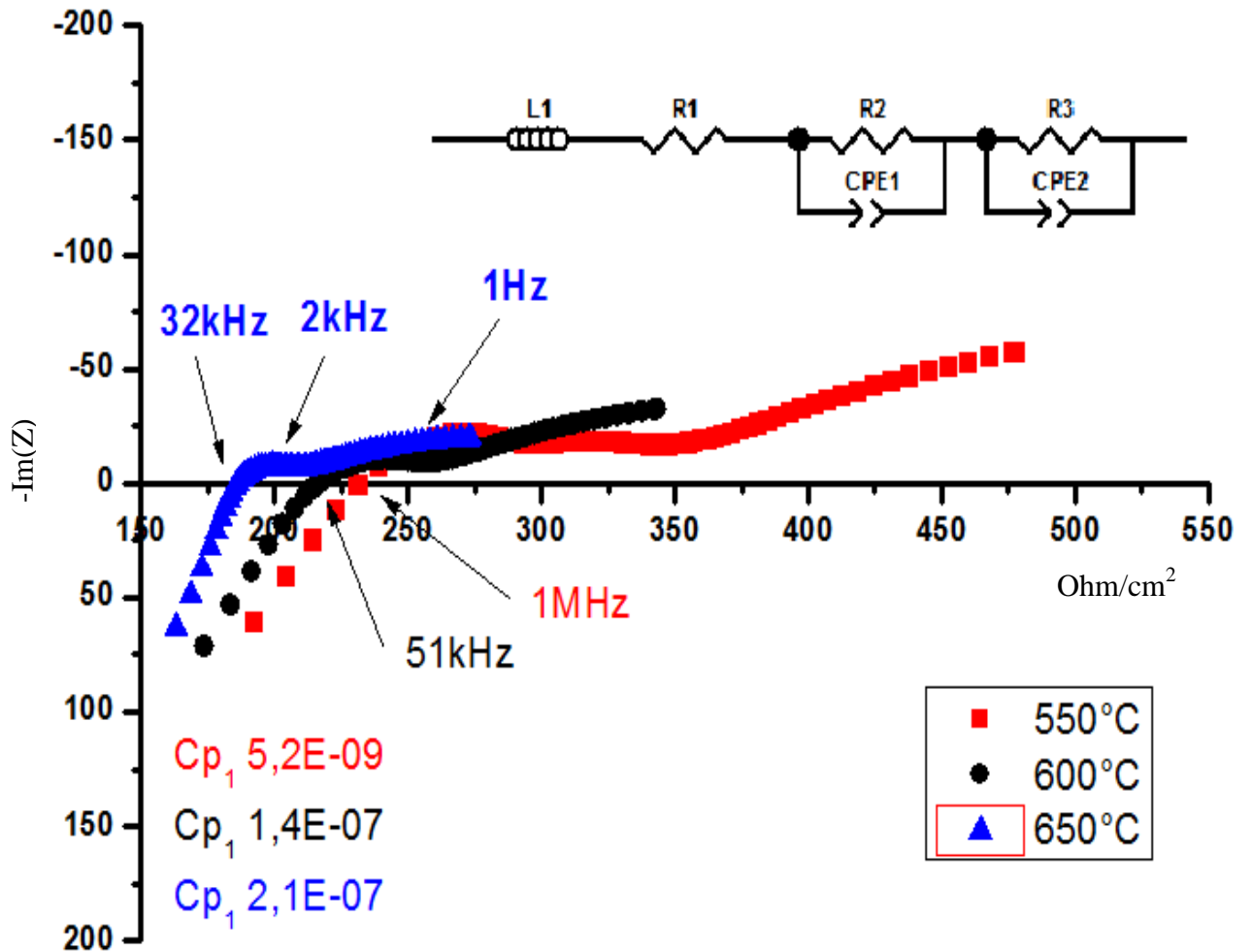


Figure 5.17- Impedance spectrum of symmetrical cell consists of a GDC electrolyte and two electrodes with composition of 50/50 LSM-YSZ. The symmetrical was co-sintered at 1400°C for 5h and AC impedance tests were carried out at a range of temperatures between 650°C and 550°C during the cooling ramp, applying a voltage of 50mV amplitude under air.

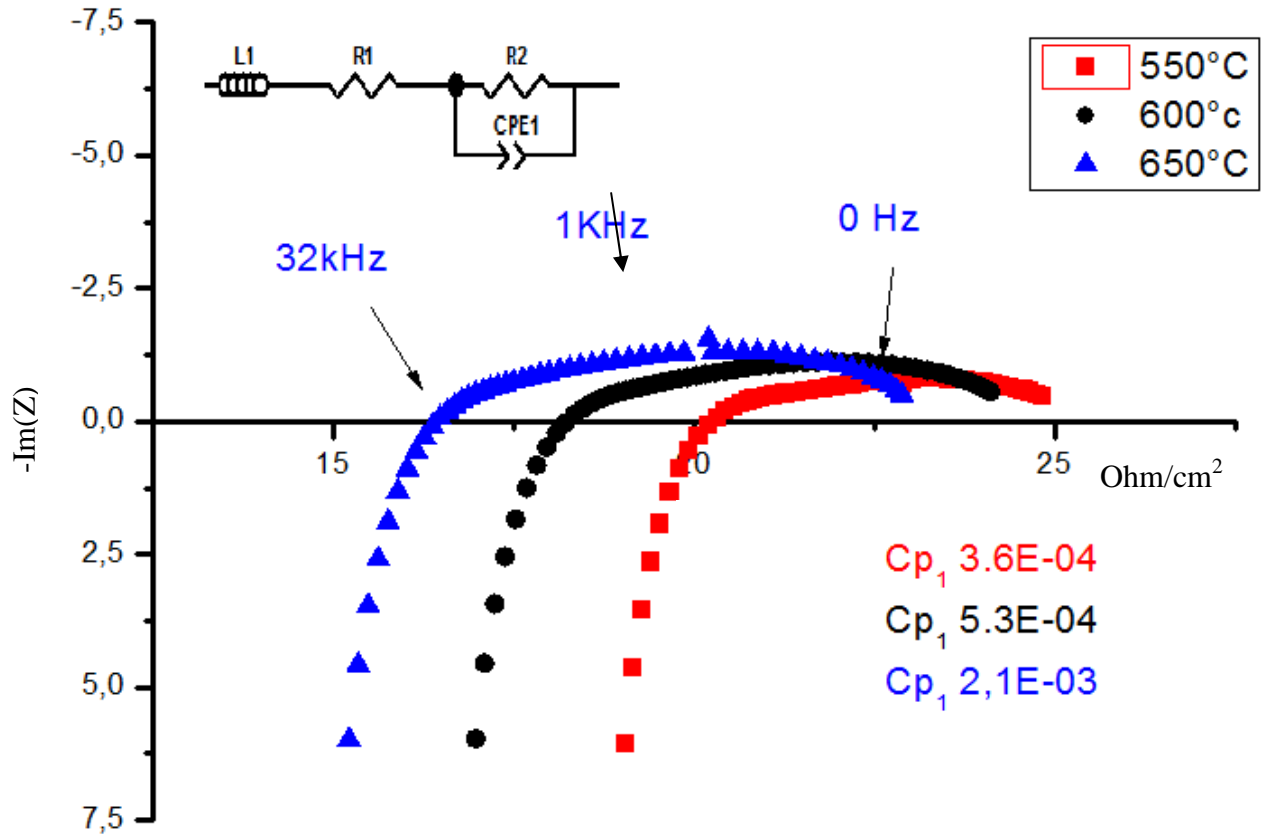


Figure 5.18- Impedance spectrum of symmetrical cell consists of a GDC electrolyte and two electrodes with composition of 50/50 LSM-GDC. The symmetrical cell was co-sintered at 1400°C for 5h and AC impedance tests were carried out at a range of temperatures between 550°C and 650°C during the heating ramp, applying a voltage of 50mV amplitude under air.

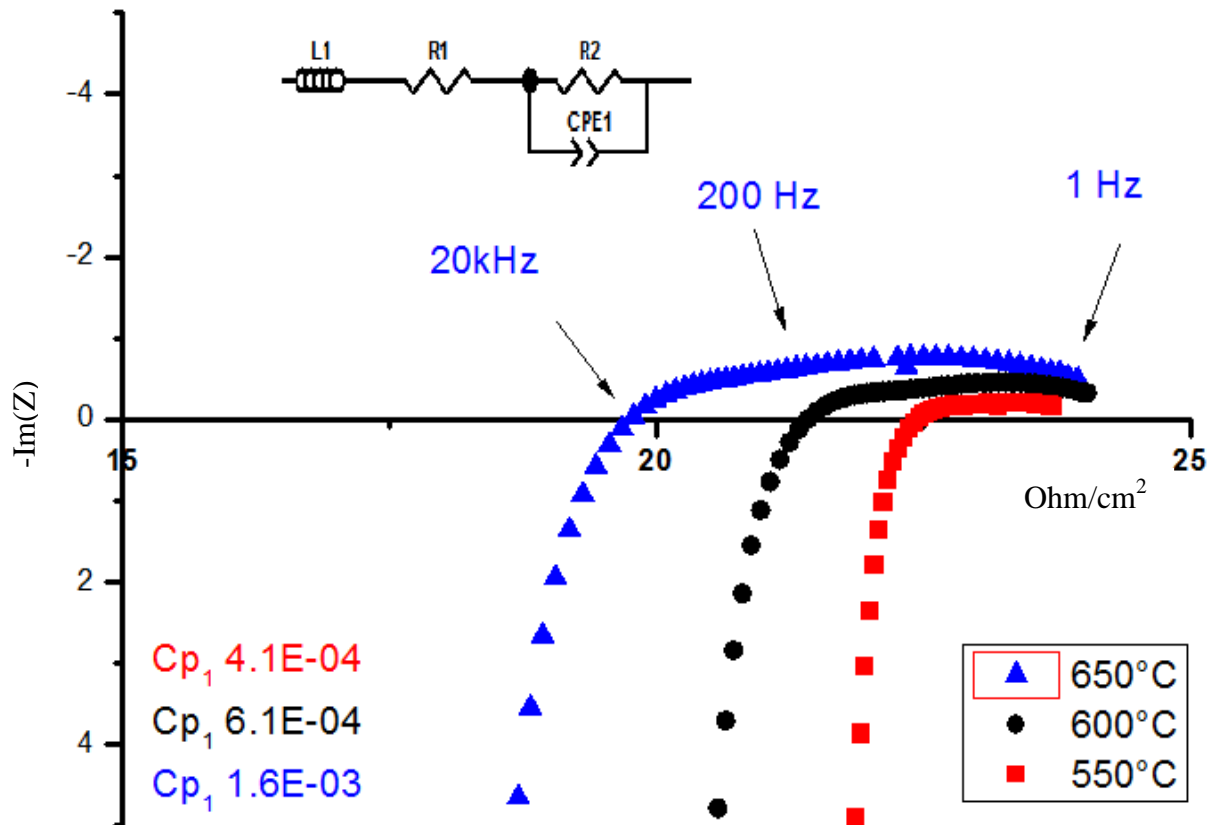


Figure 5.19- Impedance spectrum of symmetrical cell consists of a GDC electrolyte and two electrodes with composition of 50/50 LSM-GDC. The symmetrical cell was co-sintered at 1400°C for 5h and AC impedance tests were carried out at a range of temperatures between 650°C and 550°C during the cooling ramp, applying a voltage of 50mV amplitude under air.

Analysing the AC impedance spectra shown above, the differences in  $R_s$  and  $R_p$  between the two cathodes tested (LSM-GDC and LSM-YSZ) are clearly observable. The most indicative difference is given by the polarization arc, which is the most important analytic value to understand the performance of a cathode. Instead, the value of  $R_s$  could give information on the interface between cathode and electrolyte.

These differences in  $R_s$  and  $R_p$  can be attributed to several factors: Firstly the value of  $R_p$  could be due to a possible solid state reaction between LSM and YSZ caused by the high sintering temperature 1400°C as demonstrated by Gorte et al and Gauckler et al. In fact this solid state reaction can increase the polarization contributions provided by the cathode[131-132]. However, the high temperature could also reduce the cathode porosity, decreasing the TPB. Secondly, the LSM-YSZ cathode is directly connected to a GDC electrolyte, which reacts with YSZ during the sintering process, creating an additional interface resistance between the electrolyte and cathode, as explained by Takawa [142].

The last phenomenon can explain the substantial difference in ohmic resistance achieved between LSM-GDC cathodes.

This effect was not visible for LSM-GDC cathode, which has demonstrated good performance, even though it was processed under the same conditions as LSM-YSZ cathode.

However, as said previously, secondary effects such as porosity and sintering temperature can affect the performance of the cathode and thus the overall performance of the cell.

For this reason, studies on the methodologies of cathode manufacture were changed. In fact, cell manufactured by tape casting requires that each component is co-sintered. GDC electrolyte and NiO-GDC have a comparable sintering

---

temperature while LSM-YSZ cathode must be sintered at 1200°C in order to achieve good performance.

### 5.1.3.2. *Studies of LSM-GDC tape and painted LSM-GDC*

As explained previously, the sintering temperature is an important parameter that can affect the performance of the cathode. In fact, it can reduce the porosity of the cathode, influencing the gas diffusion. In addition, the bulk density is a direct function of the temperature and high bulk density decreases the TPB, influencing the performance of the cell. For this reason, the methodology of cathode manufacture was changed.

An LSM-GDC ink was prepared in order to paint the cathode on the surface of the GDC electrolyte. This methodology was faster and easier than impregnation, especially for large surfaces, such as a long tube.

The LSM-GDC ink was painted onto the sintered electrolyte and then sintered at a temperature of 1200°C for 3hrs, while the current collector was sintered at 850°C in the second step, as shown in figure 5.20:

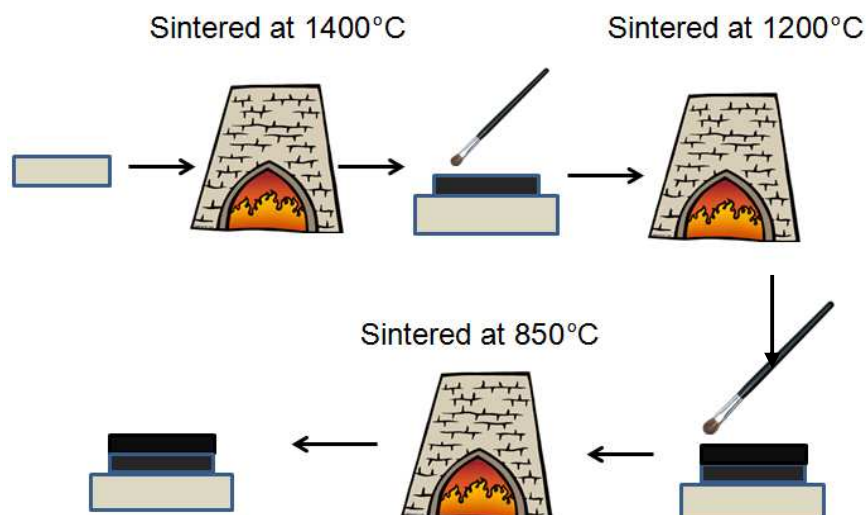


Figure 5.20- Schematic description of the painting manufacture process of a GDC pellet previously sintered at 1400°C.

The AC impedance test was carried out using a double jig with two sets of electrodes so as to be able to test two different samples at the same time. This is very important because it guarantees that both samples are tested at the same temperature. Two samples, a pellet of GDC co-sintered with LSM-GDC cathode and a GDC pellet with painted cathode, were tested simultaneously. AC impedance results obtained are shown below:

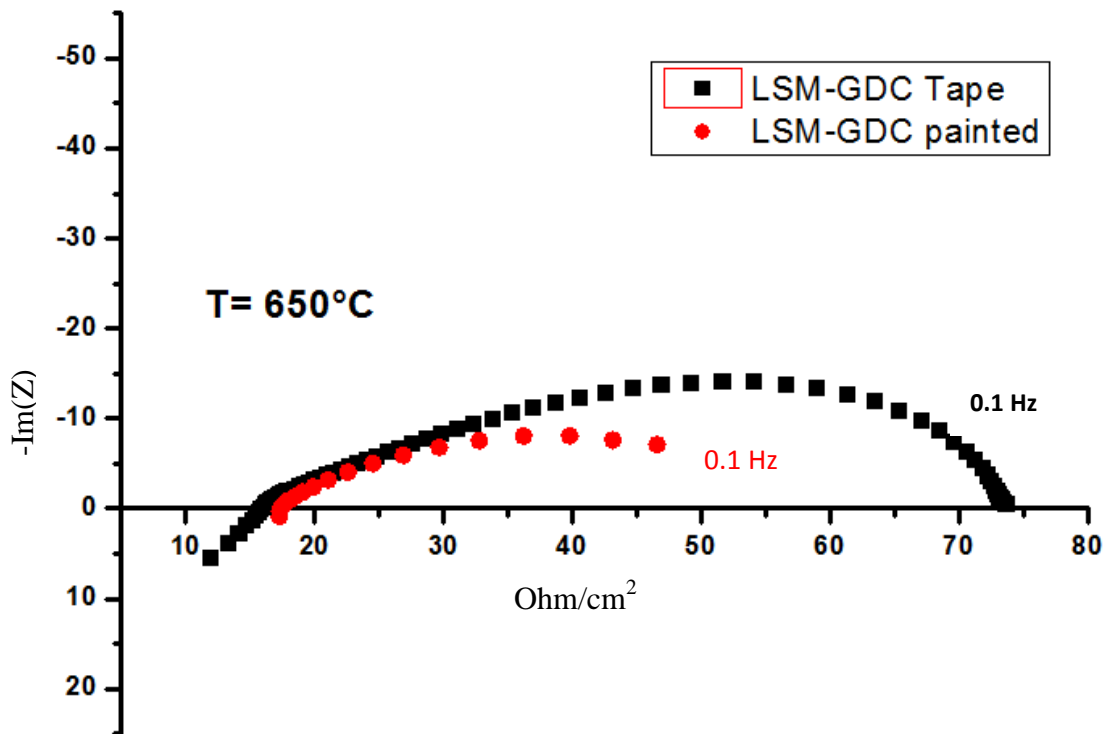


Figure 5.21- AC impedance spectrum of symmetrical cell composed of GDC electrolyte and LSM-GDC painted cathode, compared to the same symmetrical cell with painted LSM-GDC. Tests were carried out at  $600^\circ\text{C}$  applying a voltage of 50mV amplitude.

The polarization arc of the symmetrical cell with LSM tape is larger than the symmetrical cell with the LSM painted cathode. This can be attributed to the high porosity of the cathode and thus, to the faster gas diffusion process and large contact surface of the TPB, as shown in SEM pictures.

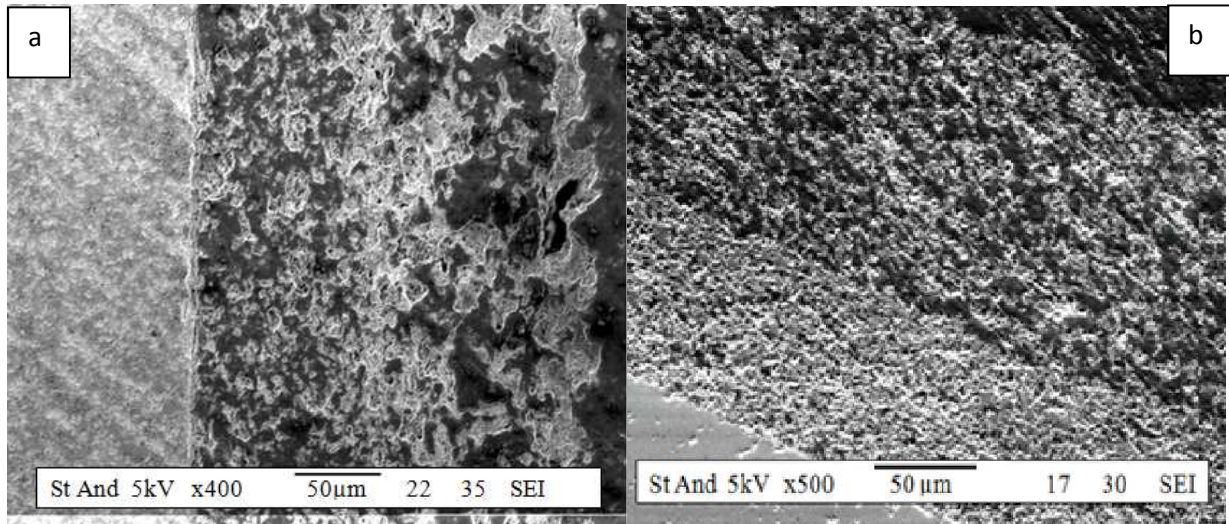
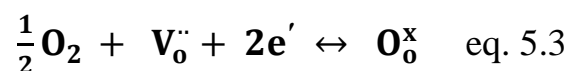


Figure 5.22- SEM picture of symmetrical cell with cathode and current collector  
 a) symmetrical cell with LSM-GDC cathode + LSM current collector tape  
 b) symmetrical cell with LSM- GDC cathode and LSM current collector.

The SEM images illustrate the higher shrink produced for the cell sintered at 1400°C than the cathode sintered at 1200°C. In addition, an evident interlayer line is visible between the cathode and the current collector.

### 5.1.3.3. Studies of LSM-GDC tape and painted LSCF-GDC

The cathode is a component which limits the performance of the whole cell because on its surface molecular oxygen is reduced to oxygen ions which pass through the electrolyte and anode to react with the fuel. The concentration of oxygen ions produced electro-catalytically by the cathode is governed by the reaction of eq.5.3.



The behaviour of the electro-catalyst material is limited by the diffusion constant  $D$  of each material at a given temperature, that is directly proportional to the flow of oxygen ions. LSM perovskite is a poor ion conductor and is electrochemically active in the TPB at high temperature ( $T > 800^\circ\text{C}$ ) and this is confirmed by the value of  $D$  measured from Steel et al. at  $700^\circ\text{C}$ , obtaining  $D = 1 \times 10^{-16}$  [143]. Hence an alternative cathode was investigated as a possible substitute for LSM perovskite.

A promising cathode for SOFC at intermediate temperature is perovskite material with cobalt and iron instead of manganese at the B site. It is a mixed ionic electronic conductive material and this increases the length of the TPB, raising the value of the diffusion constant  $D = 2.5 \times 10^{-09}$  [144]. This demonstrates that LSCF is a better electro-catalyst than LSM, due to the substitution of Sr and Fe in the  $\text{LaCoO}_3$  at sites A and B of the perovskite structure, which increases surface oxygen exchange and bulk diffusion characteristics [143]. In fact, an increase in the iron content at the B site creates positive holes while the substitution of Sr in the A site produces an increase in oxygen vacancy formation [145][146].

LSCF cathodes were investigated by AC impedance carried out on a symmetrical cell under an air environment so as to compare the performance of a commercial LSCF- GDC ink with LSM-GDC ink performance.

5.1.3.4. *Comparison of a commercial  $La_{0.4}Sr_{0.4}MnO_{3-\delta}$  and  $La_{0.4}Sr_{0.6}Co_{0.2}Fe_{0.8}O_{3-\delta}$*

Symmetrical cells were prepared using a pellet of GDC electrolyte sintered at 1410°C for 5h. Afterwards, two symmetrical cells were manufactured, painting a LSCF -GDC cathode (in ratio 60:40 %wt) on each side of the electrolyte pellet. One of these cells was then sintered at 1000°C for 3h, while the second cell was sintered at 1100°C for 3h. No current collector layer of pure LSCF was painted on the cell with the LSCF-GDC cathode because the performance of LSCF is decisively better than LSM. In addition, no current collector layer was painted in order to prevent any additional interlayer resistance.

AC impedance tests were carried out on the two different cells in which the cathode were sintered at 1000°C and 1100°C so as to investigate their performance. AC impedance tests were carried out keeping the parameter used for testing the symmetrical cell with LSM-GDC constant, in order to be able to compare the performance of three different cells.

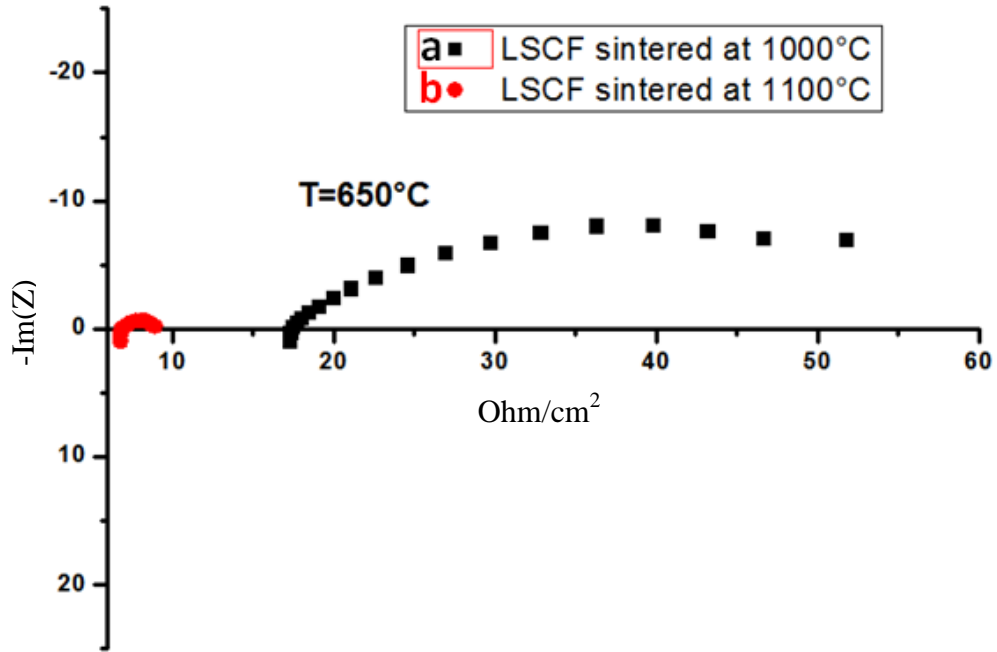


Figure 5.23- AC impedance spectra of symmetrical cell consisting of a pellet electrolyte sintered at  $1400^{\circ}\text{C}$  and two LSCF-GDC cathodes painted on both sides of GDC pellet. Cell (a) cathode was sintered at  $1000^{\circ}\text{C}$  while cell (b) cathode was sintered at  $1100^{\circ}\text{C}$  for 3hrs.

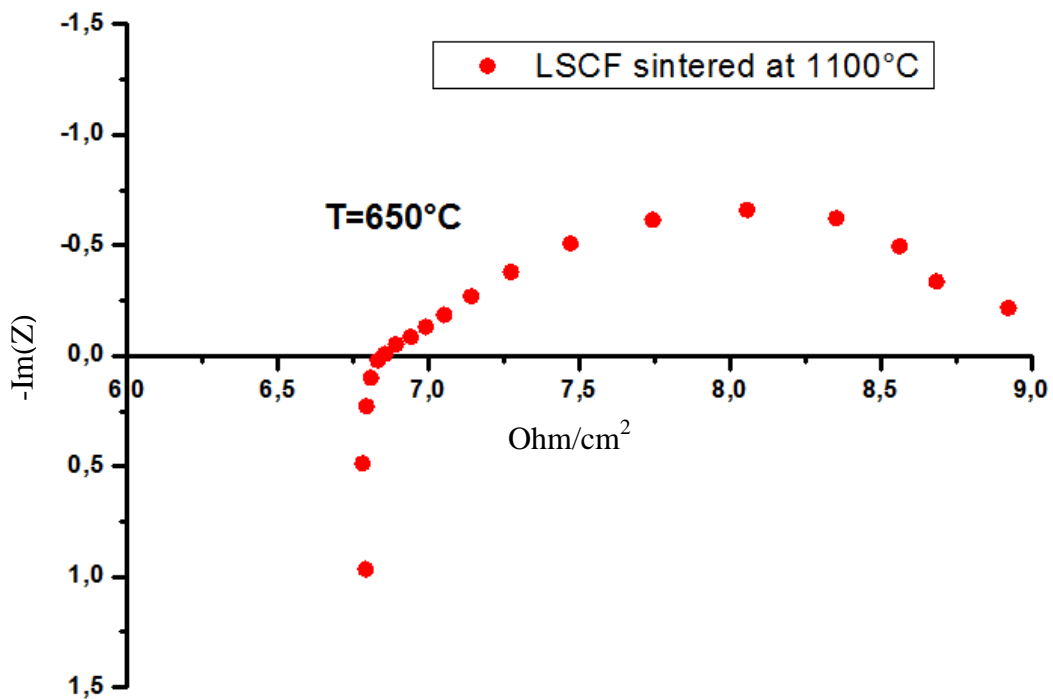


Figure 5.24- Zoom of AC impedance spectra of symmetrical cell (b) with LSCF-GDC cathode sintered at  $1100^{\circ}\text{C}$  for 3hrs.

The difference in  $R_s$  and  $R_p$  between cells (a) and (b) can be due to several factors. Analysis of cells (a) and (b) using an SEM instrument shows that in cell (a) there is not perfect adhesion between the cathode and electrolyte. This could mean that the temperature used in order to obtain a good interaction at the cathode and electrolyte interface was not enough to produce the desired effect, as shown in figure 5.25:

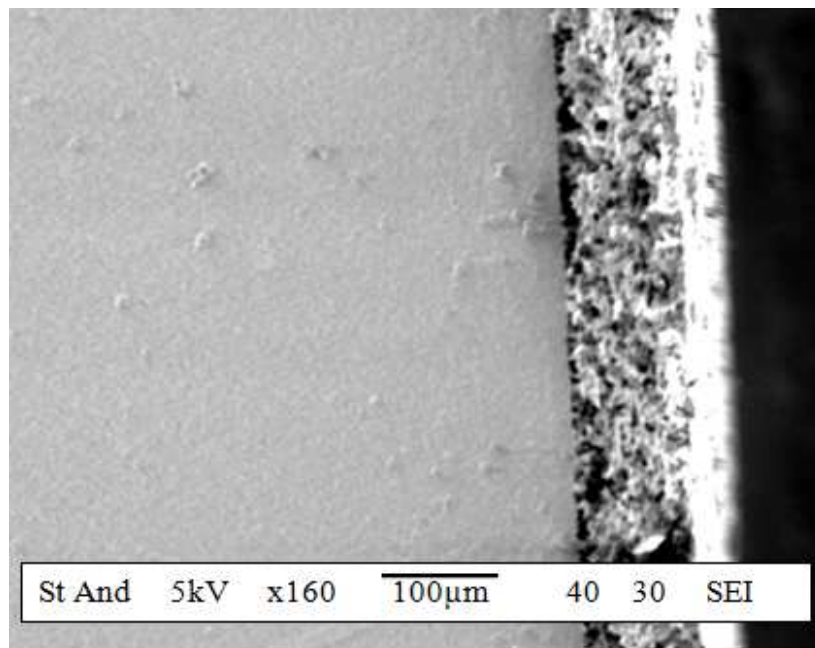


Figure 5.25- SEM pictures of symmetrical cells with LSCF-GDC cathode sintered at 1000°C for 3hrs.

This hypothesis was confirmed by analysis of cell (b). In fact, an increase of 100°C was sufficient to anchor the cathode to the electrolyte, as shown in figure 5.25(b).

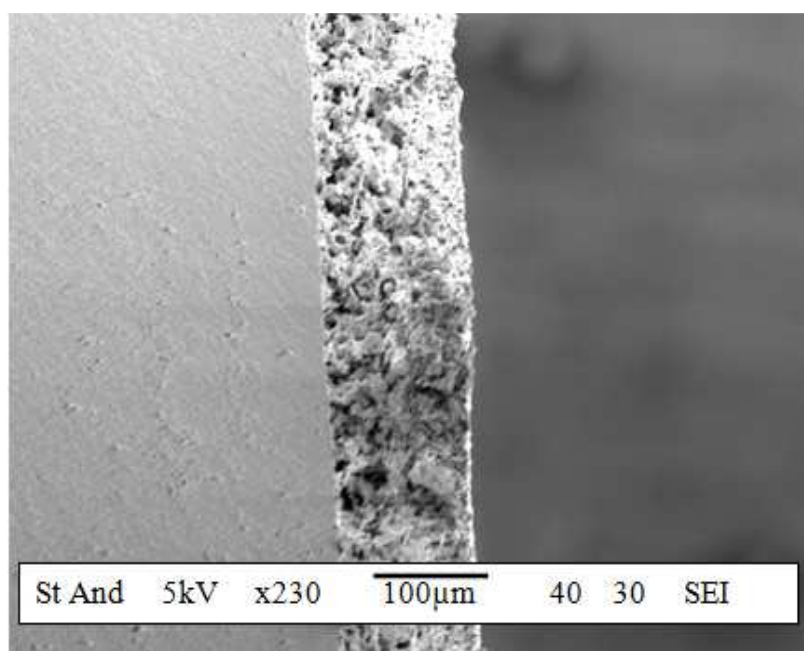


Figure 5.25- SEM pictures of symmetrical cells with LSCF-GDC sintered at 1100°C for 3hrs.

This can explain the substantial difference in  $R_s$  between cell (a) and (b) as well as the difference in  $R_p$ . However, this is not enough to explain the large difference in  $R_p$  shown by the two different cells.

This large difference can be attributed to the active surface of the cathode which is dependent on the temperature. In fact, the higher sintering temperature of cell b than cell a caused better sintering between the particles of GDC and LSCF

particles. The stronger interaction increased the active surface and consequently the TPB decreased the polarization resistance of the cathode.

By comparing the AC impedance spectra of the symmetrical cell with LSM-GDC cathode and the symmetrical cell with LSCF-GDC cathode, it is evident that the LSM -GDC cathode drastically limited the electrical performance of the cell.

## 5.2. Summary

AC impedance of symmetrical cells was carried out to study the electrochemical behaviour of the anode and cathode under different conditions.

The AC impedance carried out on the symmetrical cell with anodes at different compositions showed that a marked short circuit was observable under reducing atmosphere for the anode with high NiO content (80/20). This was due to the simultaneously reduction of NiO to Ni and Ce(IV) to Ce(III). This favoured the electron diffusion, producing a short circuit. The best compromise was reached using a composition of NiO – GDC (65/35 wt %).

Regarding the cathode investigations, it is possible to see that the manufacturing and the type of cathode play an important role on the performance of the cathode. In fact, the  $R_p$  value was further improved when the LSM-GDC cathode manufacturing process was altered, as well as when the LSM-GDC cathode was replaced with LSCF-GDC.

Starting from the manufacturing process and sintering temperature, it was evident that cells achieved better performance when the LSM–GDC cathode was painted and sintered separately from the anode and electrolyte. In fact, the low performance achieved by the cell with the co-sintered cathode was caused by the low porosity of the cathode, which was directly responsible for the decrease of the TPB. In fact, no solid state reactions were observed by XRD tests carried out on the cathode sintered at 1400°C.

### 5.3. References

- [117] Stephen J. Skinner and John A. Kilner - *Material today*- March2003
- [118] M. Anderson, Y.S. Lin - *Journal of Membrane Science*, 357 (2010), pp. 122–129
- [119] B.N. Nair, T. Yamaguchi, H. Kawamura, S.-I. Nakao- *ACS*, 87 (2004), pp. 68–74
- [120] K.N. Essaki, Kazuaki, K. Masahiro – *J. Ceram. Soc. of Japan*, 109 (2001), pp. 829–833
- [121] B.C.H. Steele, *J. Power Sources* 49 (1994) 1.
- [122] J.A. Kilner, B.C.H. Steele, in: O. Toft Sorensen (Ed.)- *Non-stoichiometric Oxides*, 1981, p. 233.
- [123] B.C.H. Steele / *Solid State Ionics* 129 (2000) 95 –110
- [124] Joo JH, Chai GM. *J Electrochem Soc* 2007;27(13e15):4273.
- [125] Tuller HL, Nowick AS. *J Electrochem Soc* 1975;122:255
- [126] Lubbe S, Wiemhofer HD. *Ber Bunsenges Phys Chem* 1998;102(4):642e9.
- [127] A. Damiano Bonaccorso and John Irvine – *International Journal of Hydrogen Energy*- in press
- [128] C. Lee et al. / *Solid State Ionics* 98 (1997) 39 –48
- [129] F.H. Wang, R.S. Guo, Q.T. Wei, Y. Zhou, H.L. Li, S.L. Li -*Mater. Lett.*, 58 (2004), p. 3079
- [130] J.H. Lee, H. Moon, H.W. Lee, J. Kim, J.D. Kim, K.H. Yoon – *SSI-*, 148 (2002), p. 15
- [131] Y. Li, Z.L. Tang, Y.S. Xie, Z.T. Zhang- *Mater. Sci. Technol.*, 9 (2001), p. 91
- [132] Chen M, Grundy AN, Hallstedt B, Gauckler LJ, Liu Y-L, Chatzichristodoulou C, Hendriksen PV, Hagen A. 2007. *Reaction*

thermodynamics at the LSM-YSZ interface in SOFCs. Paper presented at CALPHAD 36, State College, PA (US)

[133] Lee SJ, Park EW, Hjun SH. Fuel Cell 2010;10(10):145.

[134] Park S, Vohs JM, Gorte RJ - Nature (2000);404:265(7).

[135] Reiss I, Janczikowsky H, Nolting. J Appl Phys; 1987:4931e3

[136] T. Horita, et al - Electrochim. Acta, 46, 1837 (2001).

[137] S. P. Simner, et al , Electrochem. Solid-State Lett., 5, A173 (2002).

[138] S. P. Simner, et al , J. Power Sources, 113, 1 ,2003,.

[139] Y. Huang, J. M. Vohs, and R. J. Gorte, J. Electrochem. Soc., 151,(2004) A646

[140] S. P. Jiang, Solid State Ionics, 146, 1 ,2002.

[141] W. Wang, Y. Huang, S. Jung, J. M. Vohs, and R. J. Gorte, J. Electrochem. Soc., 153,(2006) A2066

[142] F. Bidrawn, J. M. Vohs, and R. J. Gorte, J. Electrochem. Soc. 157, (2010), 11, B1629-B1633

[143] Takawa - perovskite oxide for solid oxide fuel cell- chapter 7-

[144] Yingyi Huang, John M. Vohs, and Raymond J. Gorte J. Electrochem Soc.- 152 (7) A1347-A1353 (2005)

[145] T. Kawada - Perovskite oxide for oxide fuel cell – Springer - Chapter 7 - pages 164

[146] B.C.H. Steele I Solid State Ionics 86-88 (1996) 1223-1234

[147] Sahibzada M, Benson SJ, Rudkin RA, Kilner JA, Solid State Ion., 113-115, 285, 1998

[148] M.H.R. Lankhorst, J.E. Elshof - Solid State Chem., 130 (1997), p. 132

[149] L.W. Tai et al. - Solid State Ionics, 76 (1995), p. 259

## **6. Electrochemical performance of different configuration of HDCFC**

### **6.1. Introduction**

In the last chapter, the physical chemistry performance of each component, such as the anode, electrolyte and cathode, was investigated in order to comprehend their potential and what contribution they could provide after being assembled.

The performance of the whole cell will be investigated in order to improve the performance of the cell using GDC electrolyte, compared to the previous investigation carried out on the cell with YSZ electrolyte.

In fact, in the previous work undertaken at the University of St Andrews, the hybrid direct carbon fuel cell in tubular geometry showed promising results, achieving 85mW at 800°C [150].

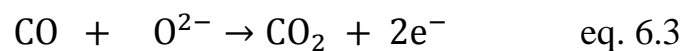
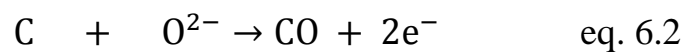
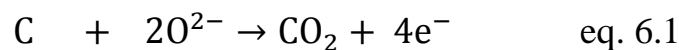
Regarding this, tubular geometry was chosen in order to reduce the stress during the sintering process and to reduce the final size of the stack. Moreover, using tubular geometry makes it easier to fuel carbon into the cell.

The main problem with this type of cell was the low OCV at temperatures lower than 800°C. In addition, the cell uses materials such as gold as current collector, which is extremely expensive. In order to improve the performance of the entire

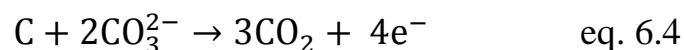
cells different aspects of the cell such as a new sealing material, electrical configuration and the influence of gases on cell performance will be illustrated.

## 6.2. Investigation of electrical configurations

As described in chapter three, a hybrid direct carbon fuel cell is a merger of a direct carbon with a solid electrolyte and a direct carbon with a molten carbonate electrolyte. In the anodic chamber, the dimension of the anode is not only limited to the NiO-GDC layer but it is extended to the liquid section that consists of carbon and carbonate mixture. Consequently, electrochemical reactions can take place in any part of the anode chamber, including in the carbon and carbonate mixture, as shown in the equations below:



Oxidation of carbon fuel by carbonate salts



For this reason, different electrical configurations for the anode were investigated so as to determine in which zone of the anode these reactions take place, improving the performance of the cell. The configurations investigated are shown in figures 6.1 a, 6.1 b and 6.1 c:

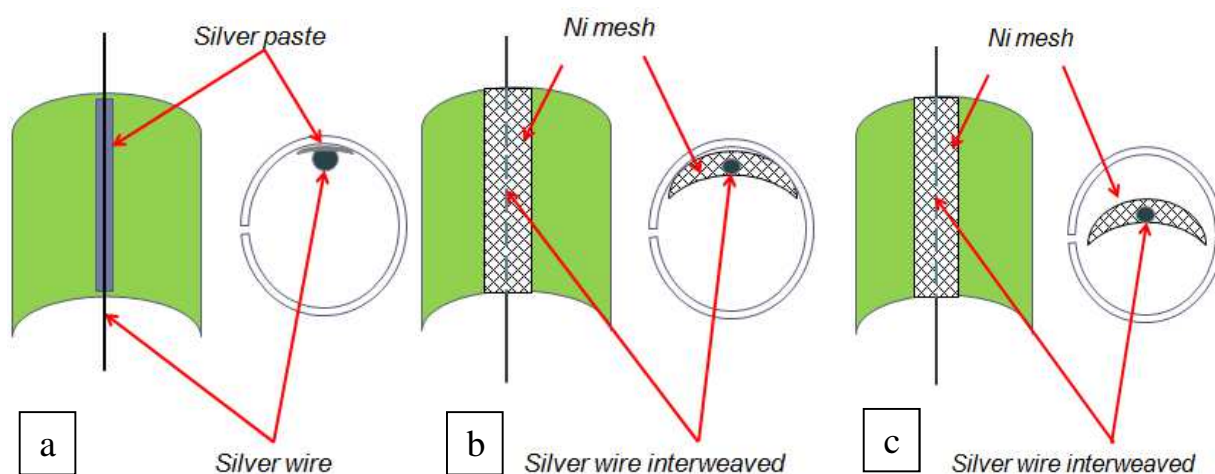


Figure 6.1- Electrical configuration in the anodic chamber (a) configuration with silver wire stuck directly to the anodic wall using silver paste and dried at room temperature (b) configuration with silver wire interwoven with nickel mesh and stuck to the anode with silver paste (c) configuration with silver wire interwoven with nickel mesh dipped fully into the carbon/carbonate mixture.

In the configurations shown above, the silver wire, silver paste and nickel mesh are the current collectors. Differences between these configurations and the setting are characterized by their position inside the anodic chamber and also by the size of the current collector. In two of the configurations, the current collector

is stuck to the anodic wall whilst in the other the nickel mesh interwoven with silver wire is dipped into the carbon-carbonate mixture in order to determine the contribution of electrons produced by reactions shown in eq. 6.4 and eq. 6.5.

### 6.2.1. Cell manufacturing

Green tapes of NiO-GDC (70:30wt%) anode, GDC electrolyte, cathode (LSM - GDC) and LSM 3% from Pi-Kem current collector were prepared using organic binder and plasticizer components. The oxide powders were homogenized in a mixture of methyl-ethyl-ketone and ethyl alcohol at a ratio of 3:1, using zirconia balls. The slurry was milled for 18h at 160rpm and after adding the organic component, it was shaken for 22min and milled again for 4h at 100 rpm. The same procedure was used for electrolyte slurry preparation but an overnight milling was added to eliminate possible air bubbles during the tape casting process. Resulting slurries were tape cast on a TTC-1000, from Mistler Inc., by a standard tape casting process. The tape was cast at room temperature with a carrier velocity of 50 cm/min. Laminates were then assembled, as shown in figure 6.2:

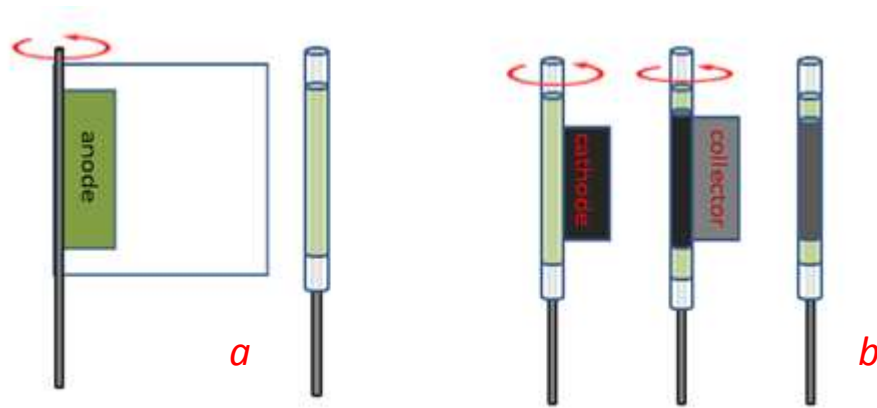


Figure 6.2 - Tubular geometry manufacture (a) laminated anode and electrolyte tapes were rolled by stainless steel tube (b) cathode and current collector were rolled respectively onto green laminate anode and electrolyte.

The cells were sintered in two different steps. In the first step, the organics and carbon in the green cells were burnt, heating them to  $1000^{\circ}\text{C}$  at a ramp rate of  $1^{\circ}\text{C}/\text{min}$ . The temperature was held at  $1000^{\circ}\text{C}$  for 5h and the cells were cooled to  $50^{\circ}\text{C}$  at a ramp rate of  $5^{\circ}\text{C}/\text{min}$ . In the second step, cells were sintered at  $1410^{\circ}\text{C}$  at  $5^{\circ}\text{C}/\text{min}$ , as this procedure was found to give good electrolyte conductivity. The temperature was also held for 5h and it was then cooled to  $50^{\circ}\text{C}$  at  $5^{\circ}\text{C}/\text{min}$ . The final size of each cell was 8cm (height) by 1.1cm (diameter) with the anode, electrolyte and cathode layers being  $60\mu\text{m}$ ,  $300\mu\text{m}$  and  $60\mu\text{m}$  thick respectively. After having sintered the cell, electrical contacts were prepared as illustrated previously. The different cells were then filled with a carbon carbonate mixture in ratio 70-30% in moles and sealed with Pi-kem 552.

## 6.2.2. Electrochemical investigation by ac impedance

The different cells were tested by AC impedance in order to investigate their electrochemical behaviour. The three cells were connected to a Solatron1280 through two wires and the results are shown in figures 6.3, 6.4 and 6.5:

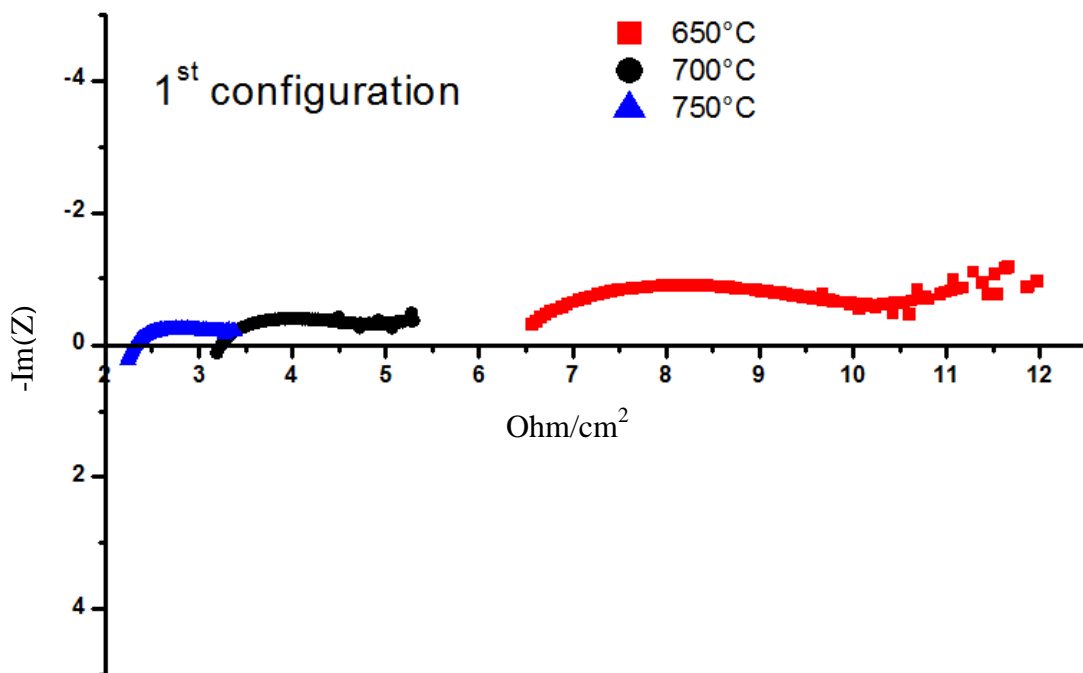


Figure 6.3 - AC impedance of cell with the 1<sup>st</sup> configuration carried out in a range between 0.1 Hz and 1 MHz at 10 mV amplitude at 650°C, 700°C and 750°C.

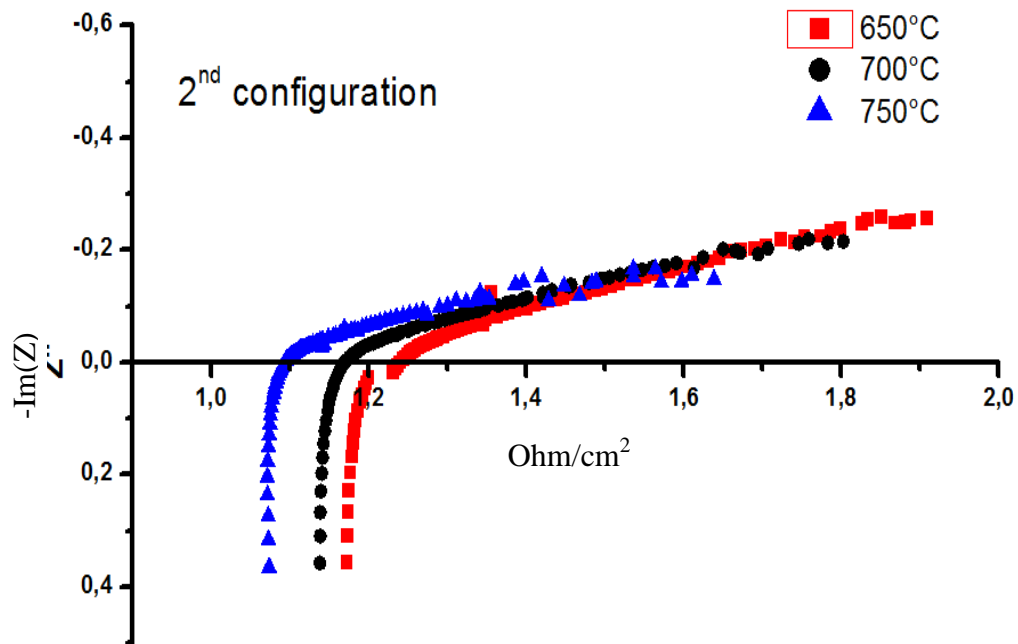


Figure 6.4- AC impedance of cell with the 2<sup>nd</sup> configuration carried out at a range between 0.1Hz-1 MHz at 10 mV amplitude at 650°C, 700°C and 750°C.

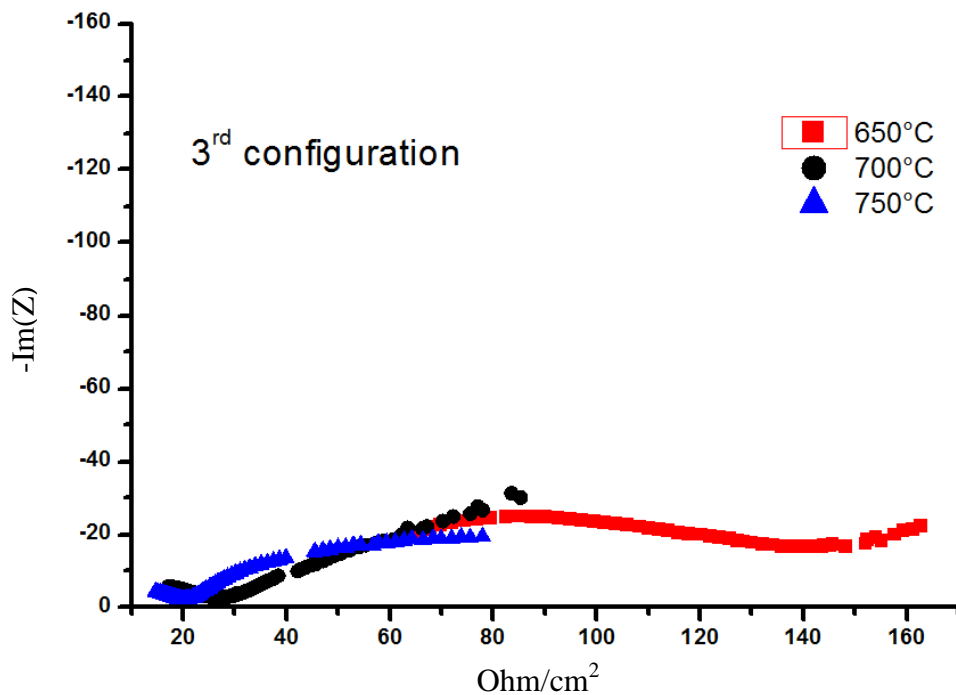


Figure 6.5- AC impedance of cell with the 3<sup>rd</sup> configuration carried out at a range between 0.1Hz-1 MHz at 10 mV amplitude at 650°C, 700°C and 750°C.

The ac impedance data clearly show that the electrochemical behaviour of the cell is affected by the electronic configuration because the values of  $R_s$  and  $R_p$  achieved for three cells with the same composition of anode, cathode and electrolyte are different. In fact, when the values of  $R_s$  and  $R_p$  obtained from the value of AC impedance by Zview analysis are plotted separately, it is possible to understand the intensity of variation in both values, as shown in figures 6.6 and 6.7:

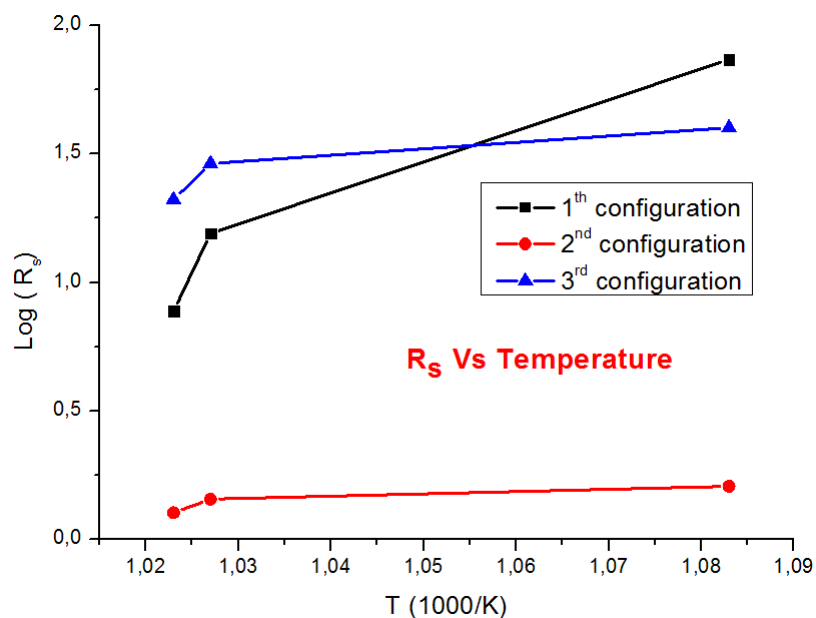


Figure 6.6-  $\text{Log}(R_s)$  plotted vs temperature of a hybrid direct carbon fuel cell filled with a mixture of carbonate and carbon in mole ratio 20/80% respectively. Data are obtained by AC impedance spectra carried out at 650°C, 700 °C and 750 °C on cells with different electrical configurations.

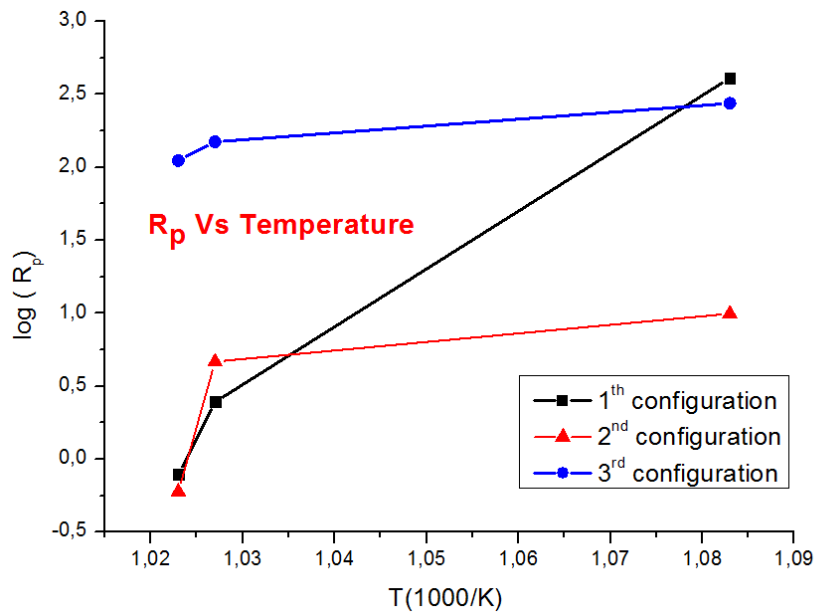


Figure 6.7- Log ( $R_p$ ) plotted vs temperature of a hybrid direct carbon fuel cell filled with a mixture of carbonate and carbon in mole ratio 20/80%, respectively. Data are obtained by AC impedance spectra carried out at 650°C, 700 °C and 750 °C on cells with different electrical configurations.

In the first two configurations, the differences in  $R_p$  were not particularly marked, even though the values of  $R_s$  and  $R_p$  at 650°C are higher for the first configuration than for the second. The  $R_s$  value reduces at temperatures higher than 650°C; in fact the  $R_s$  at 700°C and 750°C decreases to 2.02  $\Omega$  and 1.3  $\Omega$  respectively.

These differences in  $R_s$  can be correlated to the different surface area of the current collector. In the first configuration, the current collector is represented by the silver paste painted on the anode wall (silver line 0.5 cm wide and 8 cm long) and silver wire 0.25mm thick. On the other hand, the second configuration used a strip of Ni mesh that is 8 cm long by 1.5cm wide. The  $R_p$  value is also affected by the surface area of the current collector. In fact, the nickel mesh is a

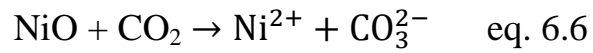
combination of single wires with empty space between them, whereas the single wire has circular geometry. For this reason it has higher polarizability than nickel mesh. In the third configuration, the electrochemical behaviour is totally different. In fact, the ac impedance spectrum shows two semi arcs instead of one semi arc, as observed in configurations 1 and 2. In addition, the sum of both semi arcs produces a value of total resistance that is eleven times higher than that of the first two configurations.

This behaviour is entirely attributable to the carbonate salts into which the current collector is dipped. In fact, the mobility of carbonate ions is lower than electrons produced electrochemically by the redox reactions that take place between the carbon and carbonate - see equations (4) and (5). In addition, the current collector is completely surrounded by the carbonate ions that polarise the electrode, creating a large polarization arc.

### 6.2.3. Nickel mesh and NiO stability in carbonate salts

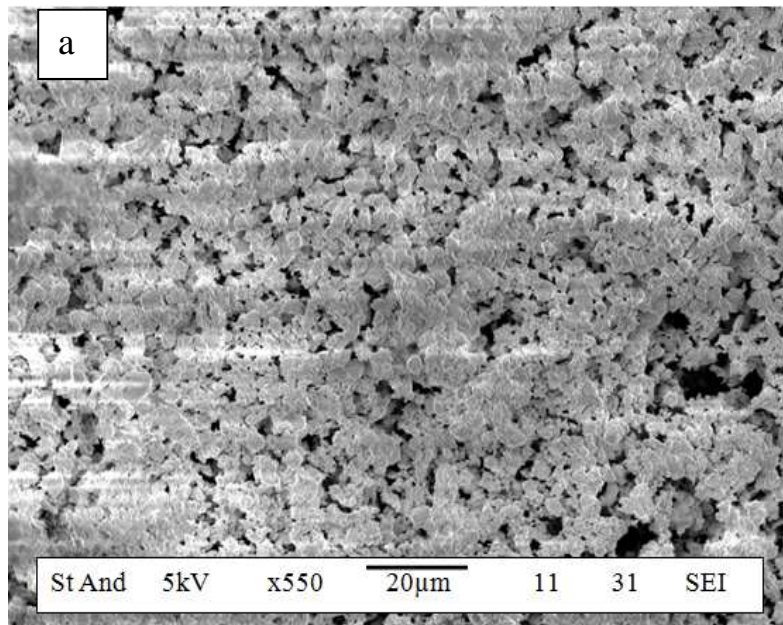
Nickel mesh and NiO are unstable in the presence of carbonate salt because the salt reacts with nickel metal to produce nickel carbonate salts.

HDCFC works under molten carbonate salts and the operating conditions favour the dissolution of Ni, according to the following acid mechanism[122-123]:



The Li-K carbonate mixture is highly reactive with nickel and it encourages the dissolution of nickel. The dissolution equilibrium is reached when the concentration of nickel is around 30ppm.[151]

A sintered piece of anode was analysed before being dipped into a binary mixture of carbonate salts (K, Li) and the same piece of anode was analysed under a microscope after 72h of testing. The dissolution is visible in the figures shown figure 6.8 a, b, c:



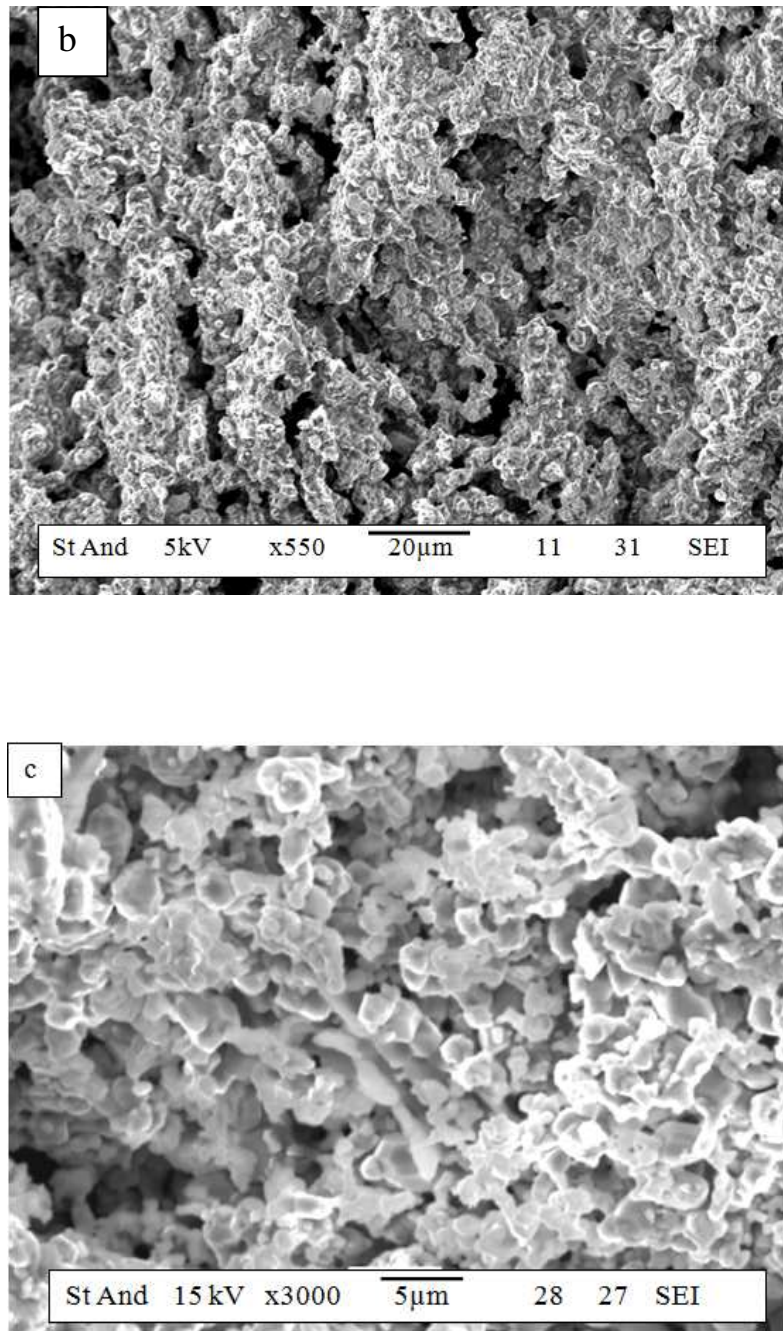


Figure 6.8- SEM image of 70/30 wt% NiO – GDC anode a) Anode after being sintered b-c) after 72 h dipped in the binary mixture.

Image 5c does not show particular degradation after 72h in the binary mixture of molten carbonate salts. In fact, particles of nickel metal are perfectly connected to the GDC structure.

---

A different effect was observed for the nickel mesh. The phenomena of degradation were visible in the SEM image shown below:

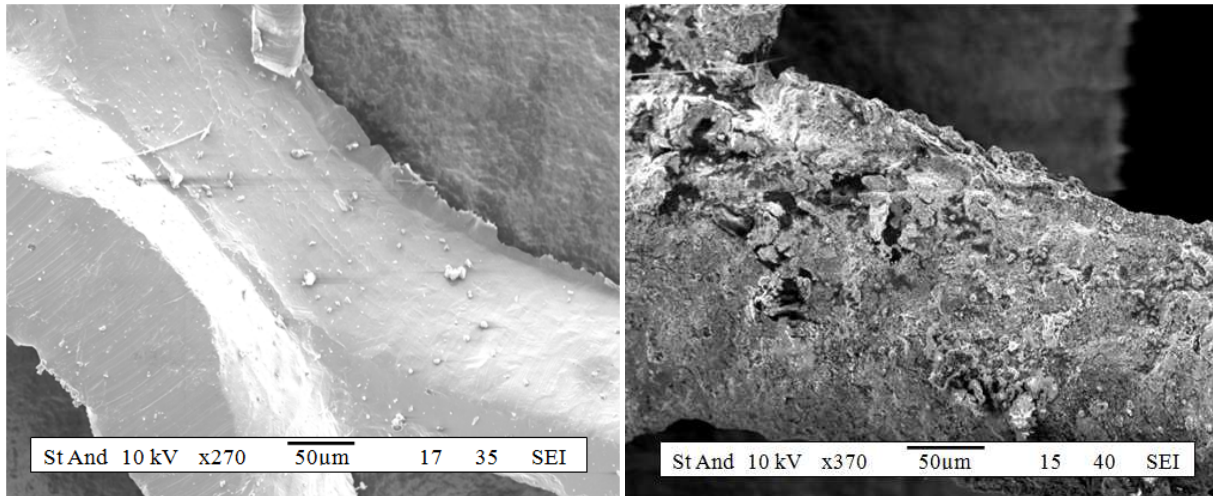
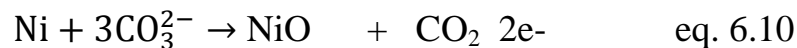
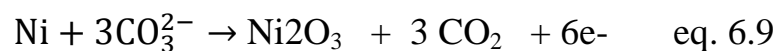
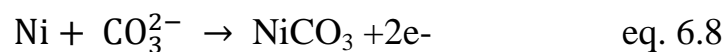


Figure 6.9- Pictures acquired by SEM technique at 50µm and 10kV (a) nickel mesh before testing (b) nickel mesh after 24 hours of testing.

Nickel metal is highly reactive with carbonate and as it is in direct contact with the carbonate, dissolution phenomena of nickel are visible. The mechanisms involved in Nickel dissolution are shown eq 6.8,6.9 and 6.10:[152-153]



The degradation of nickel mesh current collector can affect the  $R_s$  of the cell because it reduces the electron paths and consequently the number of electrons in the circuits.

Gold mesh would be the best solution as current collector because it is inert to the carbonate mixture; however the cost of gold is too high.

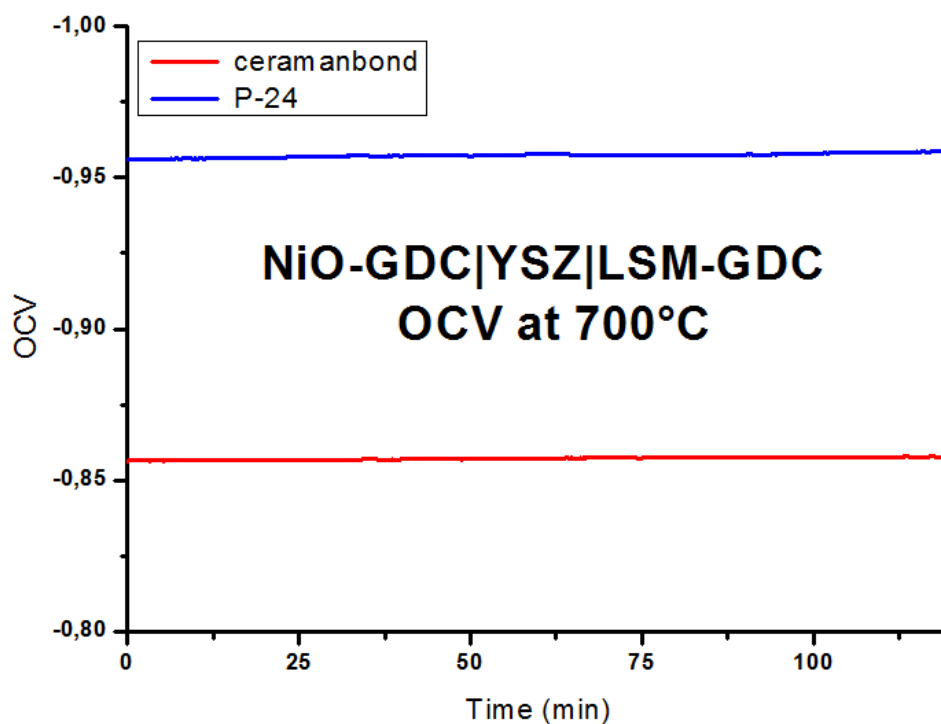
### 6.3. Investigation of leakages by open circuit voltage.

The OCV voltage of a cell provides information about the electrochemical potential produced by the reactions in eq. 6.1, 6.2 and 6.3 that take place in the anode chamber. The overall EMF was estimated at 1.02V for the three reactions mentioned above, using a thermodynamic approach which makes use of the  $\Delta G$  value estimated using FactSage software. The EMF obtained previously was recalculated using the ratio value between CO and CO<sub>2</sub> at the equilibrium obtained by Gas Chromatography at 700°C. The ratio achieved was 3:1. This value insert in the FactSage software in order to estimate the value of PO<sub>2</sub> at the anode side. EMF was obtained using equation 6.11 :

$$EMF = -\frac{RT}{4F} \ln \frac{P_{O_2,c.}}{P_{O_2,a,}} \text{ eq. 6.11}$$

Where  $P_{O_2,c.}$  and  $P_{O_2,a,}$  are the partial pressure of oxygen in the cathode and anode side respectively. These calculations were done under assuming the system and the gas concentration were constant.

The value obtained by this calculation was 0.97V that is 5 mV smaller than the value estimated using the  $\Delta G$  of each reaction involved. These values were considered as maximum limit and minimum limit. Since the temperature of the system and gas composition in the cathode were kept constant, the variation of EMF may be caused both by electron leaks and gases leaks. If the voltage value changes as a function of time, a leak is present in the circuit. Since GDC is an electronically conductive material, tests were carried out using two different cells: one of these used YSZ electrolyte which is a total ionic conductor and for this reason it produced no current leaks, while the second cell used GDC electrolyte. The tests were carried out purging 40 ml/min of air in the cathode side (figure 6.10).



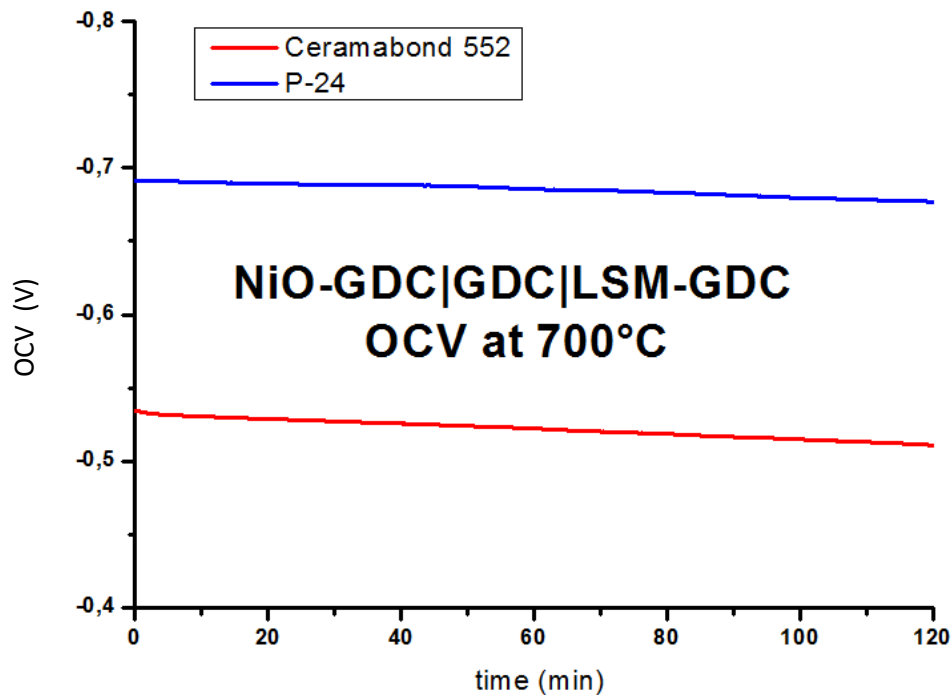


Figure 6.10- OCV curves of HDCFC sealed with two different seals: P-24 and ceramabond. The tests were carried out at 700°C for 2h a) cell with YSZ electrolyte b) cell with GDC electrolyte.

The tests demonstrated that P-24 produced by Toku Adhesive showed better performance in sealing than Ceramabond 552 produced by Pi-Kem. In fact, at high temperature the internal pressure produced by gases increased the size of the micro cracks causing a negative variation in the EMF. In addition, an increase in internal pressure favoured osmosis leakages. Another difference is that the cell sealed with Pi-kem showed cracks or micro cracks on the ceramic electrolyte next to the sealing. Instead, no cracks were observed in the sample sealed with P-24. Micro cracks and cracks were due to the strong shrinkage effect produced by the sealing during the curing process. Cracks were visible during the cell manufacture while micro cracks were not visible and cells tested

showed a sharp drop in voltage at 650°C because of the micro pores present close to the sealing.

As YSZ is a 100% ionically conductive membrane, the small drop in voltage observed is caused entirely by gas leakage and not by electron leaks. The drop is more marked for the cell with GDC electrolyte because at 700°C the electrons conductivity is quite high.

### 6.3.1. Studies of microstructure of sealing materials

In the previous paragraph, the extent of the leakages was calculated in relation to the expected value of EMF at 700°C. The causes of these leaks were explained in chapter 3, distinguishing between diffusion leakages and surface contact leakages. The contact leakages represent the amount of gas that passes through the empty space between the seal and the membrane wall. For this reason, a scanning electron microscope was used to investigate the microstructure of the different seals after curing and after exposure to the carbonate mixture at high temperature. The resistance of both seals to the carbonate salts mixture was tested dipping two pieces of seal (ceramabond 552 and P-24 ToKu Adhesive) into a pure carbonate mixture of Li-K carbonate in mole ratio of 62:38. The test was carried out filling an alumina crucible with carbonate salts and holding the two seals in direct contact with the carbonate for 72h at 800°C. The crucible contained both carbonate salts and the samples were closed using a top (maccor).

---

The crucible was put in a vertical furnace and inlet and outlet tubes were inserted into the crucible through the two holes in order to purge CO<sub>2</sub> gas at a flow rate of 25 ml/min. The CO<sub>2</sub> was used to prevent carbonate decomposition at high temperature.

Ceramabond 552 and P-24 were spread onto a flat stainless steel bar and were then dried overnight in air at room temperature. After that, both seals were cured following the parameters indicated by the company. Ceramabond 552 was cured at two temperatures: 94°C for 1-2 hrs and at 204°C for 2-4 h, while for P-24 the curing was carried out at 150°C for 1hr. After curing, the seals were observed under a microscope.

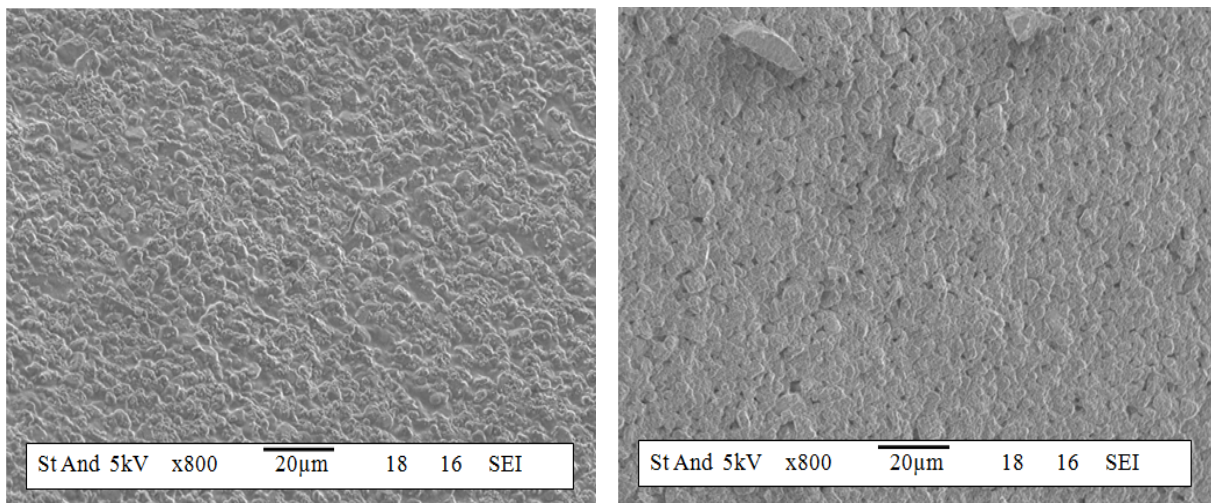


Figure 6.11- SEM pictures of Toku adhesive P-24 and ceramabond 552 before test (a) P-24 after curing (b) ceramabond 552 after curing.

The SEM pictures show that the surface of P-24 did not show any porosity while a different result was observed for ceramabond 552. In fact, most of the leakages are caused by the gases that pass through the seals (diffusion leakages). After this

---

test, seals were dipped in the carbonate salts as explained previously and held there for 72 h. After that, the samples were analysed with SEM again in order to observe any changes in their structure.

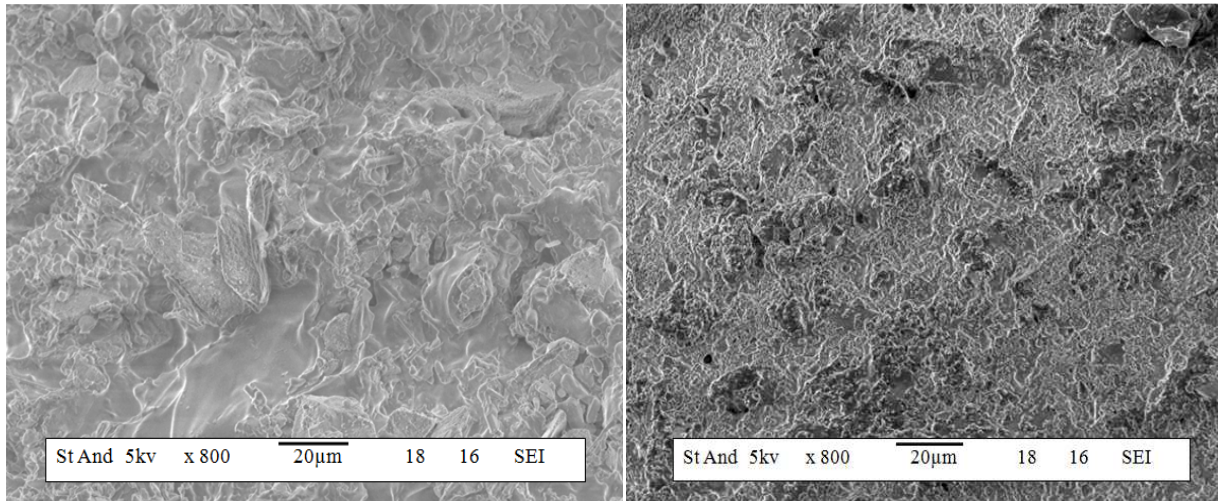


Figure 6.12 - SEM pictures of Toku adhesive P-24 and ceramabond 552 tested in molten carbonate under CO<sub>2</sub> environment to prevent the decomposition of carbonate (a) P-24 after 72hrs (b) ceramabond 552 after 72hrs.

SEM pictures show that P-24 is more resistant to the carbonate than ceramabond 552. In both cases the corrosion effect is different. In P-24, corrosion occurred only on the surface of the cement while the corrosion effect on ceramabond 552 affected both the surface and the interior, increasing the diameter of pores in the cement after contact with the molten carbonate.

### 6.3.2. Effect of composite seals on the OCV voltage

Analysing the previous results and observing the SEM pictures of the microstructure of both samples, the main problems of leakage were caused by the diffusion of gases that crossed the seals, hence several types of composite seals were investigated in order to reduce the diffusion of gases across the alumina seals. These composite seals consist of the cements used previously, combined with two solid seals. The tubular fuel cell was sealed blocking the tube cavity by the cement in order to separate the anode with cathode sides. The two solid sealing materials used in combination with the previous seals investigated were an alumina fibre disk of 0.5 cm diameter and 0.5 cm thickness and a disk composed of Mica produced by Thermiculite 886 (Flexitallic Ltd). Thermiculite 866 (Flexitallic Ltd) is a composite material consisting of chemically exfoliated vermiculite mica. Mica is a group of silicate minerals with a general structure of  $AB_{2-3}Z_4O_{10}(OH, F)_2$  in which A is either K, Na, Ca or Ba and B is either Al, Fe, Mg or Li [154][155]. In our case, the composition used was (Al, Si)- $Si_3O_{10}(OH)_2$ .

An alumina fibre disc 0.1 mm smaller than the diameter of the tubular cell could be inserted perfectly into the cell, providing good adherence to the electrolyte wall, while a multilayer of mica was cut to the same diameter as the cell so that it could cover both the entire cell and the alumina fibre disc.

The use of these discs produced a double effect: firstly, it balanced the shrinkage effect caused by the curing process from the ceramabond and secondly, the introduction of the solid disc in the cell reduces the area to be sealed with ceramabond cement. The mica barrier was used to minimize the diffusion leakages.

The two cells were assembled as illustrated in figure 6.13:

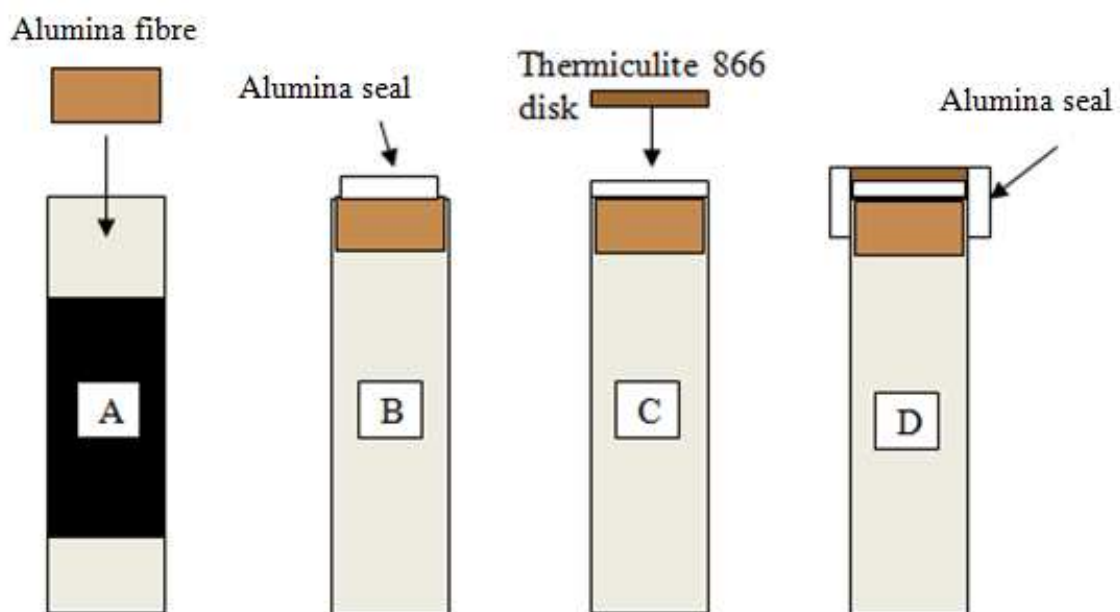


Figure 6.13- Schematic description of sealing process in different steps: a) an alumina disk is inserted into the top part of the tubular cell b) seal on alumina disk c) mica disk sticks to the seals d) plus lateral sealing.

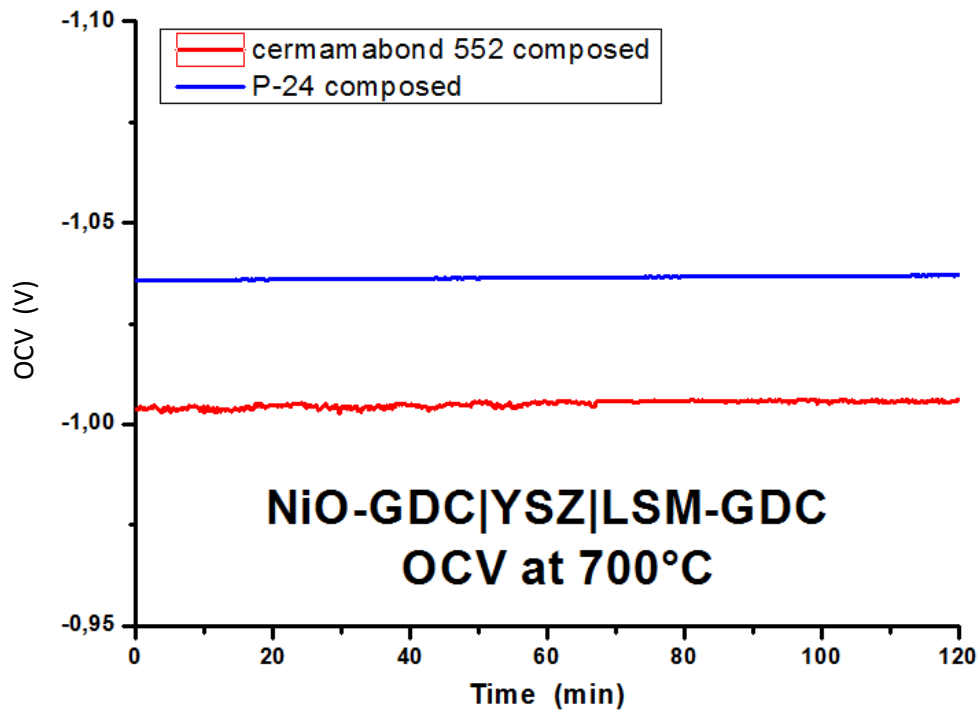


Figure 6.14- OCV curves of HDCFC cell with YSZ electrolyte and sealed using a composite seal: — (P-24+ alumina fibres disc and mica disc) — (cermamabond 552 + alumina fibre disc and mica disk). The tests were carried out at 700°C for 2hrs.

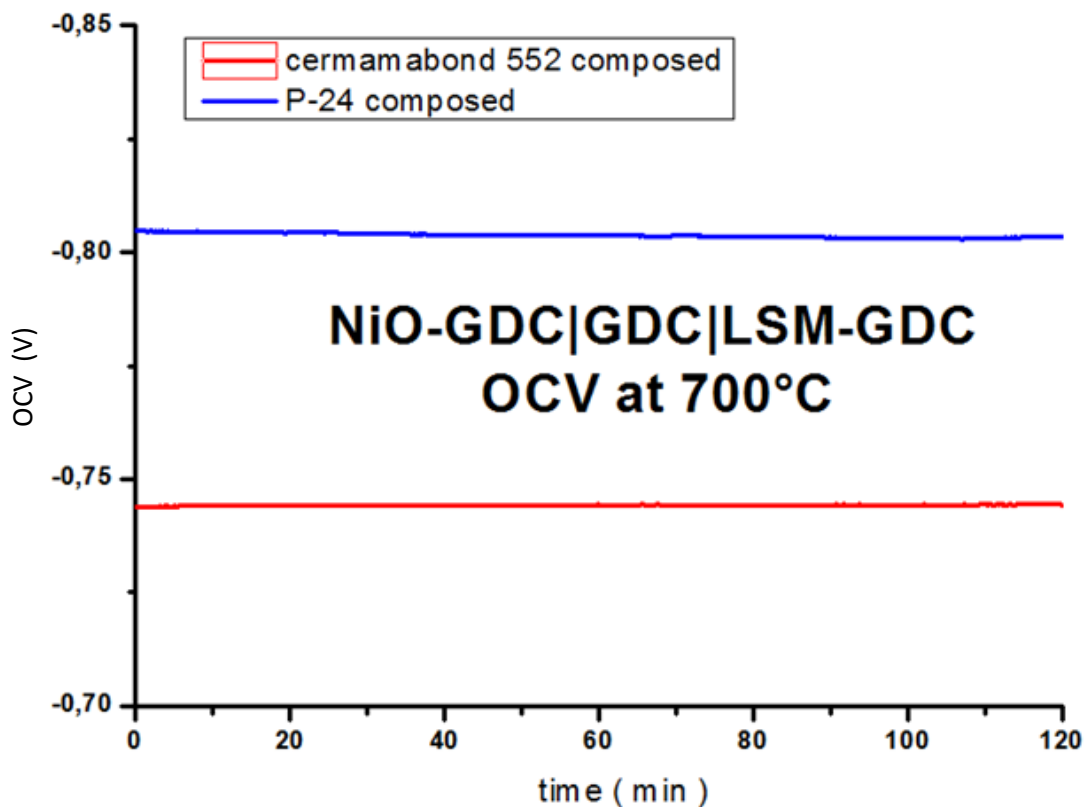


Figure 6.15- OCV curves of HDCFC cell with GDC electrolyte and sealed using a composite seal: — (P-24+ Composed) — (ceramabond 552 composed). The tests were carried out at 700°C for 2hrs.

The results obtained show that the effect of the double solid seal composed of mica disk and alumina disk reduced both the diffusion leakages and surface contact leakages, as shown above by comparing the test carried out both on cells sealed with composite seals and without mica and alumina fibres. The value of ocv measured with the double solid seal composed of mica disk and alumina disk improve the ocv value this means that the drop in EMF measured was only caused by gases leakages.

#### **6.4. Studies of hybrid direct carbon fuel cell configurations**

In the previous paragraphs, investigations were focused on a single component in order to comprehend the limits of each component and so as to be able to combine components in order to obtain the best possible performance.

The main concern for the YSZ electrolyte was due to possible reactions of YSZ with the carbonate salts and for this reason a configuration using a protection layer screen printed onto the YSZ electrolyte was tested in comparison to a configuration with GDC electrolyte (figure 6.16).

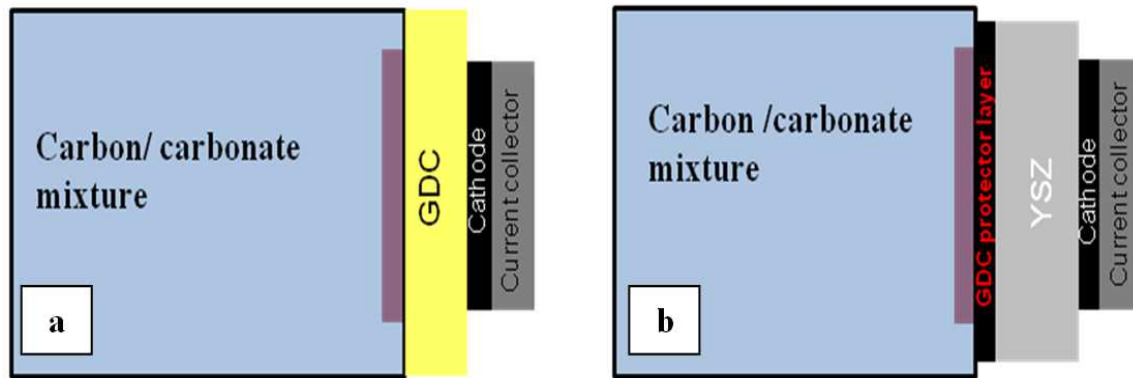


Figure 6.16- Schematic representation of different configurations of hybrid direct carbon fuel cell (a) Configuration with GDC material used as electrolyte (b) Configuration with a thin layer of GDC protection layer that was screen printed onto the YSZ electrolyte tape layer. [156]

Two different cell types were prepared and tested. In the first configuration, a thin layer of GDC (10 $\mu$ m) material was used as a protection layer to protect against the possible reaction between lithium carbonate and YSZ electrolyte. On the other hand, GDC was directly employed as the electrolyte in the second configuration (figure 6.14). Each cell tested was in a static condition without gas flow.

AC impedance and DC tests were carried out on each cell with different configurations to investigate the electrical performance. I-V curves (V vs. I) obtained from DC performance and power (W) are plotted together for both configurations in figures 6.17 and 6.18

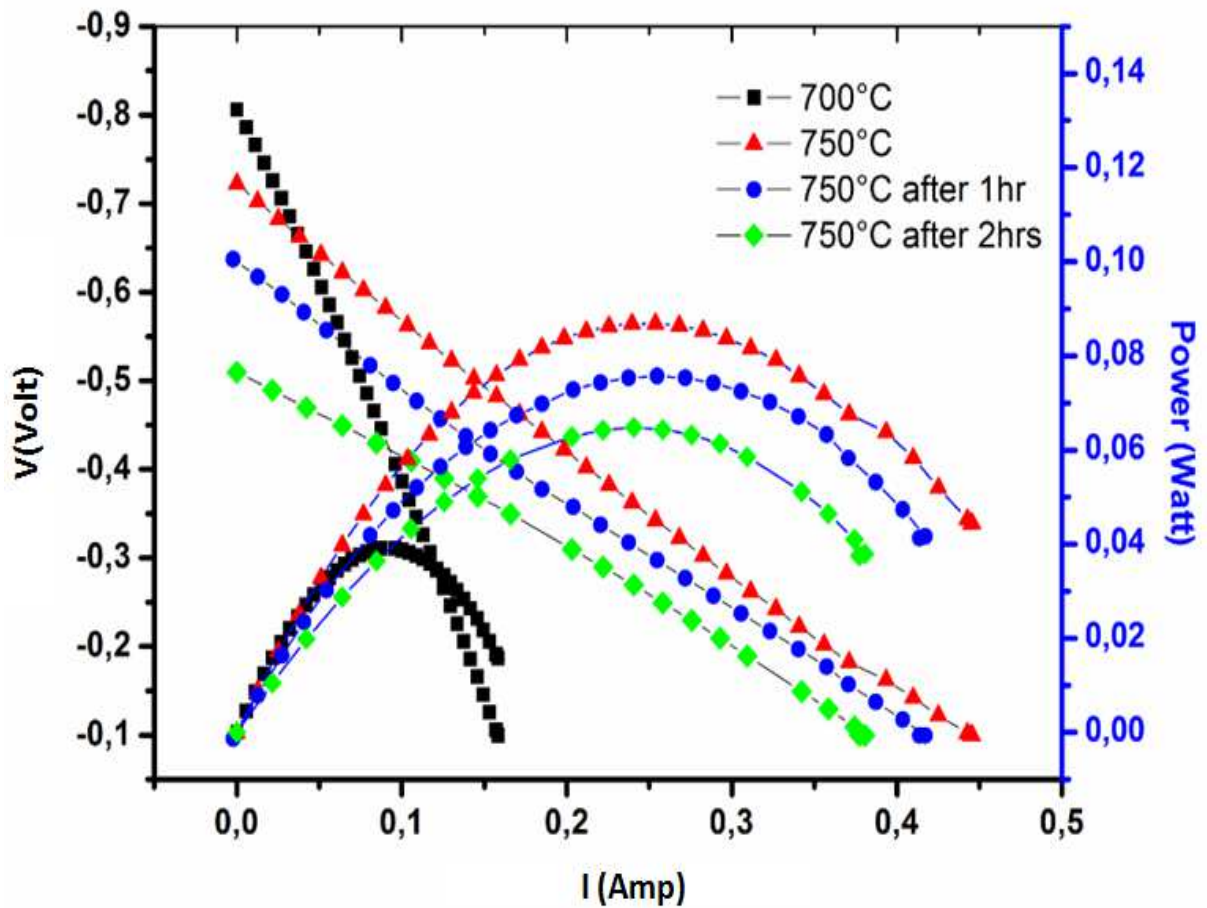


Figure 6.19- I-V curves plotted for the cell configuration with GDC used as electrolyte. Voltage and power were plotted against current at different temperatures. Electrical performance stability was also investigated holding the sample at 750°C for 2 h. [156]

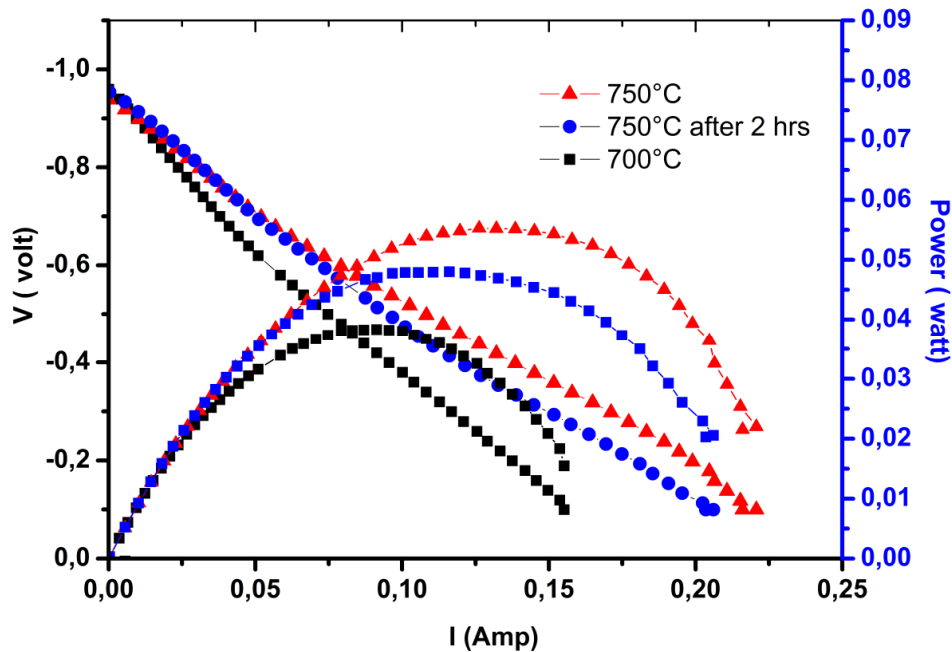


Figure 6.20- I-V curve plotted for the cell configuration with GDC used as electrolyte. Voltage and power were plotted against current at different temperatures. Electrical performance stability was also investigated holding the sample at 750°C for 1 and 2 hours respectively[156].

Analysing the I-V curves on the figures above, a different value of OCV was observed for the two different cells. The cell with YSZ electrolyte and GDC protection layer shows a value lower than expected. The small drop in voltage observed could be attributed to the effects of GDC. In fact, it is part of the electrolyte and it is not totally ionic conductive at high temperature, as YSZ. This might relate to a potential loss between the upper surface of the electrolyte and the YSZ/GDC interface.

The OCV achieved in the configuration with GDC electrolyte decreased as a function of the temperature and time. This could be attributed to the action of the

carbon, which is a reducing agent, reducing Ce(IV) to Ce(III) to produce electrons.

The values of current and power were not normalized by surface area because the type of flux of carbonate and carbon in tubular geometry is dynamic rather than static. This means that the contact surface between carbon fuel and anode changes and is difficult to define. For this reason, data of current and power will not be normalized. The configuration with GDC protection layer and YSZ electrolyte showed worse performance in terms of power at 750°C. However, the OCV value is more stable for the whole test than the cell with only GDC electrolyte. This stability is attributed to the presence of the YSZ electrolyte layer which is totally ionically conductive. The mixed conductivity and resultant ambipolar oxygen diffusion at 750°C probably explains why after two hours an increase of resistance is shown only for GDC electrolyte (figure 6.17 and 6.18), as some fuel near the electrolyte may be consumed even at an open circuit.

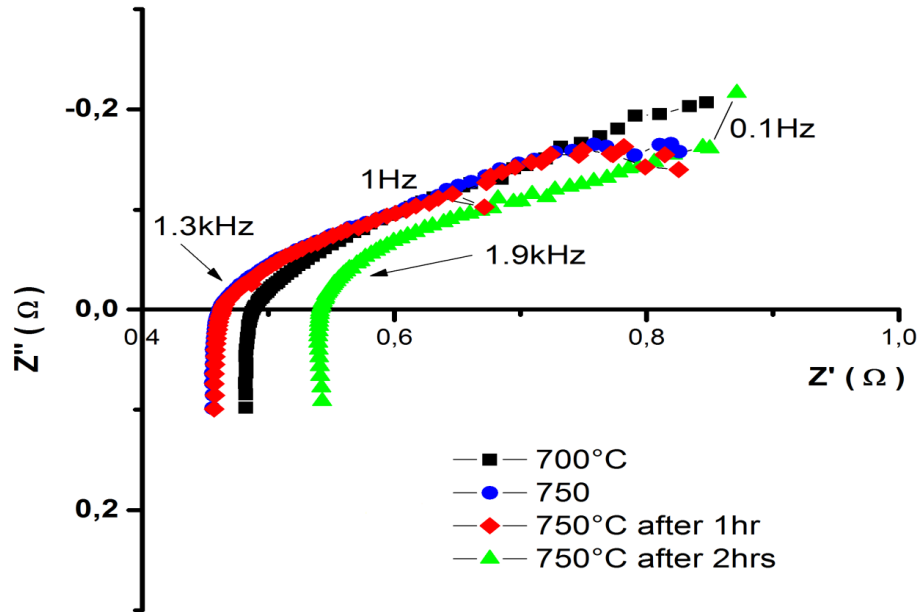


Figure 6.21- AC impedance spectra of cell with GDC electrolyte were collected at different temperatures and at 750°C after intervals of 1 and 2 hours.

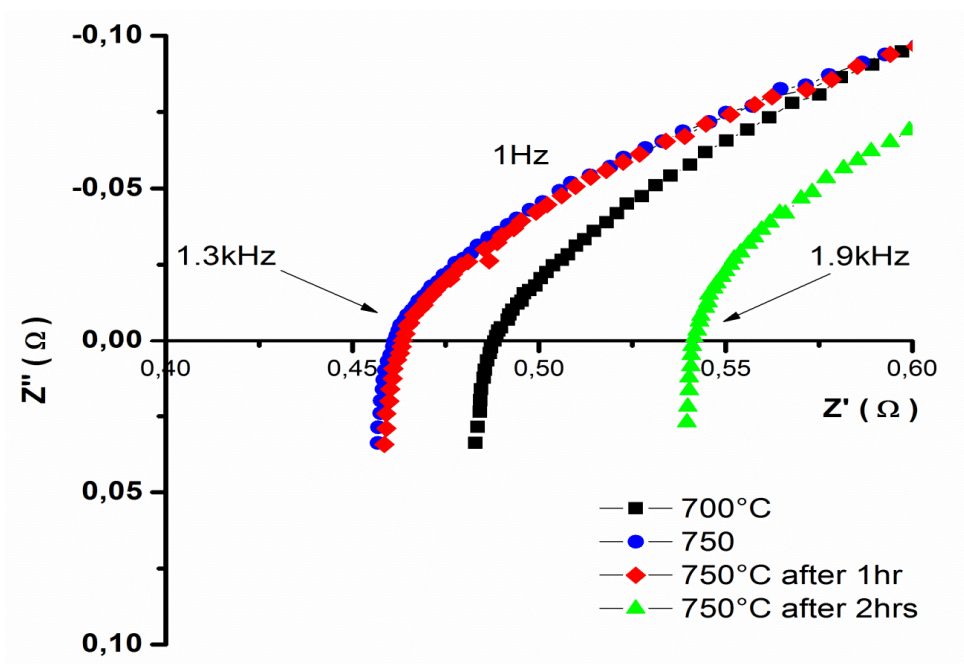


Figure 6.22- Zoom of AC impedance spectra reported in figure 6a at low resistances and high frequency at a range of temperatures between 650°C to 750°C. [156]

The configuration with YSZ electrolyte and GDC protection layer does not show any decrease in resistance after 10h of testing, as shown in figure 6.23:

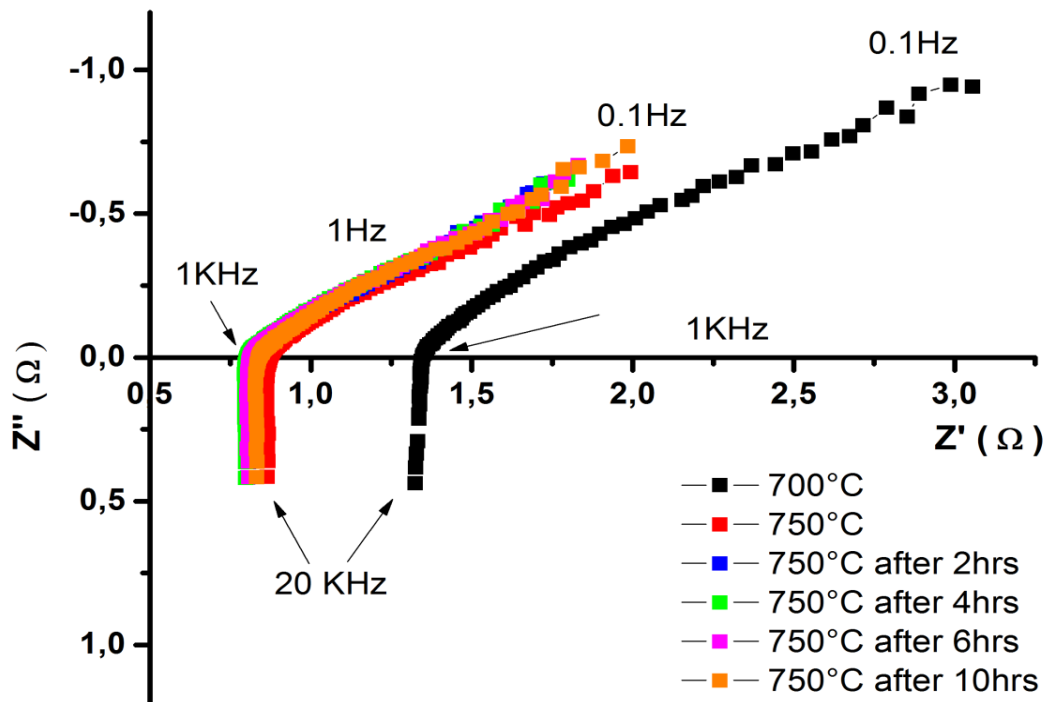


Figure 6.23- AC impedance spectra for the cell configuration with GDC used as protection layer and YSZ used as electrolyte. AC impedance spectra were collected at 700°C and at 750°C at intervals of 0,2,4,6 and 10h respectively. Range of frequencies was set up between 0.1Hz-20 kHz [156].

This is possibly due to the high ion conductivity of YSZ. However, an important variation of the polarization is evident for the cell with YSZ and GDC protection layer. In fact, analysing the curves with Zview software, the differences can be seen in the equivalent circuit components. In the configuration with GDC the equivalent circuit is shown in figure 6.24:

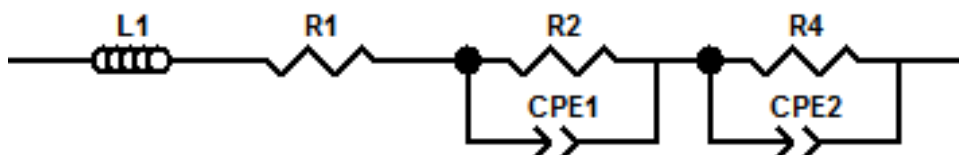


Figure 6.24- Representation of the equivalent circuit for the fuel cell with GDC electrolyte.

This means that two polarization components are observed.

On the other hand, the equivalent circuit for the cell with GDC electrolyte shows a polarization phenomenon that is attributed to the small polarization arc from 1.0 kHz to 43Hz, while the other component at frequency between 43Hz-0.1Hz is attributed to the finite length Warburg element-open circuit terminus, as shown in figure 6.25:

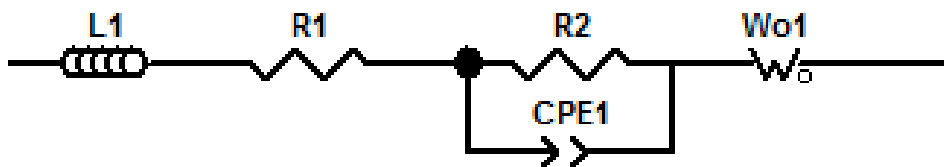
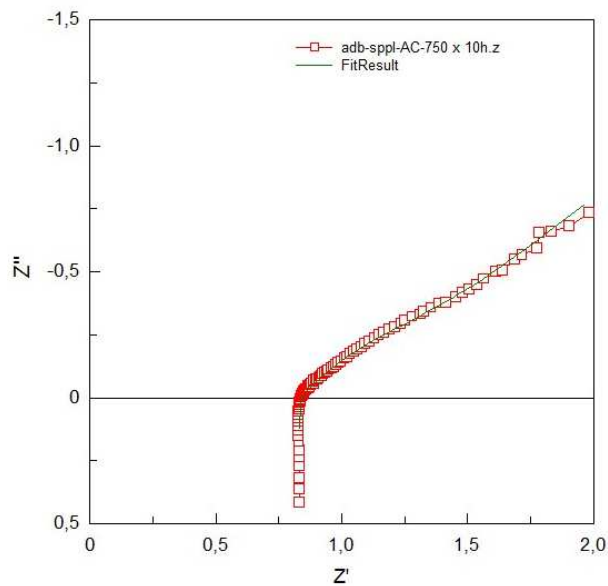


Figure 6.25- Representation of the equivalent circuit for the fuel cell with YSZ electrolyte and protection layer GDC.

The finite length Warburg element-open circuit terminus is the solution for one dimensional diffusion. This element is associated to the resistance of the diffusion of a species through a layer of finite length. This means that for during the diffusion, some species remain for a long period in the diffusion path. Applying this equivalent circuit to the AC impedance, it fits perfectly with the experimental curve, as shown in figure 6.26:



Fitting data obtained by Zview

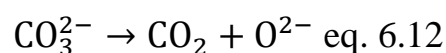
Component	Resistance value
L1	1 E-6
R1	0.823
R2	0.2
CPE1	0.7
W <sub>R</sub>	2.29
W <sub>P</sub>	0.4211

Figure 6.25- Fit curve for the AC impedance spectra of cell with YSZ electrolyte and GDC protection layer collected at 750°C in range of frequencies set up between 20 MHz-0.1Hz.

#### 6.4.1. Presence of CO<sub>2</sub> has a major influence on DCFC behaviour

Some of the parameters that have the greatest effect on the variation of OCV are the partial pressure of carbon dioxide, carbon monoxide and oxygen because of their effect on the EMF, as explained in paragraph 6.3.

Purging CO<sub>2</sub> stabilises the atmosphere inside the anodic chamber. Secondly, gas flow helps the transport of the fuel and carbonate around the anodic chamber. Thirdly, flux of carbon dioxide into the anodic chamber prevents the decomposition of carbonate salts, as shown in eq. 6.12:



In fact, a higher concentration of carbon dioxide shifts the equilibrium towards the carbonate ions. For the aforementioned reasons, in order to enhance the OCV and electrical performance of the cell, both cell configurations were tested again under CO<sub>2</sub> gas under intermittent flows of 40 ml/min for short spells of time: 1min, 5min and 10min. The best results were obtained purging CO<sub>2</sub> into the cell for 5min after each interval of 100°C increase in temperature, starting at 500°C. The carbon dioxide was purged at intervals in order to prevent the excess of carbon dioxide favouring the formation of carbon monoxide, following the reaction:



The formation of CO in the anode chamber due to the reaction shown in the eq. 6.13 produces an alternative fuel but an excess of CO produces a double effect: Firstly, it works as a reducing agent, reducing Ce(IV) to Ce(III) and consequently this increases the electron conductivity of the electrolyte. Secondly, a large excess of CO affects the voltage of the cell.

The results provided by the cell into which gases were purged are shown in figures 6.24 and 6.25:

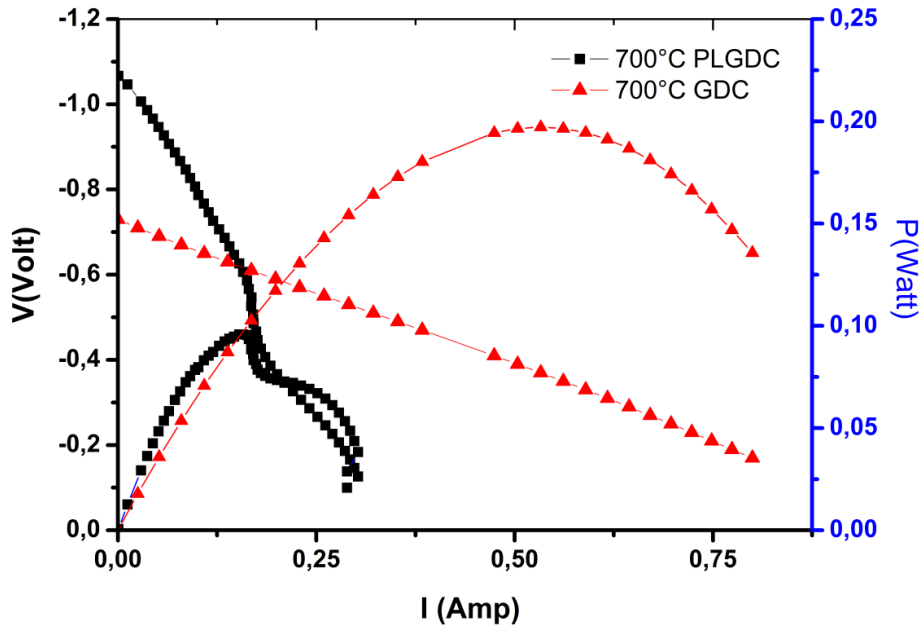


Figure 6.24- I-V curve carried out at 700°C. Data was recorded after pumping CO<sub>2</sub> for a period of 5min at a flow rate of 40ml/min; ▲ Cell with GDC electrolyte 300 μm-thick; ■ Cell with GDC used as protection layer (LP) on YSZ electrolyte.

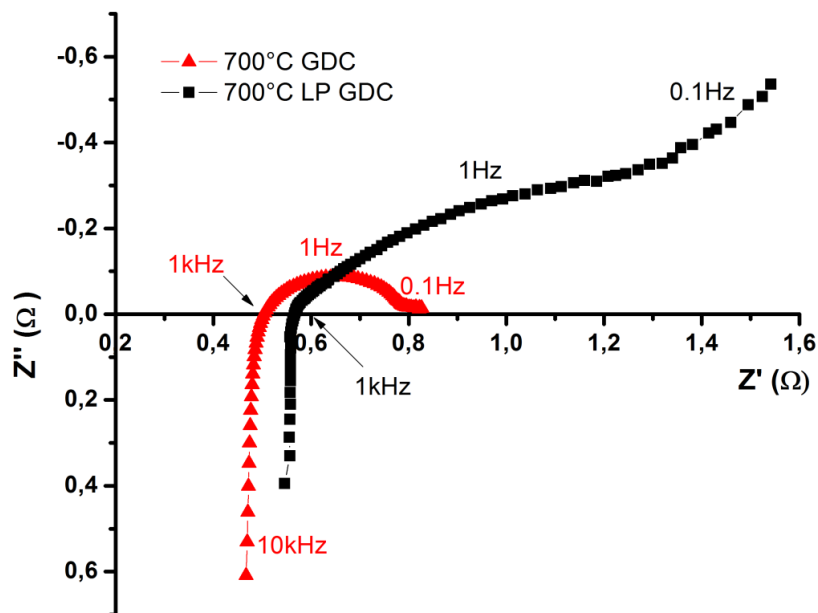
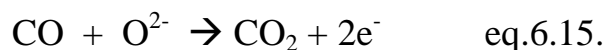
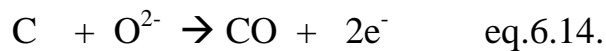


Figure 6.25- AC impedance spectra carried out at OCV at 700°C. Data were recorded after pumping of CO<sub>2</sub> for a period of 5min at a flow rate of 40ml/min; ▲ Cell with 300 μm-thick GDC electrolyte ■ Cell with GDC used as protection layer on YSZ electrolyte [156].

The highest performance was recorded at 700°C for observing a power production of 0.191 W and an  $R_s$  value of 0.5 Ohm, double the power produced by the cell with YSZ electrolyte and GDC protection layer. This significant power increase is mainly due to the effect of gas which enhances the transport of the mass of fuel inside the anodic chamber, improving the electrochemical phenomena. The evidence of mass transport limitation is clear in the I-V plot of GDC used as protection layer. The sharp drop in the curve in the maximum of power is most likely due to the bubbles of gas that are produced at the anode surface between carbon and oxygen ions. In addition, the two different arcs shown in the power curve (figure 6.25) represent two different electrochemical reactions that take place at the anode surface.



On the other hand, GDC electrolyte shows better ionic conductivity and the catalytic activity for carbon oxidation did not show more than one arc on the power curve. However, its performance is limited at high temperature by the effect of electronic conductivity, which is representative of the significant drop in open circuit voltage that is observed. In fact, a voltage of 1.08V was recorded at

---

700°C for the configuration that used YSZ electrolyte in combination with a protection layer, whilst a voltage of 0.72V was recorded for the configuration that used GDC as electrolyte. However, this value is smaller than the value expected for GDC, which should be around 0.90V. This difference of 0.18V could be caused by leaks that drive the reaction in the anode chamber.

AC impedance spectrum in figure 6.25 does not show a marked difference in the ohmic resistance value ( $R_s$ ) but it shows a noticeable difference in polarization resistance ( $R_p$ ) which is the result of the contribution of the diffusion of ions and gases at low frequency when GDC is used as a protection layer. At first this difference appeared surprising; however, it simply reflects the facilitation of the electrochemical reaction at applied potentials. On applying potential to a DCFC using YSZ or GDC protected YSZ, the diffusion element of a polarisation arc decreases as oxygen becomes more available. This also seems to occur with GDC due to oxygen leakage through the electrolyte.

The capacitance values obtained by the equivalent circuit simulation were  $10^{-2}$  and  $10^{-4}$  F for GDC and GDC/YSZ. This could be interpreted as ion diffusion limitation as gas diffusion should be independent of temperature[156].

6.4.2. Effect of GDC thickness on the  $R_s$  value

The thickness of the electrolyte is an important parameter because the oxygen flow is inversely proportional to the thickness, in accordance with the Fick equation:

$$\frac{\partial \phi}{\partial t} = -D \frac{\partial^2 C}{\partial x^2} \quad \text{eq. 6.16.}$$

Where the  $\phi$  concentration per volume unit [ $\text{mol m}^{-3}$ ],  $t$  is the time and  $D$  is the constant of diffusion [ $\text{m}^2 \text{s}^{-1}$ ]. For this reason, three different electrolyte tapes of thickness  $300\mu\text{m}$ ,  $200\mu\text{m}$  and  $120\mu\text{m}$  were tested, as shown in figure 6.26:

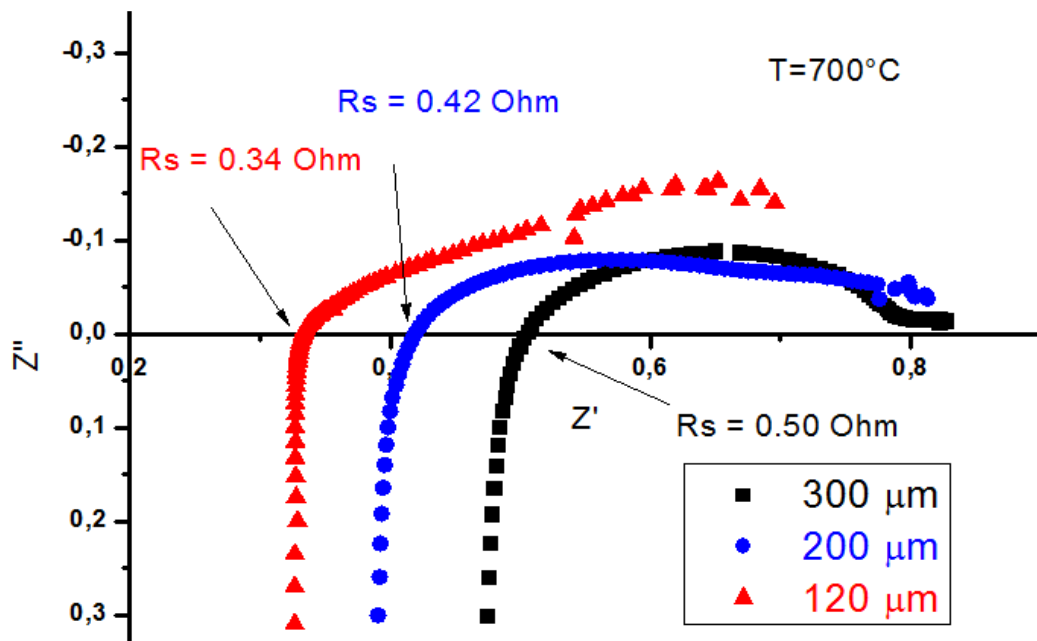


Figure 6.26- AC impedance spectra of HDCFC using different electrolyte thicknesses. The AC impedance data shown were carried out at  $700^\circ\text{C}$  under  $5\text{ml/min}$  of  $\text{CO}_2$  gas flow and  $15\text{ml/min}$  of nitrogen.

The AC impedance carried out at 700°C showed an improvement of the  $R_s$  but the  $R_p$  value is slightly different for the three different AC impedance spectra. These differences could be linked to the increase in oxygen flow to the anode and consequently the concentration of oxygen ions that can react with carbon, also increasing gas produced at the anode.

The performances achieved are better than those obtained with the cell that used a thicker electrolyte, yet the differences between the three cells are not particularly marked.

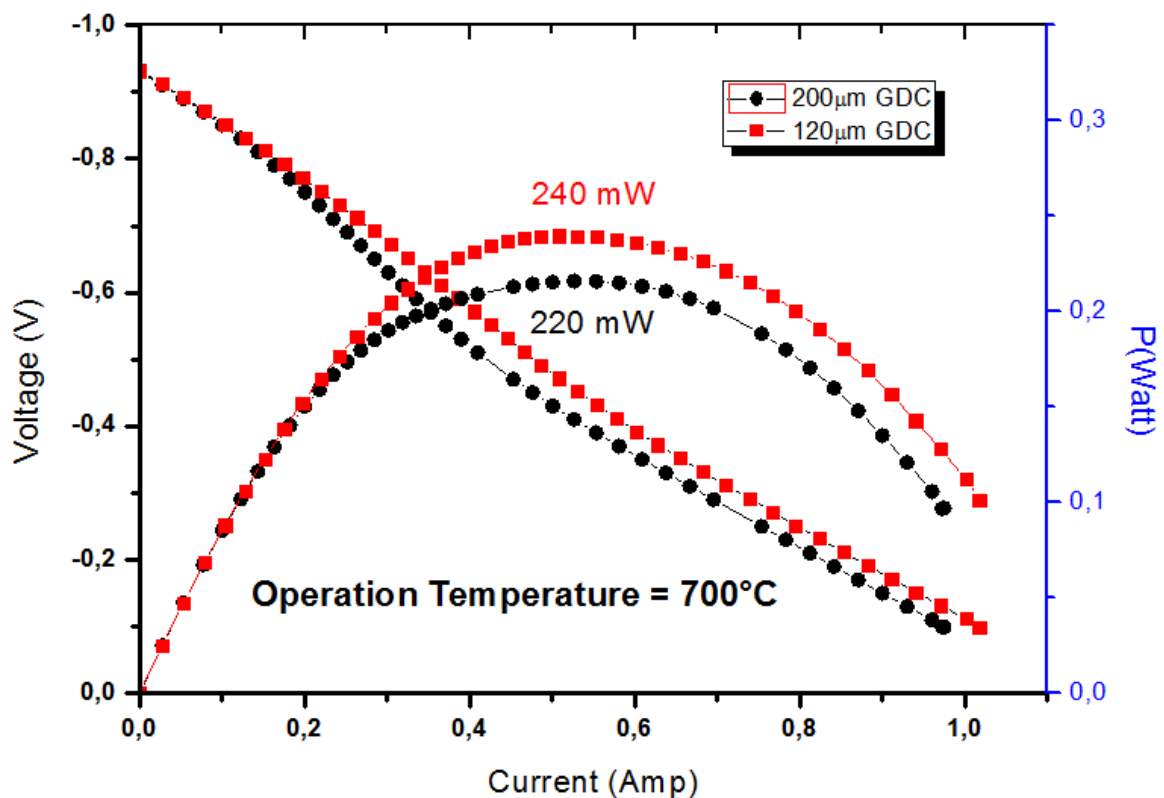


Figure 6.27- I-V curve of cell with GDC electrolyte cast at different thickness. Tests were carried out at 700°C under CO<sub>2</sub> gas flow and nitrogen.

The minor differences in terms of performance between the two cells can be justified by the limited electro-catalytic activity of the LSM on the reduction of oxygen ions at its surface. These limitations could be caused by the sintering temperature, which affects the porosity of the cathode and consequently the TPB and solid state reactions that occur at high temperature.

The limitation is thought to be due to the porosity rather than solid state reactions, because no extra peaks were observed by the XRD spectra of LSM-GDC cathode sintered at 1400°C for 5h, as shown in figure 6.28:

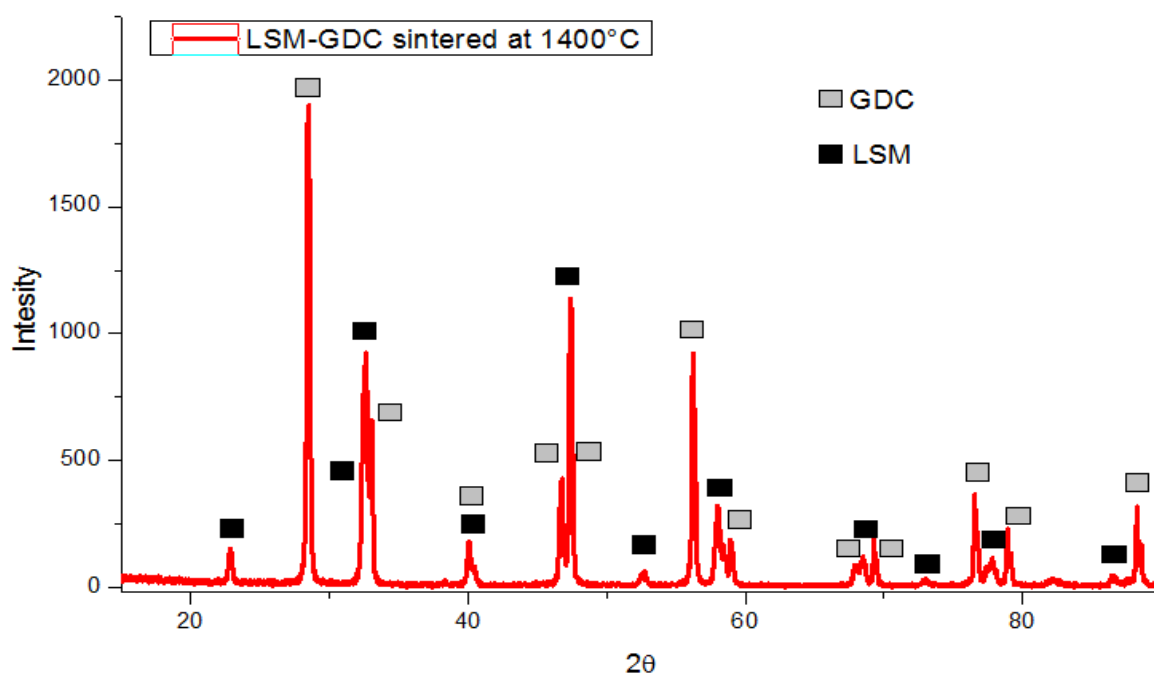


Figure 6.28- XRD spectrum of LSM-GDC cathode sintered at 1400°C for 5h. The test was carried out with a Philips x-ray powder diffractor.

The XRD pattern was interpreted by PDF and no extra peaks were observed. This confirmed that the performance of the cell is not limited by solid state reactions that usually occur at high temperature.

At this point, the limitation is most likely due to porosity and the triple phase boundary surface. In fact, the porosity is reduced at high temperature because the materials tend to produce a bulk with high density. A higher density causes a decrease in the triple phase boundary which reduces electro-catalytic activity.

### **6.5. Effect of different type and manufacture of cathode on fuel cell performance**

As explained in chapter 5, the manufacture and chemical properties of the cathode affect the performance of the cell because at the surface the electro-catalytic activity limits the production of oxygen ions, thus limiting the performance of the cell. In the next paragraphs, the effect of cathode manufacture on the performance of the cell will be analysed, as well as the effect of using a cathode based on LSCF for intermediate temperature SOFC.

#### 6.5.1. Studies of painted LSM–GDC cathode on HDCFC performance

The conventional HDCFC was prepared merging anode, electrolyte and cathode tape and each tape was then co-sintered at 1400°C. This temperature is ideal for the anode and electrolyte to have a well-sintered layer. However, that temperature is not ideal for the cathode, both because of the possible solid state reactions

---

between LSM and GDC and the final density of the cathode (see chapter 4 paragraph 4.2.3.2). For this reason, the anode tape (60 $\mu\text{m}$ ) and electrolyte tape (120 $\mu\text{m}$ ) were merged and sintered at 1410 $^{\circ}\text{C}$  and after sintering, the cathodes were painted and sintered separately at 1200 $^{\circ}\text{C}$  for 3hrs. The length of the cathode was around 7 cm. After this, the pure LSM current collector was painted and sintered at 850 $^{\circ}\text{C}$  for 2hrs. The cell was then tested following the same procedure used in previous tests. The results are shown in figure 6.29:

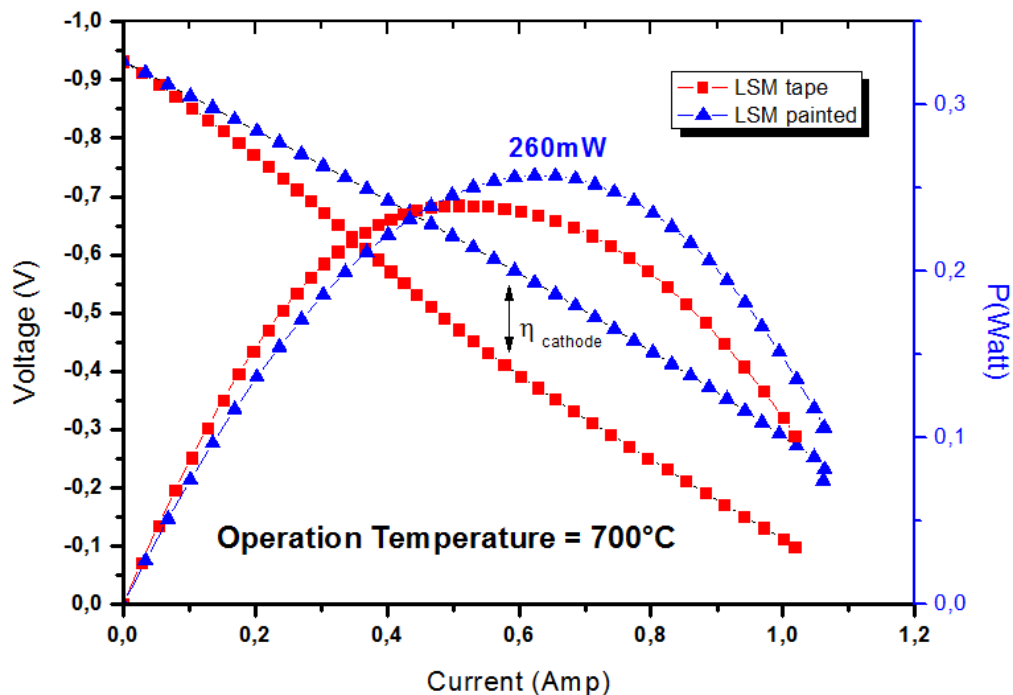


Figure 6.29- I-V curve of two cells NiO-GDC|GDC|LSM-GDC in which the cathode is manufactured in different ways. Tests were carried out at 700 $^{\circ}\text{C}$  purging  $\text{CO}_2$  and  $\text{N}_2$  into the anode chamber using a flow rate of 8ml/min and 15ml/min.

Results seem to confirm the limitations due to the manufacturing conditions of the cathode. In fact, an effect on polarization is clearly visible from the I-V curve.

The difference between the curves could be attributed to the polarization of the cathode. The cells tested use the same anode so the difference between the two cells is provided by the cathode.

#### 6.5.2. Studies of painted LSCF–GDC cathode on HDCF performance

The performance of cells with the painted LSM-GDC cathode produced interesting results. However, the aim of the project is to focus on obtaining good performance at lower temperatures. In previous work carried out at the University of St Andrews, the operation temperature was 800°C. In the new project, the operation temperature was decreased by 100°C, whilst tripling the value of power produced by the cell.

In the state of the art, the LSM cathode is employed in high temperature solid oxide fuel cells. For this reason, a new perovskite cathode was used to work at lower temperatures. In previous tests carried out, cells were in symmetrical configuration and interesting results were achieved at low temperature compared with the LSM cathode (see chapter 4 paragraph 4.2.3). The LSCF-GDC cathode was painted on the electrolyte of the tubular cell, which had been previously co-sintered with the anode at 1410°C. The length of the painted cathode was 7cm, like the LSM-GDC cathode. The LSCF-GDC cathode was then sintered at 1100°C for 3h while the LSCF current collector was sintered at 800°C for 3 h. The cell was tested using a Solatron 1280B and the results obtained are shown in figure 6.30:

---

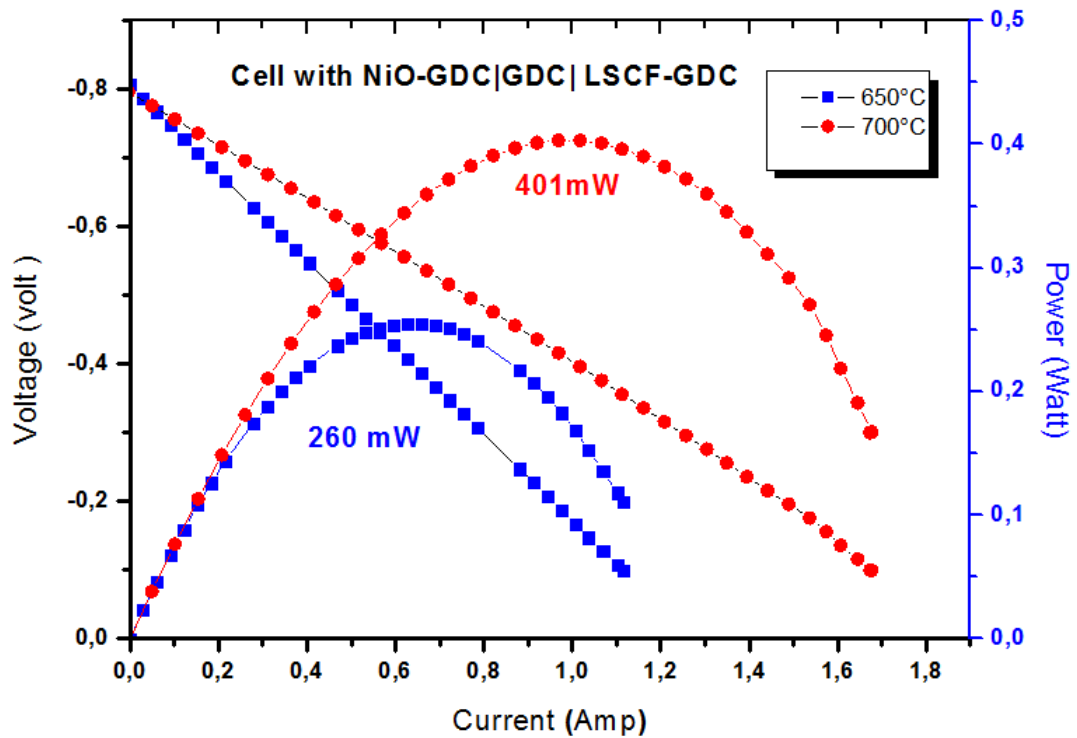


Figure 6.30- I-V curve of cell with LSCF-GDC cathode was painted on the electrolyte and sintered at 1100°C. Tests were carried out at 650°C and 700°C under CO<sub>2</sub> gas flow and nitrogen.

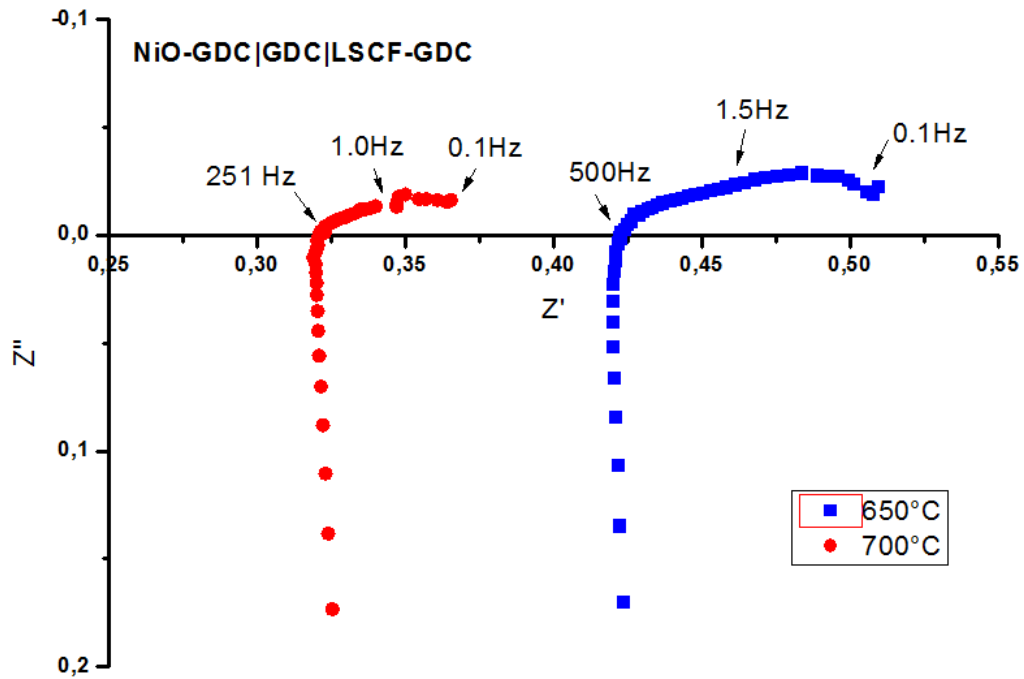


Figure 6.31- AC impedance spectra curve of cell with LSCF-GDC cathode painted on the electrolyte and sintered at 1100°C. Tests were carried out at 650°C and 700°C under CO<sub>2</sub> gas flow and nitrogen.

The AC impedance spectrum shows a low polarization arc. This is attributable to the high catalytic activity of LSCF. The AC spectra show two semi arcs and these are more noticeable in the AC spectra carried out at 650°C. The first arc is due to the polarization resistance produced by the cathode. The second arc is the effect produced by the current collector; its behaviour is comparable to that of a condenser.

The representation of the equivalent circuit is shown in figure 6.32:

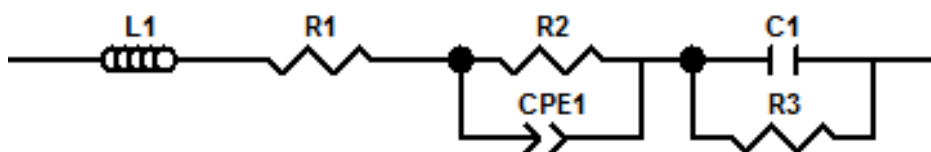
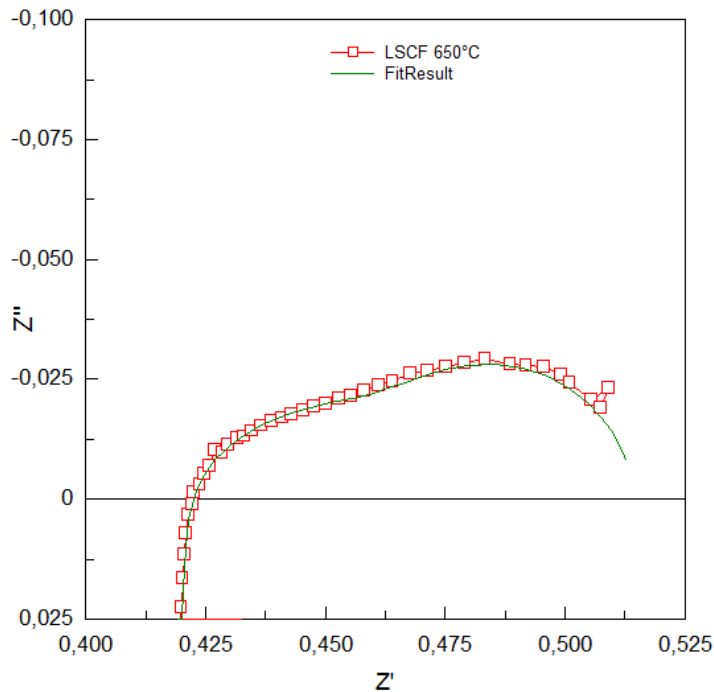


Figure 6.32- Equivalent circuit of the cell with NiO-GDC|GDC|LSCG-GDC which was determined using Zview software.

The fit of the equivalent circuit is shown in figure 6.33:



Fitting data obtained by Zview

Component	Resistance value
L1	4.22 E-6
R1	0.41
R2	0.053
CPE1	0.68
C1	5.436
R3	0.041

Figure 6.33- Fit of AC impedance curve of HDCFC with LSCF-GDC cathode achieved at 650°C.

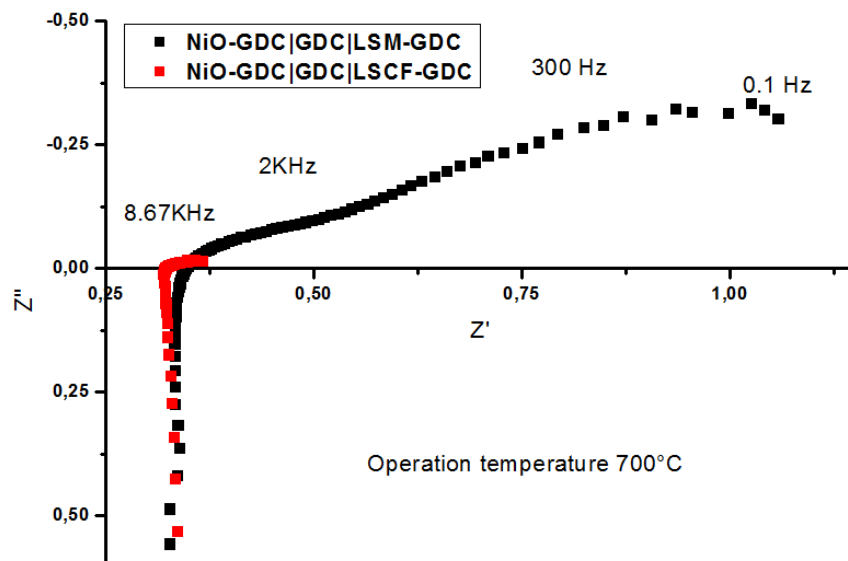


Figure 6.34- AC impedance spectra of cell with LSCF-GDC cathode and cell with LSM-GDC cathode. Tests were carried out at 700°C under CO<sub>2</sub> gas flow and nitrogen.

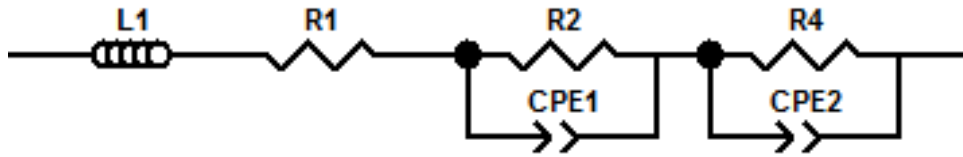


Figure 6.35- Equivalent circuit of the cell with NiO-GDC|GDC|LSCG-GDC which was determined using Zview software.

As observed on the I-V curve above, the effect of the LSCF-GDC cathode is highly significant with regards to the electrocatalytic effect and the limitations previously illustrated.

The difference between the cell with LSM and LSCF is clearly visible in terms of power produced.

### 6.5.3. Effect of LSCF on the operation temperature

As described previously, the performance achieved with the configuration NiO-GDC|GDC|LSFC-GDC was double that of the NiO-GDC|GDC|LSM-GDC at an operation temperature of 700°C.

The scope of the project was to reduce the operation temperature in order to prevent corrosion and problems caused by high temperature.

The interesting thing in using LSCF was the high performance achieved at low temperature (650°C), as shown in figure 6.36:

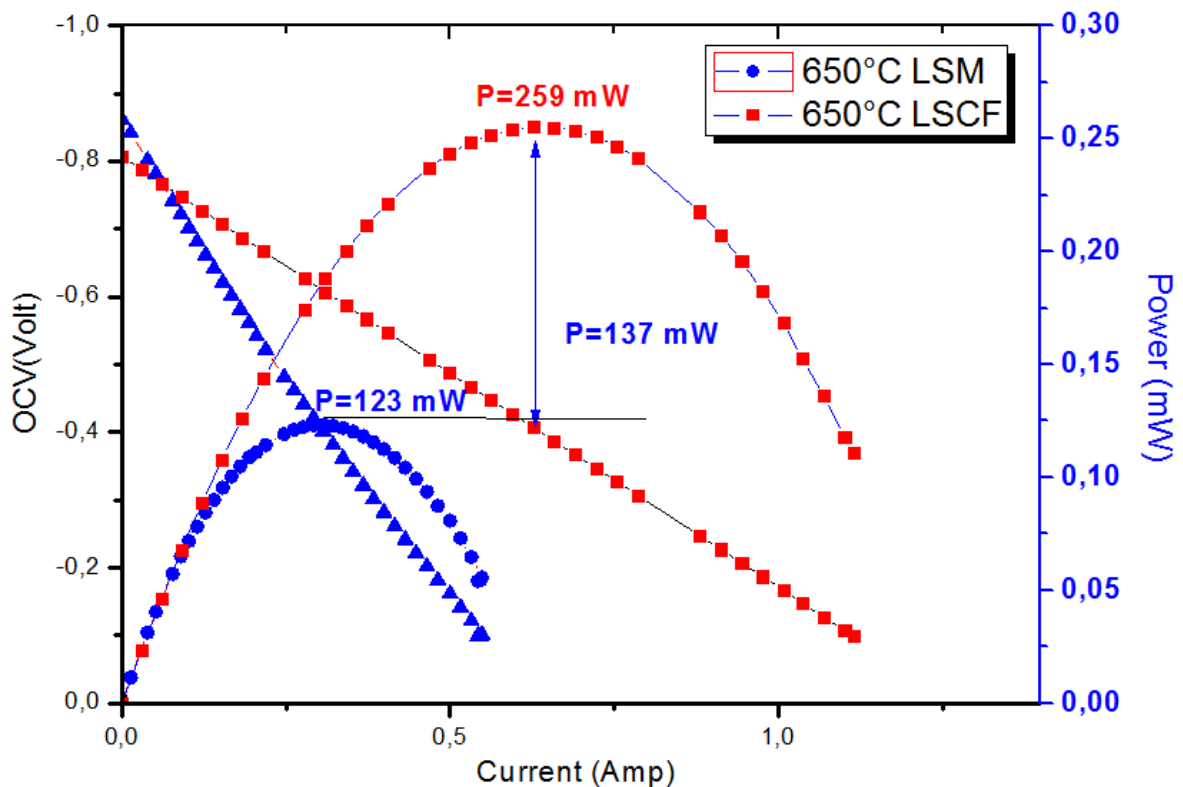


Figure 6.36- I-V curve of two different cells with LSCF-GDC and LSM-GDC cathodes painted on the electrolyte and sintered at 1100°C and 1200°C respectively. Tests carried out at 650°C under CO<sub>2</sub> gas flow and nitrogen.

The performance obtained at 650°C was particularly good. In fact, the gap in power between the NiO-GDC|GDC|LSM-GDC configuration and NiO-GDC|GDC|LSCF-GDC was 137mW. However, the interesting thing about this result is the energy produced at 650°C, which is the same amount as obtained at 700°C using the NiO-GDC|GDC|LSM-GDC configuration.

## 6.6. Summary

In this chapter several points are tackled regarding sealing, electrical contacts, effect of gas and cathode manufacturing on the performance of HDCFC.

The sealing process and seal materials investigated provided important information. The best performance was achieved by using a composite seal composed of flexible mica disk, alumina fibre disk and alumina paste (P-24 Toku). Regarding the electrical configuration, the results achieved highlighted that the second configuration, consisting of a nickel mesh strip interwoven with a silver wire, showed higher performance than others. The cause of this was attributed to the current collector surface area.

Replacing GDC electrolyte with YSZ has improved the performance of the whole cell. The improvement was confirmed by the comparison between a fuel cell with GDC electrolyte and YSZ electrolyte, where the cell with GDC electrolyte reached a maximum power value of 0.191W at 700°C.

The LSM cathode performances were improved when the cathode preparation method and the sintering temperature were changed. In fact, the performance of the cathode improved when the cathode was painted and sintered at 1200°C rather than prepared by tape casting process and co-sintered at 1400°C with the electrolyte. This high temperature reduced the surface area of the cathode and consequently the triple phase boundary, thus reducing performance. Studies on an alternative LSCF–GDC cathode were carried out, showing promising

---

results. In fact, studies showed an important improvement in the cathode performance  $R_p$  both at high temperature and low temperature. The improvement of the LSCF-GDC performance was also observed when it was employed in the whole cell. In fact, a value of power 260mW was achieved at 650°C, which is significant compared to same results obtained at 700°C using LSM-GDC cathode.

## 6.7. References

- [150] S.L. Jain et al. *Solid State Ionics* 179 (2008) 1417–1421
- [151] Yoshiyuki Izakia, et al. *J. Power Sources* (1998) 75, Issue 2, pag 236-24
- [152] Silvera Scaccia and Stefano Frangini - *J. Fuel Cell Sci. Technol.* - 3 (2006) Issue 2, 208
- [153] G. Wypych, *Handbook of Fillers – A Definitive User’s, Guide and Databook*, 2nd Edn., ChemTec Publishing, Toronto, Canada 2000.
- [154] Feodor Burgmann Dichtungswerke GmbH & Co, *Sealing Technol.* 2000, 6.
- [155] *Threebond Technical News* – Issue January 1, 2003
- [156] A. Damiano Bonaccorso and John TS. Irvine – *IJHE* -2012 -in press-



## 7. Conclusions

Carbon fuels produced by pyrolysis process were characterized by several types of analysis in order to compare their physical chemistry characteristics with the carbon fuel performance. The best result was achieved for mdf and graphite while the worse result was achieved for carbon beer. Graphite and mdf are two carbon fuels with crystalline and amorphous structures respectively, yet they demonstrated comparable performance in terms of power. This suggests that the structure does not affect the performance of the fuel. Instead, the performance of the cell was related to the percentage of functional groups present in the carbon structure and consequently to the reactivity of each sample. In fact, partially pyrolysed carbon beer has a large number of reactive groups which react easily with carbonate. Thus, the high number of functional groups favoured the gasification of carbon, reducing the amount of carbon available for electrochemical oxidation at the anode surface.

YSZ electrolyte is a purely ionic conductor and is stable under reducing conditions. In fact, the impedance arcs achieved both under oxidizing atmosphere and reducing atmosphere were not affected. This stability is particularly important because it does not cause any current leakages during the operation conditions.

On the other hand, the electrochemical performance of YSZ is lower at low temperature. In fact, the AC impedance carried out at 550°C both for YSZ and GDC shows a significant difference in total resistance. Another advantage of GDC electrolyte is that it is a good catalyst for the hydrocarbon. The sum of these advantages was visible when YSZ and GDC were used as electrolyte in the HDCFC. The cell with GDC showed double the value of power compared to the YSZ electrolyte. However, GDC has the disadvantage of being partially electronically conductive above 650°C, while YSZ is totally ionically conductive, achieving a lower OCV voltage than that observed for YSZ.

A different anode composition was investigated in order to find the best composition and cathode material. The anode composition with NiO/GDC in percentage 60-40%v seemed to be the best compromise from the performance achieved by AC impedance spectroscopy. In fact, the large amount of NiO in the anode (around 80% mass) had minimal dimensional stability because the amount of GDC was not enough to create a stable interface between the anode and electrolyte. In addition, the high percentage of Ni metal after reduction produced high electronic conductivity showed by the AC impedance that could have caused a short circuit in the direct carbon cell. The electronic conductivity was provide also by the reduction of Ce(IV) to Ceria (III) in reducing environment. The electron conductivity decreased when the Ni percentage was 60% V.

---

Different composite cathodes were investigated. The LSM cathodes with GDC instead of YSZ showed better performance due to the GDC activity. In fact, GDC is a better ion conductor than YSZ, as shown previously. The LSM cathode performances were improved when the cathode preparation method and the sintering temperature were changed. In fact, the performance of the cathode improved when the cathode was painted and sintered at 1200°C rather than prepared by tape casting process and co-sintered at 1400°C with the electrolyte. This high temperature reduced the surface area of the cathode and consequently the triple phase boundary, thus reducing performance. Studies on an alternative LSCF–GDC cathode were carried out, showing promising results. In fact, studies showed an important improvement in the cathode performance  $R_p$  both at high temperature and low temperature.

In order to improve the performance of the final cell, the seal materials, sealing process, electrical configuration and several fuel cell configurations were investigated.

The sealing process and seal materials investigated provided important information. The best performance was achieved by using a composite seal composed of flexible mica disk, alumina fibre disk and alumina paste (P-24 Toku). This composite seal strongly reduced diffusion and surface contact leakage phenomena. In fact, using only alumina paste was not enough to prevent the types of leakage mentioned previously.

---

Regarding the electrical configuration, the results achieved highlighted that the second configuration, consisting of a nickel mesh strip interwoven with a silver wire, showed higher performance than others. The cause of this was attributed to the current collector surface area. In fact, in the first configuration, in which only silver wire was used, the lower surface area of the current collector caused an increase both in ohmic resistance and polarization resistance. In the third configuration, in which the current collector was composed of nickel mesh strip interwoven with a silver wire, the performance achieved was worse because of the molten carbonate slurry. In fact, the latter was the principal factor responsible for the large increase in total resistance.

The gases in the anodic chamber affect the performance of the cell. In particular, carbon dioxide was used to prevent carbonate decomposition and in addition the carbon dioxide purged into the anodic chamber improved the transport of carbon fuel throughout the whole anode, thus increasing the number of reactions between carbon fuel and oxygen ions and consequently the number of electrons.

The better performance of GDC electrolyte compared to YSZ was confirmed by the comparison between a fuel cell with GDC electrolyte and YSZ electrolyte where the cell with GDC electrolyte reached a maximum power value of 0.191W at 700°C. The performance of the cell improved when the thickness of the electrolyte was reduced from 300 $\mu$ m to 120 $\mu$ m. The cell that used 120 $\mu$ m thick

electrolyte showed a decrease in  $R_s$  equal to 0.15 Ohm that corresponded to an increase of power from 200mW to 260mW.

The cell performance was further improved when the LSM-GDC cathode manufacturing process was changed, as well as when the LSM-GDC cathode was replaced with LSCF-GDC.

Starting from the manufacturing process and sintering temperature, it was evident that cells achieved better performance when the LSM-GDC cathode was painted and sintered separately from the anode and electrolyte. In fact, the low performance achieved by the cell with the co-sintered cathode was caused by the low porosity of the cathode, which was directly responsible for the decrease of the TPB. In fact, no solid state reactions were observed by XRD tests carried out on the cathode sintered at 1400°C.

This limitation on the cell performance was not solely caused by the decrease in cathode porosity, but also by the microstructure of the cathode. In fact, replacing a commercial LSM cathode with LSCF cathode, which is a cathode for low temperature SOFC, an important decrease in polarization resistance and consequently an increase in cell performance were observed. The key to this improvement in performance was the perovskite structure doped with Sr and Fe at the A and B sites respectively, which improved the oxygen ion diffusion because of the increase in oxygen vacancies.

The LSCF cathode has been shown to be a good substitute for classic commercial LSM because it works better at lower temperature (650°C) than LSM, achieving the same power that LSM produces at 700°C.

### 7.1. Future Work

As described in paragraph 7, the hybrid direct carbon fuel cell has shown to be a promising technology both because of the high value of power obtained and because it is able to convert all forms of biomass into carbon. These good results are a solid starting point for fully understanding the real performance of the cell. It is important that future research continues to closely study this technology in order to understand its effective potential following the points listed below:

1. Design a system which can keep carbon fuelling at the anode side constant.
2. Studies of long term stability of the cell that enable the study of degradative phenomena of the cell and the performance of the carbon fuel over a longer period.
3. Combining studies of AC impedance with gas chromatography in order to correlate the gas formation with electrochemical phenomena that take place in the anode chamber.
4. Studies of binary and ternary mixture of molten carbonate salts in order to decrease the melting point of Li-K carbonate mixture.
5. Studies of new carbons derived from pyrolysis of plastic materials such as tyre.